Piezoelectric micro-generators for energy harvesting applications

Emilie Trioux

UNIVERSITÉ GRENOBLE ALPES

THÈSE

Pour obtenir le grade de

DOCTEUR DE L'UNIVERSITÉ GRENOBLE ALPES

Spécialité : **Nanoélectronique et Nanotechnologies**

Arrêté ministériel : 7 août 2006

Présentée par

Emilie TRIOUX

Thèse dirigée par **Skandar BASROUR** et
codirigée par **Paul MURALT**

préparée au sein du **Laboratoire TIMA**
dans **l'École Doctorale Electronique, Electrotechnique, Automatisme et Traitement du Signal**

Micro-générateurs piézoélectriques pour des applications de récupération d'énergie.

Thèse soutenue publiquement le **25 Novembre 2015**
devant le jury composé de :

M. Elie LEFEUVRE
Professeur, Université Paris-Sud, Président
M. Emmanuel DEFAY
Ingénieur Docteur, Luxembourg Institute of Science and Technology, Rapporteur
M. Christophe MALHAIRE
Maître de Conférence, INSA Lyon. Rapporteur
M. Skandar BASROUR
Professeur, Université Grenoble Alpes, Directeur de thèse
M. Paul MURALT
Professeur, Ecole Polytechnique Fédérale de Lausanne, Co-directeur
M. Stéphane MONFRAY
Ingénieur Docteur, STMicroelectronics, Membre
M. Thomas SKOTNICKI
Directeur produits R&D, STMicroelectronics, Invité

Acknowledgements

For sure all this work would not have been possible without the help of numerous people that I would like to thank warmly. They contributed not only to the scientific aspect but also to the human aspect and make these three years of PhD a good time.

First of all I would like to thank my two supervisors, Skandar Basrour and Paul Muralt, for their constant optimism and enthusiasm, and their profusion of ideas to improve and guide my work. It was a really pleasure to work with them, for their expertise in their respective scientific field, but also for their very human contact. I would like especially to thank Paul for his contribution to my general knowledge on Swiss and French history, and Skandar for the interesting discussions we had around a good “espresso italiano”.

A special thought goes to Pascal Ancey, my first STMicroelectronics manager, who was full of energy and sadly passed away after my first year of PhD. Then I am really grateful to Stéphane Monfray from Advanced Devices group in STMicroelectronics for his support and Thomas Skotnicki for initiating this project.

I also wish to thank the members of the jury for their participation, their expertise and their helpful comments. They showed curiosity and interest in my work and accepted to make sometimes a long trip to come to Grenoble for my defense. In particular I would like to thank Elie Lefeuvre who accepted the presidency of the jury and Christophe Malhaire and Emmanuel Defaÿ who accepted to review my manuscript.

I have been honored to work in both TIMA laboratory in Grenoble and Ceramics Laboratory in EPFL. I thank Dominique Borrione and Salvador Mir to have welcomed me in TIMA during my thesis, and Nava Setter to have hosted me during nearly two years in her laboratory in EPFL as I were a full member of the team. They provided me with all the necessary means to carry out my work in excellent conditions.

All the fabrication realized during this thesis would not have been possible without the help of the staff working in the Center of Micro and Nanotechnologies in EPFL. I warmly thank all of them for their availability and knowledge of the different machines and processes, especially Cyrille Hibert and Anthony Guillet for the etching processes and characterization machines, Georges-André Racine and Valérian Ruhault for the photolithography processes, Guy Clerc for

the sputtering deposition and finally Jeoffrey Pernollet and Zdenek Benes for the SEM imaging. I particularly thank Patrick Madlinger who was doing the maintenance of the different machines whistling, which contribute to make the cleanroom less boring.

I received a lot of help also in Grenoble from people of CIME (Centre Interuniversitaire de MicroElectronique et Nanotechnologies) where I was performing the electrical characterization of the devices and using the servers for finite elements simulations. I warmly thank Alejandro Chagoya for his infinite kindness and availability, Loïc Vincent for the fruitful discussions and his help to find a good amplifier to collect the charges and finally Irène Peck for the bonding of some devices.

A huge “thank you” goes to my office mates in EPFL, Nachiappan and Davide, who tolerated me for nearly two years with all my questions about piezoelectricity, cleanroom processes and everything else. They patiently listened to me and answered every question. We shared our frustration and our happiness concerning CMi adventures. I wish them a successful future.
Then I would like to thank all the people from Paul’s group: Ramin, Cosmin and Andrea for their help and all the fruitful discussion we had. I am very grateful to all the people from LC lab, which contributed to my good stay in Lausanne (at work but also outside): Arnaud, for the gym lessons and morning coffee, Leo, Alex, Bàrbara, Piotr, Kostya, Kaushik, for all the cultural moments, Lino, Tomas, Sacha, Dragan, Alberto, Ludwig, Priscilla, Francesco...

The same huge “thank you” goes to my office mates in TIMA, François and Quentin, who tolerated me during the despair of characterization and the foolish moment of writing. They were always encouraging me, pushing me ahead and helping me with every aspect of my thesis. We shared memorable moments in front of a good beer or on top of a mountain.
I would like to thank also the rest of the group for their curiosity and their help: Libor, Ismail, Achraf, Adrian and Vincenzo.

Finally, I would like to thank my parents, Christian and Josette, and my little sister Amandine, for their constant support in the good and bad moments. A special thank to my boyfriend Jeyke his love despite of everything.

Table of contents

Figures

Tables

General Introduction

This PhD work is centered on the energy harvesting from ambient energy sources. The scope to harvest energy from the surrounding environment is to power sensors or actuators to render them energetically autonomous. These devices can then be part of a large-scale wireless sensor network, which can measure environmental parameters, send the information and even act to modify some parameters. The possible applications of this type of network are very attractive, especially for the connected, "smart" building, they can be placed everywhere in order to harvest different kind of energy. Applications in the environmental control of the pressure or hygrometry for instance, or the human body monitoring are also gaining a lot of interest because of their difficult access and replacement. All of these actions are possible because the electronics powering the sensors and actuators are consuming less and less power, and the energy harvested from the surroundings is sufficient to power them. More and more batteries are replaced by harvesting systems, which transform the always-available ambient energy into electrical power and do not need to be regularly changed.

Different kinds of energy are available in the environment: radiations like solar energy, temperature under the form of a gradient or a time variation, mechanical vibrations… We decide to focus this work on harvesting thermal energy, which is always present unlike the light or the vibrations. Different transductions are available to harvest thermal energy depending on the thermal source that we dispose. Indeed for a spatial gradient of temperature, the most common transduction is using the Seebeck effect present in thermoelectric materials. On the other hand, if the temperature is varying during time, the pyroelectric transduction is more adapted. These technologies have the same effect: convert temperature variations, spatial or temporal, into electrical charges.

Here we propose an alternative to the thermoelectric materials, which are hardly compatible with CMOS processes. In a previous work, a macro prototype based on the principle of the bimetallic plate has been studied. A two-step transduction is first converting the thermal gradient into mechanical buckling, and then the huge displacements of the buckling are converted into electrical charges by a piezoelectric element. The aim of this project is to downscale this prototype in order to increase the oscillation frequency and in the same time the output power. It has to be fabricated only with standard micro-machining processes into order to very integrated at a very large scale. The challenge of this study is to adapt at microscale the

prototype already realized, to conceive and fabricate it with standard processes and to characterize it in terms of output power.

The manuscript is organized in five chapters. In the first chapter, the field of the energy harvesters is presented, with a description of devices scavenging the different kinds of energies. Their output power are compared as well as the mechanisms involved in the different types of transductions. We are focusing especially on the harvesters of small size.

The second chapter is describing the mechanisms of piezoelectricity. The characterization means to evaluate the quality of a thin piezoelectric film and its efficiency are detailed. The standard deposition processes used for thin piezoelectric films are described. The Applications of thin piezoelectric films to harvest different kind of energies is discussed, with a focus on thin films.

The third chapter is describing the analytical and numerical model governing the thermal buckling mechanism of the bilayer beam. In a first time, the shape of the structure after fabrication is investigated, as well as the buckling temperatures. Then a numerical analysis is modeling more precisely the shape of the structure during thermal buckling.

The fourth chapter is presenting in detail the fabrication steps used to realize the harvester. The choices of the materials and geometries are discussed, especially the way to create the initial deflection of the plates. Despite the encountered issues, which will be described and solved, functional structures are fabricated.

The fifth and last chapter is discussing all the characterization means used in this project, from the quality of the piezoelectric film with the piezoelectric coefficients to the initial deflection of the plates. We will focus particularly on the electro-mechanical characterization to investigate the resonance frequencies of the different geometries and the response to mechanical actuation. Finally the output power during the thermal buckling is measured as well as the buckling temperatures.

The manuscript concludes with a general conclusion summarizing the results obtained and giving the perspectives.

I Context of the micro energy harvesting

The energy harvesting is the action to take profit of the non-used ambient energy that surrounds us and to convert it into usable energy, for instance mechanical or electrical energy. The energy harvesting at micro scale is intended to concern only the systems under the centimeter, by opposition of the macro-scale devices, which have dimensions over the centimeter. These systems are conceived to power small devices with low power consumption in order to make them autonomous from the energy point of view.

In a first time, the state-of-the-art of the energy harvesting at micro scale will be presented. All kind of energy is detailed, as well as their basic equations: the photovoltaic energy, the mechanical vibrations and finally the thermal energy. The thermal energy harvesters will be presented in details, thermoelectric and pyroelectric ones as well as some other exotic techniques. Finally the context of the present work is presented, the results obtained by the first macro prototypes are exanimated and the motivations to downscale them are discussed.

I.1 State of the art

The autonomous systems are an important scientific research field of the last decade. The aim is to make them work alone, sometimes in a harsh environment, difficult for human to reach, for a long period of time. In order to be considered as autonomous they have to be able to communicate with a remote control center and to have a renewable power source. In numerous applications, like for instance the tire pressure monitoring, it is difficult to put a sensor inside the tire with wires to communicate with the external controller… An autonomous system, besides measuring the pressure inside the tire, would need a energy harvesting system to power itself, a RF transmitter to communicate the pressure values and a microcontroller to manage the whole system.

The Wireless Sensors Network (WSN) is an interesting concept able to organize a network of autonomous sensors in order to multiply the data measured. A lot of applications exist in the smart home monitoring, vehicle preventive maintenance, or the human body area.

I.1.a Energy harvesting at micro-scale

The sensor of a WSN, in order to be energetically autonomous, has to take advantage of the energy of its surrounding environment. Nowadays the power is mostly furnished by lithium-ion batteries. They can make a system autonomous for a certain period of time depending on the power of the batteries, but they have to be recharged when all the Li ions have moved from the negative electrode to the positive electrode. There are four main energies that can be harvested at macro- and micro-scale:

- Mechanical energy under the form of vibrations or strain,
- Thermal energy,
- RF waves,
- Photovoltaic energy.

A lot of systems have been invented and successfully commercialized at macro-scale, but at micro-scale, the output power is much lower. There is a need to use a power management system in complement to be able to increase the conversion efficiency of the MEMS. In this paragraph we will first present the photovoltaic energy harvesting at micro-scale, with indoor and outdoor devices. Then we will speak about the mechanical energy harvesters (EH). The piezoelectric-based EH will be treated in the next chapter. The electrostatic, electret-based, magneto-electric energy harvesters will be detailed here. Finally we will briefly introduce the RF harvesters.

I.1.a.1 Photovoltaic micro-energy harvesters

Photovoltaic is now the most common energy harvesting system. The photovoltaic cells are converting directly the solar energy into electricity. The most efficient solar cells are fabricated for aerospace uses on satellites, but thanks to many years of research, the cost of the solar cells are lowered while keeping a good efficiency. Different technologies are available: mono-crystalline Si, poly-crystalline Si, thin films (CdTE and CIGS based), amorphous Si and other emerging technologies like organic solar cells or quantum dots cells [1]. One of the challenges of the photovoltaic technologies is to perform efficient solar cells able to harvest indoor solar energy, where the available power density is ten times lower than outdoor.

The photovoltaic is becoming more and more present in our everyday life; we can see it on roofs or on buildings. Germany was producing 38MW in 2014 only with photovoltaic systems. The most efficient solar cell available on the market is commercialized by SunPower corp., and is 19,5% efficient. The most efficient solar cell uses concentrator, a specific lens over

the cell that concentrates the light on it. The most efficient in 2015 is a four-junction solar cell with light concentrator that reaches 46% efficiency from CEA-Leti and Fraunhofer Institute for Solar Energy Systems [2]. It is based on III-V compound semiconductor materials. The concentrator is a Fresnel lens, which can concentrate the equivalent of 508 suns on the cell. The best solar cell without concentrator that uses triple-junction technology reaches 40% efficiency (from Boeing Spectrolab).

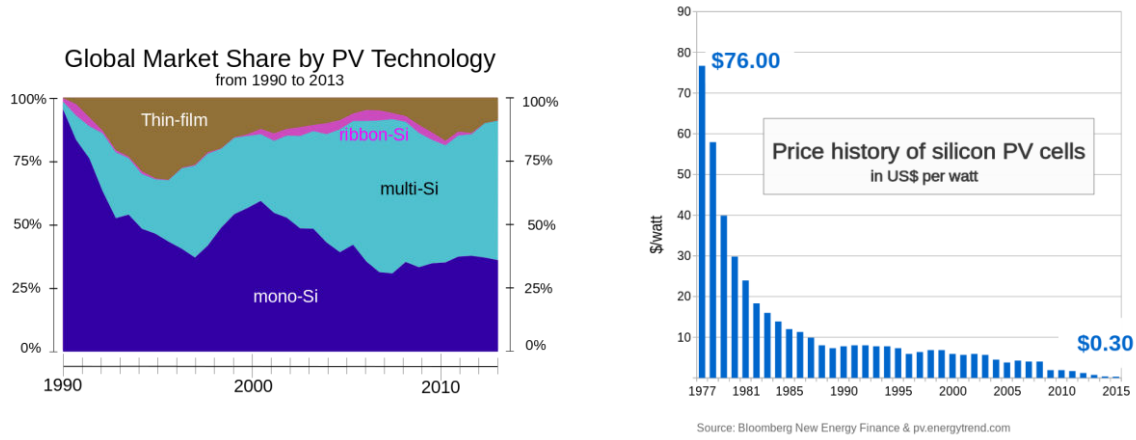

(a) (b)

Figure I-1 Repartition of the different PV technologies on the market (a) and the evolution of the price of PV over the past 40 years (b) [3]

The advantage of concentrated photovoltaic is that the dimensions of the cell can be reduced while maintaining its efficiency and a solar tracker can be added to the system to increase the efficiency of the harvesting. But there is one major inconvenient: concentrate the light on a small surface in provoking a drastic increase of the temperature. It is a critical point for solar cells as it is increasing the losses. Two solutions can resolve the problem: add a cooling system behind the solar panel, or make the solar cell even smaller to reach the microscopic scale. Indeed reducing the dimensions is increasing the thermal exchange between the cell and the environment. Moreover the micro-cells have a lot of applications, and can be integrated on cellphones, on textiles…

The research on micro solar cells showed very interesting results, comparable to the macro-scale efficiency of the solar panels. In 2013, Paire *et al.* [4] fabricated micro-cells of diameter ranging from 5 to 500µm using polycrystalline Cu(In,Ga)Se_2 (CIGS) absorber. They manage, due to the reduction of resistive and thermal losses, to increase the concentration up to 1000, with an increase of temperature less than 20°C over the ambient temperature. They measured an efficiency of 21,3% on 50µm microcell with a concentration of 475. The first

company to fabricate this kind of micro-solar cell with concentrator is Semprius. Their cell measures 600µm and the efficiency of the module ranges from 20 to 35% [5].

(a)

(b)

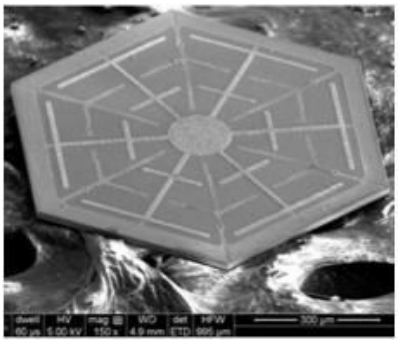

(c)

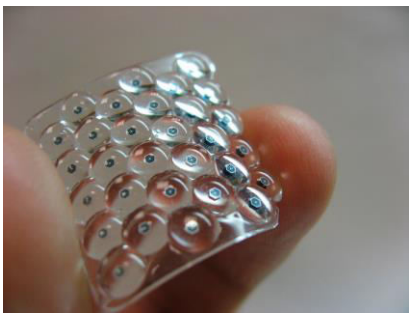

(d)

Figure I-2 Semprius micro-cell (a), Sphelar mini-dome (b) and SEM picture of a ultrathin micro-cell (c) and its module from Sandia labs (d)

Sphelar®, a Japanese company, is commercializing spherical micro solar cells. They are measuring 1 or 2mm of diameter, and a module like the one shown in Fig. I-2(b) can harvest up to 100mW. The technology is based on silicon, the core of the sphere is p-doped while a n-doped shell is surrounding it. Two electrodes, diametrically opposed, are collecting the charges. Besides, these small photovoltaic spheres can be integrated to a flexible substrate, like glass curtain walls for Building Integrated Photovoltaics [6].

Sandia Labs are producing an ultrathin micro cell with standard CMOS technologies. The thickness of the cell is between 2 to 30µm while it is 100 to 1000µm wide. The cell can then be integrated to a flexible substrate with the corresponding concentrator lenses. This technique is reducing the silicon wastes during fabrication and in the end the price of the module. They reported an efficiency of 14,9% for a 14µm thick solar cell [7][8].

Solar cells at microscale are already available, and their efficiency is comparable to macroscopic PV panels. Their advantage, besides the small size, is the enhanced thermal

exchanges, so they don't need any cooling systems compared to the macroscopic cells. They are still a bit more costly, Semprius estimated the price to be around $2 to $3 per watt, including the installation, while the macroscopic PV panels are down to $0,3 per watt.

I.1.a.2 Vibrations Micro energy harvesters

Vibrations are available everywhere in the environment, from the human body motion to the domestic activities (refrigerator, washing machine…) and the industrial machines. Each apparatus has its own resonant frequency, and the harvester has to be adapted to this specific frequency in order to be efficient. Three different transduction modes are presented: electromagnetic, electrostatic and piezoelectric. In this part we are focusing on the electromagnetic and electrostatic micro devices. The piezoelectric transduction will be explained more in details in the next chapter, with a detailed analysis of the state-of-the-art of the micro piezoelectric harvesters and the different characterization means.

Most of the devices studied are resonant devices. A general way to represent inertial vibration-based generators consists in an oscillating spring and mass system proposed by Williams and Yates [9] and presented in Fig. I-3. The input vibrations are represented as *y(t)*. The relative movement between the device and the support *z(t)*, for instance in the case of a magnetic energy harvester, it represents the movement of the magnet in the coil, corresponds also to the deflection of the spring in the Fig. I-3. $F_e(t)$ is the force generated by the electro-mechanical coupling.

For a resonant system, the spring deflection *z(t)* can be expressed as the product between the input vibrations *y(t)* and the quality factor *Q* [10]. The quality factor is given as:

$$Q = \frac{1}{2\zeta} \qquad \text{Eq. I-1}$$

ζ is a dimensionless damping ratio with the following expression : $\zeta = b/(2M\omega_n)$ where *b* is the damping constant of the system, *M* the mass of the seismic mass and ω_n the natural angular frequency. It is however more common to use the input acceleration instead of the input vibration amplitude. Finally the displacement *z(t)* can be written in function of the input acceleration *a(t)*:

$$z(t) = \frac{Qa(t)}{\omega_n^2} \qquad \text{Eq. I-2}$$

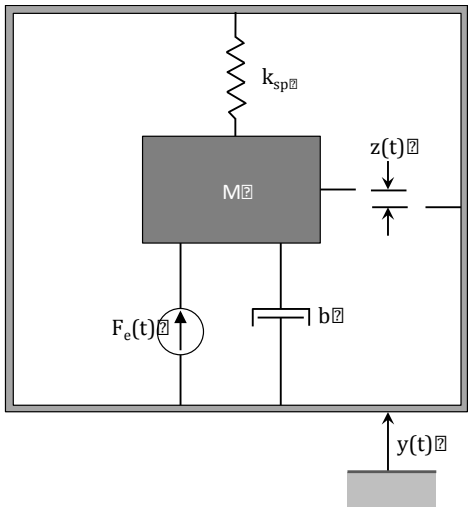

Figure I-3 Representation of vibration-based energy harvester

All three types of transductions, electromagnetic, electrostatic and piezoelectric are working based on the same principle in the case of resonant structures. As explained before, the piezoelectric transduction will be detailed in the next chapter. We will first present the electrostatic energy harvesters, the different configurations possible and then we will focus on the electromagnetic transducers.

➢ Electrostatic energy harvesters

The electrostatic energy harvesters at microscale are well represented because their fabrication process is completely CMOS compatible, and the electrostatic transduction does not require expensive materials.

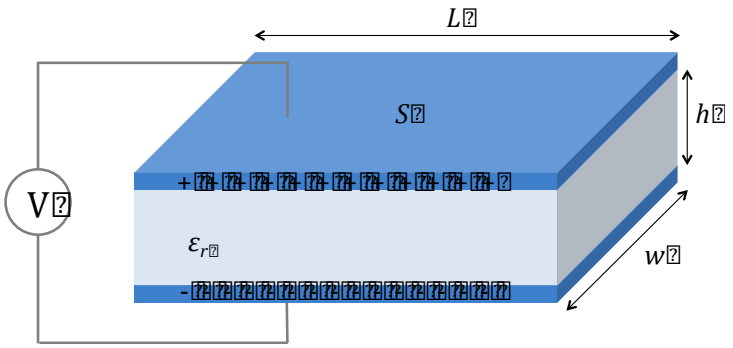

Figure I-4 Schematic of a parallel plate electrostatic device

Generally MEMS capacitive transducers are represented by two parallel plate electrodes. When the device is subjected to mechanical vibrations, it is moving and the capacitance is

changing with time, which is resulting in a flow of electrical charges between the two electrodes. The capacitance is depending on the dielectric permittivity of the material or medium between the two electrodes ε_r, the facing area of the electrodes S and the gap between the electrodes h.

$$C = {}_0 {}_r \frac{Lw}{h} \qquad \text{Eq. I-3}$$

ε_0 is the free space permittivity. In order to have a variation of charges, the capacitance has to change. There are three possibilities to vary the capacitance as presented in Fig. I-5:

- Change the gap h between the electrodes
- Change the facing area S
- Change the permittivity ε_r

There are also two operating conditions: at constant voltage or at constant charge. Depending on whether a constant Coulomb force is desired or not.

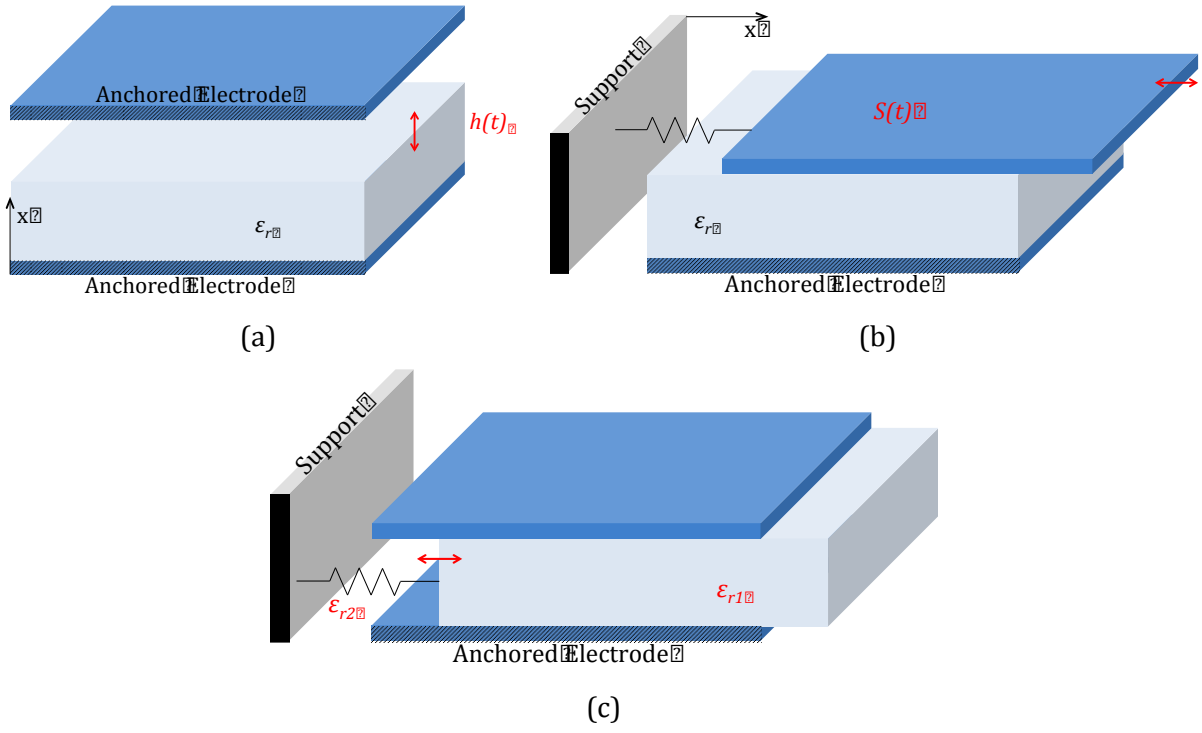

Figure I-5 Different configurations for electrostatic energy harvesters

The Coulomb force is the derivative of the energy stored in the capacitance and has the following expression [11]:

$$F_e(t) = \frac{dW_C}{dx} = \frac{Q_C^2}{2}\frac{d(1/C)}{dx} = \frac{Q_C^2}{2C^2}\frac{dC}{dx} = \frac{V^2}{2}\frac{dC}{dx} \qquad \text{Eq. I-4}$$

The following table presents an overview of the different expressions of the electrostatic force for the electrode-overlap case and gap changing case, in the two different circuit conditions: constant charge and constant voltage.

Table I-1 Electrostatic force according to the transducer type and circuit conditions

	Electrode-Overlap	**Gap-closing**
Constant Voltage	$F_e(t)=\frac{V^2}{2}\frac{dC}{dx}=\frac{V^2}{2}\frac{_0\ _r w}{h}$	$F_e(t)=\frac{V^2}{2}\frac{dC}{dx}=\frac{V^2}{2}\frac{_0\ _r S}{(h_0+x)^2}$
Constant Charge	$F_e(t)=\frac{Q_C^2}{2C^2}\frac{dC}{dx}=\frac{Q_C^2}{2}\frac{h}{_0\ _r w(L_0+x)^2}$	$F_e(t)=\frac{Q_C^2}{2C^2}\frac{dC}{dx}=\frac{Q_C^2}{2}\frac{1}{_0\ _r wL}$

The disadvantage of the constant charge condition circuit is the necessity to apply an initial charge to the capacitor when its capacitance is maximal. A large part of the devices are designed with an interdigitated comb structure. Low resonance frequencies are easily achieved.

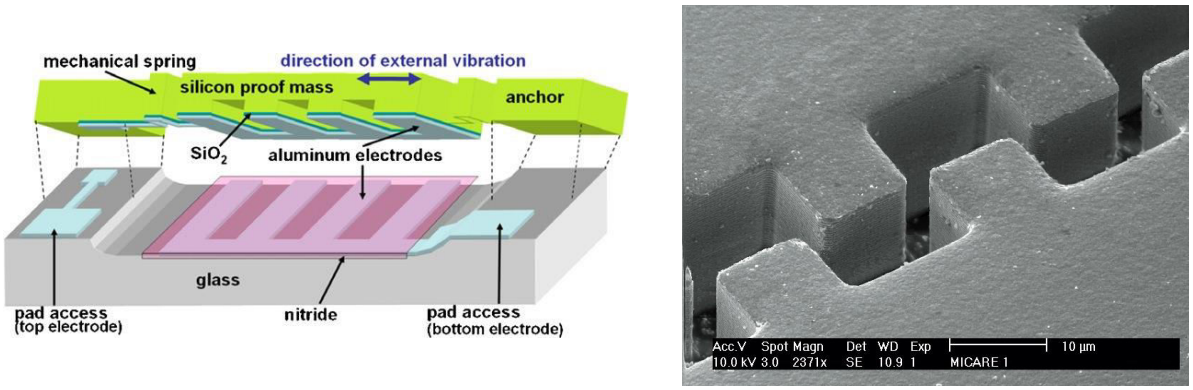

(a) (b)

Figure I-6 Electrostatic devices of Basset [12] and SEM picture of the comb structure of Despesse [13]

Despesse *et al.* [13] developed a macroscopic devices able to harvest more than 1mW when working at its resonance frequency of 50Hz and under low acceleration input (0,2g). This prototype has the highest power density of electrostatic energy harvester ever reach.

Hoffmann *et al.* [14] presented a MEMS device which is able to harvest 3,8µW. Its working frequency is relatively high (1460Hz) for ambient vibrations energy scavenging. The downscaling of the electrostatic devices implies a drastic fall of the power.

Recently, Basset *et al.* [15] developed a MEMS harvester which can work at very low frequency (150Hz) and can harvest 2,2µW for 1*g* acceleration. To achieve this result, they have

adapted the conditioning circuit to the nonlinear behavior of the structure, i.e. the hardening and softening of the damping. The spring is softening when the bias voltage is applied and it is stiffening during the impact with the mechanical stopper. But a lot of energy is lost by squeeze film dissipation mechanism. The authors estimated the dissipated power to be around 8µW, for 2,2µW harvested. The solution would be to place the structure under vacuum.

Table I-2 Performance of several electrostatic energy harvester at microscale.

	Operating frequency (Hz)	**Device area (mm2)**	**Operation voltage (V)**	**Converted Power (µW)**
Despesse* [13]	50	1800	120	1050
Basset [15]	150	100	30	2,2
Hoffmann [14]	1460	30	50	3,8

* the device presented is not microscopic

In order to avoid the charging and discharging cycles, and also to simplify the power management circuit, electrets can be implanted into one of the two parallel electrodes. An electret is a dielectric material in which electrical charges are trapped from a few 100's of seconds to several years. Nowadays, only two types of electrostatic architectures have been studied on the three presented above: the gap-closing and the facing surface change. Moreover the most developed structures are still at macroscopic scale. Mizuno *et al.* [16] concluded indeed that at small scale the reactive impedance is too high to deliver useful voltage.

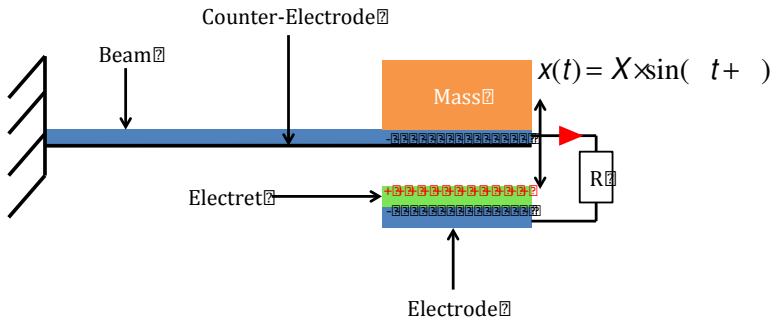

Figure I-7 Cantilever electrostatic energy harvester with electret from Boisseau [17]

Boisseau *et al.* [17] has used a simple mechanical structure, a cantilever with proof mass to harvest mechanical vibrations with electret positioned on the substrate, under the proof mass. The cantilever dimensions (30x13mm²) are not microscopic in order to lower the resonance frequency down to 50Hz. But one advantage of the electret is that we can get large amount of power with small displacement (50µW for a displacement of the cantilever of 10µm under an acceleration of 1*g*).

The University of Tokyo has developed a prototype with patterned electret and mechanical springs made of parylene to introduce nonlinearity to the structure displacement. The prototype, presented in Fig. I-8 (a), is in the configuration of a change of the facing surface of the electrodes. They achieve low resonance frequency of 63Hz [18] and 21Hz [19] thanks to the parylene springs. In both case the amplitude of in-plane displacement is as high as 0,5mm. They manage to get an output power of 1µW at 63Hz and 12µW at 21Hz, but with a high voltage bias (600V).

Finally Naruse *et al.* [20] presented a device with very low resonance frequency (2Hz) and high output power of 40µW. They use micro-balls in order to maintain a perfectly constant gap between the upper and lower electrode and also to allow the scrolling of one electrode with respect to the other.

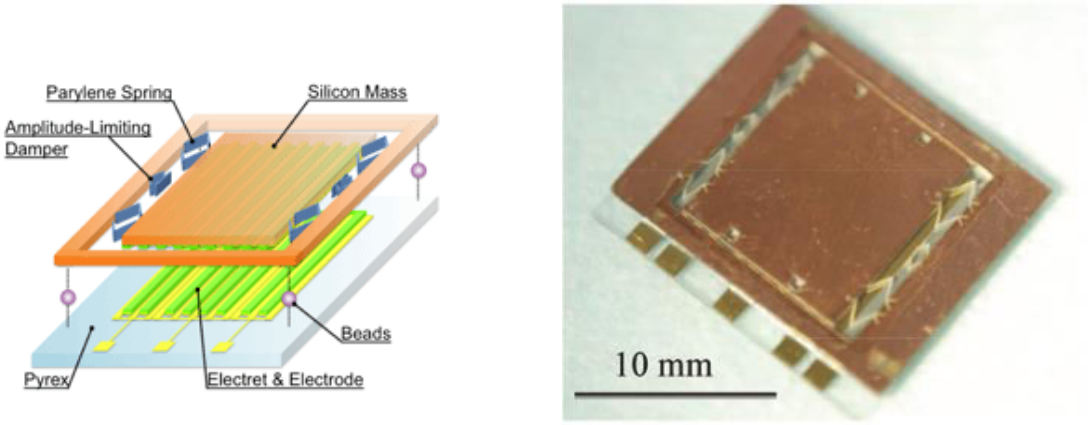

(a) (b)

Figure I-8 Schematic (a) and photography (b) of the prototype of Miki [18] and Edamoto [19]

The results are summarized in the Table I-3. A lot of investigation is still needed to improve the output power of electret-based electrostatic energy harvesters. For instance the thermal stability of the electret as well as the best charging method of the dielectric materials (Corona charging, contact charging by triboelectricity or soft X-rays charging) are hot topics for specialists.

Table I-3 Comparison of several electret-based electrostatic energy harvesters

	Operating frequency (Hz)	Device surface (cm2)	Electret voltage bias (V)	Output Power (μW)
Boisseau [17]	50 @0,1g	3,9	1400	50
Miki [18]	63 @1,57g	3	180	1
Edamoto [19]	21 @0,87g	3	600	12
Naruse [20]	2 @0,4g	9	-	40

➢ Electromagnetic energy harvester

Electromagnetic devices for energy harvesting have been studied at macro-scale, they can be very efficient and deliver high output voltage. A few examples are the Seiko watch, Perpetuum device or the dynamo on a bicycle. But at micro-scale, the materials used for the magnets are not CMOS compatible and also it is not possible to micro-fabricate coils with a sufficient winding.

The working principle of vibrations electromagnetic energy harvesters is based on the Faraday's law: when an electric conductor (coils) is moved through a magnetic field, a potential difference is induced between the end of the conductor. The induced voltage, or electromotive force (emf) is proportional to the time rate of change of the magnetic flux [21]:

$$V = \frac{d}{dt} = N\frac{d}{dt} \qquad \text{Eq. I-5}$$

Where V is the generated voltage, N the number of coils, Φ the total magnetic flux and ϕ the average magnetic flux per turn. The power generated is extracted by connecting a resistance between the two ends of the coil to let a current flow into the coil. This current creates its own magnetic field, which acts to oppose the field giving rise to it. The interaction between the two magnetic fields (from the induced current and from the magnets) is creating a force F_{em}. The mechanical energy is trying to act against this electromagnetic force and that's why it is transformed into electrical energy. This F_{em} is proportional to the current generated in the coils, so by consequence to the velocity, and to the electromagnetic damping D_{em}:

$$F_{em} = D_{em}\frac{dx}{dt} \qquad \text{Eq. I-6}$$

In order to extract the maximum power from an electromagnetic energy harvester, it is necessary to maximize the damping D_{em}, which is inversely proportional to the coil impedance and proportional to the total magnetic flux gradient [22].

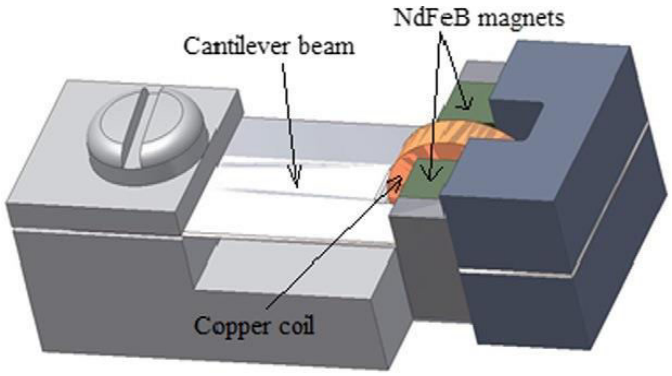

Figure I-9 Micro electromagnetic energy harvester from Beeby *et al.* [23]

Beeby *et al.* [23] proposed in 2007 a micro electromagnetic harvester using the cantilever type structure, at the end of which are bonded four magnets (NdFeB). The coil is situated in between the two columns of magnets, without preventing the movement of the beam and magnets. After optimization of the device, they manage to harvest up to 46μW at very low input acceleration of 0,06g. The authors have demonstrated that a microscale device can deliver useful power at ambient vibrations of only 0,06g, which is a breakthrough value compared to other macroscopic electromagnetic and even piezoelectric of electrostatic energy harvesters [23].

Liu *et al.* [24] studied an electromagnetic harvester with multiple vibration modes, two in-plane modes and one out-of-plane. It is composed of an energy-harvesting chip fabricated by CMOS processes, a permanent magnet on top of the chip attached to a supporting beam. The chip consists in a movable circular mass suspended by a three concentric rings. Three different coils in Al are patterned on top of the moving mass. As there are three vibration modes, there are three resonant frequencies: at 1285Hz for the out-of-plane mode, at 1470Hz and 1550Hz for the two in-plane modes. The respective output power at 1g input acceleration is respectively 0,016μW, 0,0087μW and 0,0045μW for each resonant mode.

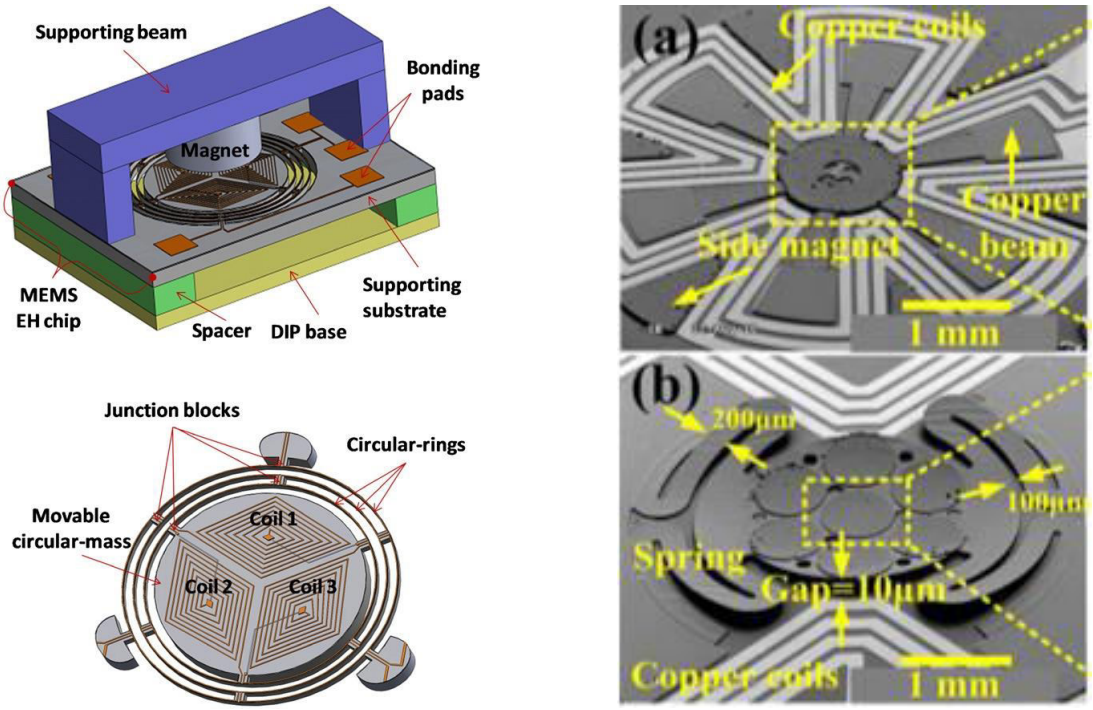

(a) (b)

Figure I-10 Multiple vibration modes EH from Liu [24] and completly CMOS fabricated devices from Han [25]

Han *et al.* [25] developed a fully integrated magnetic energy harvester, completely fabricated with CMOS compatible processes. They solved the problem of the integration of the magnets by the electroplating of CoNiMnP permanent micro magnets having two different designs as presented in Fig. I-10(b). In the upper SEM image, the circular magnet, at the center, is deposited on the moving plate and supported by six beams. Six triangular side magnets, positioned between each beam anchor, are providing a constant magnetic flux in the central annular magnet. In the second design (the lower SEM image) the vibrating plate is supported by four "snake-shaped" beams and an array of seven circular magnets is positioned on the plate. In the same way as in the first design, two side magnets (not visible in the picture) are providing constant magnetic flux inside the central magnets. This new design is intended to lower the resonant frequency of the device. The maximum output voltage for the first structure is 3,8µV at 102Hz, while for the second it is 7,5µV at 64Hz, which corresponds to an output power of 0,36nW. The performances are far below the previous devices presented, but they manage to demonstrate that it is possible to completely fabricate a magnetic energy harvester device with CMOS processes.

Table I-4 Comparison of the micro electromagnetic harvesters

	Volume (cm^3)	Resonant Frequency (Hz)	Acceleration	Output power (µW)
Beeby [23]	0,1	52	0,06g	46
Liu [24]	0,45*	1285 1470 1550	1g	16.10^{-3} $8,7.10^{-3}$ $4,5.10^{-3}$
Han [25]	0,0125	64	1g	$3,6.10^{-4}$

* Estimated value

Magnetostrictive materials have the property to deform itself while submitted to an electromagnetic field [26]. Combined with a piezoelectric material, which has the property to generate electrical charges when strained, it is possible to harvest mechanical vibrations. An AC magnetic field has to be generated by the mechanical vibrations through the movement of a magnet into a coil for instance. Ueno *et al.* [27] achieved to fabricate a harvester based only on Galfenol, a magnetostrictive material, a few millimeters long. They manage to get 5mW of output power at 200Hz with 1,7g acceleration.

I.1.a.3 RF Micro energy harvesters

The RF emitters are everywhere in our urban environment, like public telecommunications (GSM, WLAN frequencies). But even if the RF frequencies are very present, when harvesting them, we have to deal with very low power density because the farther will be the harvester from the base station, the lower will be the power of the RF frequencies. Some research are still conducted to try to improve this kind of harvester [28][29].

I.1.b Thermogenerators at macro- and micro-scale

Thermal energy is an important source of energy in the environment. Three different thermoelectric effects exist, which describe the interaction between heat and electricity in solids:

- The Seebeck effect: produces voltage sensitive to a temperature gradient across a junction between two materials.
- The Peltier effect: a junction of two materials on which is applied a voltage will absorb heat at one end and dissipate heat at the opposite end.

- The Thomson effect: when a single material is submitted to both temperature gradient and electrical current, it is dissipating or absorbing heat.

From the three thermoelectric effects, only the Seebeck effect is appropriate to harvest thermal energy and convert it into electricity. That is the reason why we will focus only on this specific thermoelectric effect.

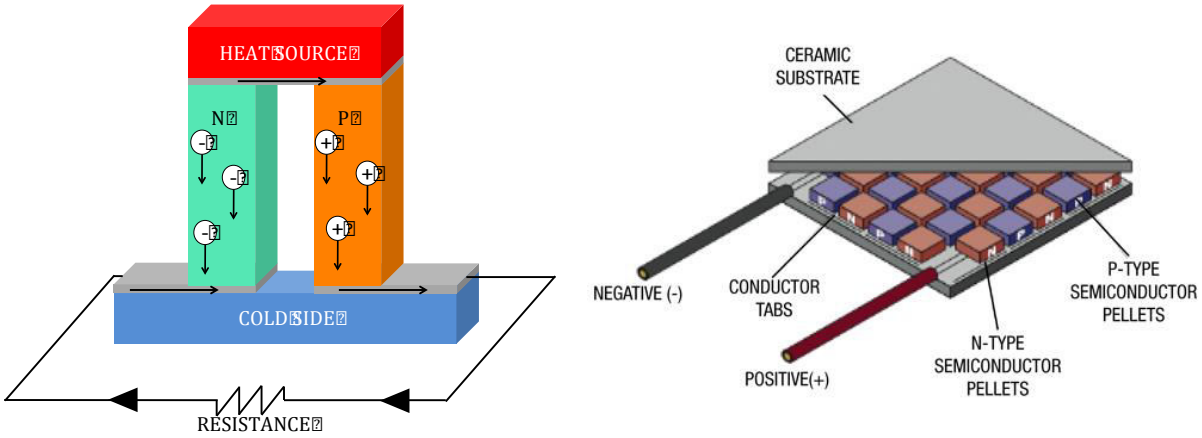

(a) (b)

Figure I-11 Schematic of a single pair of thermoelectric materials (a) and a Seebeck generator (b)

Most common Seebeck generator structure is presented on Fig. I-11. It consists of two semiconductor materials, which have high conversion efficiency metal alloys, one p-doped and the other one n-doped. They are thermally in parallel and electrically connected in series. The voltage generated by a couple of materials is given by: $V_s = (\quad_n \quad\quad_p)(\quad_H \quad\quad_C)$, where χ_n and χ_p are the relative Seebeck coefficients of the n-doped and p-doped material respectively, θ_H is the temperature of the hot point and θ_C the temperature of the cold part. When the generator is connected to an external load resistance as shown in Fig. I-11, the voltage measured is:

$$V = \frac{(\quad_n \quad\quad_p)(\quad_H \quad\quad_C)\,R_L}{R_L + R_n + R_p} \qquad \text{Eq. I-7}$$

Where R_p and R_n are the resistance of the two materials. Knowing that $V = R_L I$, one can easily deduce the expression of the current flowing through the load resistance. Consequently the power delivered to the load can be expressed as:

$$P = \frac{s}{(1+s)^2}\,\frac{(\quad_n \quad\quad_p)(\quad_H \quad\quad_C)^2}{R_n + R_p} \qquad \text{Eq. I-8}$$

where s is defined as the ratio between the load resistance and the sum of the material resistances. The maximum power is obtained at the matched load, i.e. when $s = 1$. Usually the pair of materials is put in an array to increase the output power.

If a certain heat flow W is flowing through the thermopile, a temperature difference of $= W/G$ is developing, with G the total thermal conductance of the pillars and the air between the two hot and cold plates. In order to maximize the power, the conductivity of the pillars and the air has to be equal. In reality, the conductivity of the materials is much larger than the one of the air, so the pillars are smaller than the plates. The output power on a matched load for an array of pillars is given by:

$$P = \frac{1}{64} \frac{\left(\quad _n \quad _p \right)^2}{g_{te}} \frac{W_u^2 A h}{g_{air}} \qquad \text{Eq. I-9}$$

Where ρ is the electrical resistivity of the materials (assumed to be equal for simplicity), W_u the heat flow per unit area, A the area of the plate, h the height of the pillars and g_{te} and g_{air} the thermal conductivity of the thermoelectric materials and air respectively. A figure of merit to compare the performance of the thermoelectric materials is often taken as follow, with the average temperature θ.

$$ZT = \frac{\left(\quad _n \quad _p \right)^2}{g_{te}} \qquad \text{Eq. I-10}$$

Numerous thermoelectric (TE) materials were studied and their ZT reported as well as its evolution with temperature. Indeed a good TE material should present high electrical conductivity but small thermal conductivity in order to keep a good thermal gradient between the hot and the cold source. However, thermal and electrical conductivity are interrelated.

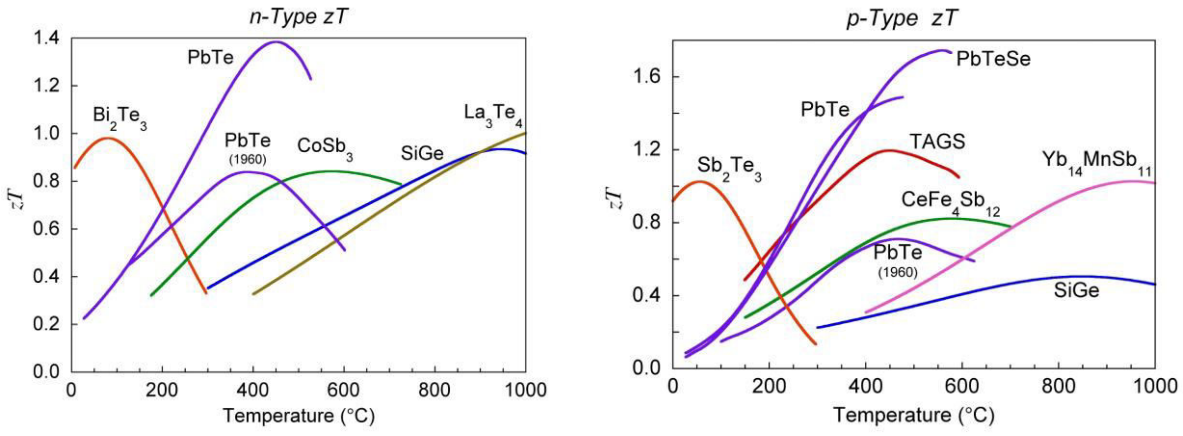

(a) (b)

Figure I-12 Figure of Merit ZT for TE n-doped (a) and p-doped (b) materials [30]

In semiconductors, the electrical carriers can be positive (holes) or negative (electrons) carriers. They have to be thermally excited across a gap for conduction to occur. There is two ways to have a high electrical conductivity in semiconductors: have a small-gap material or high-mobility carriers. Thermal conductivities are induced by lattice vibrations, called phonons. The two conductivities are correlated by the Wiederman_Franz relationship [31]. One strategy to increase the ZT is then to decrease the thermal conductivity by increasing the phonons scattering under the form of heavy atoms, disorder or large unit cells [30].

Micropelt commercializes TE generators at microscale using bismuth telluride Bi_2Te_3. The thermoelectric material is sputtered on silicon wafer with silicon oxide after the deposition of the bottom electrode. The n-doped material is deposited on one wafer, the p-doped on another one, and the two wafers are then bonded together to create the Seebeck generator. For a device volume of 8,7mm^3, it can generate up to 6mW for a thermal gradient of 30°C.

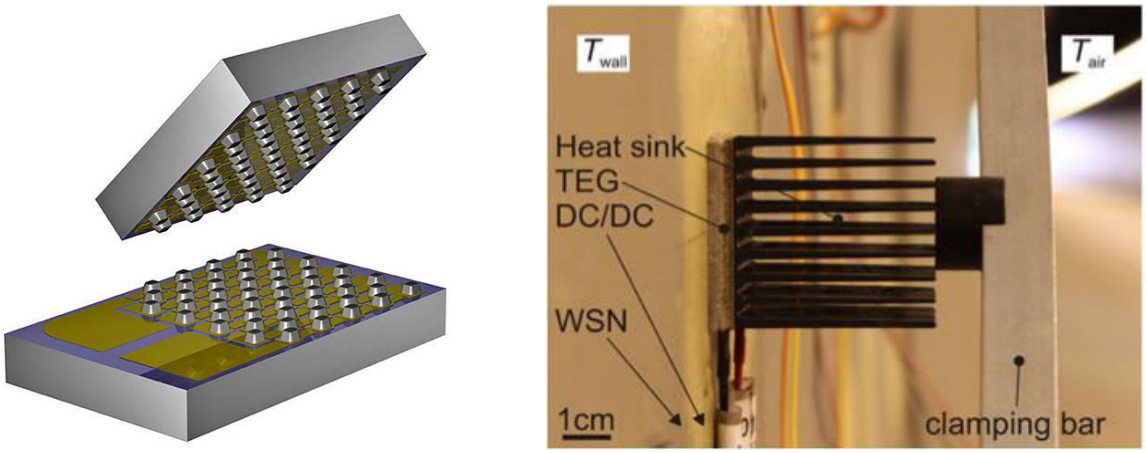

(a) (b)

Figure I-13 Micropelt [32] TE micro harvester (a) and Moser [33] TE harvester in a highway tunnel (b)

Moser *et al.* [33] used a TE generator in a highway tunnel to demonstrate the capacity of a Seebeck harvester to generate enough power under very low thermal gradient (in average 1,2K) to power a wireless sensor node via RF signals. They manage to harvest 70mJ per day in the worst case.

Hourdakis *et al.* [34] manages to fabricate a complete TE generator with standard CMOS processes, using the couple p-doped poly-Si and Al for the thermoelectric materials. The challenge was to find a way to thermally insulate the Si substrate, as it acts as the cold source of the generator. They used a 50µm thick porous Si layer, with a porosity of 60%. With a housing in Al, they harvested 0,39µW with a thermal gradient of 10K.

The advantage of TE generators is that they are mechanically robust because they don't have any moving part, compared to Stirling engines. But they present a lot of drawbacks. Indeed the most efficient TE materials are not CMOS compatible and by consequence are very expensive. Moreover the downscaling seems compromising because at microscale it is tricky to maintain a correct thermal gradient over a few 10's or 100's of microns. There is the need to use a heat sink, which is usually much bigger than the generator itself, as can be seen in [33] and [34].

I.1.c Pyroelectric devices

Unlike thermoelectric materials that are sensitive to spatial thermal gradient, the pyroelectric materials have the property to be sensitive to time-varying temperature. As also presented in the Chapter II and V, some piezoelectric materials present the characteristic to generate electrical charges when submitted to a temperature change in time. The generated electrical current is proportional to the temperature profile $\theta(t)$ over time, the area of the electrodes A and the component of the pyroelectric coefficient vector perpendicular to the electrode surface as follows:

$$i_p(t) = p' A \frac{d\ (t)}{dt} \qquad \text{Eq. I-11}$$

Xie *et al.* [35] study the performance of different pyroelectric thin films for thermal energy harvesting applications. They bonded the thin film sample to a resistive heater, which was controlling the temperature on the pyroelectric element. They measured power density of 0,2µW.cm^{-2} for PZT-5A ceramic, 0,33µW.cm^{-2} for PMN-PT ceramic and 0,12µW.cm^{-2} for PVDF, a polymer.

Sebald *et al.* [36] compares linear to nonlinear pyroelectric material and shows that with nonlinear material it is possible to harvest more energy than with traditional linear materials. In general, for a given heating frequency, increasing the heat exchange results in the increase of output power. However if the heat exchange is too high, the pyroelectric element has thermalized and stays at the ambient temperature. In order to maximize the output power, they proposed the idea of a thermodynamic cycle obtained by continuously applying an electric field to the sample synchronously with the temperature variation with a phase shift of 90°C. They are acting both on the polarization-electric field plane and on the entropy-temperature plane. The electrothermal coupling of the materials is then enhanced by the electrocaloric effect. They

estimated an increase of 10 to 600 times of the output power compared to linear pyroelectric systems. One limitation to this nonlinear pyroelectric system is that the materials, to be efficient, should have a composition near the phase transition, so the temperature range is limited by the phase transition temperature.

Chang *et al.* [37] proposed a device based on laminated composite plate composed of a pyroelectric and non-pyroelectric materials. In this way they take advantage of the first primary contribution of the pyroelectric coefficient and also of its secondary contribution originating from the piezoelectricity due to the thermal mismatch between the two materials. The harvesting device is converting a spatial temperature gradient into a temporal one in a cyclic behavior from figures (a) to (f) and back to (a) on the Fig. I-14. The laminated composite pyroelectric plate (PY on the Fig. I-14) is suspended by two one-way shape memory alloy (SMA) springs and two normal metallic springs.

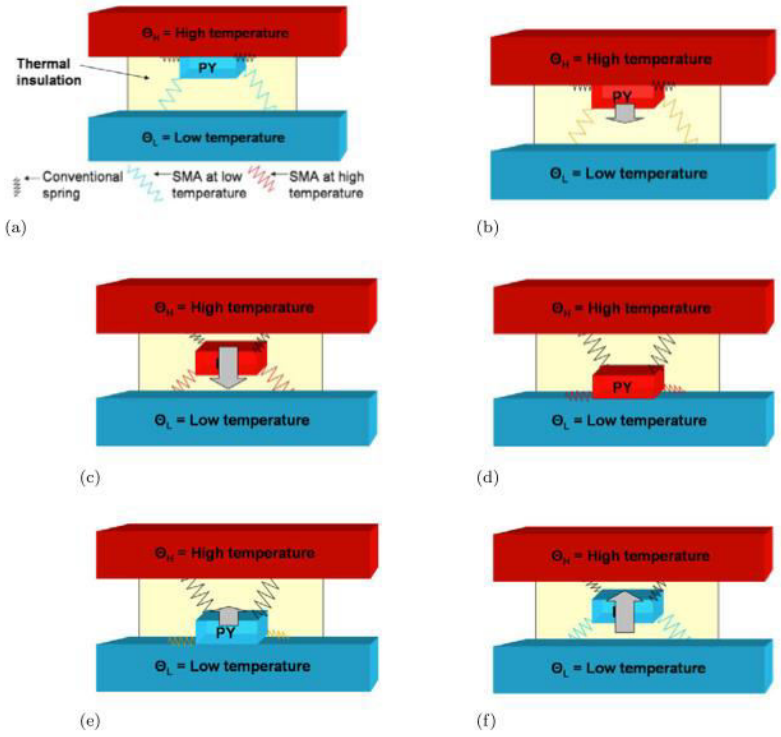

Figure I-14 Working principle of the pyroelectric device of Chang [37]

In the first stage, the temperature of the PY plate and the SMA springs are equal to the lowest temperature. The SMA springs are in the martensite phase allowing the steel springs to retract. Then the PY plate and the SMA springs heat up to reach the highest temperature: the SMA springs change their phase to austenite and are attracting the plate downward. Once in contact with the cold point, the SMA springs and the plate cool down and the springs change

again phase to martensite allowing the steel springs to pull up the plate in contact with the hot point.

They tested different pyroelectric materials and different combination of materials for the composite plate. They found out that lithium tantalate (LTO) single crystal showed the best output power density of 52,14μW.cm^{-3} compared to other pyroelectric materials. For the composite plate, the best couple was formed by PZT-5H pyroelectric material with Zn, with a thickness ratio of 1,005. It reaches 12,35μW.cm^{-3} while the temperature of the hot point is 310K and the cold point 300K.

The use of pyroelectric materials for thermal energy harvesting is a new topic, and a lot of research is still ongoing on the optimal material and the device configuration to use. One way to improve their efficiency would be to take profit of the fact that all the pyroelectric materials are piezoelectric, as proposed by Chang. Combining the thermal harvesting with the pyroelectricity and piezoelectric charge generation due to thermal mismatch between two materials can increase the output power of the system.

I.1.d Exotic thermal harvesters

It is possible to harvest thermal energy without using any pyroelectric or thermoelectric materials, but other material that change properties with temperature. This is the case of soft ferromagnetic materials. Under a threshold temperature called Curie temperature (θ_C) they present a magnetization, but once over this temperature, they become paramagnetic. This system is presented by Carlioz [38], Ujihara [39] and Chung [40]. Each of them presents a device consisting of a soft ferromagnetic material (Gd or FeNi) mass suspended by piezoelectric beams over a hard magnet (NdFeB) in contact with the hot point. When the soft material is under its θ_C, it is ferromagnetic, so it is attracted by the hard magnet. The mass is deforming the piezoelectric beams, which are producing a voltage. When the mass gets in contact with the hard magnet, it heats up till its temperature goes above its θ_C. The material losses its magnetization and goes away from the hard magnet. Again the piezoelectric beams are deformed and generate electrical charges. Once the soft material is cold enough, its magnetization returns and the same cycle begins again. In the system presented by Chung, the hard and soft magnets are not entering in contact during the cycle, the heating and cooling of the soft magnet is realized only by an optimized thermal convection.

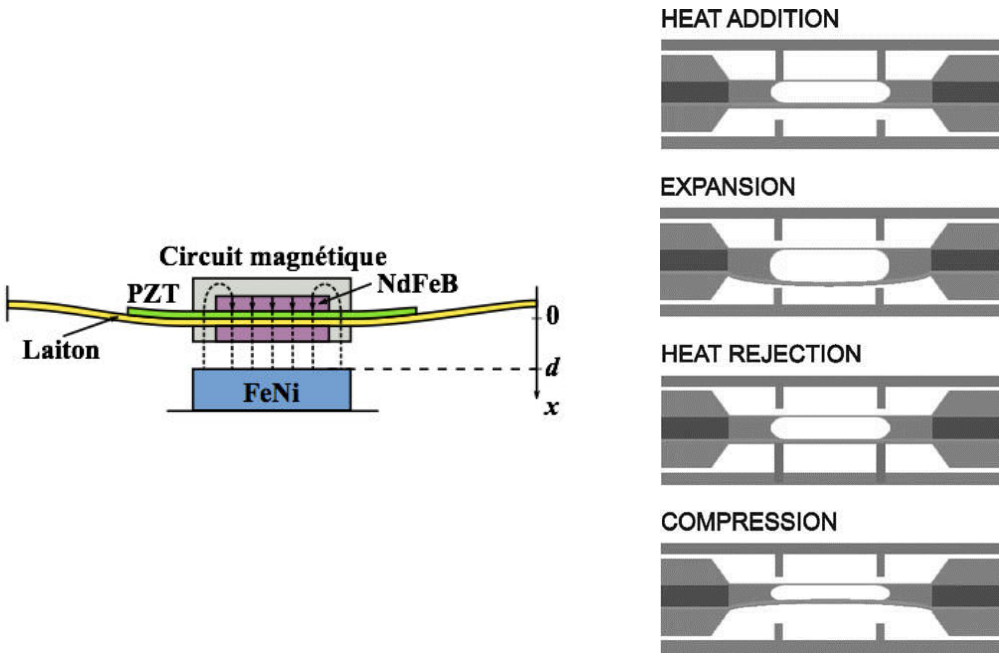

(a) (b)

Figure I-15 Illustration of a magneto-piezoelectric thermal harvester from Carlioz [41] (a) and micro heat engine from Whalen [42] (b)

Ujihara measured an output power between 0,6 and 1,3mW for a temperature difference of 50K. Chung managed to produce 9,8mW (16,6mV with a cycling frequency of 0,58Hz) for a temperature difference of 25K while Carlioz got 4,2mW with a temperature difference of 10K.

Whalen *et al.* [42] present a micro heat engine fabricated with standard CMOS technologies. The working principle is illustrate in Fig. I-15 (b). The engine is fabricated as follow: on one wafer, the bottom membrane containing a micro heater in TiW is fabricated. On another wafer, a piezoelectric membrane based on PZT thin film is micro-machined. Then the two wafers are assembled with in-between a spacer. A hole is made in the spacer, concentric with the membrane, which is filled with a two-phase working fluid. When the heater is increasing the temperature, the trapped fluid is expanding and the pressure in the chamber is increasing, making bigger the chamber. The piezoelectric membrane is strained and furnishes an electrical voltage. When the heater is not heating anymore, the temperature of the system decreases and the pressure inside the chamber also decreases. The membrane is then going back in its initial position and the piezoelectric film is furnishing again electrical charges. They manage to get 0,8µW for a thermal cycle of 4,2ms, with 1ms heating.

To conclude, nowadays it is not easy to harvest thermal energy at microscale, with usable output power. The most studied system is the Seebeck thermoelectric harvester, which presents the best energy harvesting performances up to now. But there are several drawbacks in this technology, one of them being the difficult downscaling due to the rapid decrease of thermal gradient in the material and CMOS integration of the thermoelectric materials. Other promizing technologies, like pyroelectric based devices or hybrid systems combining piezoelectric and ferromagnetic materials are showing high performances at macroscopic scale.

I.2 Presentation of the HEATec project

Another way to harvest thermal energy from a spatial thermal gradient is to use bimetal beams. This solution has been adopted by STMicroelectrics and is the subject of this thesis. The working principle of bimetal beams is the following: the beam is composed of two metals, one with a high coefficient of thermal expansion and the other one with a low thermal expansion coefficient (CTE). When such a structure is heated up, the two materials having two very different CTE, are expanding in a different way. The material with high CTE would like to expand a lot but is maintained by the low CTE material. It is then under compressive stress. On the contrary the low CTE material would not expand this much, but is stretched by the high CTE material. It is then under tensile stress. The overall beam is then curving in the sense where the high CTE material will be more stretched than the low CTE material. This principle has been used at macro-scale very often as thermal switch for boilers for example. For energy harvesting applications, piezoelectric or electrostatic transducers can be included with the bimetal beam in order to produce electrical charges every time the beam is moving.

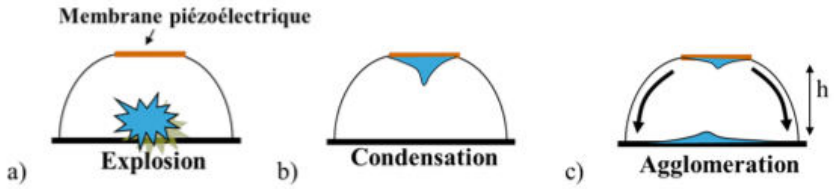

Figure I-16 Thermofluidic conversion [43]

Another approach employed by STMicroelectronics to harvest thermal energy is to use a similar working principle as the heat engine presented above from Whalen [42]: cycles of evaporation and condensation of a micro-droplet of working fluid is causing an increase and

decrease of the pressure in a chamber. A piezoelectric membrane constitutes one of the chamber walls and is deforming with the change in pressure inside the chamber.

The droplet enters in contact with a surface inside the chamber that has a temperature above its boiling temperature. The liquid is then evaporating suddenly, causing a significant increase of the pressure inside the chamber. The vapor is condensing on the cold surfaces of the chamber and by capillarity or gravity goes down to the hot surface and the cycle is closed. This part of the HEATec project will not be treated afterward, but preliminary results are shown in [44], we will focus only on the thermal energy harvesting with bimetal beams.

I.2.a Macro-prototypes

The bimetal beam described previously, in its initial state, is flat and is deforming linearly with the temperature. However if the bimetal is initially curved, the thermal stresses induced in the two materials lead to a mechanical instability called buckling: the beam, for instance initially curved downward, is suddenly deforming to invert its curvature and have an upward curvature. The buckling occurs at a critical temperature θ_{up} at which the beam becomes unstable mechanically in the down position and buckles up in a stable position. The beam is not anymore in contact with the hot source. The temperature then decreases, and the inverse phenomenon happens: the beam in the up position is becoming unstable at a critical temperature θ_{down} (which is different from θ_{up}) and it buckles down in a more stable position.

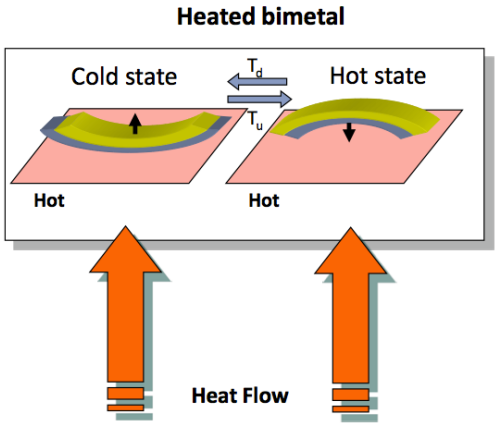

Figure I-17 Energy harvesting though the buckling of a bimetal beam

In order to take profit of the huge displacement originating from the buckling of the beam, a electro-mechanic transducer has to be introduced. Two techniques are considered: the

piezoelectric transduction and the electrostatic transduction. Macro prototypes were realized and tested with these two transduction mechanisms:

- Puscasu *et al.* [45] studied the piezoelectric one by placing a commercial piezoelectric buzzer over the bimetal beam. When it buckles, it is impacting the buzzer, which generates a voltage.
- Boisseau *et al.* [46] studied the electrostatic one by depositing a layer of electret under and over the beam. In this way, the counter-electrode necessary to the electret is part of the bimetal and each time it is buckling up and down, the change in capacitance is producing electrical charges.

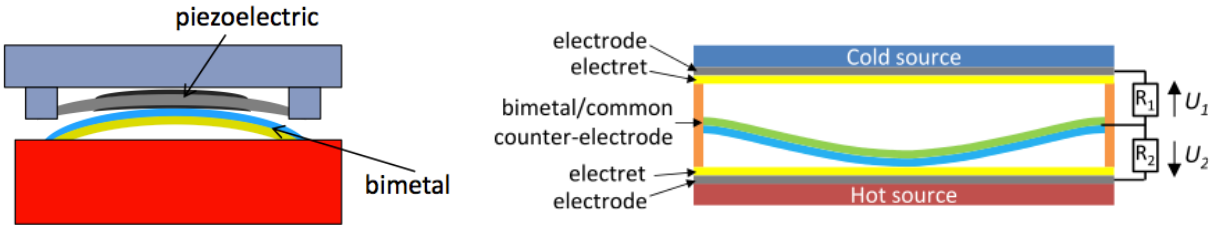

(a) (b)

Figure I-18 Piezoelectric and electrostatic schematics of the macro prototypes

Puscasu, in his thesis [47], managed to get an output power of 3,6µW for a bimetal that was buckling up at 121°C and down at 118°C, and 8,2µW for a bimetal buckling up at 40°C and down at 25°C. He also suggested that if the beams are put in a matrix configuration, that can furnish more power if they buckle at the same temperature, or can send a signal at different temperatures for sensing applications. Boughaleb *et al.* [48] managed to power an autonomous wireless sensor network with a bimetal furnishing 2,56µW without any heat sink, cooled down by natural convection.

Puscasu estimated also that downscaling the devices would imply an increase of the output power. If we divide by a factor *k* all the dimensions of the device, the output power would be multiplied by the same factor *k*. It would then be benefic to downscale the bimetals in order to get higher output power, and also to have the possibility to integrate them on flexible substrates for new energy harvesting applications as textile or tubes. They would also allow a VLSI fabrication process and reduced costs. This will be the aim of this work: to downscale the macro prototypes using piezoelectric transduction, to test and characterize them.

I.2.b Micro-prototypes design

In the macro-prototypes, the bimetals as well as the piezoelectric buzzer are fabricated by dedicated companies. For the microscopic prototypes, they have to be designed taking into account that they will be fabricated with standard CMOS processes. Three different positions of the piezoelectric element were considered:

- Over the bimetal as for the macro prototypes
- On the edge of the bimetal, in order that at every buckling the free edge of the bimetal impacts the piezoelectric element
- Onto the bimetal, in order that at every buckling of the structure the piezoelectric element is strained and furnishes a voltage.

The first two propositions were the most difficult to realize, as they need an external packaging or support to deposit the piezoelectric element. On the contrary, the third idea is more feasible because the piezoelectric layer has just to be deposited on top of the bimetal.

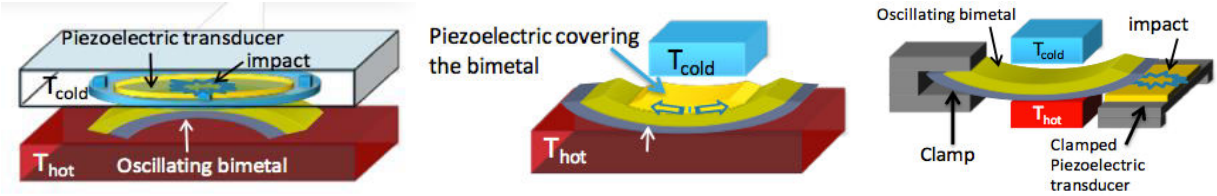

(a) (b) (c)

Figure I-19 Three considered position of the piezoelectric element at micro scale

The realization and characterization of buckling beams or plates with piezoelectric elements integrated at macro and micro-scale has already been investigated [49][50][51][52]. The beams or plates were designed to harvest mechanical vibrations or to act as an actuator. But none of them used the bilayer beam as a thermal harvester. The innovative idea of this project is that the piezoelectric layer will be directly integrated to the device; it will play the role of one of the two active materials. Moreover, as the stress in piezoelectric thin films can easily be tuned by the fabrication process, no additional procedure will be necessary to get a device with initial curvature. We have chosen the aluminum nitride (AlN) for the piezoelectric layer and aluminum Al for the metal layer. Moreover, we chose them because of their compatible thermal properties: Al has a CTE 6 times larger than AlN. The other reasons of this choice will be detailed in the chapter IV.

In a first time rectangular structures will be fabricated in order to reproduce at micro-scale the devices tested at macro-scale. The structures will have different length to width ratios, ranging from a beam-like structure to a square one. Then in order to improve the stress

distribution in the plate, new geometries, “butterfly-like” will be introduced and compared to the rectangular ones.

I.3 Conclusions

The state-of-the-art of the energy harvesting at micro-scale has been detailed. It is noteworthy that the mechanical vibrations are the most common energy scavenged at micro-scale because very different transduction mechanisms can be used and the fabrication process are mastered using CMOS standard fabrication lines. The thermal energy harvesting at macro-scale is well known when it is using the Seebeck effect. But a lot of efforts are put to downscale the Seebeck generators and reduce the thermal conductivity of the materials used in these systems. Other kinds of thermal harvesters using pyroelectric effect or the change in magnetization with temperature of certain types of materials are promising systems.

We propose in this thesis to work on a system that uses a thermally buckling beam, completely CMOS fabricated. The proof-of-concept at macro-scale has already been done and the downscaling of the device should increase the output power significantly. The piezoelectric layer will be directly integrated into the bilayer beam or plate and the initial curvature will be controlled only by the deposition parameters of the materials. Different geometries will be realized and compared.

II Piezoelectric materials at microscale

After an introduction on the energy harvesting in general, this chapter is focusing of the energy harvesting micro devices using the piezoelectric transduction. First of all the piezoelectricity is explained, the constitutive equations are detailed in order to understand better the different piezoelectric material families (pure piezoelectric, pyroelectric and ferroelectric). Once we are familiar with the piezoelectricity, several piezoelectric-based energy harvesters are analyzed and their performances are compared. Finally the characterization means of piezoelectric film quality and device performances are explained, as well as the electrical representation of a piezoelectric transducer and the electro-mechanical response.

II.1 State of the art of the piezoelectric thin film devices

II.1.a The piezoelectricity

The first evidence of the piezoelectricity was made by the brothers Jacques and Pierre Curie in 1880 [53]. From their knowledge of the pyroelectricity and crystallography, they predicted and demonstrated the capacity of different materials, the most famous being the quartz, to generate electrical charges when it is under pressure. This effect is called the direct piezoelectric effect. One year later, the inverse effect was calculated thermodynamically and verified experimentally: when an electrical field is applied to a piezoelectric material, it is extending or compressing proportionally to the amplitude of the electrical field. The first industrial application of the piezoelectric effect was during the First World War, when also the sonar transducer was conceived and realized with thin quartz plates. From then, the number of discovered piezoelectric materials, as well as the number of their applications has been growing steadily. Today, over 70 types of applications are on the market. Quartz is still used for time and frequency control in watches, computers and mobile phones by virtue of its high thermal stability and high mechanical quality [54]. Ferroelectric ceramics arising during the 1960's proved to be much stronger piezoelectric materials. They are dominating to date ultrasound imaging and non-destructive testing, and are also found in a lot of applications of everyday life. For instance the lighter employs the deformation of a piezoelectric ceramics to create high voltages leading to sparking and ignition of the gas [55]. The dentists use very precise instruments controlled by piezoelectric motors [56] to have precise control of the movement of the tip during scaling for instance to improve the patient comfort. The dominating material

among these ceramics is $Pb(Zr_{1-x},Ti_x)O_3$, a perovskite with tetragonal or rhombohedral symmetry.

For a material to be piezoelectric, only one condition has to be met by a material: its crystallographic group should not present a center of symmetry. There are 20 groups over 32, which are not centro-symmetric; by consequence every crystal belonging to one of these groups is piezoelectric. When a non centro-symmetric crystal is submitted to a mechanical pressure, there is an asymmetric displacement of the ions and a modification of the internal dipole. In Fig. II-2 (b) the perovskite unit cell of tetragonal PZT is typically formed by two positive ions, Pb^{2+} on the A-site (in black) and Zr^{4+} or Ti^{4+} on the B-site (in grey), and negative oxygen ions O^{2-} forming an octahedron around the B-site. In its tetragonal form, the negative oxygen octahedron is shifted in opposite direction to the positively charged A-ions along the (vertical) c-axis, thus forming a polar order with a spontaneous electric polarization. The one can be flipped by the application of an external electric field. For this reason the structure is called ferroelectric, in analogy to the ferromagnetic effect. The compression or extension of the cell along the polar axis will shift positive and negative charges differently. As a consequence, charges will appear on the surfaces perpendicular to the ferroelectric polarization.

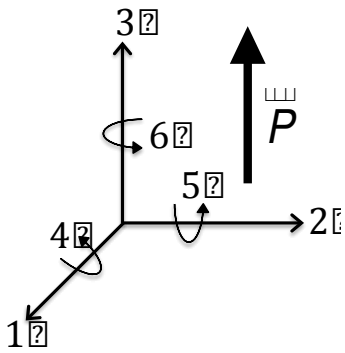

Figure II-1 Axis numbering used in the piezoelectric tensors

The Fig. II-1 presents the axis convention used in the IEEE Standards: the axis 1, 2 and 3 for the translations and 4, 5 6 for the rotations. The material polarization is always taken along the 3-axis. As longitudinal and transverse strains are linked through the Poisson effect, and because there are in addition also shear effects, the constituent equations of a piezoelectric crystal are relatively complex relations between the mechanical stress T_i, the strain S_i and the charge density displacement D_i and the electric field E_i. In order to simplify the tensors writing, a compact notation, named as Voigt notation, is used. The stiffness and compliance tensors s_{ijkl} and c_{ijkl} are then replaced by a 6x6 matrix with the following relations:

Table II-1 Relation between the tensor notation and the Voigt notation

Tensor subscript	Voigt subscript
ii = 11	p = 1
ii = 22	p = 2
ii = 33	p = 3
ij = 23 or 32	p = 4
ij = 13 or 31	p = 5
ij = 12 or 21	p = 6

The two principle equations are describing the direct and inverse piezoelectric effect:

$$D_i = d_{ik} T_k + {}_0 {}^T_{ij} E_j \qquad \text{Eq. II-1a}$$

$$S_k = s^E_{kl} T_l + d_{ik} E_i \qquad \text{Eq. II-1b}$$

where d_{ik} is a piezoelectric (charge) coefficient (C/N or m/V), s_{kl} the elastic compliance matrix of the material, ε_0 the absolute permittivity and ε_{ij} the relative permittivity matrix of the material. The indices k and l are going from 1 to 6 (reduced index notation) and the index i and j from 1 to 3. The compliance depends on the electrical boundary conditions. The upper index E of the compliance means that it is valid at constant E. The dielectric constant depends on the mechanical boundary conditions. The upper index T means that the stresses are constant.

The direct piezoelectric effect provides a linear relation between the generated electrical charge and the applied mechanical stress. The inverse effect is also linear and means the dependence between the applied electric field and the observed strain. Inside the large family of piezoelectric materials, there are 10 crystallographic groups exhibiting a polar axis. This special property allows them to be pyroelectric: they can generate electrical charges when they are subject to a time varying temperature. The best pyroelectric materials are at the same time also ferroelectric, i.e. those allowing for switching the direction of the polar axis, or the ferroelectric polarization. These materials, for instance lithium tantalate $LiTaO_3$, barium titanate $BaTiO_3$ or lead titanate $PbTiO_3$, are used for infrared temperature sensing like the automatic door opening or infrared camera [57]. Materials like AlN or ZnO having a polar axis (wurtzite structure) but no ferroelectricity show only a weak pyroelectricity. The ferroelectrics have thus the capability for the polarization vector to be switched by an external electrical field. These materials can also be used in the form of a polycrystalline ceramics because a net polarization can be obtained by a

poling process in an electric field. Typical example is lead zirconate titanate $Pb(Zr,Ti)O_3$ or PZT. This ceramic has a lot of applications in ultrasonics and actuators of all kinds. For microelectronics the switchable polarization of PZT thin films is used to realize non-volatile memories.

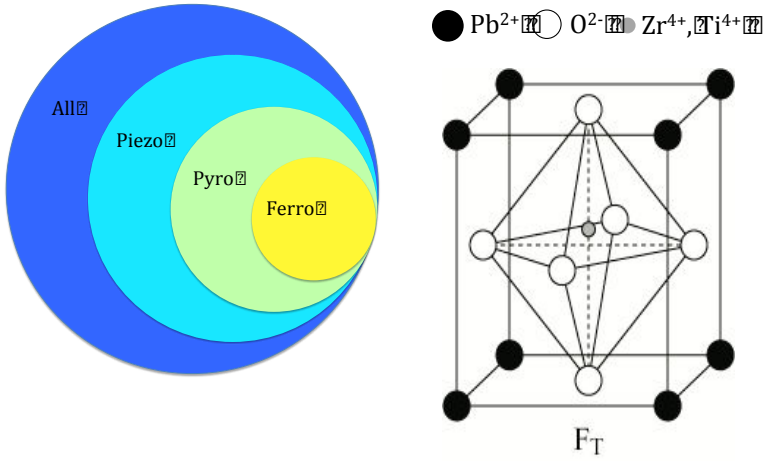

(a) (b)

Figure II-2 Schematic of the different families of piezoelectric materials (a) and perovskite lattice of tetragonal PZT (b)

The ferroelectric materials are most of the time used in the form of polycrystalline ceramics. Each of the grains (microcrystals) has another orientation, and in addition, the many ferroelectric domains in each grains result in a zero net polarization. Applying a very high electrical field (typically 10-100kV.cm^{-1}) at a higher temperature (we are poling the material), the polarization of domains and grains is aligning to have the projection onto the direction of the electric field parallel to the latter.

When the electric field is switched off and the temperature is down to ambient, the microscopic dipoles stay more or less aligned in the poling direction for a certain time, depending also on the mechanical boundary conditions of the sample. Regions of the material with the uniformly oriented spontaneous polarization are called ferroelectric domains. They form to minimize the electrostatic and elastic energy during the cooling down of the sample and the transition from the paraelectric to ferroelectric phase. After the removal of the electric poling field, the material presents a macroscopic polarization called remanent polarization P_r. The poling process is possible only for ferroelectric materials that can switch their crystal polarization. For non-ferroelectric, piezoelectric materials, polarization reorientation after growth is impossible. Such piezoelectric bulk materials can only be used in the form of single crystals, as e.g. quartz. In the case of thin films, there is another possibility when the material is

polar, like ZnO or AlN. Polar thin films may exhibit the full piezoelectric properties even when they are polycrystalline, provided that the growth is uniformly textured (e.g. all grains in (001) orientation) and in addition all the polar axes pointing in the same direction (e.g. in all grains the polar c-axis is down to the substrate. The characteristic property of the ferroelectric materials is the hysteresis in the hysteresis loop. An applied alternating, large electric field (surpassing the coercive field) will modify the polarization of the material and provoke a polarization switching in every half-cycle.

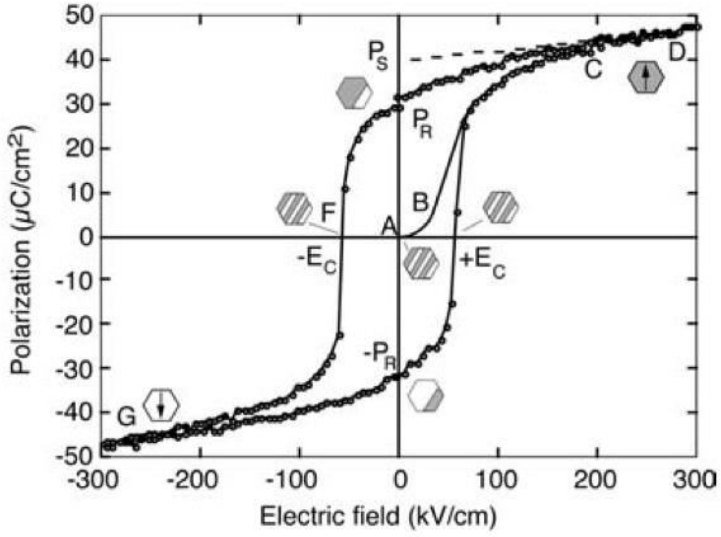

Figure II-3 Ferroelectric hysteresis loop of a 1,3μm sol-gel PZT film[58].

A typical hysteresis loop measured at a thin PZT film is depicted in Fig. II-3. The remanent polarization P_r is the polarization value at zero electric field. The coercive field E_c is the electric field necessary to bring the polarization down to zero, thus to switch roughly half of the domains. The saturation polarization P_s is the polarization of the material when all the domains are aligned along one direction. The hexagons are illustrating the progressive switching of the domains with polarization upward (grey) and downward (white).

Depending on crystalline symmetry, the macroscopic properties of the piezoelectric materials are anisotropic. Their elastic properties are very different along their polarization axis than along the other two directions. All the constitutive piezoelectric equations can be written in the form of matrices. The Eq. II-1a and 1b are the ones when choosing stress and electric field as variables (both are intensive variables), and which have d_{ik} as piezoelectric tensor. There are other types of equations that are generated with the use of all extensive variables (strain and charge: h-tensor) or mixed variables (strain, electric field: e-tensor; stress, charge: g-tensor) as given in the Table II-2 below. The model is assumed under isothermal condition. The superscripts or subscripts *S*, *T*, *E* and *D* mean that the given variable is constant.

Table II-2 Constitutive piezoelectric equations

Constitutive equations	Piezoelectric coefficients	Units
$S = s^E T + dE$ $D = dT + {}^T E$	$d_{ij} = \left(\frac{D_i}{T_j}\right)_E = \left(\frac{S_i}{E_j}\right)_T$	C/N or m/V
$T = c^E S - eE$ $D = eS + {}^S E$	$e_{ij} = \left(\frac{\partial D_i}{\partial S_j}\right)_E = \left(\frac{\partial T_i}{\partial E_j}\right)_S$	C/m² or N/Vm
$T = c^D S - hD$ $E = -hS + {}^S D$	$h_{ij} = \left(\frac{\partial E_i}{\partial S_j}\right)_D = \left(\frac{\partial T_i}{\partial D_j}\right)_S$	V/m or N/C
$S = s^D T + gD$ $E = -gT + {}^T D$	$g_{ij} = \left(\frac{\partial E_i}{\partial T_j}\right)_D = \left(\frac{\partial S_i}{\partial D_j}\right)_T$	Vm/N or m²/C

The coefficient β is the inverse of the dielectric permittivity matrix ε, and the compliance matrix c is the inverse of the stiffness matrix s. The four piezoelectric coefficients are used to describe different elements of the piezoelectric conversion. For instance the coefficient d_{ij} illustrates the displacement obtained when applying a voltage to the material. The coefficient e_{ij} is quantifying the amount of electrical charges generated by the displacement of the piezoelectric material. All the piezoelectric coefficient are correlated between them by the following equations:

$$\begin{aligned} d &= {}^T g = e s^E \\ g &= {}^T d = h s^D \\ e &= {}^S h = d c^E \\ h &= {}^S e = g c^D \end{aligned} \qquad \text{Eq. II-2}$$

Depending on the symmetry of the crystallographic lattice of the material, some piezoelectric coefficients will be zero or equal one to each other. For instance the hexagonal, wurtzite type crystal structure that ZnO or AlN exhibit would have the following type of compliance matrix and piezoelectric coefficient e matrix:

$$c = \begin{matrix} c_{11} & c_{12} & c_{13} & 0 & 0 & 0 \\ c_{12} & c_{11} & c_{13} & 0 & 0 & 0 \\ c_{13} & c_{12} & c_{11} & 0 & 0 & 0 \\ 0 & 0 & 0 & c_{44} & 0 & 0 \\ 0 & 0 & 0 & 0 & c_{44} & 0 \\ 0 & 0 & 0 & 0 & 0 & c_{66} \end{matrix}$$

$$e = \begin{matrix} 0 & 0 & 0 & 0 & e_{15} & 0 \\ 0 & 0 & 0 & e_{15} & 0 & 0 \\ e_{31} & e_{31} & e_{33} & 0 & 0 & 0 \end{matrix}$$

The indexes of all the piezoelectric coefficients represent both direction of the electric field and the direction of the applied stress. For instance the coefficient e_{31} related the generated stress in the 1-direction to the applied electric field in the 3-direction, or inversely, the generated charge density on planes perpendicular to the 3-direction to the applied strain along the 1-direction. Direction 3 is by convention the polarization direction (if there is only one).

II.1.b Piezoelectric Thin Films Energy Harvesters

II.1.b.1 Vibration energy harvesting

The energy harvester devices based on piezoelectricity become very common and in future will be present in the everyday-life objects [59][60][61]. Their application field is to harvest mechanical energy that is transmitted to the device either as deformation or as acceleration. It is particularly thought to harvest energy present in vibrations of the environment. The most widespread configuration to capture vibrational energy is the clamped-free cantilever with a seismic mass at the free end as shown in Fig. II-4. The fixed end is mounted onto a vibrating body. It is relatively easy to fabricate using the standard CMOS processes and the frequency is tunable by adjusting the weight of the mass.

Two configurations are possible: the unimorph configurations [62][63][64][65][66] where one piezoelectric layer is deposited onto an elastic material (silicon or oxide layer) and a bimorph configuration [67][68] with the layer of elastic material sandwiched between two piezoelectric layers with opposite polarization.

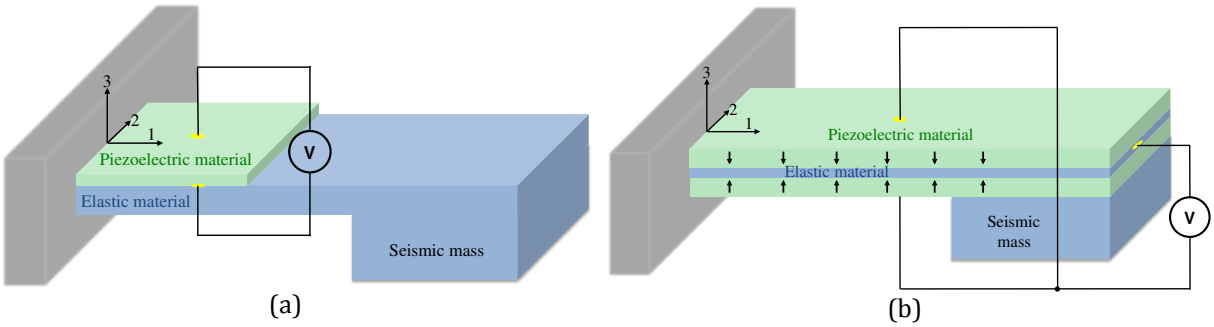

Figure II-4 Unimorph cantilever configuration with one piezoelectric layer (a) and bimorph configuration with two piezoelectric layers of opposite polarization

In this way the two piezoelectric layers act as two generators in series. These devices are optimized when they are working at their resonance frequency, but their efficiency quickly decreases if the vibration is a bit shifted from this specific resonance frequency. There exist many ways to tune the natural frequency of the cantilevers as reported by Beeby [69] but the major one consists in changing the dimensions of the cantilever.

The cantilever can be assimilated as a spring-mass structure, with the following natural frequency f_r:

$$f_r = \frac{1}{2}\sqrt{\frac{k}{m}} \qquad \text{Eq. II-3}$$

With k the spring constant and m the inertial mass. In this case if we want to tune the resonance frequency of the device we can play with two parameters: the spring constant, depending on the material properties and the dimensions of the cantilever, and its mass. Introducing the geometrical parameters the resonance frequency becomes:

$$f_r = \frac{1}{4}\sqrt{\frac{Yw_c t_c^3}{L_c^3\ (w_M t_M L_M + 0.24 w_c t_c L_c)}} \qquad \text{Eq. II-4}$$

With respectively:

Y – the Young modulus of the cantilever

ρ - the density of the elastic material

L_c – the length of the cantilever

w_c – the width of the cantilever

t_c – the thickness of the cantilever

w_M – the width of the seismic mass

t_M – the thickness of the seismic mass

L_M – the length of the seismic mass

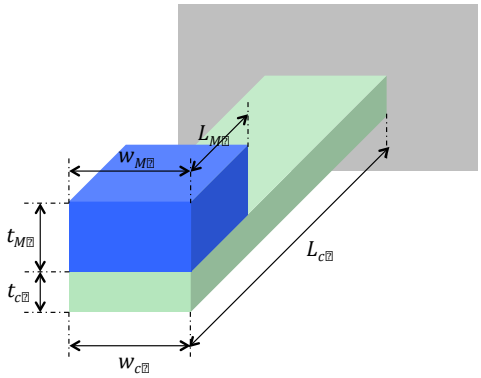

Figure II-5 Dimensions of a cantilever beam

Increasing the thickness of the cantilever will increase also the frequency, while increasing its length will decrease it. Taking into consideration the influence of the different geometrical parameters, one can conceive a piezoelectric cantilever that matches perfectly its resonance frequency to the frequency of the vibrations to be harvested. The drawback of cantilevers at microscale is that having small dimensions and light mass, their resonance frequency is high, often over 1kHz. The challenge is to conceive a MEMS cantilever with a resonance frequency under 200Hz where a lot of ambient vibration frequencies can be harvested like the kitchen tools, the washing machine or a running man impacts as explained by Defosseux in his thesis [70].

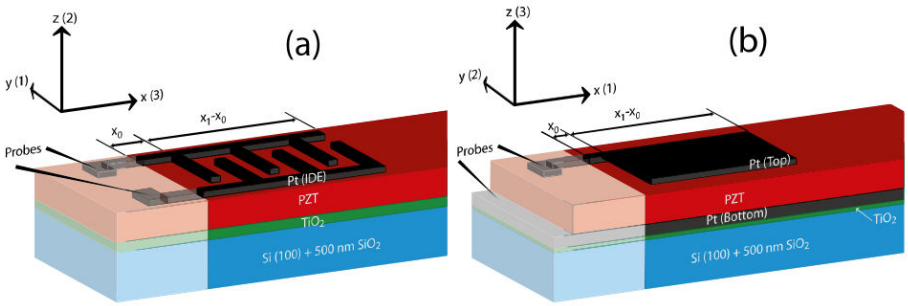

Figure II-6 IDE (a) and PPE (b) electrode configurations [71]

The choice of the electrode position can increase also the output power in harvesting devices. Indeed the most common electrode geometry is the parallel plate: one electrode is positioned on top of the thin film and the other on the bottom. This way, the material that has the lowest dielectric constant like AlN is the most favorable for energy harvesting application. But its electromechanical coupling coefficients are much lower than the ones of PZT for instance (6,5% for AlN [72] against 50% for PZT-5A [73]) and AlN is not ferroelectric. Designing interdigitated electrodes (IDE) might overcome this issue [71]. Indeed it allows us to use the $d_{33,f}$ coefficient instead of the $d_{31,f}$ which is lower (for instance for the PZT-5A d_{31} is -190pm/V

while d_{33} is 350pm/V [73]). Ahmed-Seddik *et al.* [74] proposed a bimorph-type cantilever, which has its polarization direction in plane, in the length direction. As for the classical bimorph structure, the polarization directions are of the opposite sign in the upper and lower layer. It can then take advantage of the larger longitudinal piezoelectric coefficient d_{33}.

The crystallographic orientation of the piezoelectric film has also to be adapted to the IDE configuration as shown in Fig. II-6. In PPE configuration, the polarization has to be perpendicular to the electrode, while in IDE configuration the most favorable polarization is in-plane. For instance the $e_{31,f}$ coefficient of a PZT thin film in PPE is 10.58C.m^{-2} and in IDE, with the same film, it goes up to 14.8C.m^{-2}, with 10 times more output voltage generated [71].

One solution to increase the bandwidth of the harvested frequency is to connect in series or parallel different cantilevers with various dimensions, which means various resonance frequencies. Xue *et al.* [75] connected in series ten piezoelectric bimorphs with different thicknesses of the piezoelectric layers. They manage to increase the overall output power and also to increase greatly the frequency bandwidth of the harvester. The drawback of this technique is the complexity of the fabrication process, especially if different piezoelectric layer thicknesses are implemented. Yu *et al.* [76] increased their output voltage by connecting to the same proof mass five identical cantilevers, going from 1.62V with one cantilever to 7.02V with the five cantilevers at their resonance frequency under an acceleration of 0.5g.

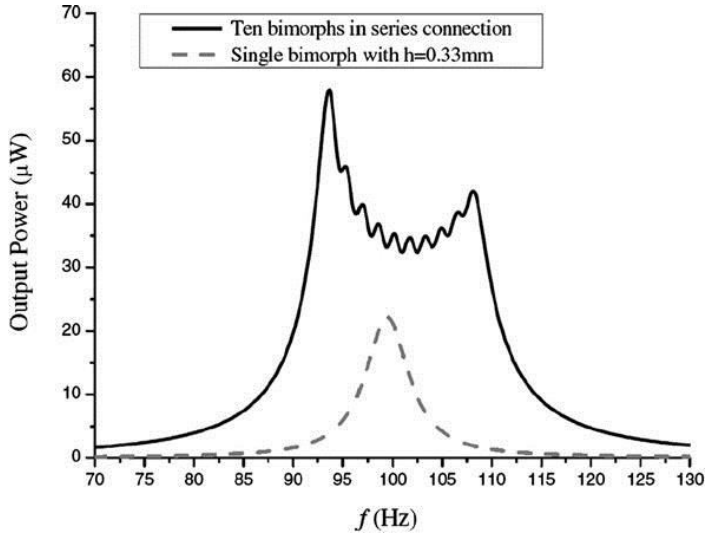

Figure II-7 Output power over frequency for one single bimorph and ten bimorphs in series [75]

Another method to widen the frequency bandwidth of a piezoelectric harvester is to introduce non-linearity. Introducing a non-linear behavior of the device can be realized by two

different ways as explained by Ramlan *et al.* [77]: by a bi-stable energy harvester and by a hardening stiffness component. The bi-stable system, as described in [50][78][79], consists in the very fast displacement of the seismic mass from one stable position to the other. The increase of velocity implies an increase of the harvested power, but not a wider operating frequency bandwidth. They replace the seismic mass by a magnet, and add another magnet in front of it. The bi-stability can also be reached by adjusting the stress into a bi-clamped beam [64][80] or a bi-stable piezoelectric plate [81].

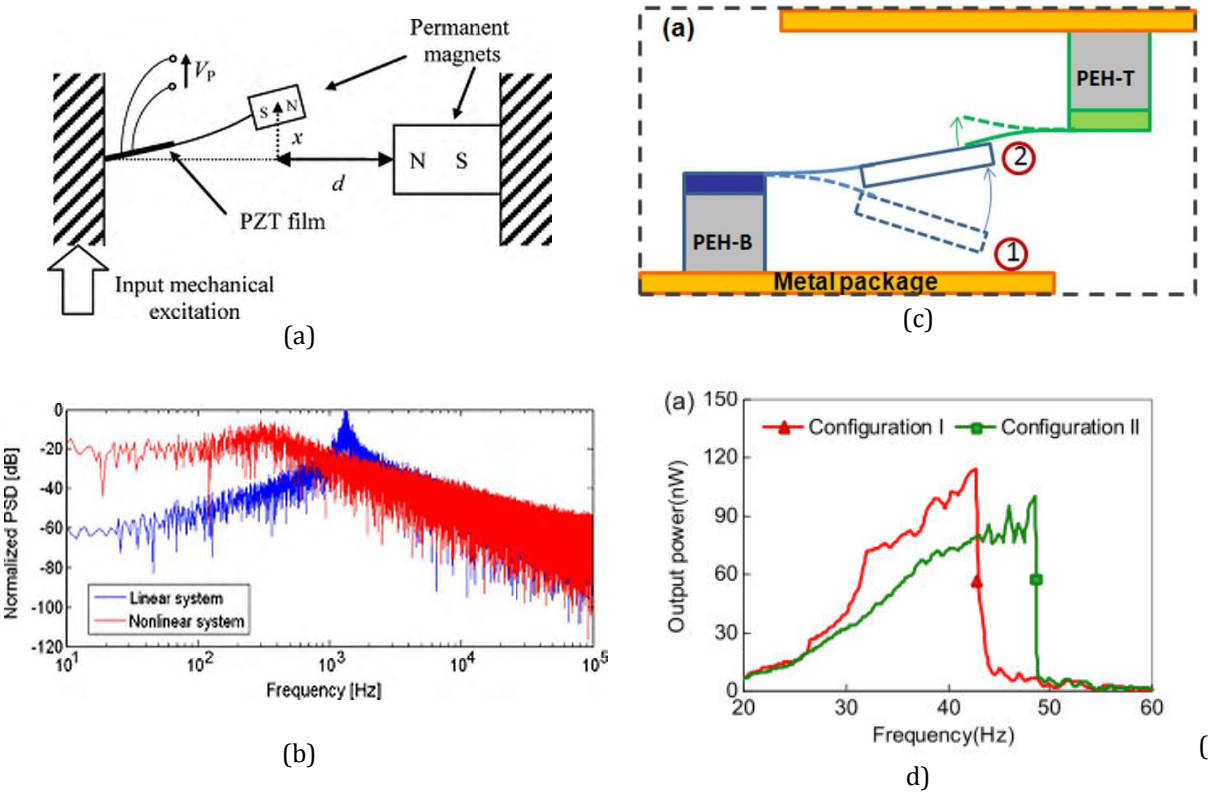

Figure II-8 Bi-stable non-linear harvester (a) with its normalized Power Spectral Density (b) [82] and a hardening stiffness non-linear harvester (c) and its output power with one stopper and two stoppers (d)[83]

In Fig. II-8 are presented the two non-linear types of vibration energy harvesters: the bi-stable configuration where the output power is a bit under the power of an equivalent linear system but the bandwidth over which power can be harvester is much larger. The second type of non-linear vibration energy harvesters consists in hardening the stiffness of the structure, which is changing its resonance frequency. For instance Liu *et al.* limited the displacement amplitude of their cantilever by adding mechanical stoppers above and under it. The cantilevers are micro-fabricated using standard CMOS processes. The package of the system is playing the role of the stopper under the piezoelectric cantilever, but another piezoelectric cantilever, shorter than the principal one, is acting as the upper mechanical stopper. The output power in the first

configuration (with only the lower stopper) as well as in the second configuration (with both upper and lower stoppers) is presented. Each time the cantilever is touching one stopper, the stiffness of the overall system is increasing and the resonance frequency of the cantilever is going higher. Which means that the configuration with two stoppers has a harder stiffness, and a larger frequency bandwidth. On the other hand the maximum output power available is lower than in the softer configuration.

II.1.b.2 Piezoelectric acoustic wave filters

Huge applications of piezoelectric thin films reside in the electronic filters: Surface Acoustic Wave (SAW) and Bulk Acoustic Wave (BAW) filter. The SAW filters production has been exponential since the development of cellphones. With the constant increase of wireless devices, it is necessary to be able to select only one electromagnetic frequency from the surrounding noise. A basic SAW device consists of a piezoelectric substrate on which is deposited two metallic interdigitated transducers (IDT), one actuator and one sensor. The surface acoustic wave, also known as Rayleigh wave, is an elastic mechanical wave, which propagates on the surface of a solid material. The 90% of the wave energy is attenuated at a depth of λ, the wavelength, from the surface. The first IDT receives an electrical signal that actuates the piezoelectric layer under it at a specific frequency. This actuation generates a SAW. The second IDT detects it and converts it into electrical signal again. It is useful to obtain delays as the wave is travelling slower in the material (its propagating velocity is typically around 3000m.s^{-1}). The frequency of the acoustic wave depends on the pitch between the interdigitated electrodes.

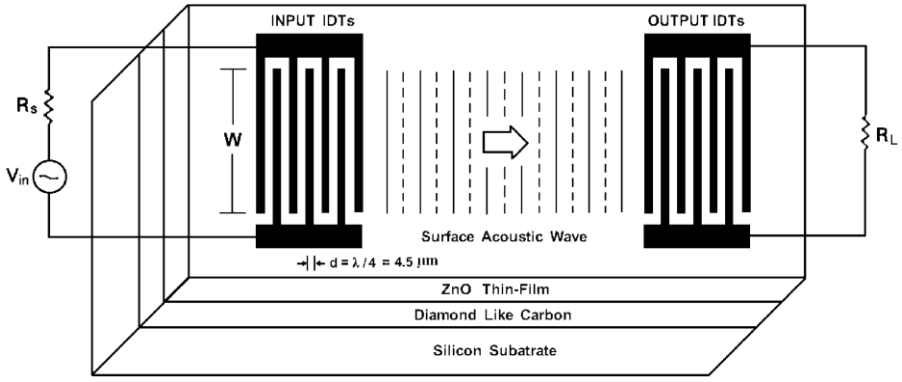

Figure II-9 Schematic of a SAW device using ZnO piezoelectric thin film [84]

ZnO [84] and also AlN [85][86] are the most suited piezoelectric materials for SAW applications because of their good piezoelectric properties and their low propagating loss.

Different substrates can be used depending of the application of the future filter. The central frequency of a conventional SAW device, *f,* is determined by the following relation: $V_s = \quad f = (4d) f$, where V_s is the phase velocity, λ the wavelength of the SAW and d the width of one electrode finger. On standard lithium niobate $LiNbO_3$ substrate the central frequency with 1,53µm wide fingers IDT is 634MHz. In order to get over the GHz applications, one can make the IDT fingers thinner or change the substrate to increase the phase velocity. High resistivity Si and/or diamond-like carbon thin film can increase the central frequency up to 2,4GHz with 1µm wide fingers. SAW devices have two main drawbacks: their size cannot be downscaled and is limited by the size of the two IDTs, and submicron IDT fingers require specific photolithography technique which is increasing the cost of the device.

Bulk Acoustic Wave (BAW) filters overcome the above-mentioned drawbacks. They are thickness mode resonators with much reduced dimensions and their central frequency is given by the piezoelectric film thickness and not anymore by the electrode pitch. The operating frequency can go higher than SAW devices and they can be fabricated on a large variety of substrates CMOS compatible, which is not the case of the $LiNbO_3$ used for the SAW. Different configurations of BAW exist: Film BAW Resonator (FBAR), Thin Film BAW Resonator (TFBAR) [87] and the Solidly Mounted Resonator (SMR). All three designs aim in one goal: insulate the resonator from the substrate in order to confine the acoustic wave. The FBAR and TFBAR are achieving it by creating a cavity under the resonator, while the SMR uses the Bragg principal of the reflection of an acoustic wave between mediums with different acoustic impedance. The alternation of thin films with low and high acoustic impedance Z and with a thickness of a quarter of the wavelength is acting as a Bragg mirror. The best material for the active piezoelectric layer is AlN because of its higher phase velocity in the longitudinal direction compared to ZnO (11600m/s instead of 6400m/s). The best pair of materials for the Bragg reflector is AlN/SiO_2 because of their thermal stability and their low mechanical loss characteristics.

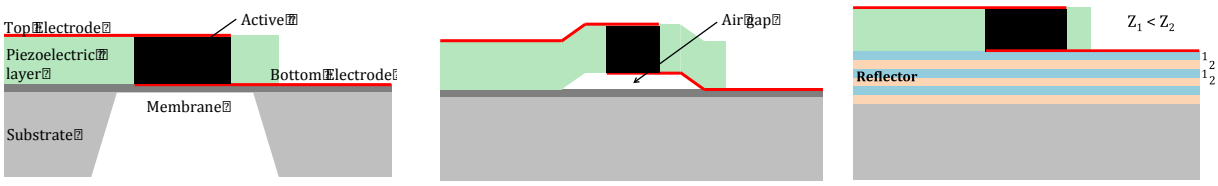

Figure II-10 Three different types of Bulk Acoustic Wave Resonators :
(a) FBAR, (b) TFBAR and (c) SMR

II.1.b.3 Other kinds of energy scavenged by piezoelectric systems

The temperature can also be scavenged thanks to piezoelectric materials, as in this project, taking advantage of a bilayer device experimenting a snap-through mechanism. The temperature dependence of some magnetic materials can also be combined to a piezoelectric bimorph to create a temperature switch [38]. Under a threshold temperature, a hard magnet position at the center of the piezoelectric bimorph is attracted by another soft magnet positioned under the piezoelectric part. The system is motionless.

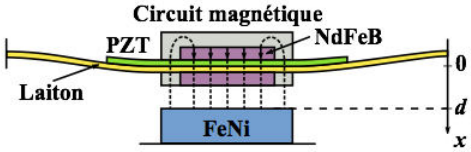

Figure II-11 Thermomagnetic switch combined with piezoelectric energy harvesting [38]

Once the temperature above the threshold, the soft magnet looses its magnetic properties and becomes paramagnetic. The hard magnet is not attracted anymore by it and the system oscillates at its natural frequency. If the temperature decreases and goes under the threshold, the inverse phenomenon occurs: the soft material acquires again its magnetic properties and the hard magnet is suddenly attracted by it. The piezoelectric bimorph is not oscillating but generates charges due to its displacement.

Table II-3 Summary of the ouput power of different piezoelectric energy harvesters

Reference	Material	Configuration	Operating frequency (Hz)	Power
Marzencki [64]	AlN	Cantilever with seismic mass	1371	2µW
Marzencki [64]	AlN	Doubly-clamped beam	2400	90nW
Elfrink [88]	AlN	Cantilever with proof mass	325	85µW
Defosseux [70]	AlN	Cantilever with proof mass	214	0,6µW
Renaud [89]	PZT	Cantilever with proof mass	1800	40µW
Muralt [90]	PZT	Cantilever beam with IDE	855	1,4µW
Jeon [91]	PZT	Cantilever beam with IDE	13700	1µW
Yu [76]	PZT	Array of cantilever with proof mass	235	66,75µW
Xue [75]	PZT	Bimorph in series	93 – 110	60 – 45µW
Liu [83]	PZT	Non-linear cantilever with one stopper	32 – 42	72 – 114nW

Liu [83]	PZT	Non-linear cantilever with two stoppers	30 – 48	34 – 100nW
Carlioz [38]	PZT	Hybrid piezoelectric device	-	3,5mW

The Table II-3 is summarizing all the different piezoelectric devices presented above. In general, one can notice that putting in series cantilevers increase greatly the output power harvested as well as the frequency bandwidth. The non-linear devices are producing less power but their advantage is in their wide frequency bandwidth. The hybrid technology, combining the piezoelectric harvesting with temperature has higher output power because it is a mesoscopic device, the piezoelectric disk of Carlioz measuring 24mm of diameter. Carlioz, as he doesn't have a resonant device, is calculating the instantaneous output power of his switch.

II.2 Deposition techniques of piezoelectric materials

Many means are available to grow piezoelectric thin films. Depending on the material we want to use (purely piezoelectric or ferroelectric) or its future application (CMOS compatible process or not) we can choose one or the other techniques described below. Purely piezoelectric materials as polycrystalline AlN or ZnO have to be textured, i.e. all the grains should be aligned in the same direction (mostly perpendicular to the substrate surface) in order to observe a piezoelectric effect. On the other hand, ferroelectric materials as PZT or PMN-PT don't need to be textured as the polarization of each grain can be aligned when an electric field is applied on the film.

The most utilized technique to deposit piezoelectric as well as ferroelectric materials is the Sputter Deposition technique, as frequently applied Physical Vapor Deposition (PVD) technique. The process is performed in a high vacuum or UHV chamber, filled with a specific rarified gas (sputter gas) having its mean free path in the centimeter range. A glow discharge (cold plasma) is produced between the anode and a cathode of a sputter source. A target is mounted on the cathode. Positive ions formed in the plasma are bombarding the negatively biased target on the cathode, and are sputtering off the atoms from the target. For sputtering pure metals, the sputter gas is normally pure argon. For growing oxides, oxygen is added and for growing nitrides, nitrogen is added. The process for AlN deposition is described precisely in Chapter IV. It is a reactive process, because it works with pure Al target in nitrogen gas and plasma to form the AlN. Effectively AlN is formed in a thin skin at the Al target surface, and then sputtered off. In order to avoid electrical break-downs through the insulating nitride layers that may form on anode and target, the pulsed DC power supply is employed. In the case of PZT, the process is

more complex. The target is a ceramics target obtained by pressing and sintering PZT powder. As the target is insulating, a RF source is needed. In general, quite some deviation of composition can be faced with this approach, and the target composition must be optimized to achieve the desired composition in the film. In the case of PZT, this deviation is rather small (in the few % range). An alternative to this process is to use multiple, pure metallic targets and to do the deposition under oxygen atmosphere [92][93]. The deposition rate is higher due to the higher plasma power that is possible to use, and the composition of the film can be controlled precisely by tuning the power distribution to the various magnetron sources.

Another method employed to deposit piezoelectric as well as ferroelectric thin films is the MetalOrganic Chemical Vapor Deposition (MOCVD). It produces an excellent film quality, very reproducible and of very well controlled composition. Precursors gases (typically alkoxides or similar) are streaming over a heated substrate. Pyrolytic decomposition of the gases leads to the formation of metal-oxide species as needed for the growth of an oxide. The major drawback of this technique is the very high temperature required to activate the chemical reaction (over 1000°C [94] for AlN and between 400°C [95] and 600°C [96] for PZT). Despite its success in ferroelectric memories, CVD is – however - not applied for MEMS (low deposition rate, expensive).

The last technique largely used to deposit ferroelectric materials, such as PZT is the Chemical Solution Deposition, or more precisely sol-gel deposition. Precursors (typically alkoxides with short chains) are dissolved in alcohol, having in principle the composition of the desired film. Some lead loss is anticipated by a higher Pb precursor concentration. More modern processes do also consider the diffusion of Ti and Zr, which flow in opposite directions when driven by the free energy of formation. Hence, modern solutions anticipate also this phenomenon, and a series of different precursor solutions are fabricated to adjust the migration of these species during the process [97]. Once the solutions are prepared, the solutions are spin coated on the substrate and pyrolized at 350°C for 20s. The process is repeated 4 times, the last precursor solution having slightly more lead. Once the four layers are spin coated and are pyrolized, the PZT thin film is annealed at 650°C for 1min in a Rapid Thermal Annealing machine (RTA). Each layer is 60nm thick, so if we want a 250nm thin PZT film, this process has to be done only once, but if we need a 2μm thick PZT film, it should be done 8 times! This technique produces a very high film quality (as soon as the substrate is adapted). Automated sol-gel deposition tools are available today, and some companies work on the industrialization of this process for ink jet printing heads.

II.3 Characterization means – Important parameters

Various parameters have to be checked in order to estimate the quality of a piezoelectric film and/or piezoelectric harvester. First of all the film has to be perfectly oriented in the correct direction, depending of its crystallographic lattice, and should not present too much stress. Its polarization can also be visualized by Piezoresponse Force Microscopy (PFM), which is very interesting in case of ferroelectric materials and domain walls. Of course the piezoelectric coefficients should be measured in order to estimate the efficiency of a piezoelectric thin film or device. Each technique is detailed and two major piezoelectric materials will be taken as example: the AlN for piezoelectric, non-ferroelectric material and PZT for ferroelectric material.

II.3.a Stress and Orientation

The deposition processes of every material, in case of chemical or physical deposition, imply sudden change in temperature between ambient and the high temperature of the process. This creates huge thermal stress in thin films, because of the different thermal expansion of the substrate. During sputtering, the bombardment of the atoms on the substrate is adding even more stress to the film [98]. If they are too high, they can lead to the cracking of the film, or the performance of the device in time will be reduced. Stresses are also diminishing the piezoelectric constant of the material, especially tensile stress. They can influence greatly piezoelectric devices, like cantilevers of membranes, because once the substrate is thinned or even etched away, the device can deform itself. We take advantage of this deformation to measure the stress created in the thin film after deposition. A laser beam measures the curvature of the substrate before and after the deposition and thanks to the Stoney formula we can estimate the built-in stresses in the film. This process is more detailed in the Chapter IV.

Crystallographic orientation of the film with respect to the substrate is also a crucial parameter. In order to give advantage of one preferential orientation, seed-layers are deposited before the piezoelectric film. In case of AlN it can be Pt oriented in its (111) cubic direction. This allows us to obtain (002) oriented hexagonal AlN because their lattice parameters are very similar. In case of PZT, one can deposit a very thin layer of TiO_2 on platinum electrodes to obtain a (111) textured PZT [99] or a few nm-thick $PbTiO_3$ layer to get (100) textured PZT [100].

The orientation is measured by X-Ray Diffraction (XRD) in the θ - 2θ mode. The X-Rays bombarding the surface of the film are reflected only by crystallographic planes that are

oriented at an angle θ following the Bragg equation. Whenever the X-Rays are diffracted, we observed a peak that is corresponding to certain (*hkl*) Miller index.

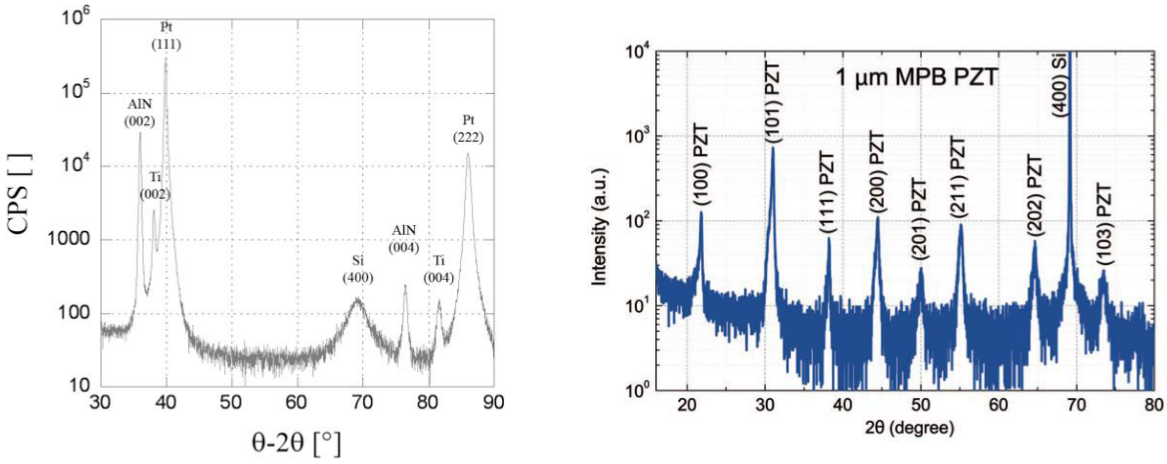

(a) (b)

Figure II-12 XRD patterns of AlN grown of Pt-Ti electrode (a) [101] and of sol-gel PZT on Ti/TiO_2 seed layer (b) [102]

In Fig. II-12 are presented two XRD patterns of AlN and PZT. AlN is sputtered on Pt-Ti electrodes. Peaks of AlN (002), Pt (111) and Ti are visible, as well as Si from the substrate. The PZT is deposited by sol-gel on a Ti/TiO_2 seed-layer. It is called MPB PZT for Morphotropic Phase Boundary PZT. Indeed the phase diagram of PZT is displaying all the different crystallographic lattices possible for the different ratio between Zr and Ti.

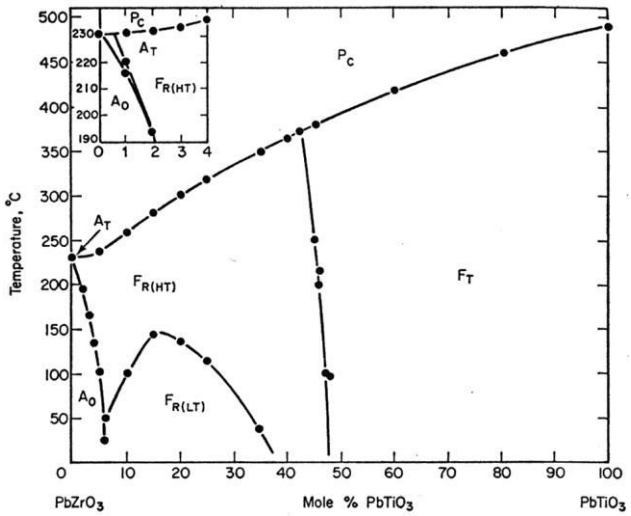

Figure II-13 Phase diagram of $Pb(Zr_x,Ti_{1-x})O_3$ solid solution [103]

The phase diagram of PZT is presented in Fig. II-13. Depending on the ratio Zr/Ti, the lattice can be rhombohedral (F_R), tetragonal (F_T), or orthorhombic (A_O). Above the Curie temperature, the material is not anymore ferroelectric and has a cubic lattice (P_C). A

morphotropic phase boundary is an abrupt crystallographic change at a constant temperature. PZT has a MPB at 52% of Zr and 48% of Ti, separating the tetragonal to the rhombohedral phase. The piezoelectric coefficients are higher at this specific composition. In Fig. II-12(b) we can see that the film is randomly oriented because every orientation is represented.

II.3.b Polarization

At microscale, the polarization is very difficult to determine. However a lot of insight can be gained by studying the piezoelectric response at the nanoscale, revealing domain walls and giving information about polarization direction. Indeed a lot of work is done to explain the movement of the domain walls, how and when they are created and if they can be controlled. Applications in the field of electronic memories are very promising [104].

The technique described here is named Piezoresponse Force Microscopy (PFM). It is based on the Atomic Force Microscopy (AFM): a small tip mounted at the free-end of a cantilever is scanning the surface (Fig. II-14). A laser beam is focused on the cantilever, at the localization of the tip, and measures the displacement of the cantilever. The difference between these two techniques is that for PFM an AC-modulated voltage is applied to the sample surface. The ferroelectric material surface is then moving, following the applied voltage. The simplest PFM measurement consists in measuring only the vertical displacement of the cantilever, which should be proportional to the applied voltage with by the d_{33} coefficient. The phase change between the actuation and the displacement indicates the polarization orientation. The lateral precision of PFM is of a few 10nm, while it can reach the picometer range in vertical detection [105][106].

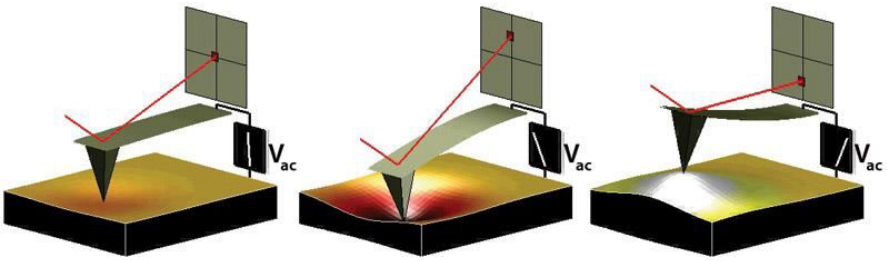

Figure -II-14 Working principle of PFM technique

II.3.c Piezoelectric coefficients

The most useful piezoelectric coefficients able to characterize an actuator or harvester are d_{33} and e_{31}. d_{33} coefficient applies for a free bulk piezoelectric material with its polarization along

the 3-axis, and describes the piezoelectric strain along the 3-axis upon application of an electric field along the polarization (longitudinal effect). e_{31} coefficient describes the behavior of a clamped bulk material (the strain is zero) with its polarization along the 3-axis, and describes the stress generated in the transverse direction (1) when an electric field is applied along the polarization. In case of thin film, the coefficients have to be modified to take into account that the thin film is clamped on the substrate. This means that when an electric field is applied, the in-plane strain components remain zero, and the out-of-plane stress component is also equal to zero. These conditions lead to two effective coefficients [107]:

$$e_{31,f} = \frac{d_{31}}{s_{11}^E + s_{12}^E} \qquad \text{Eq. II-5}$$

$$d_{33,f} = d_{33} \quad \frac{2s_{13}^E}{s_{11}^E + s_{12}^E} d_{31} \qquad \text{Eq. II-6}$$

These coefficients, even if it's not visible in the formula above, are sensitive to the electrode size and the substrate stiffness [108]. The smaller are the electrodes, the lower is the $d_{33,f}$ coefficient. But this effect tends to disappear if the stiffness of the substrate increases. These two coefficients can be measured directly with the following techniques: the double-beam interferometer for $d_{33,f}$ coefficient (Fig. II-15), and a cantilever bending technique for $e_{31,f}$ coefficient (Fig. II-17). A standard cantilever structure is used in both characterizations, with a thin piezoelectric film on top of a thick silicon substrate. The cantilever is clamped on one side. As $d_{33,f}$ is describing the change in thickness of the device, it is necessary to measure the displacement on both upper and lower sides. That's why a double laser beam interferometer based on the principal of a Mach-Zehnder interferometer is used. One laser is focused on the piezoelectric film side and another one on the substrate side. The advantage of this setup is that it allows us to discriminate the change in thickness due only to $d_{33,f}$ coefficient from the bending of the cantilever that is due to the in-plane coefficients. Indeed the total length of the optical path of the laser will not be modified by the bending of the sample; it will increase or decrease only by the change in thickness.

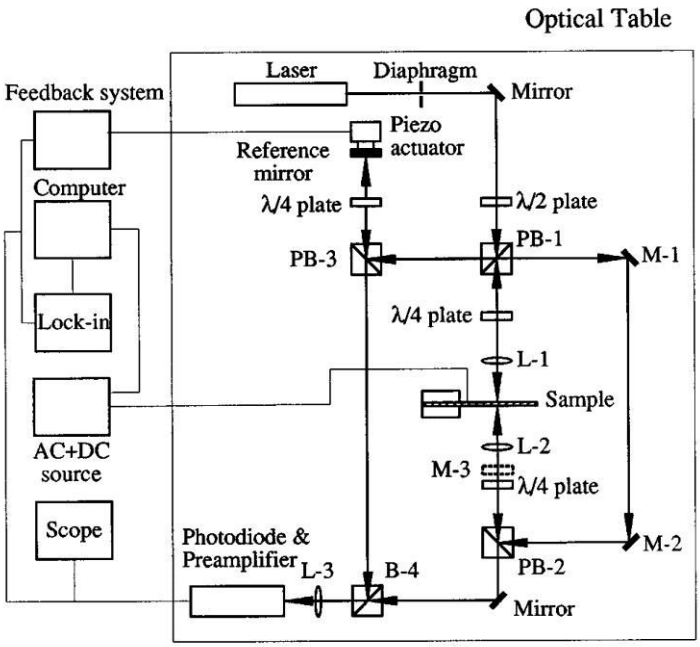

Figure II-15 Schematic of the double-beam laser interferometer [101]

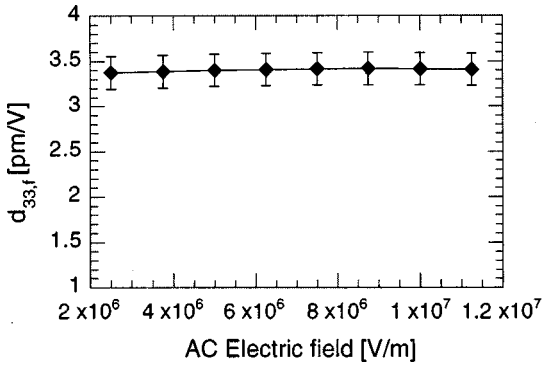

Figure II-16 $d_{33,f}$ coefficient in function of the applied ac voltage at 10kHz for a 1µm thick AlN thin film [87]

$e_{31,f}$ coefficient, describing better the converse piezoelectric mode, is characterized in another manner. We are presenting only two methods, but they are not the only ones[109]. The same cantilever, still clamped on one side, is placed vertically. On the substrate side, an insulating tip in alumina, driven by a piezoelectric actuator, is furnishing a given displacement to the free end of the sample (Fig. II-17). The tip needs to be insulating to avoid any electrical charges to flow away. A sinusoidal voltage is applied to the tip, which is displacing also in a sinusoidal way. Initially it is put in contact with the sample, in order to always push it. The charges are then collected between the top and bottom electrode by a charge amplifier. This technique is more detailed in Chapter IV.

Another way to characterize $e_{31,f}$ coefficient is done in actuator mode, by measuring the displacement of the free-end of the clamped cantilever by a single-beam interferometer. Indeed there is a direct relation between the in-plane stress and the electric field applied to the thin film [107][102]:

$$T_1 = e_{31,f} E_3 \qquad \text{Eq. II-7}$$

$$T_1 = \frac{1}{3(1-\nu)c_f} \frac{Yt_s^2}{x_1(2x_2 - x_1)} \frac{w(x_2)}{t_p} \qquad \text{Eq. II-8}$$

The stresses T_1 are measured indirectly with the displacement at the free-end of the cantilever $w(x_2)$, the Young modulus Y and the Poisson coefficient ν of the substrate, c_f the width ratio between the piezoelectric film and the top electrode, the thicknesses of the substrate t_s and piezoelectric film t_p and the length of the top electrode x_2 and the point where the displacement are measure x_2 following the Eq. II-8.

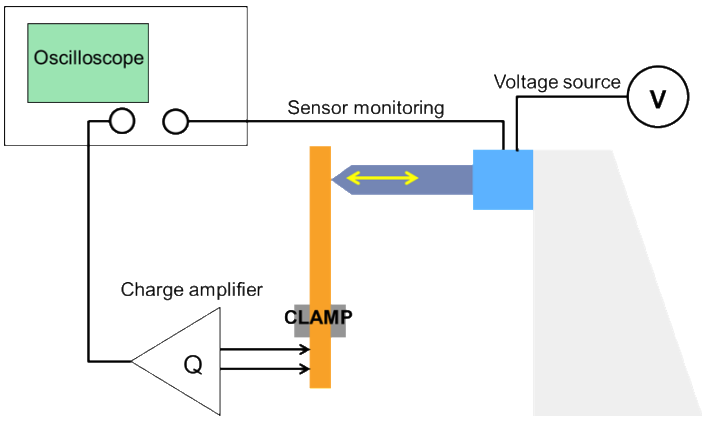

Figure II-17 $e_{31,f}$ characterization setup

For ferroelectric materials as for instance PZT, the value of the $e_{31,f}$ coefficient depends strongly on the amplitude of the electric field applied. On Fig. II-18 we can see clearly the hysteresis when we apply an increasing electric field or decreasing one. This corresponds to the switching of the polarization.

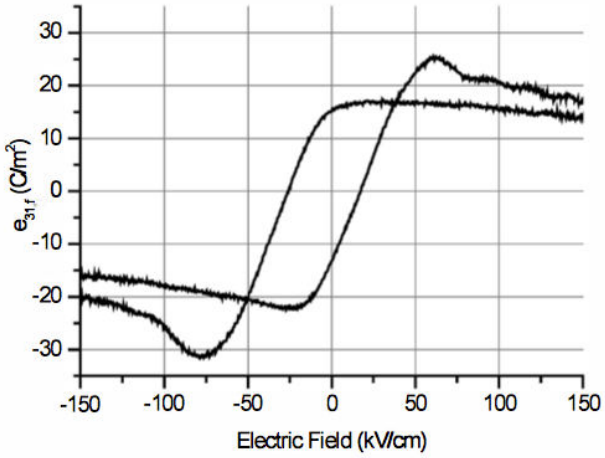

Figure II-18 $e_{31,f}$ loop of a 1,18µm thick sol-gel PZT derived from stress-measurement [110]

Another important parameter of a piezoelectric material is its ability to convert the electrical energy into mechanical energy and vice versa and is described by the electromechanical coupling coefficient *k*. It is the ratio of the electrical energy over the total energy in the material. We consider the first two constitutive equations of the Table II-2, in the case of a cantilever where the polarization is along the 3-axis and the stress is in the 1-axis. If the material is in short-circuit configuration, the electric field E_3 is zero in both equations and we obtain the expression of the strain in short-circuit:

$$S^{short} = s_{11}^{E} T_1 \qquad \text{Eq. II-9}$$

In open-circuit configuration we can consider the electric displacement D_3 equal to zero. From the first constitutive equation we deduce an expression of the electric field, and we can introduce it in the second constitutive equation to get the strain in open-circuit condition:

$$E_3 = \frac{d_{31}}{\varepsilon_{33}^{T}} T_1 \qquad \text{Eq. II-10}$$

$$S^{open} = (s_{11}^{E} - \frac{d_{31}^2}{\varepsilon_{33}^{T}}) T_1 = s_{11}^{D} T_1 \qquad \text{Eq. II-11}$$

We can consider the strain in short-circuit as the total energy stored by the material. The amount of electric energy is the difference between the strain in short and open-circuit conditions. The ratio between the two gives us a definition of the electromechanical coupling coefficient:

$$\frac{S^{short} - S^{open}}{S^{short}} = \frac{s_{11}^{E} - s_{11}^{D}}{s_{11}^{E}} = \frac{d_{31}^2}{s_{11}^{E} \varepsilon_{33}^{T}} = k_{31}^2 \qquad \text{Eq. II 12}$$

k_{31}^2 is valid only in the 31-mode, when the polarization is along the 3-axis and the applied stress along the 1-axis. The subscripts have to be adapted to the configuration of the device.

In order to compare the performance of different piezoelectric materials, Figures of Merit (FOM) can describe the ability of a material to harvest energy for instance. Two FOM can be used in a cantilever configuration (31-mode): one describing the ability of the material to harvest energy [111][107] and the other one, describing the behavior of the device off-resonance from Priya [112], taking into account the dielectric losses of the device:

$$FOM_{mat} = \frac{e_{31,f}^2}{\varepsilon_0 \varepsilon_{33}} \quad \text{Eq. II-13}$$

$$FOM_{off\ resonance} = \frac{d_{31} g_{31}}{\tan\delta} = \frac{d_{31}^2}{\varepsilon_{33} \tan\delta} \quad \text{Eq. II-14}$$

Thanks to these FOM, we are able to compare the performance of different piezoelectric materials used for energy harvesting applications. Table II-4 summarizes the results obtained in the literature.

Table II-4 FOM of different piezoelectric material for energy harvesting applications

Material	$e_{31,f}$ **(C/m²)**	ε_{33}	**FOM$_{mat}$ (GPa)**	d_{31} **(pm/V)**	$tan\delta$	**FOM$_{off\text{-}res}$**
PZT-poly [113]	-9.6	1545	6.74	93.5	0.04	141
PZT-epi [114]	-18.2	100	374	135		
AlN-poly [107]	-1.05	10.5	11.9	2.625	0.001	656
AlN-epi [111]	-1.37	9.5	22.3			
ZnO [107]	-1	10.9	10.4	5.2		
PMnN-PZT-epi [115]	-12	100	163	83	0.01	6889

Three most represented materials are presented: AlN polycrystalline and epitaxial thin film, ZnO polycrystalline thin film and PZT polycrystalline and epitaxial thin film, with a derivative PMnN-PZT ceramic grown epitaxially. In general, the materials grown epitaxially exhibit better performances when the FOM_{mat} is used than the same polycrystalline material. Epitaxially grown thin films have better piezoelectric and ferroelectric properties than polycrystalline films, but the major advantage of PZT epitaxial thin films is their reduced dielectric constant compared to the polycrystalline ones. This specificity is due to the highly c-

axis orientation of the epitaxial films. The drawback of the epitaxial films is their complex fabrication process; several seed-layers are needed to achieve the epitaxy [115][116]. For energy harvesting applications, the polycrystalline AlN is more suitable than polycrystalline PZT, even if it presents lower piezoelectric coefficients. The high dielectric constant of the PZT-poly is impacting on the output voltage that is furnished by the final device.

II.4 Electrical representation and characterization

In the 1930s Van Dyke created a model that describes the behavior of a resonant piezoelectric device around its resonance frequency by an equivalent electrical circuit. Mason has widened the possibilities of this model describing the elastic, piezoelectric and dielectric properties of the material around the resonance frequency of the vibrating device.

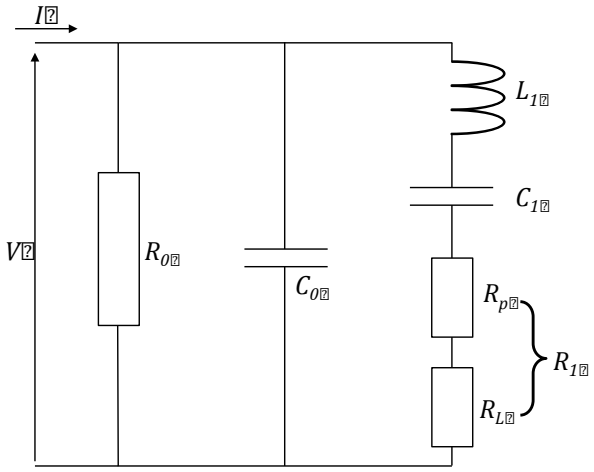

Figure II-19 Simplified Mason equivalent piezoelectric model

In Fig. II-19 is presented the equivalent electrical circuit modeling the behavior of a piezoelectric material. Each electrical element corresponds to a specific property of the device [117]:

- R_0 the dielectric losses,
- R_p the mechanical losses,
- R_L the load resistance,
- C_0 the capacitance of the element,
- C_1 the flexibility of the vibrating element,
- L_1 the dynamical mass.

The element is actuated by a voltage *V* with negligible impedance. The LCR branch is called the motional branch and describes the vibrating part of the device. The following relation gives the mechanical impedance:

$$z_m = R_1 + jL_1 \quad \frac{1}{jC_1} \qquad \text{Eq. II-10}$$

The resonance angular frequency ω_s is taken when the imaginary part of the impedance is zero, in other words when $L_1 C_1 \ {}_s^2 = 1$. The quality factor of the structure is $Q_m = L_1 \ {}_s / R_1$.

The global admittance of the element is given by:

$$Y = \frac{1}{R_0} + jC_0 \ + \frac{1}{z_m} = \frac{1}{R_0} + jC_0 \ + \frac{jC_1}{1 \ L_1 C_1 \ {}^2 + jR_1 C_1} \qquad \text{Eq. II-11}$$

In the complex space, the admittance can be drawn as a circle and the parameters are easier to extract. To do that, we have to define a new admittance, named as reduced admittance *y*, which corresponds to a translation of the admittance by the expression:

$$\overline{O} = \frac{1}{R_0} + \frac{1}{2R_1} + jC_0 \ {}_s \qquad \text{Eq. II-12}$$

Assuming that the material has low loss, which means that its quality factor is high, the reduced admittance can be written as follow, which corresponds to a circle of center Ω and radius $1/2R_1$:

$$y \quad \frac{1}{2R_1} \frac{1 \ L_1 C_1 \ {}^2 \ jR_1 C_1}{1 \ L_1 C_1 \ {}^2 + jR_1 C_1} = \frac{1}{2R_1} e^j \qquad \text{Eq. II-13}$$

We can define on the diagrams of Fig. II-20 the points A, B, C and D which have very important properties for the characterization:

- Point A: the **resonance frequency f_s**
- Point B and C: the **quadrantal frequencies f_{q1} and f_{q2}** for which the argument of the reduced admittance is equal to $\pm\pi/2$.
- Point D: the **anti-resonance frequency f_p.**

The anti-resonance frequency corresponds to the frequency when the denominator imaginary part of the admittance (Eq. II-14) is equal to zero, assuming that the dielectric loss R_0 is zero:

$${}_p^2 = \ {}_s^2 \ 1 + \frac{C_1}{C_0} \div \qquad \text{Eq. II-14}$$

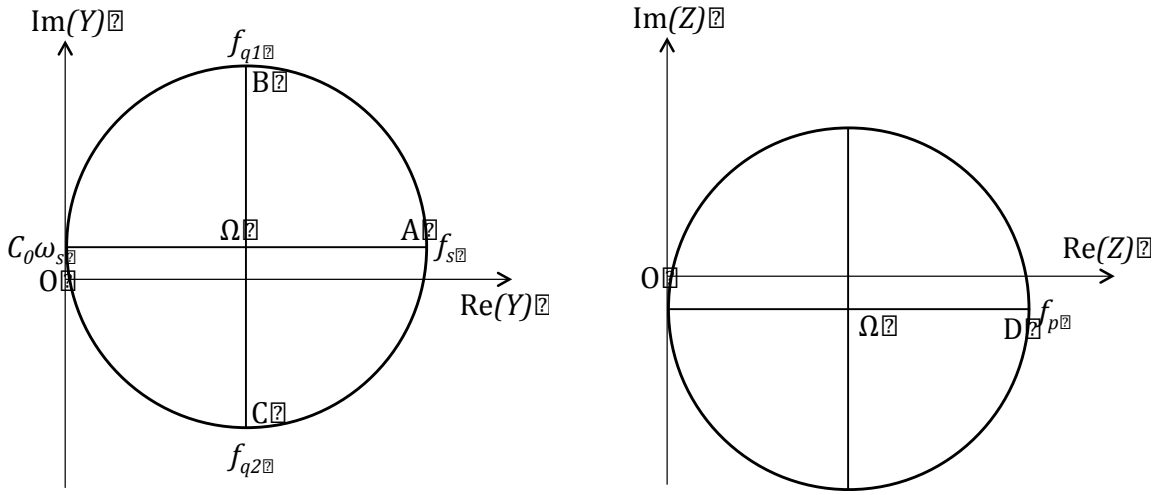

(a) (b)

Figure II-20 Representation of the admittance and impedance.

In the diagram shown in Fig. II-20, we have to take the impedance not from the admittance *Y* but from the reduced admittance *y*. The angular frequency where the imaginary part of this impedance is zero is:

$$\frac{2}{D} = \frac{2}{s}\left(1+\frac{C_1}{C_0}\right)\left(\frac{1}{2Q_m^2}\div\right) \qquad \text{Eq. II-15}$$

This expression is not exactly the anti-resonance frequency, but the higher is the quality factor the closer is the value to the real f_p. At a Qm of 10, the discrepancy between f_D and f_p is of 0.25%. The apparent coupling coefficient is defined from the resonance and anti-resonance frequencies by the following relation:

$$k_{app}^2 = \frac{f_p^2 \quad f_s^2}{f_p^2} \qquad \text{Eq. II-16}$$

The previous consideration and the Mason model in general is valid only around the resonance frequency of the device. Out of resonance, the piezoelectric material can be considered as a capacitor, which can be modeled by a capacitance C_p in parallel with resistance R for the dielectric losses. The total impedance of the capacitor can be represented by its vector diagram as in Fig. II-21.

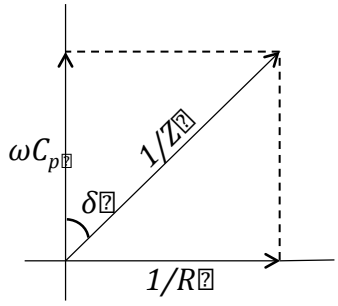

Figure II-21 Vector representation of a lossy capacitor impedance

The $tan\delta$ is called the energy loss in the insulator. It corresponds to the amount of energy absorbed by the material. A perfect insulator would have a $tan\delta$ equal to zero.

The extracting circuit is very important for the output power optimization of the harvesting device. Different kinds of circuits have been implemented, the most common ones are the rectifier-based circuit, which is a passive one as it is composed exclusively of passive components, and non-linear circuits using appropriate time switches to enhance the energy conversion like the synchronized switched harvesting on inductor (SSHI) technique[118] or the synchronous electrical charge extraction (SECE) [119]. The SSHI and SECE circuits are not passive, but semi-active, which means that they need a small amount of power to work. Most recent techniques allow to work at lower frequency [120] or to increase the frequency bandwidth [121] of the harvester.

II.5 Conclusion

The bibliographic results presented in this chapter focus on the piezoelectric materials, especially piezoelectric thin films, their applications in energy harvesting and their characterization. The piezoelectric devices for energy harvesting are popular research subjects and the cantilever with a proof mass is the most widespread configuration. Its fabrication process is mastered and its mechanical behavior well understood. At micro-scale, a large majority of piezoelectric devices harvest mechanical vibrations. The major issue for MEMS energy harvester is to broaden the bandwidth and to lower the resonance frequency to adapt it to ambient vibrations. In order to be efficient, a piezoelectric thin film has to be well oriented, to have high piezoelectric coefficients and/or low dielectric constant in order to get more output voltage in harvesting applications. Different piezoelectric materials are compared and one has to

make a compromise between the efficiency of the material and the complexity of its fabrication process, which is not always CMOS compatible.

For our project, AlN is the most convenient material, even if it is not the material with the best properties. Indeed it has low dielectric constant, which means high energy harvesting FOM. It is also completely CMOS compatible, and its deposition process does not require specific seed-layers. Moreover, the stress in the film is tunable by adjusting the deposition parameters. Several other energy harvesters based on AlN showed impressive output power, which is promising for us.

III Analytical and numerical modeling

In this chapter we will present an analytical model of the behavior of a beam-type bilayer structure. Its buckled shape after the fabrication process is demonstrated as well as an estimation of the buckling temperature deduced from the initial deflection obtained before. This model is valid for a Bernoulli structure, a slender beam, where its width is much lower than its length. The structures fabricated here, for the major part, cannot be considered as Bernoulli structure, as they have a width comparable to their length. They are considered as plate and the analytical model is more complex and will not be treated here. On ANSYS (v15) we investigate the evolution of the critical load on the different structures as well as their resonance frequency. The buckling caused by a mechanical force of the structures is presented and the impact of the initial deflection and of the geometry of the structure on the critical buckling force is analyzed.

III.1 Analytical model

In this part the method to get the buckled shape of a multilayer beam is detailed. This demonstration is valid only for slender beams. In a second time the temperatures of snap up and snap back are estimated using the theory of Timoshenko, which is also valid only for slender multilayer beams.

III.1.a Buckled shape for multilayer beams

The buckling occurs when the axial load produced by residual compressive stress or thermal compressive stress exceeds a critical limit, called Euler's load. It converts small in-plane strains into comparatively large out-of-plane displacements and results from a mechanical instability of the device while the materials are still in the elastic domain. A lot of studies have been realized on the buckling of beams [50][122][123][124][125][126], in particular for their application as thermal switches. In this model, which is largely inspired from [127] we take into account the finite torsional stiffness as well as finite axial stiffness at the supporting ends to describe them as elastically constrained. Indeed in real MEMS structures the supporting ends are never perfectly clamped or perfectly hinged.

The structures that are studied are composed of 0,3µm of a bottom layer with an equivalent Young modulus of the multilayer: 0,1µm of Pt and 0,2µm of AlN seed-layer, one layer of AlN and one layer of Al, which thicknesses are varying. The stress induced by the fabrication process into the different layers is varied to see its effect on the initial shape of the device. The simulated structures are measuring 2000µm by 200µm and 1400µm by 700µm. The first one

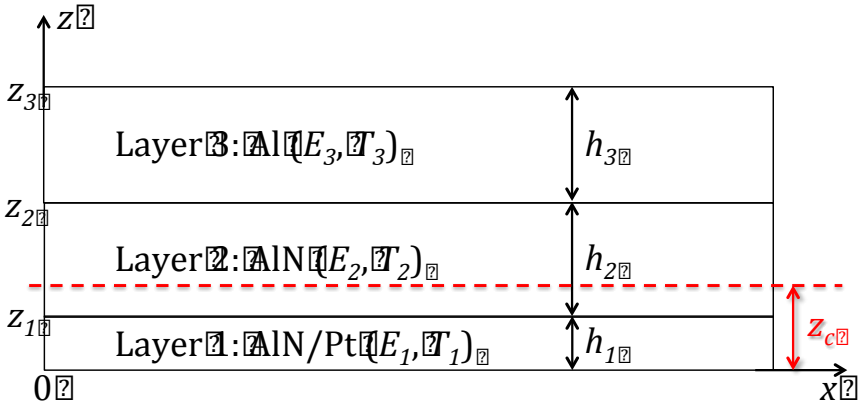

corresponds to a slender beam while the second one is considered as a plate. The model is applied on these two structures.

Figure III-1 Cross-section of a multilayer micro bridge considered here.

The neutral axis of the structure illustrated in Fig. III-1 is situated at a distance z_c from the *x0y*-plane and is calculated as follow:

$$z_c = \frac{\sum_i \frac{1}{2} E_i \left(z_i^2 - z_{i-1}^2 \right)}{\sum_i E_i h_i} \qquad \text{Eq. III-1}$$

where E_i and h_i are the Young modulus and the thickness of the ith layer. Such multilayer bridge can be considered as a single layer bridge with effective parameters, which are weighted averages of each parameters such as the Young modulus E_{eff}, the thickness h_{eff}, the residual stress T_{eff} and the flexural rigidity per unit width $(EI)_{eff}$, given as:

$$h_{eff} = \sum_i h_i \qquad \text{Eq. III-2}$$

$$E_{eff} = \frac{\sum_i h_i E_i}{h_{eff}} \qquad \text{Eq. III-3}$$

$$T_{eff} = \frac{\sum_i T_i h_i}{h_{eff}} \qquad \text{Eq. III-4}$$

$$(EI)_{eff} = \sum_i \frac{1}{3}(z_i - z_c)^3 - (z_{i-1} - z_c)^3 E_i \qquad \text{Eq. III-5}$$

At one end of the beam, for instance in $x = 0$ as shown in Fig. III-2, there are several loads acting when the beam is deflecting in the z-direction of the quantity $w(x)$:

- → Net axial load per unit width P_t due to the change in temperature for example,
- → Residual moment M_r due to the inhomogeneous distribution of the stress between the different layers,
- → A moment due to the supporting end $-r\frac{dw}{dx}(x=0)$ introducing the torsional stiffness per unit width α_r,
- → A bending moment $(EI)_{eff}\frac{d^2w(x)}{dx^2}$.

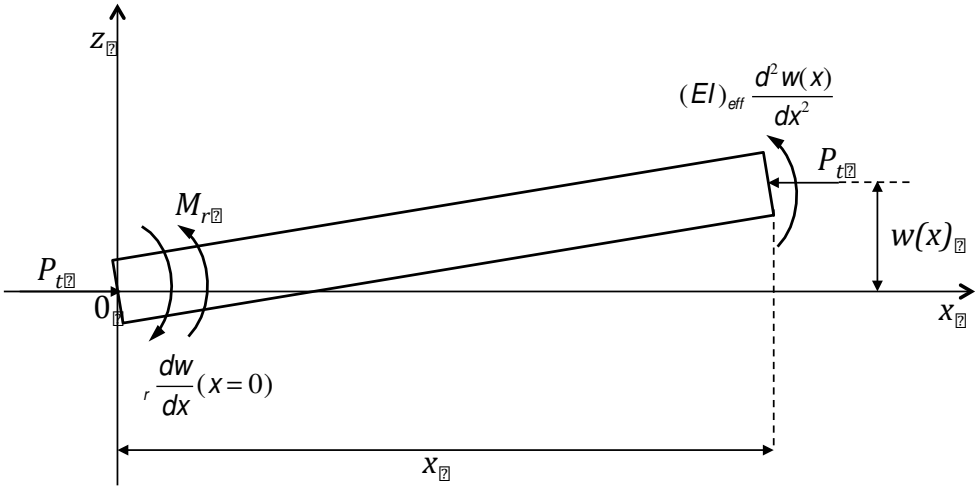

Figure III-2 Free body diagram of the beam with all the loads acting on it

With the assumption that the beam acts in small deflections, the equilibrium condition is that the sum of the moments acting on the beam is zero:

$$M_r - r\frac{dw}{dx}(x=0) + P_t w(x) + (EI)_{eff}\frac{d^2w(x)}{dx^2} = 0 \qquad \text{Eq. III-6}$$

Differentiating twice the Eq. III-6 we obtain the differential equation for small deflection of a beam under a compressive axial load P_t:

$$\frac{d^4w}{dx^4} + \frac{P_t}{(EI)_{eff}}\frac{d^2w}{dx^2} = 0 \qquad \text{Eq. III-7}$$

The general solution of the previous differential equation is given as follow:

$$w(x) = C_1 \sin(\ x) + C_2 \cos(\ x) + C_3 x + C_4 \qquad \text{Eq. III-8}$$

where $^2 = \frac{P_t}{(EI)_{eff}}$ and C_1, C_2, C_3 and C_4 are constants determined by the boundary conditions of the system. We can assume that the beam is symmetric with respect to the mid-point $x = L/2$, where L is the length of the beam, and that there is no deflection at the anchors $x = 0$ and $x = L$. The boundary conditions are then defined as follow:

$$w(0) = w(L) = 0 \qquad \text{Eq. III-9(a)}$$

$$\frac{d^2 w}{dx^2}(x=0) = \frac{1}{L}\frac{dw}{dx}(x=0) \qquad \text{Eq. III-9(b)}$$

$$\frac{d^2 w}{dx^2}(x=L) = \frac{1}{L}\frac{dw}{dx}(x=L) \qquad \text{Eq. III-9(c)}$$

Where $= \frac{(EI)_{eff}}{{}_r L}$. Applying these boundary conditions to the general solution, we obtain a set of four equations that allow us to find the four unknown constants. These linear equations can be written under the form of matrices as follow:

$$\begin{matrix} 0 & 1 & 0 & 1 \\ \sin & \cos & L & 1 \\ & {}^2 & L & 0 \\ {}^2\sin + \cos & (\ {}^2\cos + \sin\ ) & L & 0 \end{matrix} \begin{matrix} C_1 \\ C_2 \\ C_3 \\ C_4 \end{matrix} = \begin{matrix} 0 \\ 0 \\ 0 \\ 0 \end{matrix} \qquad \text{Eq. III-10}$$

Where $= L$. In order to find a non-trivial solution, the determinant of the matrix has to be zero, which defines the occurrence of buckling, the first solution being the first mode of buckling, and is given as:

$$\tan \frac{}{2} \div = \qquad \text{Eq. III-11}$$

Due to the symmetry of the structure with respect to the mid-point, we can assume that the constant C_3 is equal to zero. We obtain then the following relations:

$$C_3 = 0 \qquad \text{Eq. III-12(a)}$$

$$C_2 = \quad C_4 \qquad \text{Eq. III-12(b)}$$

$$C_1 = \qquad C_2 \qquad \text{Eq. III-12(c)}$$

Introducing these values into the Eq. III-8 we obtain the following deflection equation:

$$w(x) = C_4 \qquad \sin\ \frac{}{L}x \div +1 \quad \cos\ \frac{}{L}x \div \div \qquad \text{Eq. III-13}$$

The constant C_4 is determined by assuming that the mid-point deflection $w(L/2)$ is equal to δ_0, we can replace x by $L/2$ in the previous equation. Moreover, using Eq. III-11, we can demonstrate that:

$$\cos\frac{}{2} = \frac{1}{\sqrt{1+\tan^2(\ /2)}} = \frac{1}{\sqrt{1+(\quad)^2}} \qquad \text{Eq. III-14(a)}$$

$$\sin\frac{}{2} = \frac{\tan(\ /2)}{\sqrt{1+\tan^2(\ /2)}} = \frac{}{\sqrt{1+(\quad)^2}} \qquad \text{Eq. III-14(b)}$$

Taking Eq. III-14(a) and (b) into account, the constant C_4 can be given as:

$$C_4 = \frac{0}{1+\sqrt{1+(\quad)^2}} \qquad \text{Eq. III-15}$$

Thus the shape of the first buckling mode is defined by $w_0(x)$ and is given, combining Eq. III-13 and Eq. III-15, as:

$$w_0(x) = \frac{0}{1+\sqrt{1+(\quad)^2}} \qquad \sin\ \frac{}{L}x \div +1 \quad \cos\ \frac{}{L}x \div \div \qquad \text{Eq. III-16}$$

For the particular case of a doubly clamped beam, the torsional stiffness, α_r, is infinite, and by consequence λ is zero. Using the Eq. III-11, we can deduce that the first buckling mode is obtained for $\phi = 2\pi$, and the buckled shape of the clamped beam can be simplified to:

$$w_c(x) = \frac{0}{2}\ 1 \quad \cos\ \frac{2}{L}x \div \qquad \text{Eq. III-17}$$

On the other hand, for a doubly hinged beam, the torsional stiffness α_r is zero, and λ is infinite. From Eq. III-11 we deduce that the first buckling mode occurs when $\phi = \pi$, and the buckled shape of the hinged beam can be reduced to:

$$w_h(x) = {}_0 \sin \frac{}{L} x \div \qquad \text{Eq. III-18}$$

There is a minimum axial load per unit width for which the buckling occurs, and it is called Euler's load per unit width P_E. It is given combining the definitions of ζ and ϕ as follow:

$$P_E = (EI)_{eff} \frac{}{L^2}^2 \qquad \text{Eq. III-19}$$

where ϕ should satisfy the condition of buckling fixed by the Eq. III-11. The axial load per unit width after buckling can be expressed as [128]:

$$P_t = P_E \ 1 + \frac{b}{2L} \div \qquad \text{Eq. III-20}$$

Where δ_b is the deflection of the beam after buckling and in presence of the axial load P_t:

$$_b = \int_0^L \frac{dw_0}{dx} \div^2 dx \qquad \text{Eq. III-21}$$

We can relate the effective stress σ_{eff} to the mid-point deflection δ_0 by using the compatibility of strain relation. It requires that the distance between the two supporting ends doesn't change with the application of the different loads on the beam. It leads to the following relation:

$$\frac{T_{eff} L}{E_{eff}} = \frac{P_t L}{h_{eff} E_{eff}} + \frac{1}{2} \int_0^L \frac{dw_0}{dx} \div^2 dx \qquad \text{Eq. III-22}$$

The first term refers to the change in length due to the effective stress, the second one to the application of an axial load per unit width P_t and the third one to the deflection of the beam. Combining the Eq. III-20 and III-22 we obtain the following relation:

$$T_{eff} = \frac{P_E}{h_{eff}} \ 1 + \frac{b}{2L} \div + \frac{E_{eff} \ b}{L} \qquad \text{Eq. III-23}$$

From the geometrical and initial stress conditions of the beam, we can calculate the Euler's load P_E. It can then be injected into the Eq. III-23 to get the deflection δ_b. With the value of δ_b we can use the Eq. III-21 to obtain the initial deflection δ_0 and then we have the initial buckled shape of the beam as defined in Eq. III-16.

We applied this model to our structures by computing the previous equations in Maple. We consider here two kinds of rectangular structures: one measuring 2000µm by 200µm, which can be assimilated to a slender beam, and another one measuring 1400µm by 700µm, which is a plate and not a beam, but which will be intensively studied and characterized later. The material properties are taken as follow:

- AlN: Young modulus of 318GPa, 0.21 for the Poisson coefficient and $3.1.10^{-6}K^{-1}$ for the thermal expansion coefficient [129],
- Al: Young modulus of 70GPa, 0.35 as the Poisson coefficient and 24.10^{-6} K^{-1} for the thermal expansion coefficient [130],
- Pt: Young modulus of 168GPa, 0.38 for the Poisson coefficient and $8.8.10^{-6}$ K^{-1} for the thermal expansion coefficient [130],

The evolution of the mid-point deflection of the device in function of the stress in the Al layer and the AlN layer is depicted in Fig. III-3 where the stress in the hybrid AlN/Pt layer is kept constant. As explained in details later, stress in films is adjusted and tuned with the deposition parameters to obtain the initial curvature of the device. Four combinations of layer thicknesses are compared to study the effect of each layer and the thickness ratio between them:

- Case 1: stack of 0,3µm of AlN/Pt, 0,5µm of AlN and 0,5µm of Al, with the neutral axis situated at 0,5µm from the bottom, in the lower part of the AlN layer,

- Case 2: stack of 0,3µm of AlN/Pt, 0,5µm of AlN and 1µm of Al, with the neutral axis situated at 0,61µm from the bottom, in the upper part of the AlN layer,

- Case 3: stack of 0,3µm of AlN/Pt, 2µm of AlN and 1µm of Al, with the neutral axis situated at 1,32µm from the bottom, exactly in the middle of the AlN layer. This configuration has no practical applications because as the neutral axis is in the center of the AlN layer, it will not produce any output power.

- Case 4: stack of 0,3µm of AlN/Pt, 1µm of AlN and 4µm of Al, with the neutral axis situated at 1,75µm from the bottom, in the bottom of the Al layer.

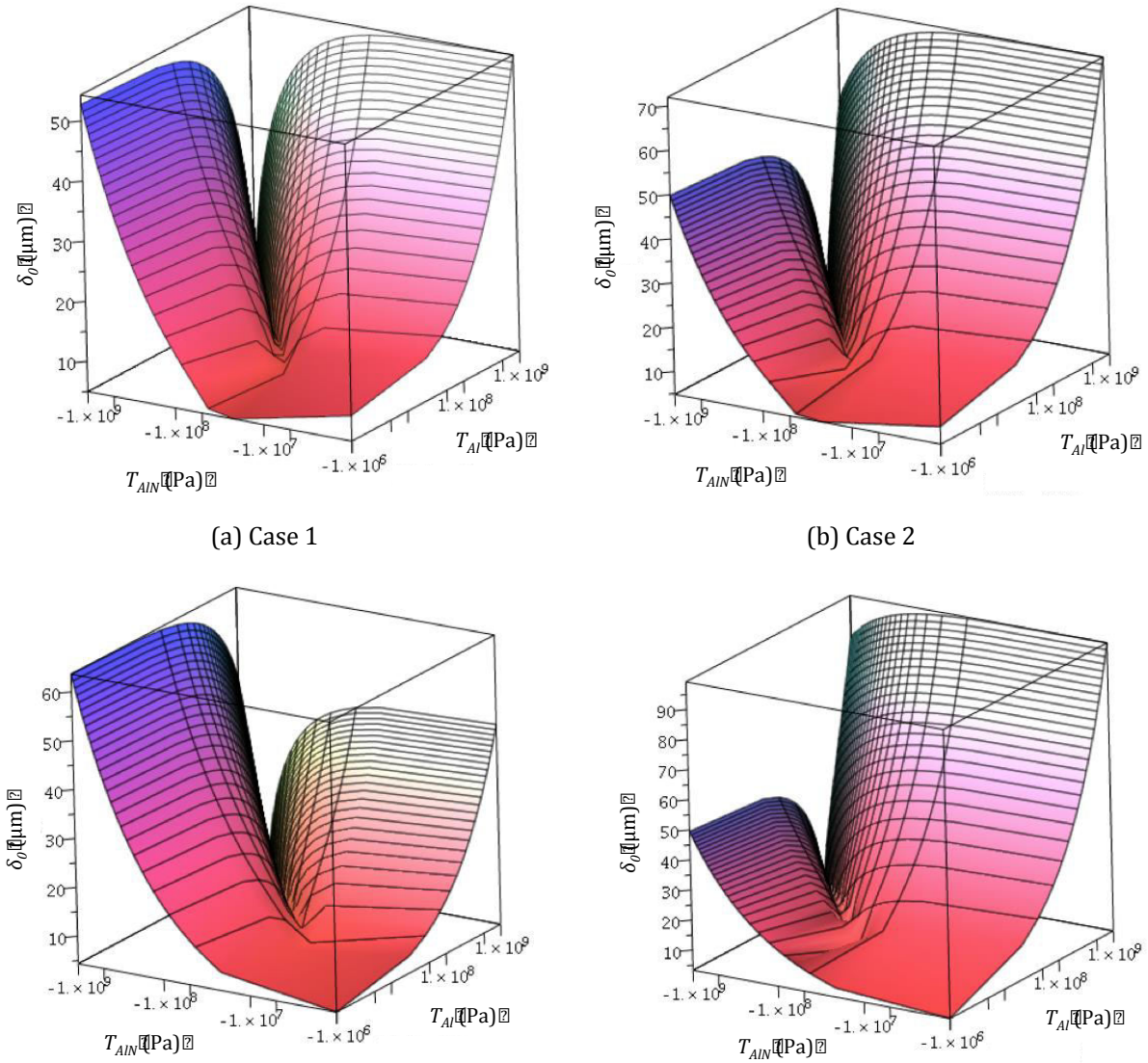

(a) Case 1 (b) Case 2

(c) Case 3 (d) Case 4

Figure III-3 Evolution of the initial mid-point deflection in function of the stress in the layers

Experimentally, the stress in AlN will tend to be compressive while the stress in Al will be tensile. In Fig. III-3 is plotted the modulus of the mid-point deflection for the structure 2000x200 for the different thickness stacks cited above for positive Al stress and negative AlN stress. We chose to plot the modulus of the deflection because when solving the Eq. III-21 to get the value of δ_0, the solution is under the form $_0 = \pm a\sqrt{bT_{AlN} + cT_{Al} + d}$, where a, b, c are constants depending on the geometry of the structure, and d is depending also on the stress in the seed-layer AlN/Pt in addition to the geometry. The deflection can be either positive or negative because it is calculated from Eq. III-21. Moreover, for certain combinations of values of the stress T_{AlN} and T_{Al}, the relation under the square root can become negative, and the deflection is then a pure imaginary number.

For all the cases, we can observe that at very low stress levels, the deflection is very small and not much influenced by the stress difference between AlN and Al layers. On the contrary, for stress levels over 100MPa, the deflection begins to increase drastically and is very sensitive to the combination of stress in the two layers. We can see that for the Case 1 where AlN and Al layers have the same thickness, the maximum deflection obtained when one of the layers has high stress and the other one low stress is relatively the same. In the Case 2 and 3, one of the layers is twice thicker than the other, the deflection is higher for the thicker layer compared to the thinner layer at the same stress level. But the deflection when the Al layer is thicker than the AlN layer is slightly higher than the case where the AlN is thicker than the Al.

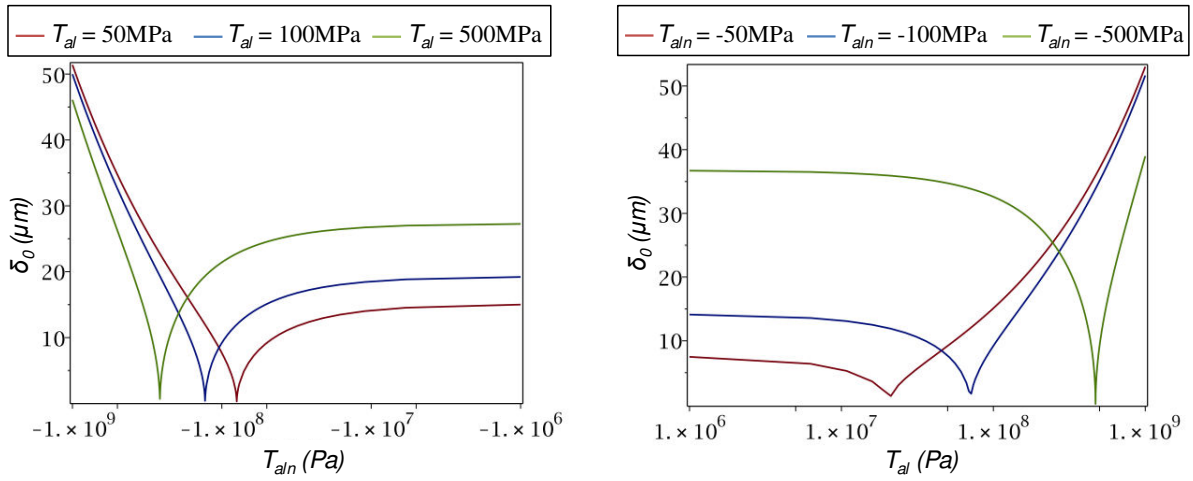

Case 1 (a)

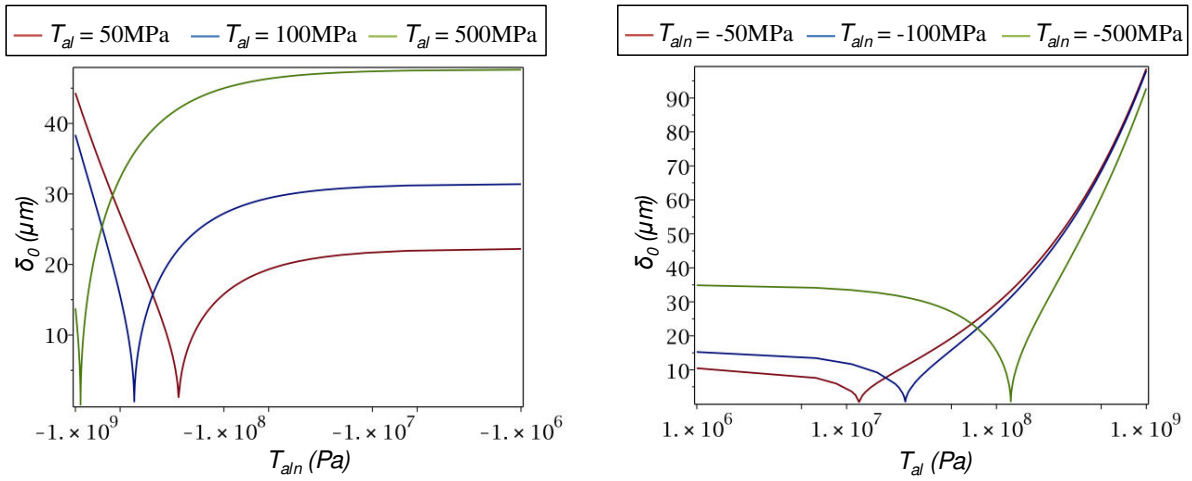

Case 4 (b)

Figure III-4 2D graphs of the evolution of the deflection in function of the film stress in the Case 1 (a) with equal thickness layers and Case 4 (b) with thicker Al layer

More detailed curves are presented in Fig. III-4 and show the difference between the Case 1 and Case 4. Curves for discrete values of stress in AlN and Al (which corresponds to values coherent with the experience) present a non-continuous point, which corresponds to the transition between a real value for the deflection and a pure imaginary value. In both cases, there is a different shape of the curve: when the T_{Al} is kept constant the non-continuous point is sharper than when the T_{AlN} is kept constant because the Young modulus of AlN is nearly 5 times higher than the Al one. Moreover, when the Al layer is thicker than the AlN the stress in the AlN necessary to reach the non-continuous point is higher than for the equal thickness case, while in the other hand, as expected, the stress in the Al layer is lower than in the Case 1 to reach the non-continuous point.

The effect of the stress in the seed-layer of AlN/Pt on the deflection is of importance at lower stress level. Indeed during the fabrication process we will try to tune it with the deposition parameters to be between 10MPa and 100MPa tensile. In the previous simulations, we took a value of 50MPa. In Fig. III-5 is presented the 3D graphs of the evolution of the mid-point deflection in function of the stress in the AlN and Al layer for a stress in the Aln/Pt layer of 10MPa and 100MPa in the Case 1. The deflection is increasing at low AlN and Al stress level, when the stress in the seed-layer is relatively high, but it is not affecting much the deflection at higher stress level. Experimentally the stress in this seed-layer should remain the same as its thickness and the deposition conditions will be exactly the same for all the samples.

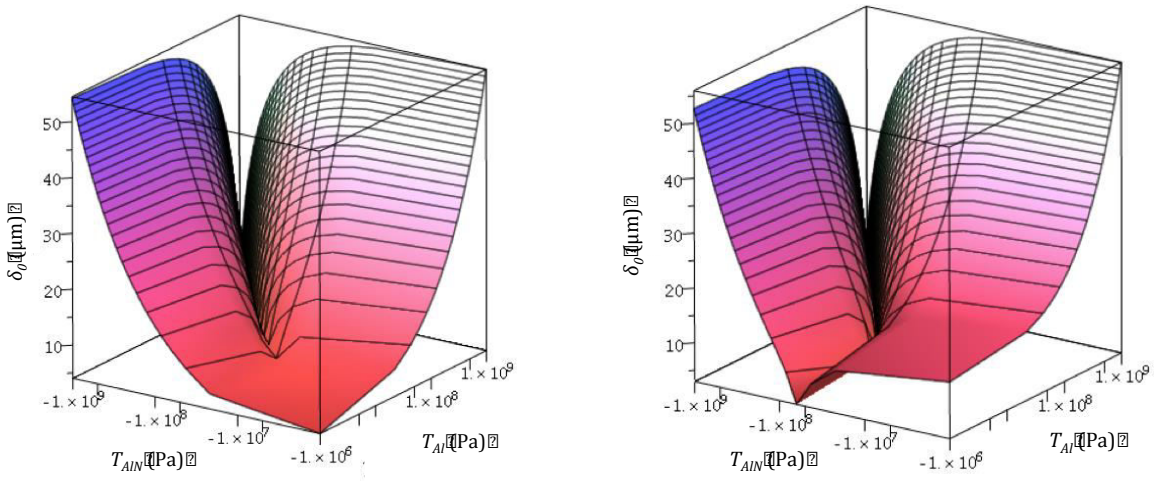

(a) (b)

Figure III-5 Evolution of the mid-point deflection in function of the stress in the AlN and Al layers, for 10MPa stress (a) and 100MPa stress (b) in the AlN/Pt layer

We are now investigating the importance of the torsional stiffness α_r on the shape of the structure. The values for the stress of the different layers are chosen as standard values obtained during the deposition processes: 100MPa for the AlN/Pt layer, -300MPa for the AlN layer and +100MPa for the Al layer. For the Case 1 we plotted in Fig. III-6 the deflection $w_0(x)$ of the 2000x200 beam for different values of torsional stiffness α_r, from a value tending toward 0 to simulate the hinged supporting end condition, to high value to simulate the clamped supporting end condition.

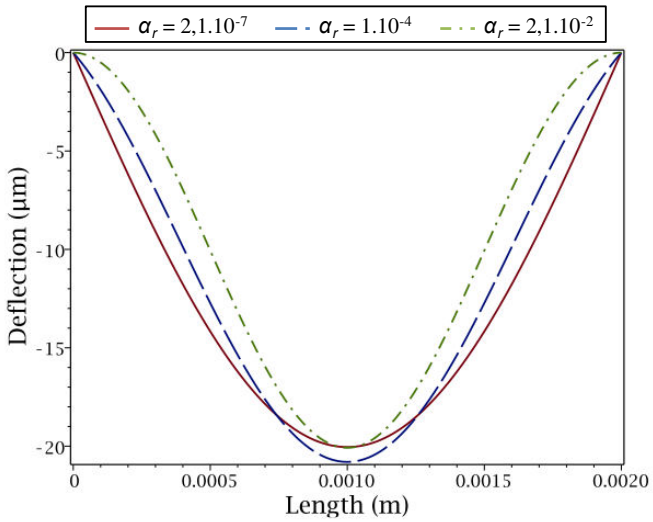

Figure III-6 Buckled shape of a 2000x200 plate for different values of α_r (in Nm.m^{-1}) with a infinite K

We can notice that the mid-point deflection doesn't change a lot between the different shapes. There is a difference of 0,7µm between the maximum and minimum value, which corresponds to an increase of 4% of the mid-point deflection. But the torsional stiffness affects most the slope at the ends of the beams. For hinged conditions (α_r = 2,1.10^{-7} Nm.m^{-1}), the slope is high because the beam can rotate at the supporting ends; while for clamped conditions (α_r = 2,1.10^{-2} Nm.m^{-1}) the rotations are zero which results in a very small slope. These simulations allow us to understand better the nature of the boundary conditions and its impact on the slope of the device. Experimentally, the boundary conditions are close to fully clamped conditions with a high value of torsional stiffness.

In the model we can also introduce the axial stiffness per unit width K. It refers to the lateral movement of the supporting ends. But these displacements are very small compared to the length of the beam, so the same boundary conditions than before are still valid, especially that $w(0) = 0$. The compatibility of strain relation can be modified to become:

$$\frac{T_{eff}L}{E_{eff}} = \frac{2P_t}{K} + \frac{P_t L}{h_{eff}E_{eff}} + \frac{1}{2}\int_0^L \left(\frac{dw_0}{dx}\right)^2 dx \qquad \text{Eq. III-24}$$

Introducing the mid-point deflection δ_b as defined in Eq. III-21, the previous equation can be rewritten as:

$$T_{eff} = \frac{P_E}{h_{eff}}\left(1+\frac{2E_{eff}h_{eff}}{KL}\right)\left(1+\frac{b}{2L}\right)+\frac{E_{eff}\,b}{L} \qquad \text{Eq. III-25}$$

From the Eq. III-25 the δ_b is calculated and introduced in the Eq. III-16 by replacing the δ_0 by it. The axial stiffness per unit width for a beam with a rectangular cross-section is:

$$K = \frac{E_{eff}h_{eff}}{L} \qquad \text{Eq. III-26}$$

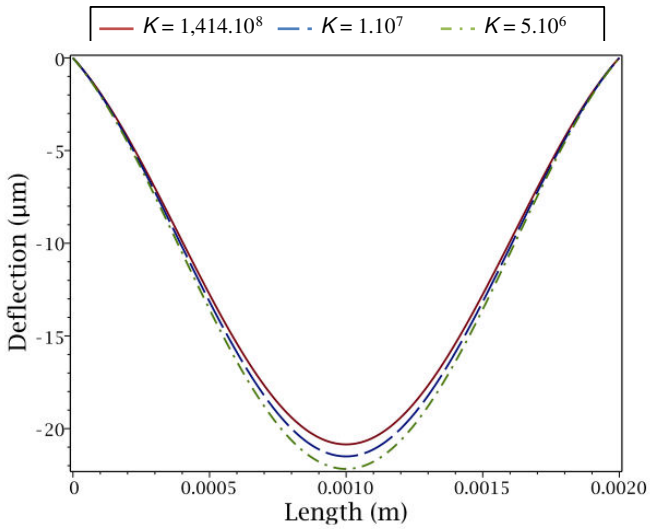

Figure III-7 Buckled shape of a 2000x200 plate for different values of K (in N.m^{-2}) for an α_r of 10^{-4} Nm.m^{-1}

In Fig. III-7 is plotted the shape of a 2000x200 plate for different axial stiffness and with an intermediate value of α_r where the bridge is neither fully clamped nor fully hinged. The first value of K (1,414.10^8 N.m^{-2}) is calculated with the Eq. IIII-26 and corresponds to the particular value of the structure. The change in axial stiffness is mainly affecting the mid-point deflection, which is changing from 19.47µm at the highest K value to 20.88µm at smallest K value.

Table III-1 Initial deflection for the different configurations with an infinite and finite K

	2000x200		1400x700	
	δ_0 (µm), $K\infty$	δ_0 (µm), K	δ_0 (µm), $K\infty$	δ_0 (µm), K
Case 1	20.04 + 4%	20.85	14.04 + 4%	14.61
Case 2	10.47 + 3%	10.62	7.12 + 3%	7.52
Case 3	30.65 + 3%	30.92	21.48 + 3%	21.70
Case 4	17.17 + 3%	16.62	11.83 + 2%	10.73

The initial deflection for the different cases studied is presented in the Table III-1 for infinite *K* and finite *K* values calculated for the structure. For the infinite K values, the deflection calculated is the one for the fully clamped or fully hinged conditions, with the increase in % of the deflection due to values of α_r which are intermediate values. We can see that the influence of the axial stiffness in our case is very small on the initial deflection. But this influence increases with the increase of the difference in thickness of the layers. We have now the shape of the beam, we have now to investigate on the buckling temperature.

III.1.b Buckling temperatures

Timoshenko has studied intensively the bimetallic strips for thermostatic applications [131][132]. He demonstrated that a bimetallic strip, with an initial deflection δ_0 and with the material with the larger coefficient of thermal expansion in the concave side, has the following change in curvature when uniformly heated from θ_0 to θ:

$$\frac{1}{}+\frac{1}{}=\frac{6(\ _2\ \ _1)(\ \ \ _0)(1+m)^2}{h_{eff}\ \ 3(1+m)^2+(1+mn)\ \ m^2+\frac{1}{mn}\div\div} \qquad \text{Eq. III-27}$$

Where ρ_0 and ρ are respectively the initial radius of curvature and the radius of curvature after heating, α_1 and α_2 are the thermal expansion coefficients of the two materials, $m = h_1/h_2$, $n = E_1/E_2$ and $h_{eff} = h_1 + h_2$. Here we consider that the bimetal is heated up and the metals are deforming linearly with the temperature. The deflection of a simply supported beam is an arc of a circle with a radius of curvature ρ and a deflection equal to $(2\ \ \ \ )=(L/2)^2$ .We can

approximate the deflection of the curved beam assuming that the deflection is small compared to the radius of curvature by:

$$= \frac{L^2}{8} \qquad \text{Eq.III-28}$$

When heated up, the beam with an initial deflection δ_0 is first deforming linearly to reach a critical deflection δ_1 at which the sign of its curvature is changing and the snap-through occurs. Assuming hinged boundary conditions, the buckled shape of the beam is expressed in Eq. III-18. We can define η as the difference between the length of the beam and the length of the chord at the center of the beam as:

$$= \frac{1}{2} \int_0^L \left(\frac{dw}{dx} \right)^2 dx \qquad \text{Eq. III-29}$$

Replacing the expression of *w(x)* into Eq. III-29, we obtain $= \frac{^2_0 \; ^2}{4L}$, value that is also valid for the expression of *w(x)* in clamped conditions. Then the compression of the strip due to the diminution of deflection from δ_0 to δ_1 is expressed as: $\frac{^2_0 \; ^2}{4L} \quad \frac{^2_1 \; ^2}{4L}$. The corresponding compressive force acting on the beam with a width of *b* is:

$$P = \left(\frac{^2_0 \; ^2}{4L} \quad \frac{^2_1 \; ^2}{4L} \right) \frac{E_{eff} h_{eff} b}{L} \Leftrightarrow \frac{PL^2}{(EI)_{eff}} = \frac{3}{h_{eff}^2} \, {}^2_0 \left(1 \quad {}^2_1 \right) \qquad \text{Eq. III-30}$$

This relation describes the relation between the compressive force *P* generated by the change in deflection. We are now trying to express the force *P* necessary to prevent the snap-through of the beam. Let assume that the beam is hinged, it has the same initial shape as described in Eq. III-18. The snap-through of the beam can be described as an increase of *w* from the original deformation: $w(x) + \sin \frac{x}{L}$. Introducing this expression into the differential equation we obtain:

$$(EI)_{eff} \frac{d^2}{dx^2} \left[w(x) + \sin \frac{x}{L} \right] = P w(x) \qquad \text{Eq. III-31}$$

Calculating the solution of this differential equation we can deduce the following equations:

$$\frac{PL^2}{(EI)_{eff}} = - + 1 \qquad \text{Eq. III-32}$$

Substituting δ by the expression of Eq. III-27, we obtain the P necessary to maintain the beam in its initial sense of curvature:

$$\frac{PL^2}{(EI)_{eff}^{\ 2}} = \frac{6L^2(\ _2\ \ _1)(\ \ \ _0)(1+m)^2}{h_{eff\ 0}\ 3(1+m)^2+(1+mn)\ m^2+\frac{1}{mn}\div\div}\ \ 1\div\ _0+1 \qquad \text{Eq. III-33}$$

We have obtained two equations relating the axial force P and the ratio δ_0/δ_1. If the force obtained in Eq. III-33 becomes lower than the force obtained in Eq. III-30, then the reaction force of the supporting ends are large enough to prevent buckling.

In order to find the buckling temperature of the strip, we can rewrite the Eq. III-30 and Eq. III-33 as follow:

$$y = a\ 1\ \ \frac{1}{x^2}\div \qquad \text{Eq. III-30bis}$$

$$y = bx+1 \qquad \text{Eq. III-33bis}$$

With the following coefficients:

- $\frac{PL^2}{(EI)^{\ 2}} = y,$
- $\frac{3\ \ ^2_0}{h_{eff}^2} = a,$
- $\frac{\ _0}{\ _1} = x,$
- $\frac{6L^2(\ _2\ \ _1)(\ \ \ _0)(1+m)^2}{h_{eff\ 0}\ 3(1+m)^2+(1+mn)\ m^2+\frac{1}{mn}\div\div}\ \ 1\div = b.$

We can calculate the derivative of Eq. III-30bis and introduce it in the Eq. III-33bis by replacing the b. In the same time, we can replace the expression of y in Eq. III-33bis by the one of Eq. III-30bis. We find the expression of x in function of a:

$$x = \sqrt{\frac{3a}{a\ \ 1}} \qquad \text{Eq. III-34}$$

Using this value for *x*, we have a second expression of the coefficient *b*, the slope of the function. The equality of the two expressions allows us to find the increase in temperature that causes the buckling of the structure:

$$b = 2a\left(\frac{1}{3}\right)\left(\frac{1}{3a}\right)^{3/2} = \frac{6L^2(\quad_2 \quad_1)(\quad_0)(1+m)^2}{h_{eff}\ _0\ 3(1+m)^2 + (1+mn)\left(m^2 + \frac{1}{mn}\right)} \quad 1 \qquad \text{Eq. III-35}$$

$$(\quad_0) = \frac{h_{eff}\ _0\ \frac{6\ ^2_0}{h_{eff}^2}\ \frac{1}{3}\ \left(\frac{h_{eff}^2}{9\ ^2_0}\right)^{3/2} + 1 \quad 3(1+m)^2 + (1+mn)\left(m^2 + \frac{1}{mn}\right)}{6L^2(\quad_2 \quad_2)(1+m)^2} \qquad \text{Eq. III-36}$$

The last equation describes the increase of temperature necessary for the buckling to occur. The temperature of snap back θ_1 is obtained assuming that the decrease in temperature to cause the instability is the same than the increase of temperature provoking the snap up. Timoshenko demonstrates that:

$$(\quad_1 \quad_0) = \frac{1\quad b}{1+b}(\quad_0) \qquad \text{Eq. III-37}$$

In the Table III-2 we report the temperature of snap up and snap back of the different structures studied with the reference temperature θ_0 set at 20°C. Some snap back temperatures are below zero, which means that these structures seem not usable in real applications. The most interesting ones are the Case 2 and 4, which have working temperatures around the ambient temperature. These two cases correspond to the case where the Al layer is thicker than the AlN layer. It gives lower initial deflection and the working temperatures are then much lower. When the AlN layer is thicker than the Al layer or of equal thickness, the snap up temperatures are relatively high, and the snap down temperature is below zero. A functional device is then a device with a thicker Al layer. Then the difference of buckling temperatures when the plate is initially curved up or down is not very significant.

Table III-2 Snap up and snap down temperatures for the different cases studied

	2000x200	Temperature (°C)		1400x700	Temperature (°C)	
	δ_0 (µm), K	Snap up	Snap down	δ_0 (µm), K	Snap up	Snap down
Case 1	-20.85	121.62	-82.03	-14.61	91.12	-51.7
	20.85	122.03	-81.62	14.61	91.7	-51.21
Case 2	-10.62	28.74	10.95	-7.52	26.15	13.4
	10.62	29.05	11.26	7.52	26.6	13.85
Case 3	-30.92	129.4	-91.21	-21.7	96.14	-58.73
	30.92	131.21	-89.4	21.7	98.73	-56.14
Case 4	-16.62	29.05	9.33	-10.73	24	13.87
	16.62	30.67	10.95	10.73	26.13	16

All the presented structures have been investigated analytically. We manage to find their initial deflection based on the thickness of the different layers and on the intrinsic stress generated during fabrication in these layers. Then, based on this value of initial deflection we estimated their snap-up and snap-down temperatures. But the analytical model is limited to Bernoulli structures, which is the case for the 2000x200 structure but not for the 1400x700 plate. We will be able to verify this model by the experimental results. The values of the stress in the layers for which the results are calculated are typical values that might not correspond to the experimental values obtained afterward. A numerical model with finite elements simulations is able to simulate any kind of structures; and will verify or not the analytical model presented here for Bernoulli structures.

III.2 Finite Elements Model

With the analytical model presented previously, we have understood better the mechanism of the buckling, the important role played by the boundary conditions on the buckled shape of the structure, and the effect of the thickness ratio on the buckling temperatures. But as mentioned before, this analytical model is involving constraining

hypothesis, especially because it is valid only for slender, Bernoulli-type beams. Finite-elements simulations are more fitted to simulate our multi-physics problem involving structural, thermal and piezoelectric field. To realize these simulations we used ANSYS 15.0.

The first attempt to simulate our structure was to design them as pre-shaped device having a prefect arc-of-a-circle form. This shape is much simpler than the real one, and it is completely free of any residual stress or strain, but for a first approach it is easier to do simulations, as we don't have to restart any previous analysis.

The transverse load applied to a central part of the plate and necessary to provoke buckling is interesting to study in a first time. The effect of the initial deflection as well as the different length to width ratios on the value of this critical load is giving an idea of the dependence of these parameters on the buckling temperature. To simulate the structure we used the multilayer SHELL181 element, in which the thickness is considered as a real constant of the element. The boundary conditions are considered as clamped and the transverse force is applied on a surface of 5µm by 5µm at the center of the plate. A static analysis is performed with at least 10 sub-steps and the applied load is ramped, i.e. the applied load is divided by the number of sub-steps and is continuously increasing according to the increasing of the sub-steps number.

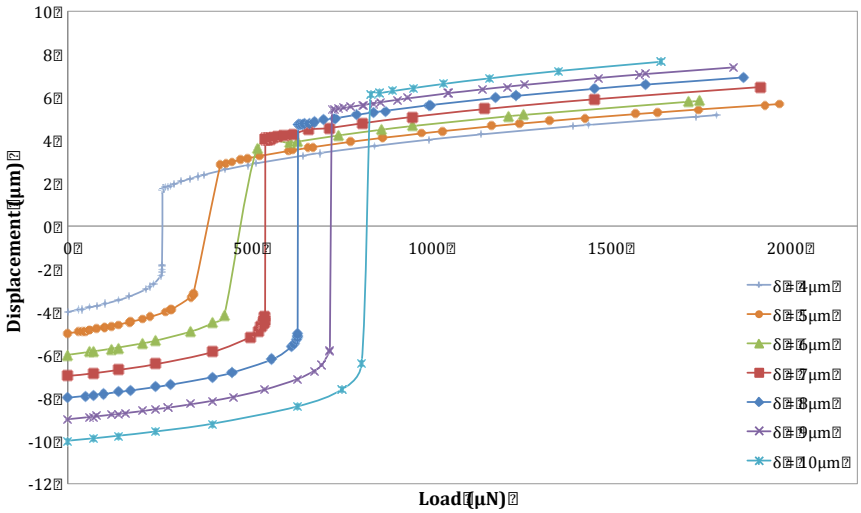

Figure III-8 Displacement of a 300x100 plate with 1µm of AlN and 1µm of Al for different initial deflections

The Fig. III-8 shows the displacement of a node at the center of the plate along the z-axis of a plate measuring 300µm by 100µm with 1µm of AlN and 1µm of Al for different values of the

initial deflection. As expected, we can see that the higher is the deflection, the higher is the critical load that is necessary to the buckling. The Fig. III-9 is showing the critical loads causing the buckling for the different structures that will be fabricated with different values of the initial deflection. These structures were chosen with a range of length-to-width ratio from 1, with a square plate of 400µm by 400µm, to 10 with a Bernoulli-type beam measuring 2000µm by 200µm. The square plate has the highest critical loads, while the slender beam has the lowest. For some devices, 1000x250 and 2000x200, under a certain value of initial deflection, no buckling occurs, the displacement when the transverse force is applied is linear and no sudden

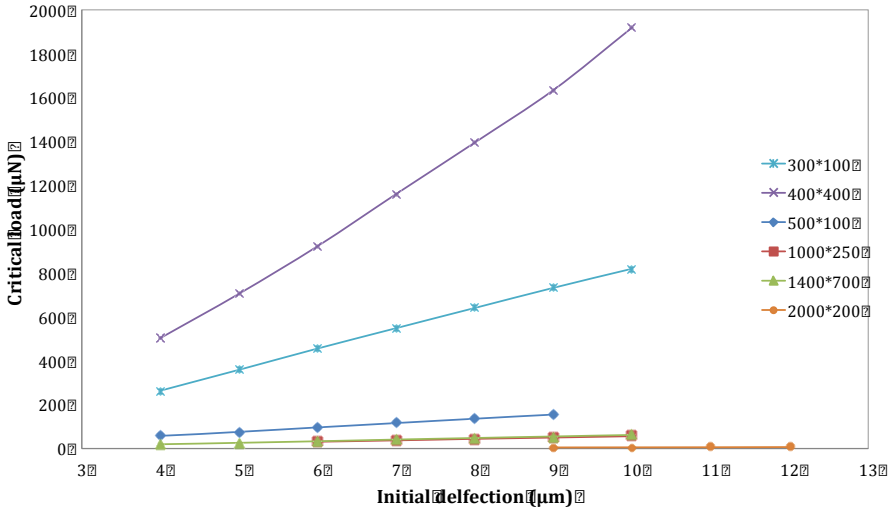

change in curvature is observed.

Figure III-9 Critical loads for 6 different rectangular geometries

With a 2D layered element like SHELL181, we are also able to predict the resonance frequencies of our device by a modal analysis. Indeed a first static analysis can be run in order to determine the initial shape of the structure with the equivalent initial stress found by Eq. III-4. A pressure is then applied on the two opposite edges of the beam corresponding to its equivalent initial stress, constraining only the translations along *y* and *z* as shown in Fig. III-10, and leaving the translation along *x* free for the pressure to have an effect.

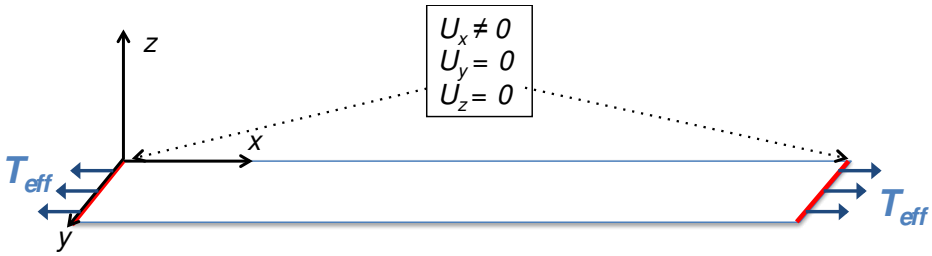

Figure III-10 Schematic of the 2D initial static analysis for following modal analysis

The results obtained after the first static analysis are then reused by restarting a static analysis using the option "perturb". It is summarizing the structural results obtained before and after cancelling of the applied loads perform a modal analysis from it. For instance for a 2000x200 and a 1400x700 plates corresponding to the Case 4 with 0,3µm of AlN/Pt, 1µm of AlN and 4µm of Al, we obtained the resonance frequencies reported in the Fig. III-11 with the corresponding mode shapes illustrated. Only the first 3 modes are presented for the 2000x200 plate, which are pure flexural or torsional mode shape. For the 1400x700 plate, the first 2 shape modes, flexural and torsional, are shown as well as the fifth, which is a combination of flexural and torsional modes.

2000x200 **1400x700**

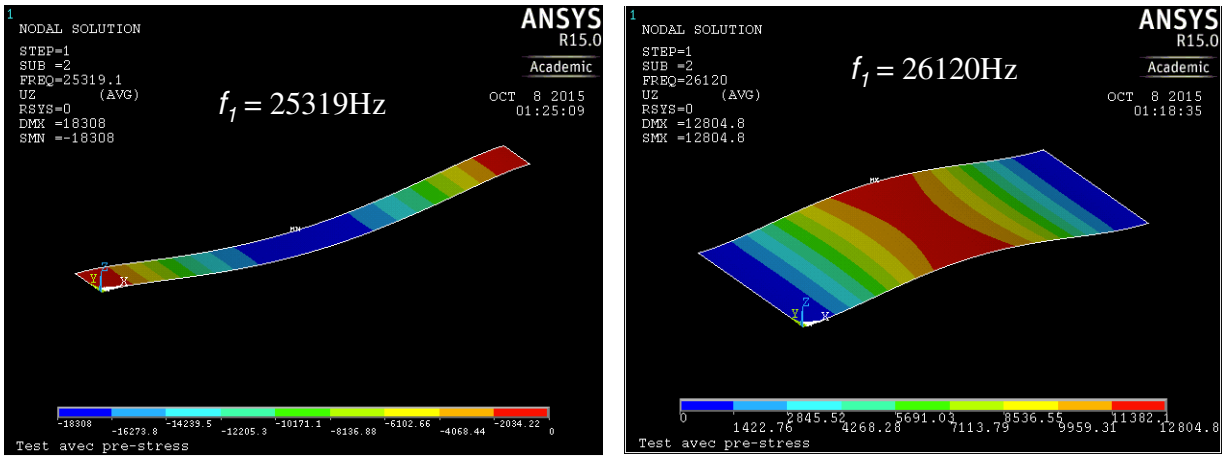

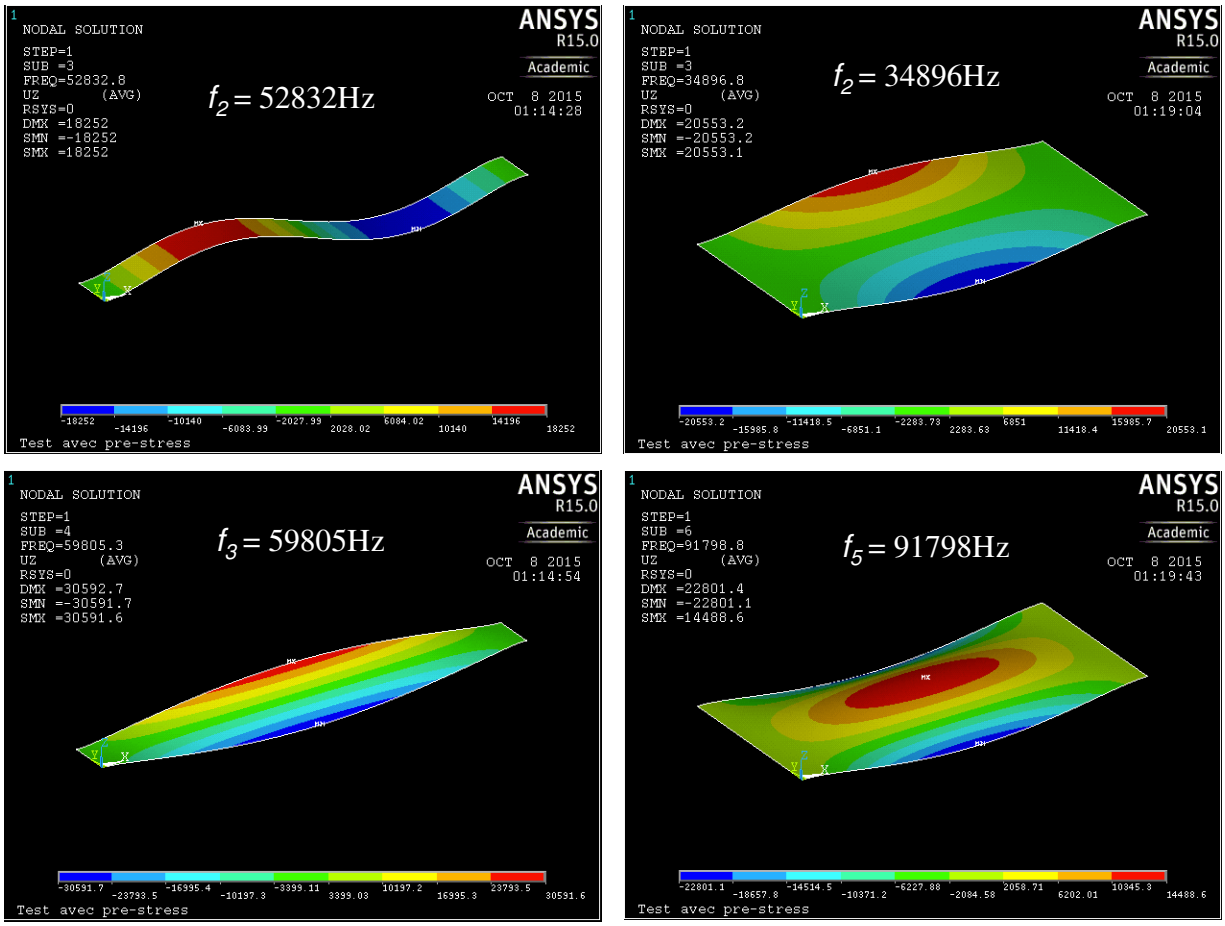

Figure III-11 Mode shape of a 2000x200 and a 1400x700 plates in the Case 4

We can also vary the effective stress applied on the plate and see its effect on the resonance frequencies. This study was performed on a 2000x200 plate of the Case 1 and the results are presented in the Table. III-3. The first 6 resonance frequencies are showed as well as the mode shape: "Flex1" means that it is the first flexural mode and "Tor1" the first torsional mode. With the increase of the effective stress, for all the mode shapes their resonance frequency increases, more or less quickly.

Table III-3 Resonance frequencies for different effective stress for a 2000x200 plate in Case 1

T_{eff} (MPa)	f_1		f_2		f_3		f_4		f_5		f_6	
200	2496	Flex1	5087	Flex2	9823	Flex3	10968	Tor1	15990	Flex4	21886	Tor2
250	2889	Flex1	5396	Flex2	10226	Flex3	11348	Tor1	16365	Flex4	22338	Tor2

A 3D model is built to simulate the thermo-mechanical behavior of the plate during the buckling. The element used here is the thermo-structural SOLID226. A lot of efforts have been

put to create the exact shape of the structure after the fabrication. The thermal residual stresses are created during the fabrication process, when the thin film is deposited at high temperature (over 300°C) and the wafer is cooled down to room temperature. The intrinsic stresses are due to ionic bombardment during the growth of the thin film. This parameter can be controlled by the deposition parameters as for instance the power density of the plasma.

The model is built taking into account these two contributions. The plate is initially flat. The element SOLID226 is used for all the materials, but with thermo-structural option for the Al and hybrid Pt/AlN materials and with thermo-piezoelectric option for the AlN. The translations in all three directions are zero at the anchors on a length of 10μm for the bottom nodes to simulate the clamping on the Si substrate as shown in Fig. III-12.

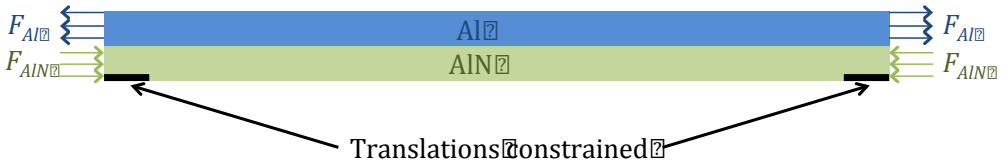

Figure III-12 Schematic of the cross-section of the structure with the applied loads

A lot of problems with the 3D model were encountered, especially concerning the convergence of the solution. The mesh size cannot be reduced as fine as in 2D and the results are not converging with the increase of the mesh density. Moreover, as the Al layer is on top of the structure, the curvature due to thermal stress tend to be upward because the Al layer is expanding most. But we will see that in our experimental results, most of the curvatures are downward. If the curvature is upward, the Al layer has then more “space” to expand than if the curvature is downward, and the increase in temperature necessary to provoke buckling is then much larger than if the curvature is downward. We might even reach the melting temperature of the Al which is around 600°C. The forces necessary to invert the curvature in the simulations were huge, in the order of several hundreds of GPa. The stress created by bombardment can be as high as a few GPa, especially in AlN, but it cannot go much higher, or the plates will crack. Maybe there is a problem of boundary conditions, which are too constraining.

There are several limitations on this model. During the fabrication process, the different layers have seen several thermal cycles. For instance the lower seed- layers of AlN and Pt have been deposited at 300°C and the films, clamped on the Si substrate, are cooled down to room temperature to pattern the Pt. Then it is heated up again to deposit the active AlN film at 300°C and the wafer is again cooled down to room temperature, but this time the AlN and Pt seed layers are clamped also by the AlN active layer on top. Its boundary conditions are changed. So

the stress measured after the deposition might change during the process performed after. The single step to simulate thermal residual stresses is then approximated.

III.3 Conclusion

In this chapter, we built a model to understand better our structure, both analytically and numerically. Based on the initial intrinsic and residual stress present in the different layer, we tried to predict the initial deflection of the structure, under the hypothesis that it can be considered as a slender beam. We observed its evolution while tuning the stress in the Al and AlN layers. Then, thanks to the value of the deflection, we used Timoshenko model to estimate the buckling temperatures, snap-up and snap-down, for the different thickness combinations considered. However in both cases we encountered limitations, either on the type of structure for which the model is valid, or in terms of calculations capacitance. Nevertheless these models, even simple, allow us to see how the different geometrical parameters act on the buckling temperature of the final structure. The boundary conditions as well as the stress in the different layers are crucial parameters influencing the initial deflection and by consequence the buckling temperature of the device. Improvements can be done analytically by working with the energy involved in the system: the mechanical energy developed during the initial buckling of the structure, the mechanical energy necessary to make the curved plate snap through and the thermal energy associated. A more precise analytical model can be found here [133].

IV Fabrication Process

Our aim in this project is to fabricate the same kind of bimetallic plate for thermal energy harvesting as previously done at macro-scale. Indeed it has been foreseen that downscaling the devices will increase their working frequency and the output power will be equal to the macroscopic one. In a first time we will explain the conception of the structure and the choice of the piezoelectric material as well as the innovative choice to integrate directly the piezoelectric layer in the bilayer plate. Then the fabrication will be detailed and especially how the initial curvature of the structure is controlled by the deposition parameters only. The issues during the etching processes of Pt and AlN are presented and also how we overcame them.

IV.1 Choice of materials – Geometries

One of the major constrains we had was to find two materials, completely CMOS compatible, easy to process and having largely different coefficient of thermal expansion to achieve the bimetallic plate principle. The PZT and AlN were the best two candidates [107][111] for the piezoelectric material: their fabrication process is well known, their piezoelectric properties are suited for energy harvesting applications and their thermal expansion coefficients are $3{,}1.10^{-6}$ and 3.10^{-6} K^{-1}respectively for AlN and PZT-5H.

Table IV-1 Piezoelectric properties and Figure of Merit (FOM) of PZT and AlN

Material	$e_{31,f}$ (C/m²)	d_{31} (pm/V)	ε_{33}	tanδ (%)	FOM_{EH} (GJ/m³)	FOM_{ACT} (m²/N)	Ref
PZT-5A	10,4	-171	1700	2	7,19	11,54	[73]
PZT-5H	16,6	-274	3400	2	9,16	21,49	[73]
Epitaxial PZT	12,1	-	350	-	47,26	-	[134]
$Al_{0.83}Sc_{0.17}N$	1,46	-	13,6	0,2	17,71	-	[135]
AlN	1	2,625	10,5	0,1	10,76	6,56	[135]

In the above table are presented the piezoelectric properties of three different types of PZT and two types of AlN. These materials are compared using two figures of merit: one describing the charges generation for energy harvesting applications [136][137]:

$$FOM_{EH} = \frac{e_{31,f}^2}{\varepsilon_{33}\varepsilon_0} \quad \text{Eq. IV-1}$$

and one describing more the behavior of the material in actuation mode from Priya [112]:

$$FOM_{ACT} = \frac{d_{31}g_{31}}{\tan\delta} = \frac{d_{31}^2}{\varepsilon_{33}\tan\delta} \quad \text{Eq. IV-2}$$

where $e_{31,f}$ is a piezoelectric coefficient defining the effective amount of charges measured for a defined displacement, ε_{33} is the relative dielectric constant along the c-axis, ε_0 is the vacuum permittivity, d_{31} is a piezoelectric coefficient defining the displacement corresponding to a defined electric field, g_{31} the shear modulus coefficient and $tan\delta$ the dielectric losses.

For actuation applications AlN is clearly under the performances of the PZT. Indeed the d_{31} coefficient of PZT is much higher. On the other hand, when the FOM describing the energy harvesting applications is used, AlN is better than conventional PZT. Doping AlN by adding Sc increases its performance. However the best candidate as energy harvester is epitaxial PZT thanks to lower dielectric constant, and high $e_{31,f}$ coefficient at a comparable value of conventional PZT.

Finally AlN was chosen for several reasons:

- its fabrication process is less time-consuming than PZT,
- it doesn't contain lead,
- the residual stresses in the film are easily tuned by the deposition parameters,
- aluminum, compatible with AlN, has a thermal expansion coefficient more than 6 times higher than AlN.

Regarding the geometrical parameters of the rectangular plate, six different length-to-width ratios were designed to see the influence of a structure being beam-like compared to a plate-like structure:

- 2000µm x 200µm
- 500µm x 100µm
- 1000µm x 250µm
- 300µm x 100µm
- 1400µm x 700µm
- 400µm x 400µm

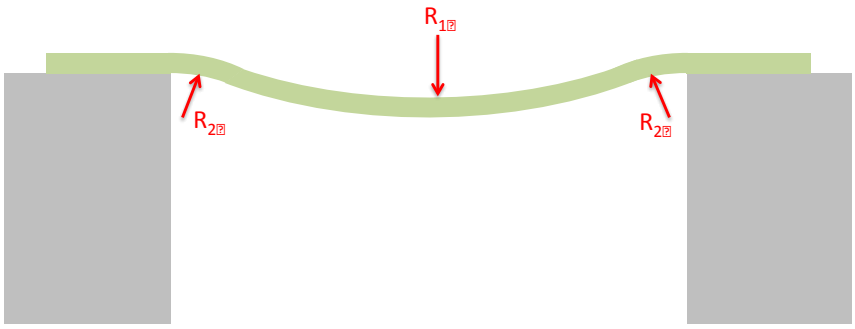

Figure IV-1 Schematic cross-section of a structure with the inverse radius of curvature

The electrodes are designed in order to take advantage of the radius of curvature of the structure. Indeed a structure initially curved downward will have a positive radius of curvature in the center but a negative one at the anchors (as shown in Fig IV-1). Three capacitances are placed in these three strategic places. The stresses in AlN will be of the opposite sign and connecting these three capacitances in series can increase the output signal compared to one parallel plate electrode at the center of the device. In addition, the center is where the highest displacement is expected during buckling, and the highest stresses are expected at anchors level. Al layer deposited on top of AlN acts as a floating electrode while three platinum electrodes are designed on the places of interest: one at the center and two at each anchor. Two different designs were tested during this thesis: this first one and a second one having cantilever test structures and new device geometries that will be detailed more precisely in chapter V.

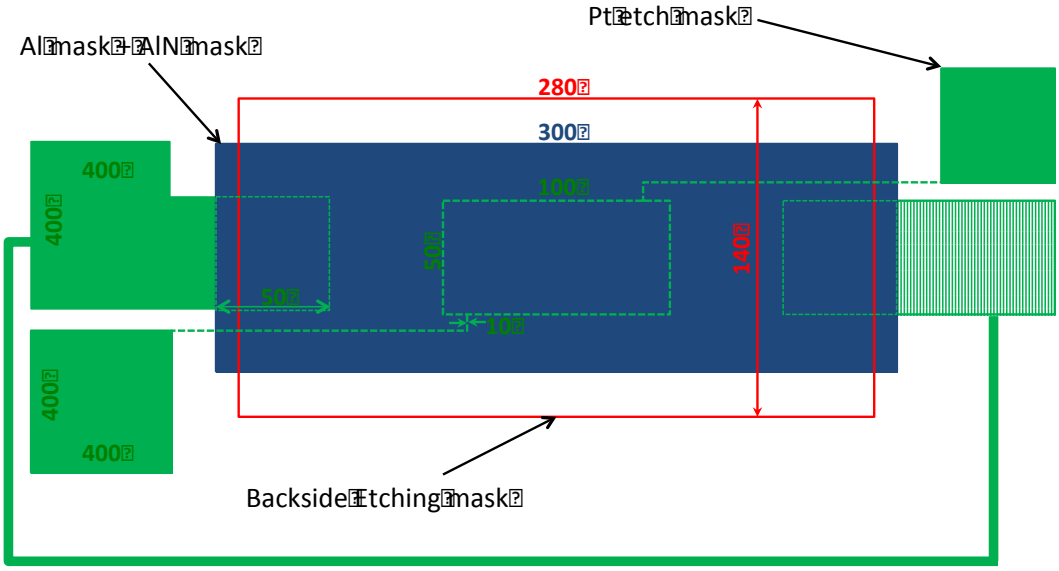

Figure IV-2 Schematic of a rectangular structure of 300µm by 100µm (dimensions in µm)

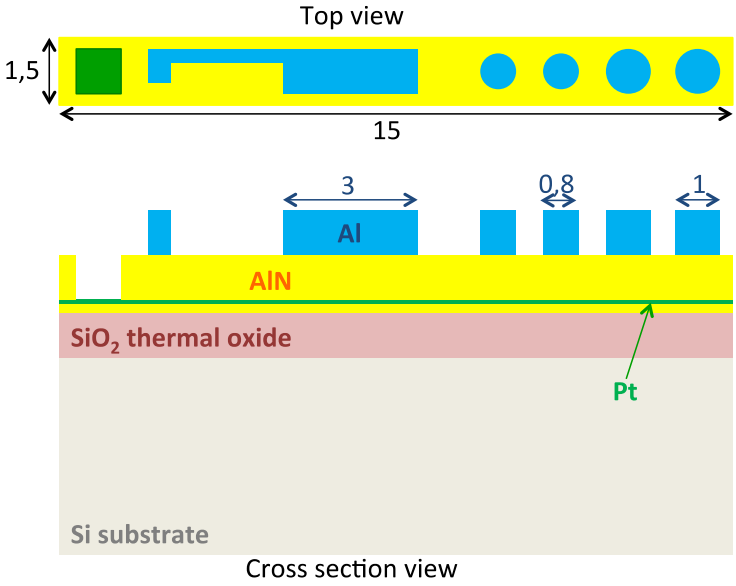

Figure IV-3 Schematic of a test cantilever structure (dimensions in mm)

For both designs the same process flow as described below has been implemented. Regarding the thickness ratio between AlN and Al layers, an analytical model detailed in the previous chapter has highlighted the influence of Al and AlN thickness on the initial deflection. From a technical point of view, it was more risky to deposit "thick" layer of more than 2µm because the film might delaminate more easily. We then chose to fabricate the following combinations of the two active layers: 0,5µm of AlN/0,5µm of Al, 0,5µm of AlN/1µm of Al, 1µm of AlN and 1µm of Al and finally 1µm of AlN and 2µm of Al. The AlN seed-layer and Pt have equal thickness for all the samples fabricated: 200nm of AlN seed-layer and 100nm of Pt.

IV.2 Process Flow

All the processes described here were realized in the Center of MicroNanotechnology from EPFL. This center dedicated to teaching and research is composed of cleanrooms from class 100 to class 10'000 for different applications. It allows undergraduate and PhD students to work and handle the machine themselves under the constant supervision and help of the staff members. Each area is dedicated to one process step, for instance one zone for the etching processes, another one for lithography… The machines are optimized for 100mm wafer processing, and some equipment can handle 150mm wafers.

The first step of the fabrication process was to design and fabricate the chromium masks that will be used to illuminate with the correct pattern the photoresists during the several photolithography steps. The photolithography masks are made of a square substrate of 5 inches and 2mm thick, composed essentially of silicon oxide. On top is coated 100nm of low reflective Chrome. A positive resist is coated on top. The design of the masks was done on the software Expert. As said before, six different geometries were designed. The wafer was divided into "unit cells" where the structures were connected in series or in parallel or isolated. On the right and left side of the wafer the alignment marks were designed for the third and fourth masks to be aligned with the first one.

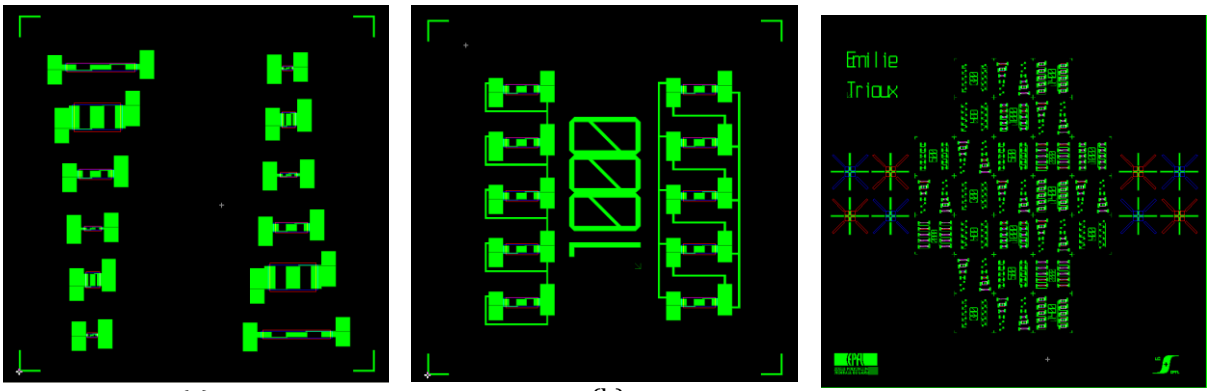

(a) (b) (c)

Figure IV-4 Layout of two unit cells: isolated devices (a) and interconnected devices (b) and the full wafer layout (c)

Four masks are needed for the fabrication process: one mask is defining the Pt pattern and the alignment marks, another one is opening a hole to see the alignment marks after the deposition of different layers on top of Pt, next one is patterning the devices and the last one is opening the wafer from the backside. The machine used to "write" the masks (Heidelberg DWL200) consists of a laser with a wavelength of λ = 407nm which is focused on the mask. During the writing the mask is moving under the laser illuminating the photoresist line by line. The laser is controlled by a computer, which switches it on and off following the designs previously send to the computer.

The fabrication was realized on 100mm double-side polished silicon wafers, <100> oriented. Thermal silicon oxide of 1µm thick was grown on both faces, and then etched on the front side with buffered hydrofluoric acid (BHF 7:1). The oxide on the backside was kept to act as a hard mask for the last step of back-side etching.

A first 200nm thick layer of AlN was deposited by reactive magnetron sputtering, immediately followed by the sputtering of 100nm of Pt. Both depositions are done at high temperature (resp. 300°C and 350°C).

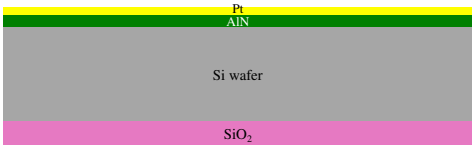

Pt layer is etched away by dry, reactive plasma etching using Cl_2. This step was very critical because of the resist which is reacting with the Cl_2.

The two active layers of AlN and Al were also deposited at high temperature by reactive magnetron sputtering.

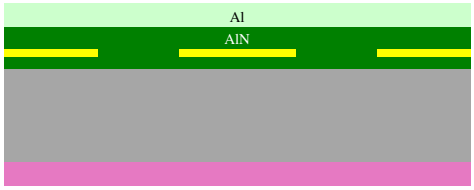

Al layer is then etched away by plasma etching using a BCl_2/Cl_3 plasma. Then without stripping the resist the AlN is etched chemically by phosphoric acid (H_3PO_4) at 70°C.

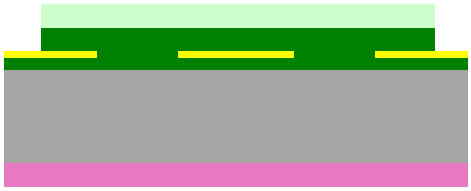

In order to protect the structures on the front-side during the backside etching, 2µm of Parylene C was deposited. The deposition is done at room temperature and the parylene can be removed by O_2 plasma.

After the backside photolithography, the SiO_2 layer is firstly etched by C_4F_8 plasma. Then the Si is etched by Bosch process. Finally the Parylene is removed by oxygen plasma and the membranes are liberated.

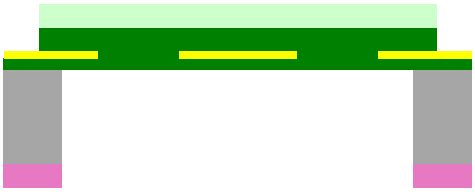

Figure IV-5 Process Flow

Each step will be described precisely in this chapter, especially the issue encountered during the dry etching of Pt and the physical parameters playing a role in the sputtering and the etching of AlN.

IV.1.a AlN deposition and Curvature control

AlN deposition by reactive, pulsed, direct current magnetron sputtering is a very specific process well mastered in CMi. The sputtering of an Al target in reactive N_2 plasma can produce polycrystalline AlN thin films on many different substrates at relatively low temperature. A DC current is applied between the cathode (target) and the anode (substrate) to create the plasma (Fig. IV-6). But because AlN is a dielectric material (relative dielectric constant of 10,5), charges tend to accumulate on the surface of the substrate. To limit this phenomenon, the DC current, usually around 300V, is pulsed at 20kHz, which means that it is inverted every 5µs to discharge the surface and prevent the apparition of electrical arcs. The magnetron system creates a magnetic field just below the target surface that concentrates the plasma in this zone. The mean free path of the ions is longer which limits the self-heating of the target. The optimal temperature and gas flows (Ar and N_2) for a high piezoelectric quality AlN were already studied [138][139].

One critical parameter to control in order to get a high piezoelectric quality of AlN thin film is the ionic bombardment of the surface during deposition. It can be controlled by the gas pressure but also by the applied RF bias on the substrate. Indeed during the deposition, the ionic bombardment will create a self-induced bias between the substrate and the chamber walls (voltage ground). This RF bias can control this self-induced substrate voltage and thus control the ionic bombardment on the film. As Dubois explained [139], there are two types of particles bombarding the substrate surface: the neutral particles and positive ions. The ions, accelerated toward the target, bounce back toward the substrate crossing the plasma to reach the sample, some being neutralized by the plasma. These neutral particles are only affected by the gas flows and pressure. On the other hand, the positive ions are attracted by the self-induced bias of the substrate. So higher is the RF bias applied to the substrate, the higher is the bombardment and the higher are the residual stresses created in the thin film.

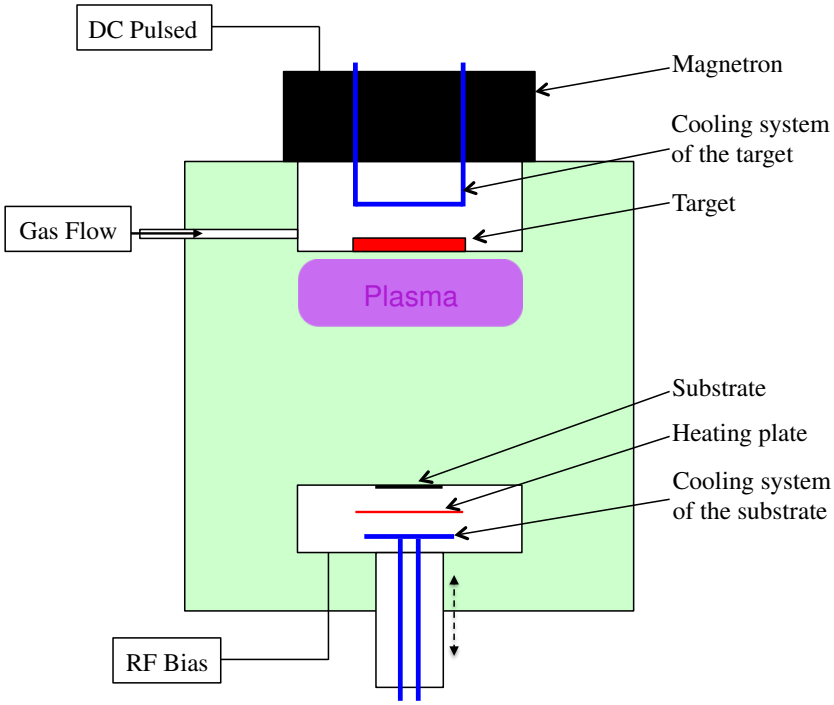

Figure IV-6 Scheme of the deposition chamber used for the AlN sputtering deposition

The machine used in CMi for AlN deposition is the SPIDER 600 from Pfeiffer. It has 4 different deposition chambers, one being entirely dedicated to AlN and AlScN deposition. The DC pulsed power is fixed to 1500W and the temperature at 300°C. RF substrate power is then tuned from 0W to 7W (which corresponds to 60V and 110V) and stresses in the thin film are measured before and after deposition. Indeed the curvature of the wafer is directly related to stresses in the thin film by the Stoney formula [140]:

$$= \frac{E_s}{(1 \quad _s)} \frac{h_s^2}{6h_f} \frac{1}{R_1} \quad \frac{1}{R_0} \div \qquad \text{Eq. IV-3}$$

where E_s is the Young modulus of the silicon substrate <100> oriented [141], v_s its Poisson ratio, h_s its thickness, h_f is the thickness of the thin film, R_0 and R_1 are respectively the radius of curvature before and after deposition.

A laser beam hits perpendicularly the substrate and scans the wafer on a diameter. A detector is measuring the angle made by the reflected beam with the incident one and gives the curvature profile of the sample.

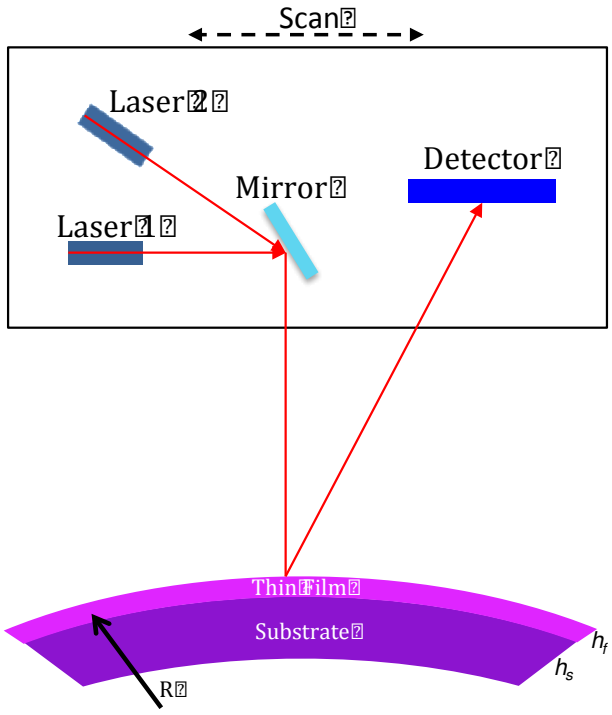

Figure IV-7 Optical measurement setup of the built-in stress [142]

Using this specific technique, the residual stress of the AlN thin film was measured after each deposition. First of all, in the design proposed at the beginning, a thin layer of AlN is deposited directly on the silicon wafer to act as a seed layer for the thicker AlN layer which will be deposited after the patterning of the Pt electrode on top of this seed layer. But it can also play another role: it can act as a controller of the initial curvature of the device. As just discussed, the residual stress in the piezoelectric layer is easily tunable by the deposition parameters, especially the RF power applied on the sample. Once the membrane released from the backside, the layers, which have built-in stress, will tend to minimize them by deformation. Having two different layers of AlN, the stresses can be tuned on a wide range, from tensile to very compressive values. We chose to tune the stress only on the AlN seed-layer because the thick AlN layer, being the active piezoelectric layer, needs a high piezoelectric efficiency and quality. If we lower the ionic bombardment on the growing film, we lower also its piezoelectric coefficient d_{31}. The second reason is that the stresses are also dependent on the thickness of the film [143]. The thinner the film is, the more sensitive the stresses will be to the ionic bombardment.

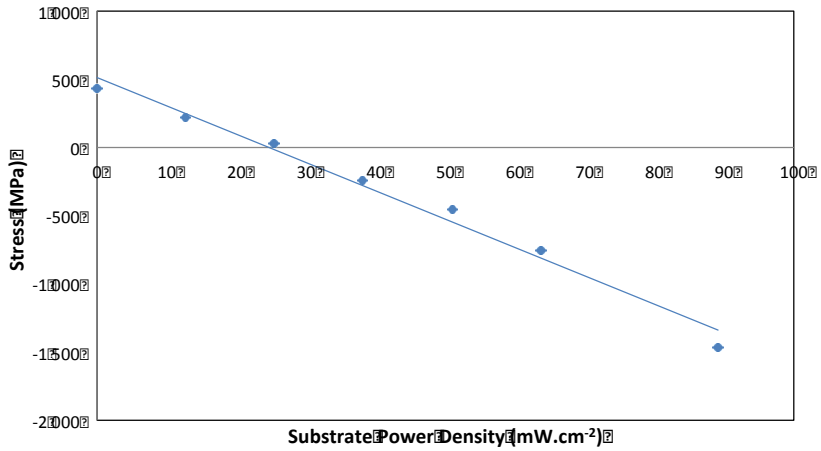

Figure IV-8 Evolution of residual stress in 200nm thick AlN film with the RF power applied during the deposition[144]

As the stress in the thick AlN layer are constant; it can be adjusted and compensated by tuning the stress in Al layer, changing the deposition temperature [145]. In this way, the stress in Al and thick AlN films are compensating each other, and AlN seed-layer remains the only one to control the curvature of the final device.

The stresses for different RF power applied to the substrate were measured for a 200nm thick AlN film as shown in Fig. V-8. It corresponds to 4min deposition time. The stress is linearly dependent of the ionic bombardment, and goes from 500MPa tensile stress to -1500MPa compressive stress. In order to have a curvature downward for the buckling to happen, the stress in the AlN seed-layer has to be compressive. On the other hand, a too high compressive stress will cause too much initial deflection, and the plate will be too rigid to buckle at a reasonable temperature. The membrane can even crack if it cannot withstand the amount of stress. A power density of 40mW.cm^{-2} seems to be a good compromise to have both the downward curvature and a relatively small deflection. This value will be used for all the devices fabricated further on.

IV.1.b Etching processes

After the deposition of 200nm AlN, without breaking the vacuum, 100nm of Pt was deposited at 350°C on top of AlN. The Pt is a common electrode material for AlN based devices because the <111> crystallographic direction of the cubic structure has the same symmetry as

the <001> hexagonal direction of the AlN. The AlN is then growing in a very textured manner, c-axis oriented.

In order to pattern the Pt electrode we did a photolithography step. To prepare the wafer for the coating of the photoresist, we put it into a furnace at 160°C for at least 10min to dehydrate it. The adherence of the resist is much better without humidity on the surface. Then 2µm of the positive photoresist AZ1512HS was spin coated on the wafer. The spin coating was done automatically on the EVG150. The wafer is loaded on a cassette and the recipe is loaded on the computer. For the AZ1512HS, the recipe was:

- Alignment of the wafer (with respect to the principle flat),
- Dispense of 2900µL of resist in the center of the wafer,
- Rotation at 1800rpm for 30s to get 2µm thick resist film,
- Pre bake at 250µm from a hot plate at 112°C for 1min30s,
- Cooling on a cold plate for 10s.

The wafer is then immediately exposed to UV light. The machine, MA6/BA6 from SüssMicrotec, was used because it can do both front side and backside alignment. The UV source, a Hg lamp, can be used in two different modes: for short exposition time (<3s) the lamp will deliver constant power of 275W and for longer exposition time it will deliver constant intensity of 10mW/cm^2.

The exposure time was previously calibrated by the CMi staff and for a film of 2µm of AZ1512 an exposure time of 2,5s is necessary. The constant power mode is then selected. As it is the first exposition, there is no alignment to do. So once the mask is placed on its holder, its position is adjusted to be central with respect to the wafer holder. The wafer is loaded and put in "hard contact" with the mask with a gap between them of 30µm. This limits the refraction of the light that can reduce the precision of the exposition.

Once the exposure is finished, the wafer is put on a cassette back to the EVG for the developing step. The following recipe is loaded on the computer:

- Alignment of the wafer,
- Dispense at the center of the rotating wafer (30rpm) of developer for 4s,
- Waiting time of 25s with the developer solution on the steady wafer,
- Quick acceleration of the sample at 1000rpm to evacuate the developer solution,
- Same three previous steps,
- Rinsing in de-ionised water while the wafer is rotating and 15s while the wafer is not moving,
- Post bake at 250µm from the hot plate at 112°C for 1min30s,

- Cooling on a cold plate for 10s.

The post bake is very important to stabilize the non-exposed resist, especially during the next dry etching. To ensure that the backside of the wafer is clean, without any residue of developer that could contaminate the etching machines, it is cleaned in de-ionised water one more time.

The procedure is exactly the same for the other photolithography steps using a different resist, the AZ9260. The only changes are the rotating parameters, the baking temperature and the exposure time.

The sample is then ready for the dry etching of Pt. The etching machine is dedicated to metals, especially chlorine based processes. It disposes of high-density plasma, inductively coupled, which means that the electric currents supplying the plasma are created by induction. The clamping of the substrate is made electrostatically. Circulating liquid helium controls the temperature of the chuck. The intensity of the plasma is controlled by the RF bias of the substrate the same way as for the AlN deposition process.

Pt is etched using a mixture of 5sccm Cl_2 and 25sccm Ar to create the plasma. It results in a combination of reactive etching with Cl_2 ions and physical etching with Ar ions. The machine has an End Point Detection (EPD), we can easily check when the Pt is etched away all over the wafer (the etching is quicker at the border of the wafer). The first trials were not conclusive. Even after the stripping of the resist by putting the wafer in remover solution and oxygen plasma, a thin resist film was remaining over the electrode. It is very problematic because it causes a huge contact issue between the electrode and the following AlN active layer that is be deposited over it.

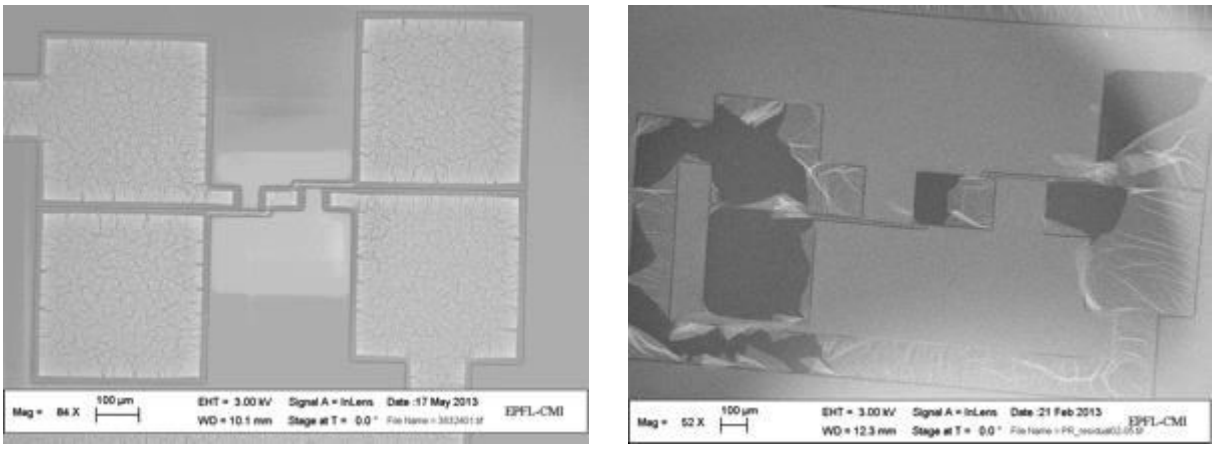

(a) (b)

Figure IV-9 SEM images of two structures with resist residues after Pt etching (non optimized process)

Different stripping methods are tested to get rid of the residues: hot remover, O_2 plasma (Fig. IV-9, a), remover combined with ultra sounds (Fig.IV-9, b), but the most efficient way was putting the wafer into the hot remover immediately after the etching without waiting for the plasma chamber to purge. The less time the wafer spent in contact with the atmosphere the better was the stripping (Fig.IV-10). One supposition is that the resist in contact with the chlorine is reacting with it and forms a harder superficial layer that doesn't go away with the remover. The contact with the atmosphere is accelerating the process.

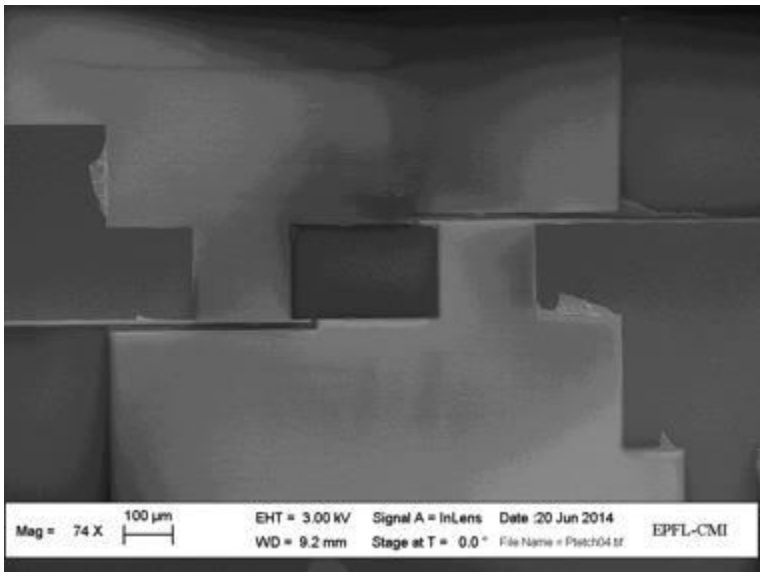

Figure IV-10 SEM image of the bottom Pt electrodes (optimized process)

The following step is the deposition of the active layers of AlN and the Al. For the AlN the same process as described before was used, the only difference is that the stress in the film isn't tuned. This time the deposition lasted 21min for a 1µm thick layer. A constant RF power density of 80mW.cm^2 was applied for all the samples to ensure a good piezoelectric quality of the film. The stresses then were more or less reproducible, generally around -500MPa. So by tuning the stress in the Al film adjusting its deposition temperature between 250°C and 350°C, the stresses in Al and AlN can cancel each other. More tensile stress in Al was obtained by lowering the temperature and vice-versa [145]. The deposition temperature of AlN is fixed at 300°C because as explained in [146] a temperature of at least 200°C is necessary to obtain a highly textured AlN thin film.

The next step, the photolithography on the Al layer for the etching of both Al and AlN was critical. Indeed a thicker resist is needed because around 2µm of material need to be etched away and also two etching processes have to be performed with the same photoresist mask. We

deposited 5µm of the positive resist AZ9260 following the same procedure as described before. The following changes are applied due to the higher viscosity of the AZ9260:

- Spin coating: Dispense of 4000µL at 1000rpm and then rotation at 6800rpm for 1min40s to get a 5µm thick resist film,
- Prebake at 300µm from the hot plate at 115°C for 4min,
- A minimum rehydration time of 8min is needed between the coating and the exposition of the resist to stabilize it,
- The recommended exposure time was 17,5s, which is long and the resist can heat up and begin to flow. The exposition was done in two steps of 9s, with 10s between the two expositions to cool down,
- The developer is not dispensed at the center of the wafer but sprayed all over it while the wafer is rotating at 250rpm,
- Postbake at 300µm of the hot plate at 115°C for 4min.

The wafer is then ready for the next etching steps. The Al layer is first etched with BCl_3 and Cl_2 plasma using the same ICP etching machine. Once the etching of the Al is completed, the wet etching of the AlN is done just after to limit the damaging of the resist, already exposed to the etching corrosive gas. The etching of the AlN was in a first time done only chemically, with a solution of phosphoric acid H_3PO_4 concentrated at 85% and heated up at 70°C to accelerate the reaction. It takes around 3min to etch completely 1µm of AlN and the result is on the right picture of the Fig. IV-11 (a). The Al and AlN were completely etched away. This is due to the AZ9260. Indeed the only drawback of the thick resist used in this step is that the developer solution is a buffered KOH solution, which is attacking and etching the Al. After the developing step, the Al exposed directly to the developer solution was nearly white, not reflective anymore. The adhesion of the resist on the Al is also lowered, some developer solution going between the Al and the unexposed resist, and the mask was lifted-off during the wet etching of the AlN.

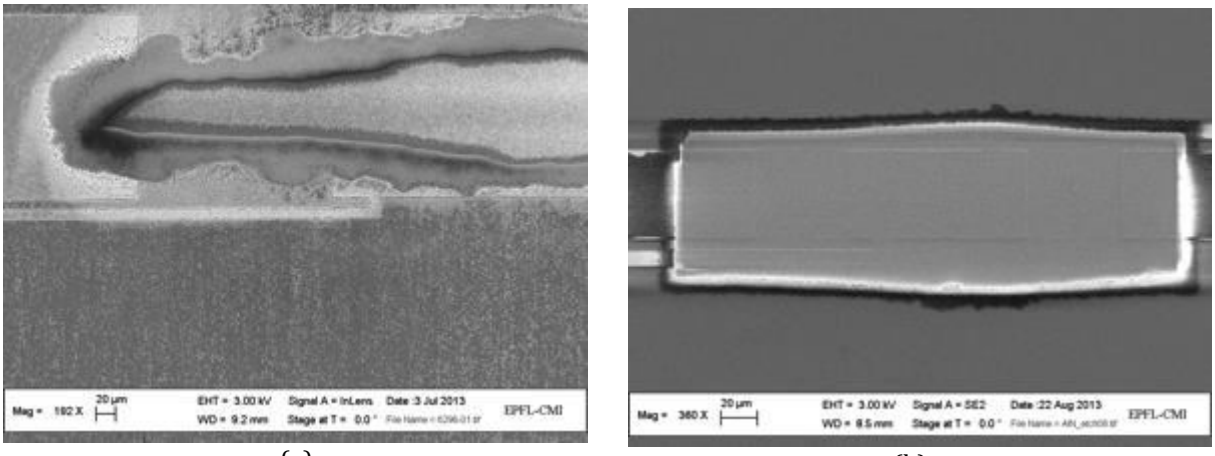

(a) (b)

Figure IV-11 SEM images of the structure after AlN wet etching without (a) and with (b) a Ti film on Al layer

The solution was to deposit 50nm of Ti on top of Al to protect it from the developer solution. It induces no additional stress and is deposited at room temperature, which is a very quick process. The adhesion of the resist was much better and the mask was remaining till the end of the process. There is still approximately 10µm of under-etch on etch side of the device (Fig. IV-11 b), because the H_3PO_4 is etching also the Al layer. The resulting membrane was not rectangular; its mechanical behavior afterward will be more complicated than a rectangular structure.

In order to reduce the exposure time of the Al to the acid, a plasma etching of the 1µm thick AlN with 15sccm Cl_2 and 5sccm Ar is performed to reach the Pt electrode. Then the remaining AlN is etched away with the acid to reach the Si substrate. In fact the plasma, which is composed of the same gases as for Pt etching, would etch away the Pt electrodes. There is only 200nm AlN to etch chemically with hot H_3PO_4; the reaction takes only 10s and the Al is less exposed to the acid. The etching was much more homogeneous, we reduced the under-etch of the AlN and Al as shown in Fig.IV-12.

One interesting AlN characteristic visible during the wet etching is the orientation of the AlN cell. The AlN is growing in the wurtzite structure along its c-axis. This crystallographic unit cell is composed of two interpenetrating hexagonal lattice, one made of Al and one made of N. Each atom is surrounded by four equidistant atoms of the other kind, forming a tetrahedron. When an Al atom is at the center of the tetrahedron, the AlN crystal has an Al-polarity and when the N is at the center it has a N-polarity [147]. Usually the sputtered AlN has a N-polarity. We can observe it very easily when the AlN is wet etched, because when the crystal is Al-polarized, it is much more resistant to the acid than when it is N-polarized. Furthermore, the N-polarity is forming typical hillocks (Fig. IV-13), while the Al-polarity is forming hexagonal holes.

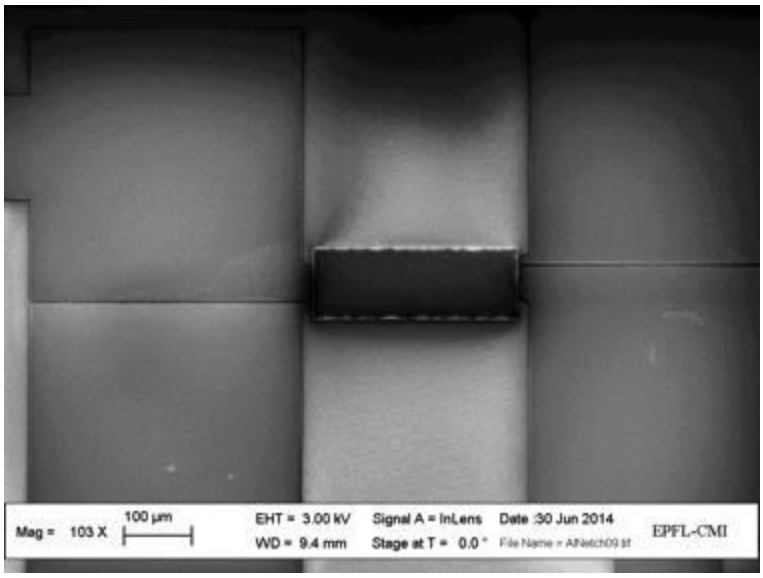

Figure IV-12 SEM image of a 300µm*100µm plate etch with the combination of dry and wet etching

One way to achieve the deposition of AlN with an Al-polarity is to deposit it by Molecular Beam Epitaxy (MBE) or Metal Organic Phase Vapor Deposition (MOPVD) at very high temperature (between 800 and 900°C). Milyutin *et al.* [147] manage to control and alternate the polarity of AlN using a seed layer of AlN deposited by MOPVD and having a Al-polarity. On top of it was deposited by evaporation a thin layer of SiO2 using a shadow mask. Finally a 1µm thick layer of AlN was deposited by DC-pulsed magnetron sputtering using the same technique as described before. The thick AlN layer is then Al-polarized when it is sputtered on the AlN seed layer and N-polarized with it is sputtered on SiO_2.

The process of the front side is now optimized, the final step is to etch through all the wafer thickness to open from the backside and liberate the structures. It is done using the well-known Bosch process. It consists of a plasma etching process dedicated to etch high thickness materials. The succession of an isotropic Si etching plasma (SF_6) and the deposition of a passive layer of C_4F_8 is allowing a very directional etching.

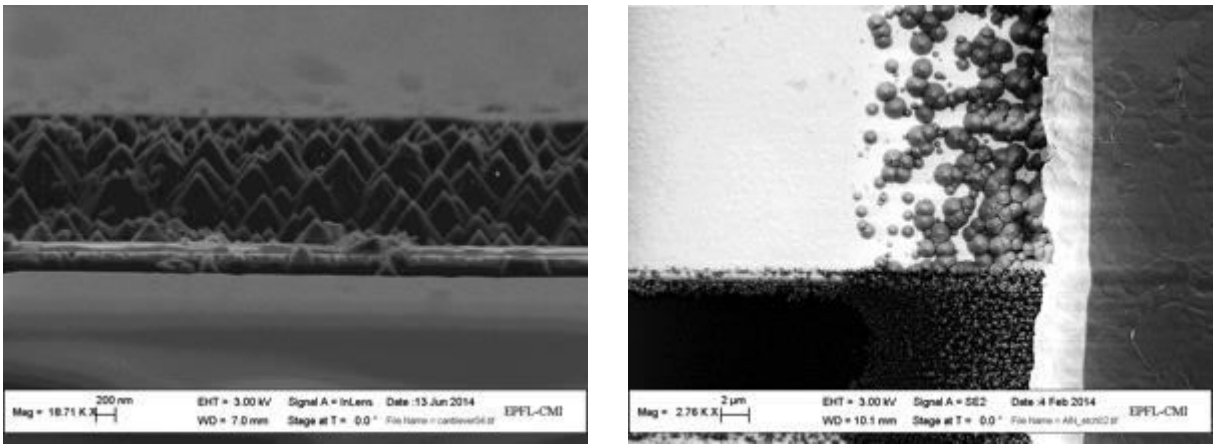

(a) (b)

Figure IV-13 SEM images of AlN hillocks. (a): cross-section, (b): top view

After the photolithography on the backside of the wafer with 8µm of AZ9260 photoresist, the front side of the wafer needs to be protected during the plasma etching of the backside. A thin layer of parylene C (between 2 to 5µm thick) is deposited on the wafer. It has several advantages: it induces no stress, it is deposited at room temperature and it is very conform. Once the front side of the sample is protected, the silicon oxide on the backside is first etched away by C_4F_8 plasma and then without breaking the vacuum the silicon is etched by the Bosch process. The wafer is clamped electrostatically and is cooled down during the etching to prevent any damage of the resist and the parylene (stable up to 150°C).

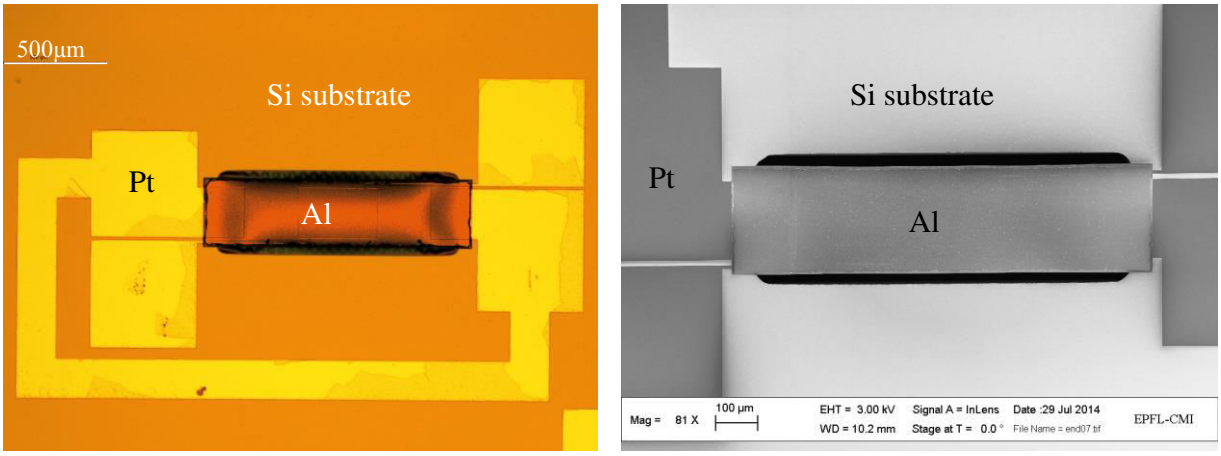

(a) (b)

Figure IV-14 Picture (a) and SEM image (b) of a 1000µm*250µm at the end of the process

An End Point Detection system based on laser interferometry is allowing us to follow the etching of the SiO_2 precisely and to detect immediately when there is no more Si to etch. There is no risk to damage the front side structure by etching a little more (the smallest holes are slower to be etched), because the AlN seed-layer is a good etch stop layer.

Once the Bosch process is finished, the parylene layer is eliminated by O_2 plasma, being careful not to put the wafer parallel to the oxygen flow for not breaking the membranes. Due to the stress in the layers, the membranes are initially curved without any other manipulations as shown in Fig. IV-14 and 15.

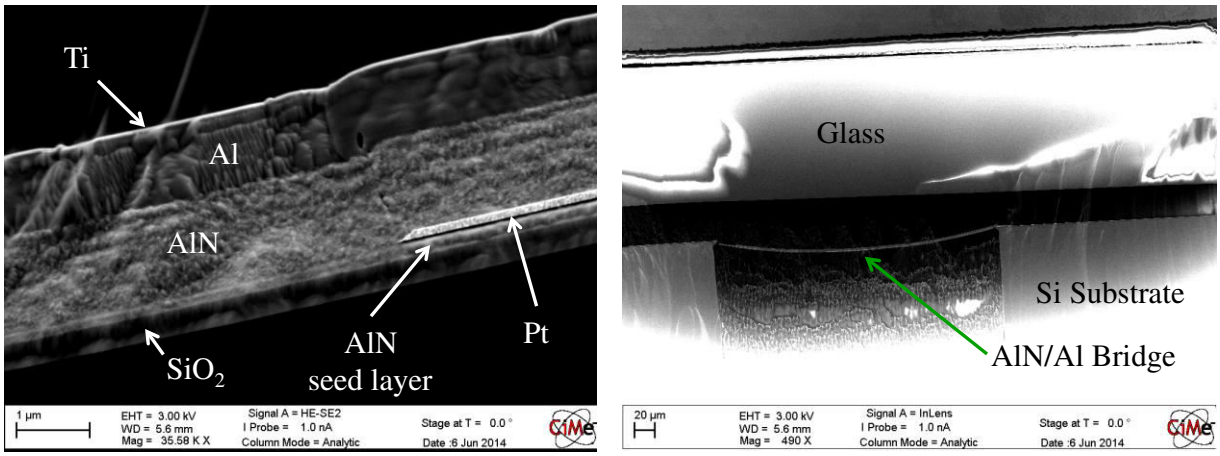

(a) (b)

Figure IV-15 Cross section of a freestanding membrane

The cross section of a final curved structure is shown on Fig. IV-15. A special SEM technique was used to prepare the sample. One single structure was diced from the wafer. The front side of the structure was glued on a piece of glass (top part on the right picture in Fig. IV-15) and the backside hole was filled with epoxy. The prepared sample was then put into the SEM and bombarded by gallium ions to etch the sample away until the middle of the structure is reached. The aim of this manipulation was to observe the curved structure is SEM along its length and to see if there was any defect in the AlN layer.

IV.3 Conclusion

In this chapter the fabrication process as been presented. The different steps in order to achieve the final structures have been detailed. The issues encountered at the beginning are explained as well as the solution to overcome them. A lot of efforts have been done during the etching processes of both Pt and AlN. The structure will then be fully characterized to make sure that the piezoelectric film is of good quality and that the process parameters are adapted.

V Characterization

The characterization of the previously fabricated devices is presented in this chapter. The structure geometry like its initial deflection as well as the piezoelectric film quality are investigated. The piezoelectric coefficient $e_{31,f}$ is measured both in actuator and sensor mode. The crystallographic orientation of the AlN is controlled and its pyroelectric response to small temperature variation is characterized. The electromechanical response of the structure is measured to determine its resonance frequencies. The results are compared to finite-elements simulations. The performance of the buckling harvester actuated mechanically and thermally is presented. Different geometries are tested and their output power is measured. Finally new geometries having a butterfly shape are presented and characterized.

V.1 Initial deflection

At the end of the fabrication process, the most important parameter to control is the initial curvature of the freestanding membrane. Indeed as explained in the previous chapter, the curvature is controlled by tuning the residual stress induced during the sputtering of the thin films, especially AlN. The sputtering process is very homogeneous, but the stress a bit less due to the non-homogeneous etching processes, which are quicker at the border and slower in the center. This phenomenon is accentuated when a layer is deposited onto a patterned material, for instance when we deposit AlN and Al over the patterned Pt electrodes.

Two techniques are used to measure the deflection of the structures: mechanical profilometer and optical interferometer. The mechanical profilometer [148] is giving an image of the surface along a defined linear path (Fig. V-1 a). A probe is applying a given force onto the surface and is following its asperity. It is very precise and allows seeing small impurities as well as huge gaps of 100µm. The drawback of this technique is that it has to follow a linear path and we cannot see the transverse curvature that our devices may have along their width. If the force applied by the probe is too high, it might also change the curvature of the device by making it buckle.

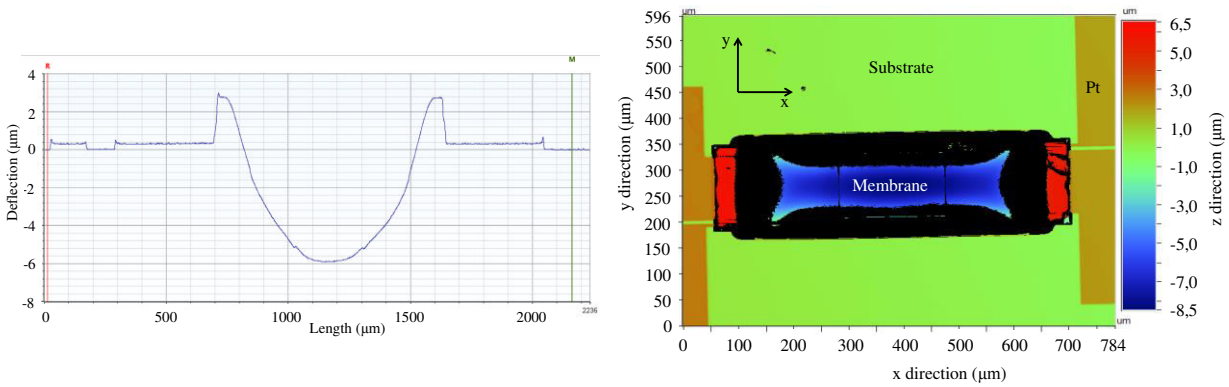

(a) (b)

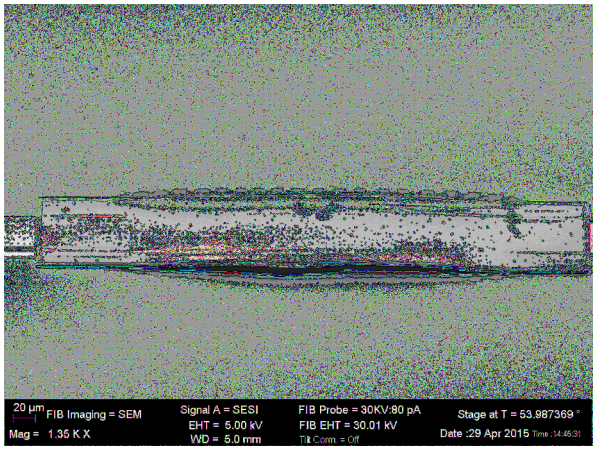

(c)

Figure V-1 Profile with the mechanical profilometer (a) and the optical interferometer (b) of a 1000µmx250µm plate and SEM picture of a 500µmx100µm plate (c)

On the other hand, the optical profilometer [149] is an interferometer based on the same principle as a Michelson interferometer. Interference fringes are created on the surface of the device and by moving the objective up and down we can get an image of the profile of an entire device and its surroundings. The curvatures in the two directions are well visible (Fig. V-1 b). This technique has two major drawbacks. It is less precise than the mechanical profilometer (3nm instead of 0,1nm) and the repeatability of the measurements might be slightly changed because the origin is not fixed exactly in the same place. The surface has to be reflective and not too much bent because the reflected light has to go back to the detector. If the deflection of the membrane is too high, the light is deviated elsewhere and no signal is observed. That is the reason why there are a lot of black areas on the picture (b) of Fig. V-1: the membrane just after the anchor is too much bent and the light is not reflecting anymore in the detector.

A mapping of an entire wafer was done with the mechanical profilometer. This way, we consider only the variability of the curvature in the length of the devices. No information is given on the transverse curvature.

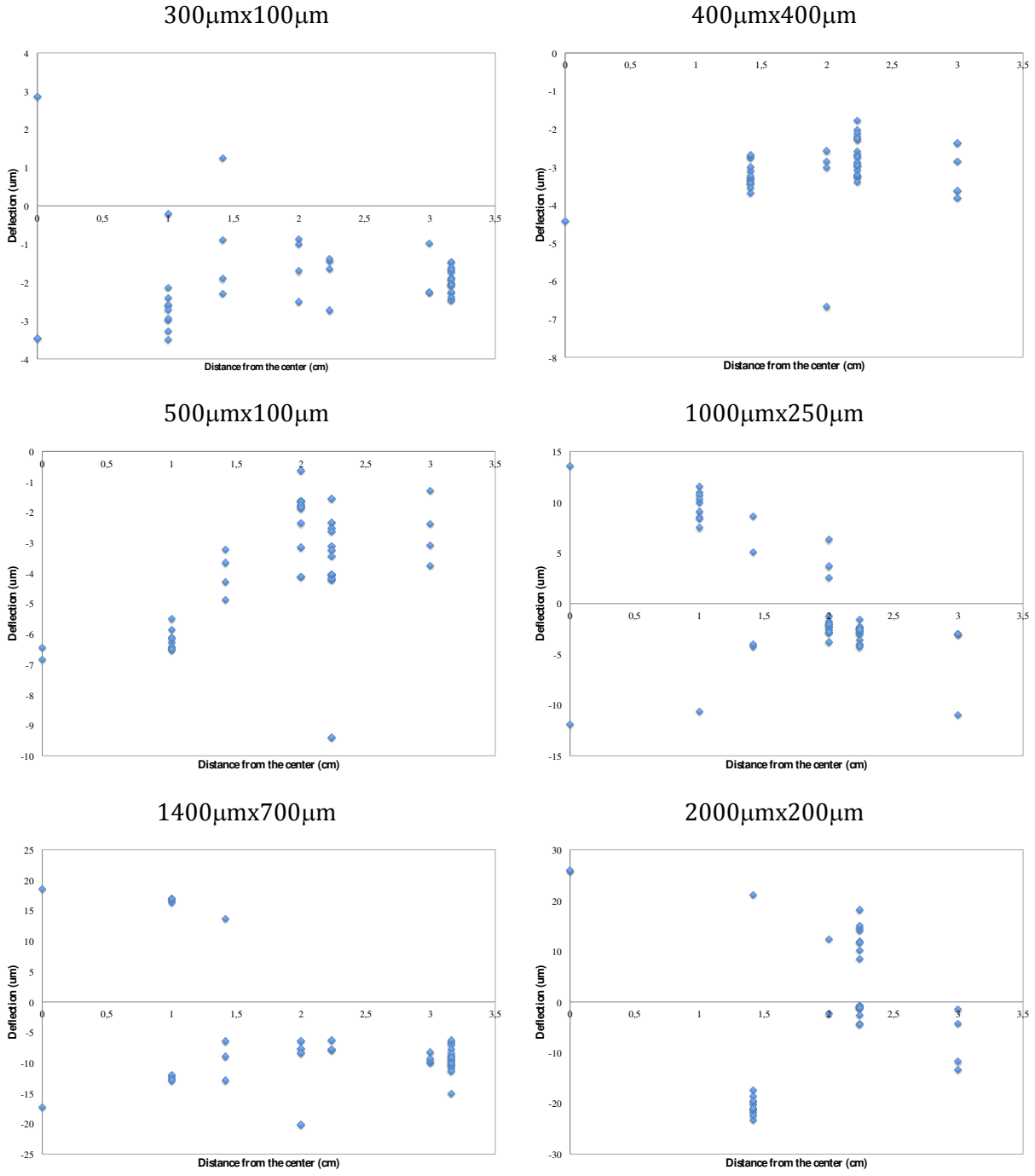

Figure V-2 Initial deflection measured on one wafer with 1µm of AlN and 1µm of Al for the different geometries

The results are shown in Fig. V-2 for each dimension because of the dependence of the deflection with the length of the structures. To illustrate the variability of the curvature with the

inhomogeneous stress caused by the etching processes, we plot the data with respect to the position of the sample on the wafer, the origin being at the center of the wafer. There was between 40 and 48 valid structures for each dimension. The tested wafer was composed of a seed AlN/Pt layer of 360MPa tensile stress, an AlN layer of -116MPa compressive stress and an Al layer of 98MPa tensile stress. The overall residual stress for the membrane is around 340MPa tensile.

The following initial curvatures are obtained using the analytical model developed in chapter III for the different devices:

- 2000x200: +/- 17,75µm
- 1400x700: +/- 12,24µm
- 1000x250: +/- 8,53µm
- 500x100: +/- 3,72µm
- 300x100: +/- 2,37µm

We can see that the experimental values are very dispersed, but the value calculated analytical can be observed when the structure is situated at 1,5 or 2cm from the center of the wafer. Several explanations are possible: the stress in the films are not homogeneous throughout the wafer area, and as shown by the analytical model the slightest change in the stress value can cause a great change in the initial curvature of the plate, especially with stress levels around 100MPa. Moreover, the analytical model is valid for slender beam structure, and only the 2000x200 plate can be considered as a slender beam.

We can assume that the stress measured in the Al film is the most reliable as it is a reflective material (on the contrary the AlN is transparent) and its thickness after processing is not decreased (as for the AlN seed-layer during patterning of the Pt). The deflection of the 2000x200 of 27µm at the center of the wafer with 98MPa stress in the Al layer would corresponds to a stress in the AlN layer of -431MPa, which is 4 times higher than the experimental value. Moreover, when the Pt is patterned, some seed-layer of AlN is etched away, and its thickness is lower at the border of the wafer than at the center. Indeed if we lower the thickness of the AlN/Pt from 300nm to 200nm and 100nm, keeping the same stress in the layer we obtain a stress in the AlN layer of respectively -372MPa and -324MPa.

Moreover, for the AlN/Pt seed-layer, we took effective values for the thickness and the Young modulus, and the stress measured experimentally is measured before the patterning of the Pt. However, as nearly all the surface of Pt is etched away, the stress after patterning is changed because the AlN seed-layer is not etched away completely. For instance if we take the 2000x200 device with an initial deflection of +27µm at the center, we can assume that the AlN

seed-layer is not under etched, so we have a thickness of 300nm of AlN/Pt. For the measured stress, +360MPa, the stress in AlN is -420MPa as said before, but if the stress is +200MPa in the AlN/Pt layer, the stress in the AlN decreases to -372MPa and on the contrary if the stress is +500MPa in the AlN/Pt layer, the stress in AlN goes up to -462MPa.

The first observation we can make is that the membranes are for the majority curved downward (a negative deflection means a downward curvature). The second observation is that for the longest structures, more upward curvature is measured. We applied the model developed in Chapter III to the experimental values of the deflections. We can observe that the theoretical value of the deflection is matching only for structures that are not situated at the center or at the border of the wafer. Moreover from the experimental value of the deflection we can calculate the stress in the films. We can see a large dispersion of the deflection, especially for the 2000x200 devices. This can be explained analytically by the approximation made on the AlN/Pt seed-layer for the Young modulus and for its thickness that is not constant over the wafer, the AlN being etched quicker at the border than in the center of the wafer during Pt patterning. Another approximation was made during the measurement of the stress. Indeed as explained before it is performed by a laser, which is measuring the curvature of the whole wafer before and after deposition and deduced the stress applying the Stoney formula. First of all, the Stoney formula has limitations, especially when the thickness of the film/substrate is not equal on the whole wafer [140][150] and as the AlN is transparent, the radius of curvature is then measured reflecting on the Pt electrodes and the Si wafer, visible by transparence through the AlN layers.

V.1 AlN Film Quality

As described before, the process for the deposition of the AlN was optimized in order to obtain the highest piezoelectric film quality. The temperature, gas pressure and RF power were adjusted to get highly c-axis oriented crystals, the only way to ensure good piezoelectric transduction afterward [139][151]. Three aspects of the film quality were investigated: its crystallographic orientation, its piezoelectric coefficient $e_{31,f}$ and its pyroelectric response. The crystallographic orientation, characterized by X-Rays diffraction ensures that the deposition parameters are adapted. The $e_{31,f}$ coefficient, characterized either in direct or inverse mode, quantifies the piezoelectric quality of the film, especially for energy harvesting applications. Indeed one Figure of Merit (FOM) is given by the ratio between this coefficient and the dielectric constant of the material [136][152][111]. Finally the pyroelectric response of AlN film will give

us the amount of charges generated by the effect of the temperature on the device and estimate the proportion of pyroelectric and piezoelectric charges generated for the final functional device.

V.1.a Crystallographic properties

To determine the crystallographic orientation of the AlN thin films, we performed exactly the same fabrication process as established for the final devices, but after the Al etching, the sample was analyzed by θ-2θ X-ray Diffraction. The principle of this technique is to irradiate the sample with X-rays of wavelength λ at an angle θ with the surface and to collect diffracted radiation leaving the surface at the same able (Fig. V-3). In this way the detected diffractions are restricted to the ones at crystal planes parallel to the surface. The Bragg law $n\lambda = 2d\sin\theta$ allows to quantify the lattice spacing di and thus to identify the type of planes parallel to the surface of the film (or sample). The name of the technique comes from the way the different elements are rotating: the X-ray source is fixed, the sample rotates from an angle θ and the detector by the angle 2θ.

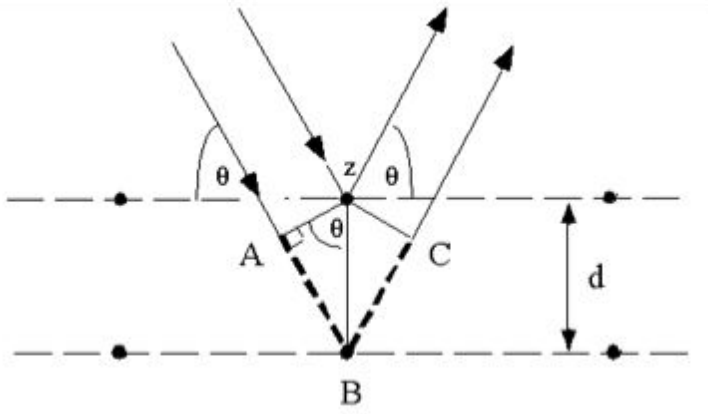

Figure V-3 Bragg law illustration for θ-2θ diffraction.

As the lattice constants are quite typical for a given material or material phase, the presence of the detected lattice can discriminate one kind of material or material phase. If only one plane is parallel to the surface, grains have a specific orientation, or in case of polycrystalline films, the film exhibits a texture. The diffracted X-rays are collected at an angle 2θ from the incident beam. When a family of planes with a pitch *d* between each plane diffracts the X-rays, a peak is observed. Knowing the distance *d* between each parallel planes for each material, we can observe the nature of the materials deposited on the sample as well as their orientation.

On Fig. V-4 is the result of the analysis of one wafer just after Al etching. The highest picks are from Si (400), the substrate, AlN (002), the thin film oriented along its hexagonal c-

axis, and the electrode Pt (111), oriented along its cubic diagonal, in the right way to enhance the growth of the AlN film deposited on top. A small peak of Ti is visible, but as the film is very thin (50nm), it doesn't reflect much the X-Rays. The Al thin film is also not clearly visible, because it is patterned. Its diffracting volume is much smaller than the one of AlN.

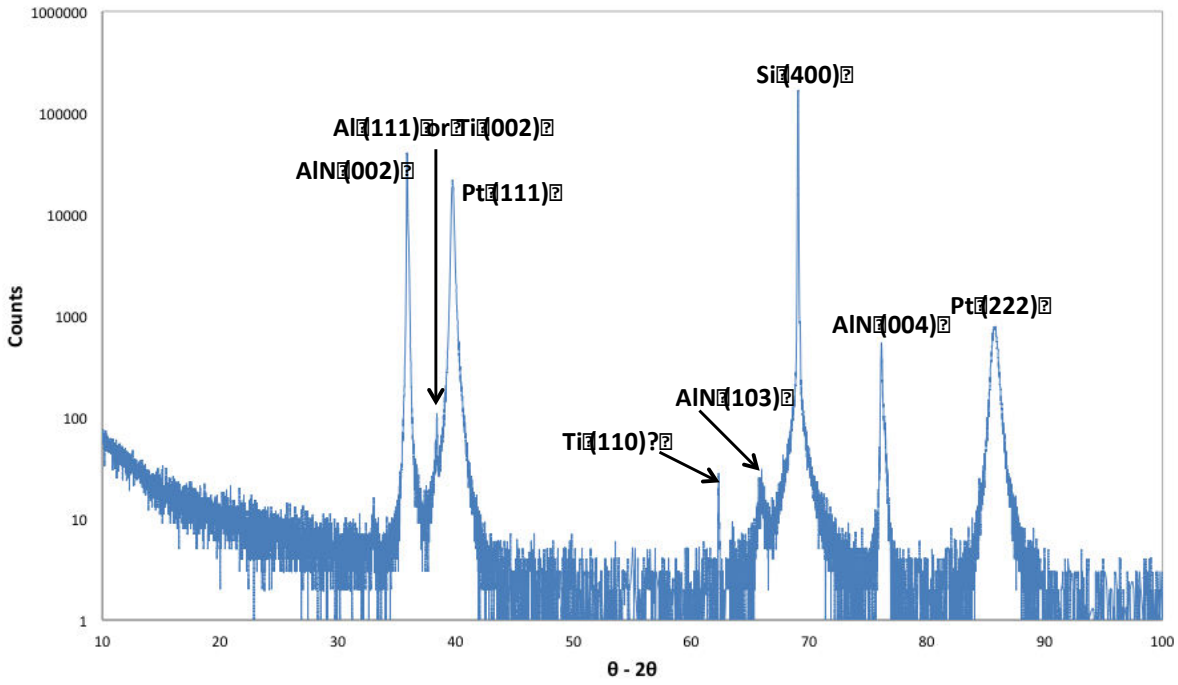

Figure V-4 X-rays Diffraction scan over a sample diameter after Al etching

Additionally, a very weak (103) peak of AlN is visible (1000 times smaller than the (002) peak). In about 0.1% of the grains, the c-axis is tilted away from the normal axis to the plane of the film, which is typically observed for the films grown on rough surfaces, or eventually at the border of patterned electrode. Possibly this diffractions does not concern the active AlN layer but the layer below the Pt bottom electrode, which should promote a good (111) texture of the Pt thin film. As a matter of fact, we adjusted the RF bias during its deposition. Anyway, their quantity is low compared to the (002) oriented AlN.

To conclude the AlN thin film is well oriented along its c-axis. The Pt played his role thanks to its (111) orientation and enhancing the growth of a textured AlN. A good piezoelectric response is then expected.

V.1.b Piezoelectric properties

Once the AlN film is deposited with a crystal orientation along its c-axis, the piezoelectric response has to be measured. Two different techniques were used to characterize the piezoelectric coefficient $e_{31,f}$: the direct mode measuring the electrical response of a cantilever when a mechanical force is applied at its free end and the converse mode when the mechanical displacement of the free end is measured when a voltage is applied. The sample is clamped mechanically under the top Al electrode in a way that the maximum stress is localized under the electrode area. Aluminum circles are also designed at the free end to enhance the reflection of the laser during the measurement of the displacement. Two probes are contacting the Al layer and Pt bottom electrode.

V.1.b.i Direct Mode

The piezoelectric film is first characterized in the direct mode, which means that the quantity of electrical charges in response to a given displacement is measured. To compare with the results of the literature [111][109][137] we fabricated a test structures: full-wafer-thickness cantilevers, which were exposed to exactly the same processes as the freestanding devices. At the end of the fabrication process they were diced from the wafer. The piezoelectric films present then the same stress and the same characteristics as the final devices.

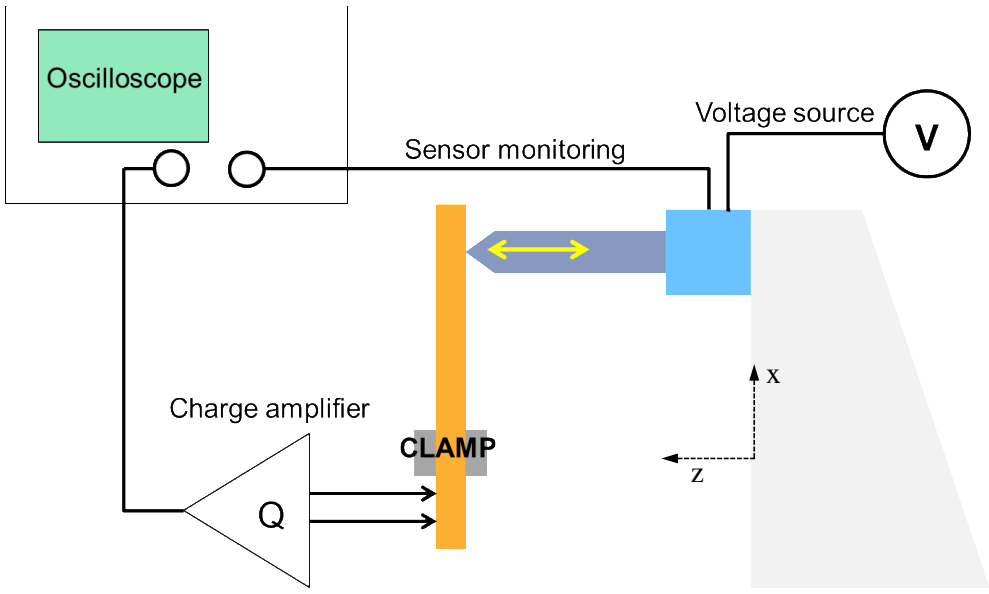

Figure V-5 Direct Mode characterization setup [137]

The setup is shown in Fig. V-5. The sample is clamped in the position between the contact pads and the Al top electrode. With an insulated alumina tip driven by a piezoelectric

actuator we apply a displacement *z* on the free end of the cantilever. The probes are contacted to the top and bottom electrodes, the bottom electrode being connected to the ground. The generated charges are converted by a charge amplifier Kistler 5011B into voltage to get the $e_{31,f}$ coefficient. The voltage source is applying a sinusoidal signal of 1V peak-peak to the piezoelectric actuator of the tip, which is calibrated to furnish a displacement of 4,5µm at this voltage. The positive voltage corresponds to the push movement and the negative voltage to the back movement.

The cantilevers are 15mm long and 1,5mm wide. They were fabricated along two orientations of the silicon substrate: (110) and (100). The major parameters impacted by the anisotropy of the silicon for these two orientations are the Poisson coefficient and the Young modulus, which are 0,068 and 169GPa respectively in the (110) direction and 0,24 and 130,5GPa in the (100) direction [141].

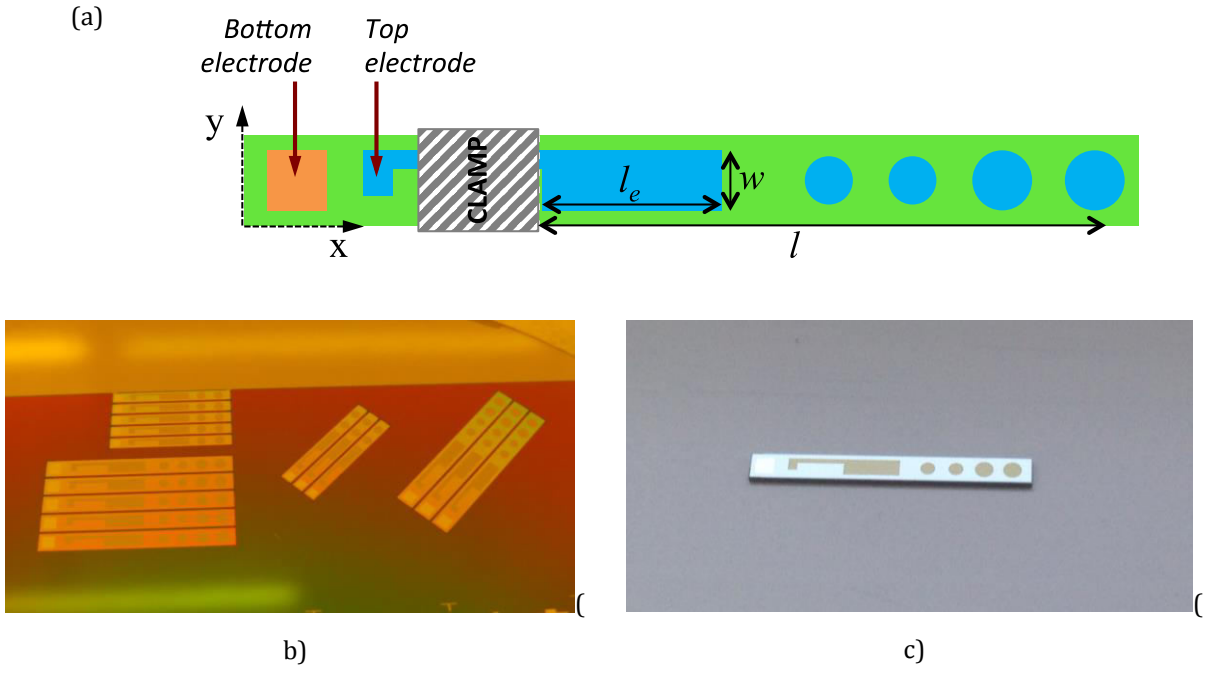

Figure V-6 Schematic (a) and images of the cantilevers before (b) and after (c) dicing.

For all the tested devices, the output signal was in phase with the driving actuator signal. This means that during the pushing movement (positive input voltage), the output voltage is positive and the piezoelectric charges generated by the sample are negative. The charge amplifier was set with a gain G of 1000pC/V. The effective length of the cantilever *l* is the distance between the clamp and the tip actuation point and is about 9,5mm.

All the parameters necessary to calculate the coefficient $e_{31,f}$ are known. With the collected charges $Q = V_{pp} \; G$ and the effective area $A = w \; l_e$ the electrical displacement can be deduced:

$$D_3 = \frac{Q}{A} \qquad \text{Eq. V-1}$$

It is also linked to the $e_{31,f}$ coefficient from the piezoelectric equations, assuming two hypothesis:

- the stress in the z-direction is zero as the film is free to move,
- in sensor mode the charges are measured at zero electric field as the charge amplifier short-circuits virtually the sample.

Following these assumptions a new expression of the electrical displacement in *z*-direction is obtained:

$$D_3 = \frac{d_{31}}{s_{11}^E + s_{12}^E}(S_1 + S_2) = e_{31,f}(S_1 + S_2) \qquad \text{Eq. V-2}$$

Where d_{31} is a piezoelectric coefficient, s_{11}^E and s_{12}^E are coefficients of the elastic compliance matrix, S_1 and S_2 strain components in the x and y direction respectively. The strain in the cantilever when a mechanical force is moving the free end with a displacement *z* as well as its radius of curvature are given by [131]:

$$S_1 = \frac{t_{sub}}{2R}$$
$$\frac{1}{R} = \frac{3z(l - x)}{l^3} \qquad \text{Eq. V-3}$$

Where *l* is the length of the beam from the clamping to the probe position and t_{sub} the thickness of the silicon substrate.

As the film is much thinner than the cantilever total thickness, the strain components S_1 and S_2 are considered constant throughout the film thickness. The strain in the transversal and longitudinal directions are linked by the relation $S_2 = \_\_{sub} S_1$, so the electric displacement can be written as:

$$D_3 = e_{31,f}(1 \quad \_\_{sub}) S_1 \qquad \text{Eq. V-4}$$

The strain S_1 is obtained by replacing the value *x* of Eq. V-3 by the length of the electrode l_e, resulting to the formula:

$$S_1 = \frac{3zt_{sub}}{2l^2}(1 - \frac{l_e}{l}) \qquad \text{Eq. V-5}$$

Finally the corresponding $e_{31,f}$ is given by:

$$e_{31,f} = \frac{D_3}{S_1(1 \quad _{sub})} = \frac{Q}{A}\frac{2l^2}{3zt_{sub}(1 \quad _{sub})(1 \quad l_e/l)} \qquad \text{Eq. V-6}$$

From these equations we can measure for each sample and each substrate orientation the voltage amplitude (peak to peak) by the charge amplifier and deduce the piezoelectric charges generated by the AlN film. The peak-to-peak amplitude is chosen because the cantilever is always pushed forward by the probe, it will not be bent in the other direction.

Table V-1 $e_{31,f}$ values for the different samples tested in sensor mode

AlN / Al Thicknesses - Orientation	**1µm /1µm**		**1µm /2µm**		**0,5µm /1µm**		**0,5µm /0,5µm**	
	90°	45°	90°	45°	90°	45°	90°	45°
Charges (pC)	59,2	48	60	48	60,8	49,6	56,8	43,2
$e_{31,f}$ **(C/m²)**	-0,88	-0,88	-0,89	-0,93	-0,9	-0,96	-0,85	-0,84

From the Table V-1 the values of the piezoelectric coefficient $e_{31,f}$ are relatively constant, whatever the thickness of the film or the orientation of the silicon substrate. The film quality is very reproducible. The mean value of $e_{31,f}$ coefficient is -0,9C/m², which is close to the best literature value of -1,01pC/V. The 10% difference may be due to the etching of the aluminum layer. Indeed in the best reference paper, the top electrode was deposited by a lift-off process, which is less aggressive for the AlN film than the etching gases. Actually the Cl_2 plasma used for the etching of Al is also etching the AlN, so it can damage slightly the surface of the AlN layer.

Table V-2 Comparison of the $e_{31,f}$ coefficient for different piezoelectric materials

	AlN	**PZT**	**ZnO**	**AlN (This work)**
$e_{31,f}$ **(C/m²)**	-1,02	-17,7	-1	-0,9
Ref	[137]	[97]	[107]	[153]

V.1.b.ii Converse mode

After the characterization of the piezoelectric film in direct mode, the same samples were characterized in inverse mode. The same $e_{31,f}$ coefficient should be calculated. The technique presented here is an alternative of the previous technique to quantify the piezoelectric quality of the AlN film. For energy harvesting applications it is more useful to use the previous technique but for actuator applications the converse mode is more interesting to characterize.

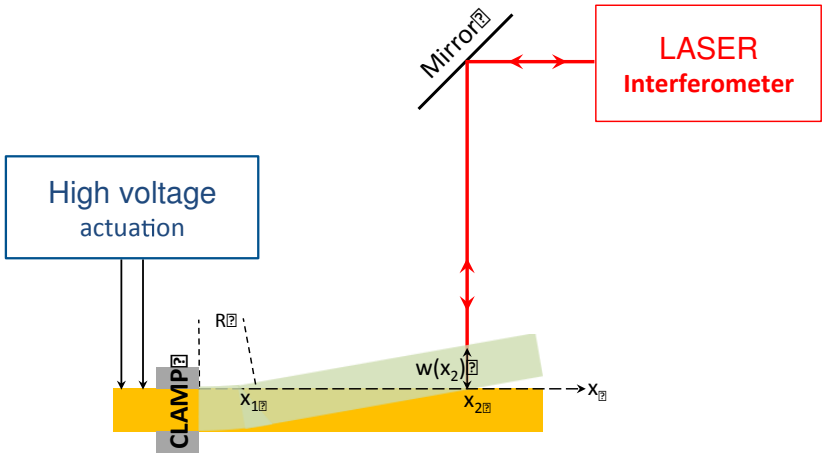

Figure V-7 Converse mode experimental setup

The setup is a Thin Film Analyzer produced by the Aixacct company (TF Analyzer FE 2000). It is originally designed to characterize ferroelectric thin films, but it is also suitable for piezoelectric films. It can measure the hysteresis loop and calculate directly the piezoelectric coefficients in function of the geometrical and material characteristics. The displacement of the cantilever is measured by a single beam laser interferometer. The cantilever is contacted by two probes, which can deliver high voltage up to +/- 400V.

The stresses generated in the piezoelectric film are calculated from the measured displacements. Indeed the in-plane stress in the *x*-direction T_x is proportional to the electric field E_3 following this equation of the piezoelectricity:

$$T_1 = e_{31,f} E_3 \qquad \text{Eq. V-7}$$

In order to calculate the stresses in the AlN film, we assume that the cantilever is bending only in the region of the active part, which means under the top Al electrode. The rest of the cantilever is following the deformation imposed by the radius of curvature *R*. In the Fig. V-6 the origin of the x-axis is taken at the end of the clamped part of the cantilever. x_1 corresponds to the

length of the top Al electrode and x_2 to the focus point of the laser, where the displacements are measured. The radius of curvature of the active region can be found thanks to the Stoney formula, the piezoelectric film being much thinner than the substrate.

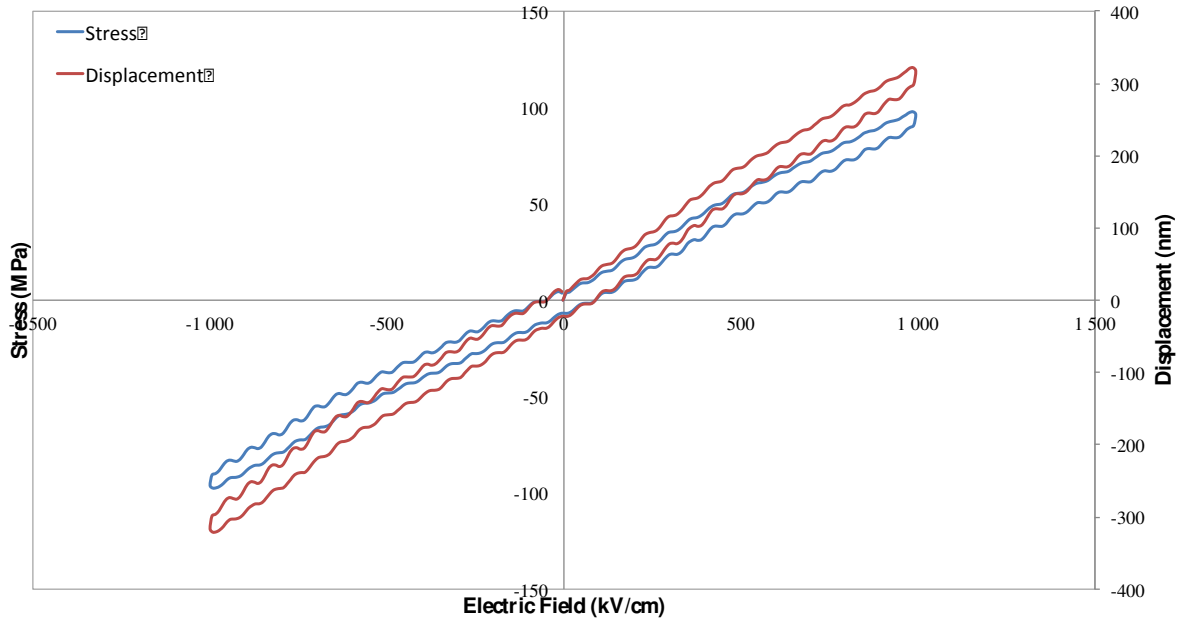

Figure V-8 Stress and Displacement of the free end of the cantilever in actuator mode

The final formula to calculate the stress corresponding to a displacement $w(x_2)$ measured by the laser is developed in the paper [154] and is given by:

$$T_1 = \frac{1}{3(1 \quad _{sub})b_r}\frac{Y_{sub}}{}[b_r + (1 \quad b_r)(1 \quad _{sub})]\frac{w(x_2)}{x_1(2x_2 \quad x_1)}\frac{t_{sub}^2}{t_p} \qquad \text{Eq. V-8}$$

where t_{sub} and t_p are respectively the substrate and the piezoelectric layer thicknesses, Y_{sub} is the Young modulus of the silicon substrate, ν_{sub} its Poisson ratio and b_r is the ratio between the cantilever and the electrode width. Plotting the stress in function of the electric field, the slope of the curve corresponds exactly to the coefficient $e_{31,f}$. As for the direct mode, different samples were tested and their piezoelectric coefficient is calculated following the technique just explained.

Table V-3 $e_{31,f}$ values for the different samples tested in actuator mode

AlN / Al thicknesses	**1µm /1µm**	**1µm /2µm**	**0,5µm /1µm**	**0,5µm /0,5µm**
Displacement at 100V (nm)	342	338	365	328

$e_{31,f}$ (C/m^2)	-1,042	-1,017	-1,101	-0,991

The Table V-3 summarizes the results obtained for the different samples. We observe that for all the samples the value of the $e_{31,f}$ coefficient is always higher than in direct mode. Moreover, the samples with the highest and lowest coefficient are the same in both characterization techniques. The error on the $e_{31,f}$ coefficient in the sensor and actuator mode is estimated to be 0,1C/m^2.

V.1.c Pyroelectric effect

The AlN is a piezoelectric material, we characterized its coefficient $e_{31,f}$, but it is also a pyroelectric material. The pyroelectricity is the property of a material to generate electrical charges when subjected to a temperature change and vice versa. As for piezoelectricity, it is characterized by a coefficient p_3, which is defined as follow:

$$p_3^T(\ ) = \frac{I}{A_{eff}\frac{d}{dt}} \qquad \text{Eq. V-9}$$

where θ is the temperature, t the time, I the pyroelectric current and A_{eff} the effective area (area of the electrode). The subscript of the pyroelectric coefficient indicates the flowing direction of the charges. The pyroelectric coefficients are describing the variation of the polarization along the c-axis of the material with the temperature at constant stress T and constant strain S [155][87]:

$$p_3^T = \left(\frac{P_3}{\ }\right)_T \div$$
$$p_3^S = \left(\frac{P_3}{\ }\right)_S \div \qquad \text{Eq. V-10}$$

The difference between these two coefficients is the contribution of the piezoelectricity. When the material, in the case of a thin film configuration, is heated up or cooled down, it dilates or retracts itself. As the substrate and the thin film have different coefficient of thermal expansion (α_s and α_f respectively) they create thermal stresses and generate piezoelectric charges:

$$p_3^f = p_3^T + 2e_{31,f}(\ _s \quad _f) \qquad \text{Eq. V-11}$$

The superscript or subscript f means that the measured value is an effective value. The setup used to characterize the sample is presented in Fig. V-8. The wafer, with 1µm AlN and 1µm

Al, was processed with the standard process described before. Just before the backside etching it is diced into unit cells of 1mmx1mm, with the different structures. The cell is placed on a Peltier cell, which can heat up or cool down the sample of a few degrees around the ambient temperature. The top Al layer of a 1400x700 device and the silicon substrate were contacted by two probes connected to a charge amplifier and a Labview interface. The temperature range and the frequency could be tuned.

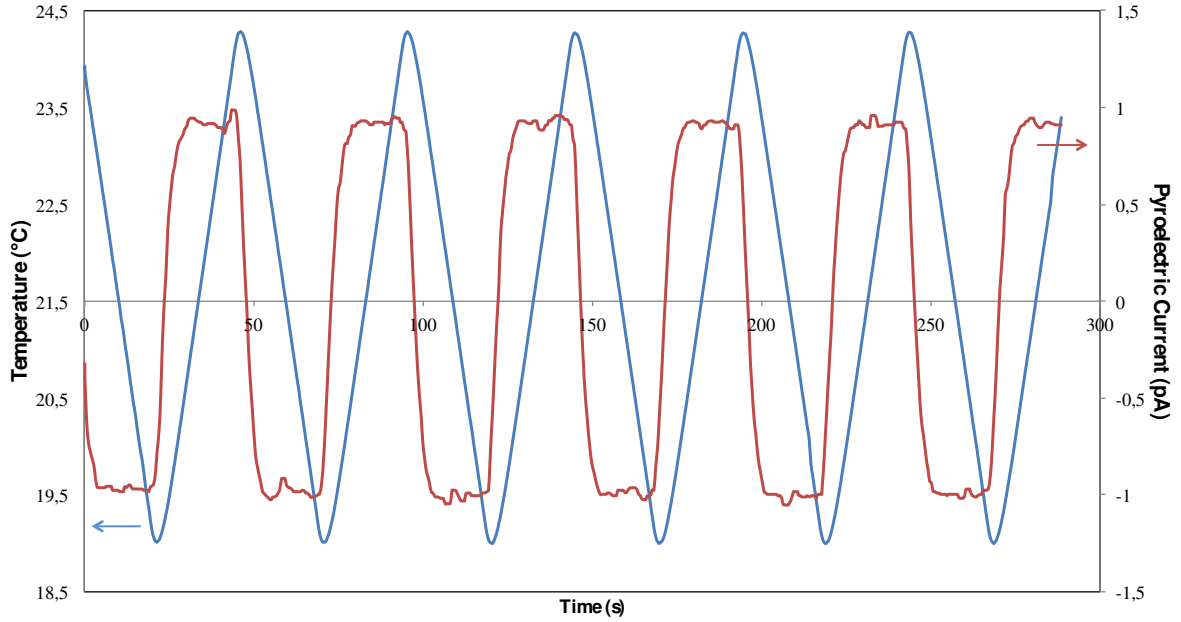

Figure V-9 Pyroelectric response of a 1µm thick AlN film

A triangular temperature variation of 3°C around the ambient temperature is applied on the substrate at the frequency of 20mHz. The sample is placed in a thermally insulated chamber to prevent any ambient temperature change (door opening, person passing by…) during the measurement.

The Fig. V-9 presents the output signal obtained. As expected, for a linear temperature change (constant slope) the pyroelectric current is constant. Its sign is inverting when the temperature is rising up and cooling down and its absolute value is 1pA for negative slope and 0,94pA for positive slope. The corresponding p_3^f coefficient is 3,93µC/(m²K).

Taking the $e_{31,f}$ value obtained before, we calculate the p_3^T coefficient to be -0,95µC/(m².K). This latest coefficient is defining the contribution of purely pyroelectric effect, without any piezoelectricity. We clearly see that the pyroelectric charges are essentially piezoelectric charges generated by the thermal expansion of the materials. Anyway, these

coefficients are very small compared to other pyroelectric materials like PZT (p_3^f of -268μC/(m²K)) or ZnO (p_3^f of -9,4μC/(m²K)) [155].

V.2 Dynamic Electrical Characterization

In the previous paragraph the material properties were characterized: the piezoelectricity and pyroelectricity. There is no influence of the geometry of the structure on the properties. This part is now dealing with the electro-mechanical response of the structure, how does it behave at high frequencies, what are the resonance frequencies of the different geometries. Two techniques are used: the impedance analyzer, which is measuring the electrical response of the device and the vibrometer, which measures the displacement of the membrane in response to a small signal excitation voltage. Then the results obtained with the two techniques are compared to modal and harmonic analysis realized by finite element simulations.

V.2.a Impedance Analyzer

The working principle of an impedance analyzer is the following: an AC voltage signal is applied on the sample and the voltage across and the current flowing through it are measured. From these two values the module and the phase of the impedance can be calculated. Some other parameters can also be deduced, like the admittance or the parallel capacitance and tanδ. These last two parameters are describing the dielectric behavior of the piezoelectric thin film. Indeed it is represented as a pure capacitor with a capacitance in parallel with a resistance. The loss tangent tanδ corresponds to the ratio of the imaginary over the real part of the dielectric constant of the material. It describes the energy loss in the insulator. At EPFL the Keysight 4294A was used. It has a frequency range from 40Hz to 100MHz.

V.2.a.1 Capacitance issue

The first measurements that were performed on the devices before the backside etching show very high losses values for our AlN thin film. Usually if the film is of high quality the tanδ value is around 0,1% at low frequencies and here we obtained values as high as 45%!

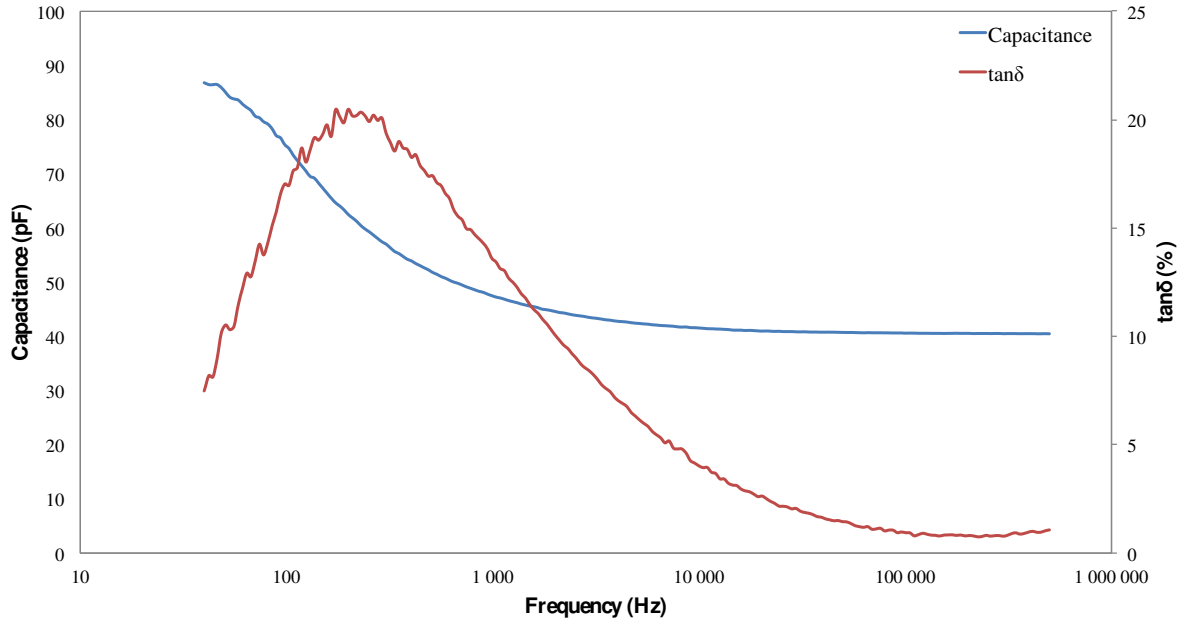

Figure V-10 C_p and tanδ values for a 1000x250 plate

As demonstrated before, the AlN film is of good quality in terms of crystallinity and piezoelectric coefficient. Two hypotheses might explain the high dielectric losses of the structure: a bad contact between the electrode and the film or parasitic capacitance through the silicon substrate. The contact between the electrode and the AlN film is good, the issue has been solved during the fabrication process: the photoresist left on the Pt electrodes after dry etching has been successfully removed. Which means that the high losses are due to a parasitic capacitance that is formed between the Pt electrodes and the silicon substrate. Indeed the charges of the parasitic capacitance are very mobile at low frequency but once we go higher in frequency the losses diminish drastically.

A simple model has been realized to calculate theoretically the capacitance of the device adding a parasitic capacitance as described before in parallel to the device capacitance. The piezoelectric layers (the active layer as well as the seed layer) are considered as simple capacitors because only their electrical behavior is concerned.

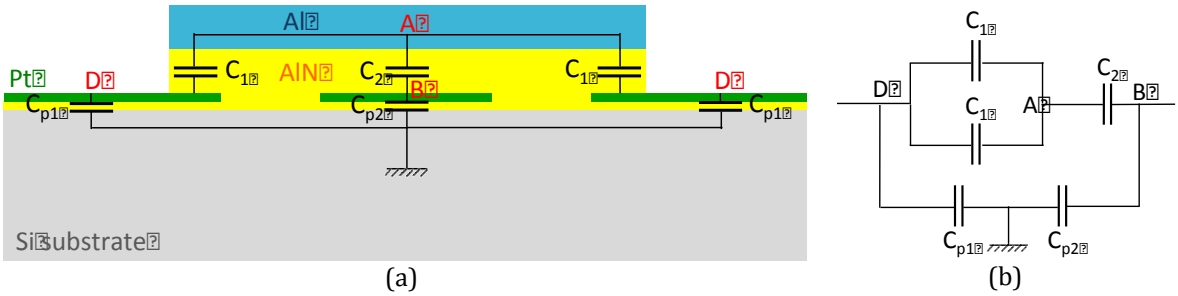

(a) (b)

Figure V-11 Schema of the cross-section of a device and the equivalent electrical circuit

All the capacitors are shown in Fig.V-11: the device capacitors and the parasitic capacitors. The equivalent electrical circuit is also presented, and the total capacitance is calculated:

$$C_{eq} = \frac{2C_1C_2}{2C_1 + C_2} + \frac{C_{p1}C_{p2}}{C_{p1} + C_{p2}}$$

$$C_{eq} = {}_0 {}_{AlN} \frac{1}{2}\frac{A_2}{t_{AlN}} + \frac{A_{p1}A_{p2}}{t_{seed}(A_{p1} + A_{p2})} \qquad \text{Eq. V-12}$$

where A_1 and A_2 are the active areas of the capacitance C_1 and C_2 respectively, with $A_1 = \frac{1}{2}A_2$; A_{p1} and A_{p1} are the active areas of the parasitic capacitance C_{p1} and C_{p2} respectively; t_{AlN} and t_{seed} are the thicknesses of the active AlN layer and the seed layer respectively and ε_{AlN} is the dielectric permittivity of AlN and ε_0 the vacuum permittivity.

Table V-4 Theoretical value of the capacitance for different devices

Structure	**1400x700**		**1000x250**		**2000x200**	
	No SiO_2	SiO_2	No SiO_2	SiO_2	No SiO_2	SiO_2
C_{device} **(pF)**	11,57		2,69		2,1	
C_{para} **(pF)**	102,54	7,42	77,46	5,6	81,34	5,88
C_{eq} **(pF)**	114,11	19	80,16	8,3	83,44	7,98

The Table V-4 presents the capacitance value for different structures:

- the capacitance of the device only C_{device}
- the parasitic capacitance only C_{para}
- the sum of the two as it is measured by the impedance analyzer C_{eq} between the points D and B of Fig. V-10.

The devices fabricated following the process flow described in the previous chapter don't have any oxide film under the AlN seed layer. In this case, the parasitic capacitance without SiO_2 is at least 10 times higher than the device capacitance for all the devices. The charges are then "trapped" by this large capacitance and that is the reason why the losses are very important. Moreover, the value of the equivalent capacitance corresponds more or less to the one measured experimentally.

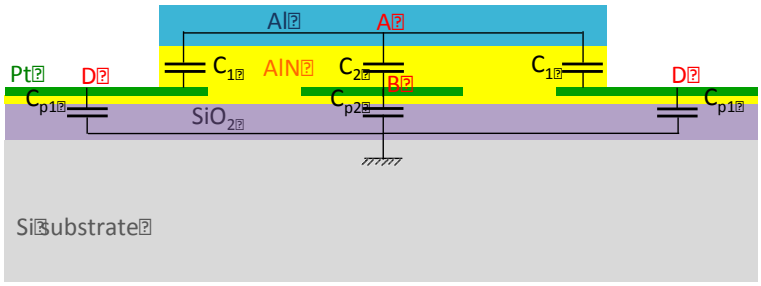

Figure V-12 Cross-section schematic with the thermal oxide layer

One solution to avoid the charges to flow through the silicon substrate is to have an insulating layer between the AlN seed layer and the substrate (Fig. V-12). The wafers are delivered with 1µm of thermal silicon oxide on both faces. The oxide on the front side can play perfectly the role of the insulation layer, and it will not modify much the process flow afterward. The only additional step will be to etch this front side silicon oxide at the end of the Bosch process. The parylene is still protecting the front side of the wafer and the same recipe as the one used to etch the backside silicon oxide can be used. Thanks to this SiO_2 layer the parasitic capacitance is drastically reduced.

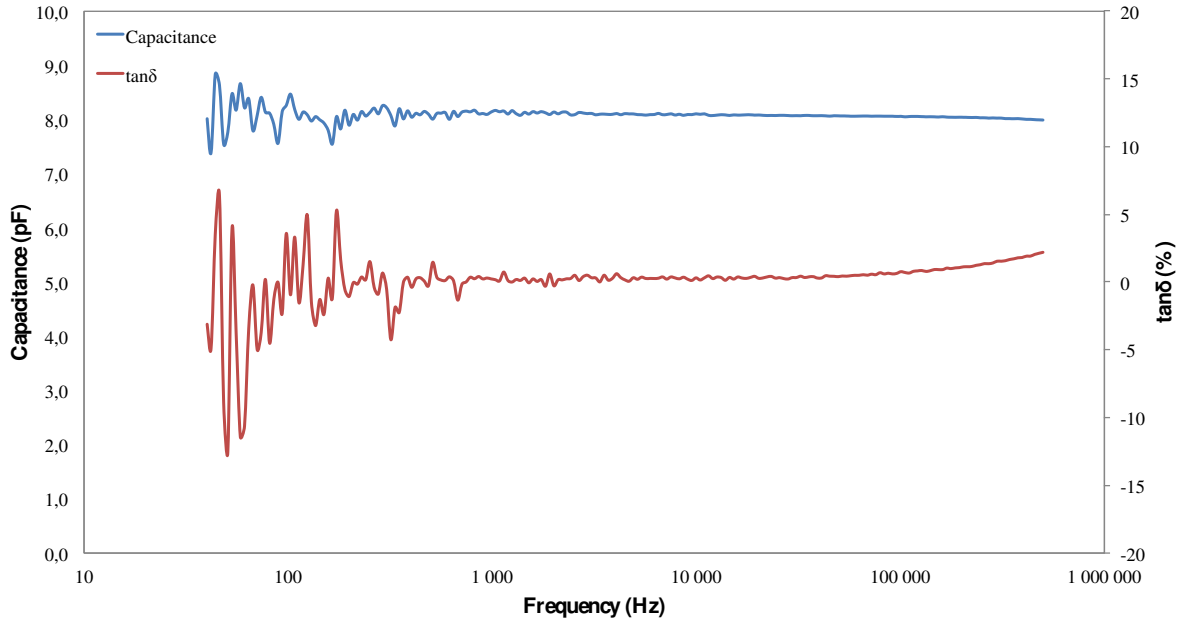

Figure V-13 C_p and $tan\delta$ values for a 1000x250 plate with silicon oxide

The measurements of the devices with the oxide layer on the impedance analyzer show a capacitance much more stable over 1kHz with a value around the equivalent capacitance calculated previously. The losses are also reduced at around 0,1% which corresponds to a

piezoelectric film of good quality. The very unstable values at low frequencies are due to the impedance analyzer.

The presence of the SiO_2 reduces the loss of charges through the silicon substrate. Indeed the permittivity of SiO_2 is 3,9 and the one of the AlN being 10; the parasitic capacitance is much lower. The charges produced by the piezoelectric layer will then be collected by the probes and not be trapped by the parasitic capacitance.

V.2.a.2 Resonance frequencies

The impedance analyzer is now utilized to measure the impedance of the devices and analyze the electro-mechanical resonances. The piezoelectric resonance occurs whenever the driving electric field frequency is equal to the natural mechanical resonance frequency of the piezoelectric device. As before a sinusoidal signal with low AC amplitude (around 0,5V) is applied on the device and the voltage and current on the electrodes are measured to deduce the impedance

For highly coupled material such as PZT, when a resonance is measured, the phase of the impedance is flipping from -90° to 90° very suddenly. The impedance module is minimum at the resonance frequency. As the AlN is not a strongly coupled material (effective coupling coefficient k^2 around 6% [98]) the changes in phase and module will not be so evident but peaks are clearly visible (Fig. V-14).

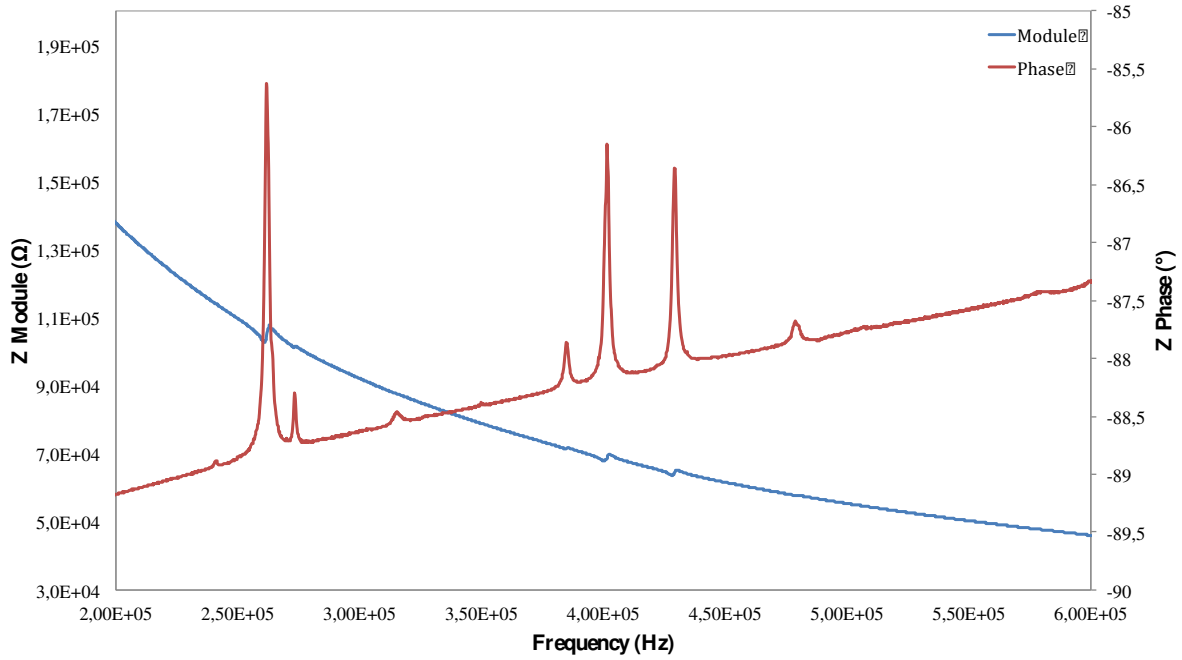

Figure V-14 Module and Phase of the Impedance of a 1400x700 plate (wafer 4715)

The impedance of the device Z is connected to other material parameters as the dielectric constant, the capacitance and the quality factor of the device. All these parameters are deducible from the measurements following the modified Butterworth-Van Dyke representation [117]. A capacitance C_0 and a resistance R_0 in parallel represent the electrical behavior of the material, the resistance corresponding to the dielectric losses. In parallel of the electrical part a series LCR circuit is modeling the mechanical resonant behavior of the device (Fig. V-15).

$$Y = \frac{1}{Z} = \frac{1}{R_0} + jC_0 \quad + \frac{jC_0}{1 \quad L_1 C_1 \quad ^2 + jR_1 C_1} \qquad \text{Eq. V-13}$$

A fitting using Matlab is then used to post-process the data. For a defined resonance frequency, the program will fit the curve representing the real part in function of the imaginary part of the impedance or admittance using the least squares method. From this fit and using the Butterworth-Van Dyke (BVD) model, it deduces the coefficients C_0, R_0, L_1, C_1 and R_1 of the device at this particular resonance frequency as well as the series resistance R_a.

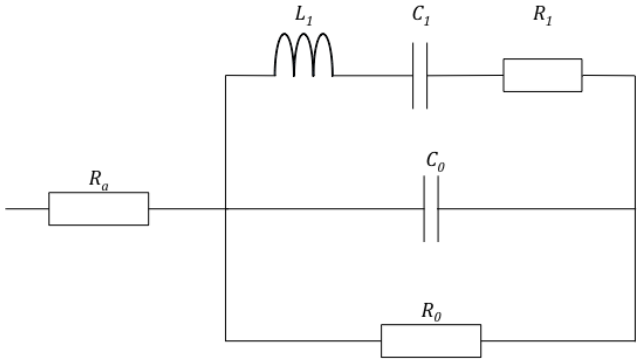

Figure V-15 Butterworth-Van Dyke electrical circuit representation for piezoelectric material

As for all resonant systems, the resonance frequency is defined when the imaginary part of the impedance of the mechanical branch (the only resonant part) is zero, which means:

$$f_s = \frac{1}{2 \quad \sqrt{L_1 C_1}} \qquad \text{Eq. V-14}$$

Experimentally, if the material has no losses and has a huge quality factor Q_m, the graph Im(Y) = f(Re(Y)) is a circle of radius $1/2R_1$ tangent to the y-axis. The resonant frequency occurs when the real part of the admittance is at a maximum. The quadrantal frequencies are the absolute maxima of the imaginary part of the admittance. All the parameters are graphically represented in Fig. V-16, where the experimental case of AlN is shown.

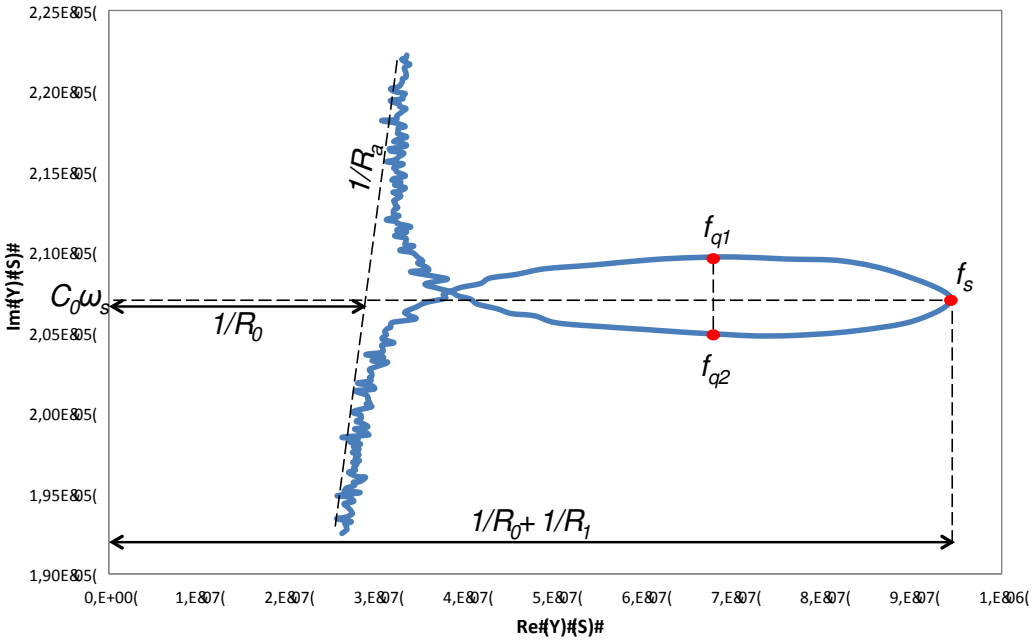

Figure V-16 Experimental determination of the BVD parameters.

From the resonant frequency f_s we can easily deduce the C_0, the imaginary part of the admittance at the resonance being equal to the product between C_0 and the angular frequency ω_s. With the value of the two quadrantal frequencies f_{q1} an f_{q2}, R_1 can be calculated knowing that the $Re(Y(f_s))$-$Re(Y(f_{q1}))=1/R_1$ and then R_0. The other model parameters can be calculated following these equations:

$$Q_m = \sqrt{\frac{f_{q1} f_{q2}}{(f_{q1} - f_{q2})^2}}$$
$$Q_m = \frac{1}{R_1}\sqrt{\frac{L_1}{C_1}} \qquad \text{Eq.V-15}$$

The different electrical parameters (C_0 and R_0) and mechanical parameters (R_1, C_1, L_1 and Q_m) are calculated for two different resonance frequencies and for different devices of a same wafer (0,5µm AlN / 0,5µm Al).

Table V-5 BVD parameters for different structures

	1000x250		**1400x700**		**2000x200**	
f_r (Hz)	677 240	983 670	284 800	480 060	118 320	294 680
R_a (Ω)	3420	3366	1087	1223	2719	2134

R_0 (Ω)	3,16.10^{-14}	4,92.10^{-14}	2,11.10^{-13}	1,04.10^{-13}	4,76.10^{-14}	1,07.10^{-13}
C_0 (pF)	5,65	5,68	20,97	21,03	7,98	7,93
R_1 (MΩ)	1,75	1,83	0,097	2,65	2,72	4,59
C_1 (F)	3,75.10^{-16}	1,49.10^{-16}	2,41.10^{-15}	1,69.10^{-16}	2,80.10^{-15}	3,79.10^{-16}
L_1 (H)	147	175	130	649	646	768
Q_m	396	593	245	738	177	310

Some issues were encountered while extracting the parameters, especially at low frequency. For a lot of samples, the value of the phase impedance were lower than -90° at frequencies lower than 100kHz. This means that the sample is considered as an inductance and not a capacitance and the model is becoming invalid. That's why there is no resonance frequency lower than 100kHz analyzed.

From the Table V-5, the capacitance C_0 is constant for a given sample size, whatever the resonance frequency is. The value corresponds also to the estimated value calculated in Table V-4.

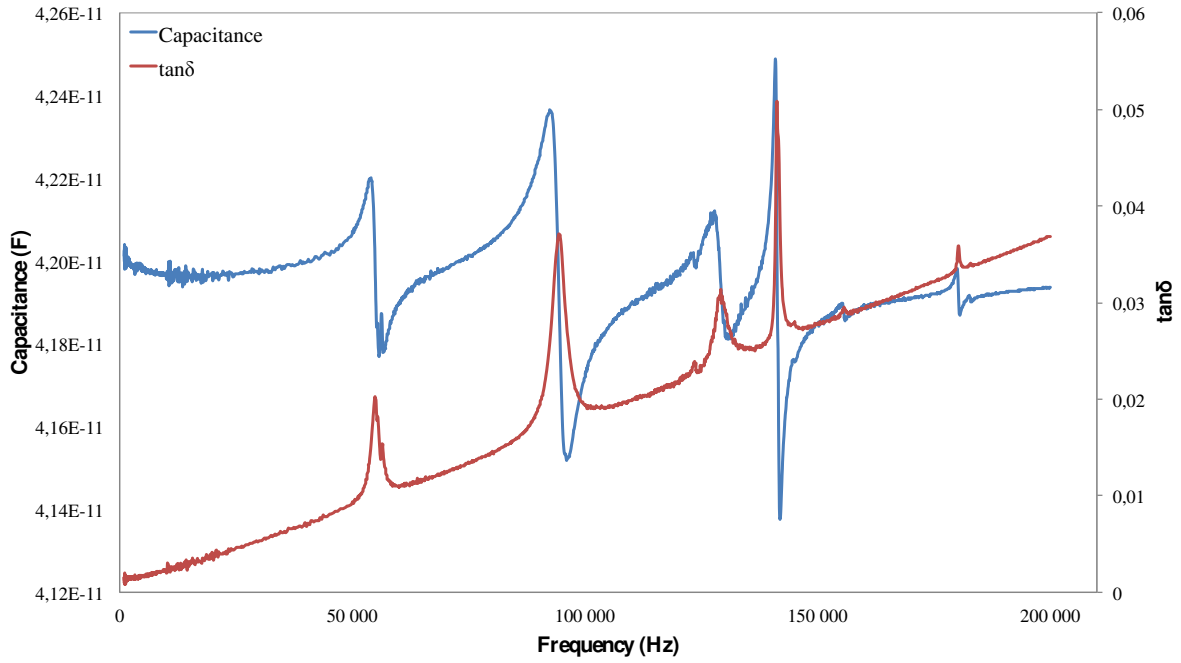

Figure V-17 Capacitance and $tan\delta$ of a 1400x700 plate (wafer 4795)

On Fig. V-17 is presented the whole frequency spectrum of a 1400x700 plate with multiple resonances on a frequency range from 1kHz to 200kHz. The graph represents the capacitance and the dielectric losses because the resonances are more visible than with the phase and

module of the impedance. The $tan\delta$ value, 0,001 at 1kHz, is increasing proportionally to the frequency. This indicates the presence of a resistance series R_a on Fig. V-15.

No resonance frequency was observed under 50kHz. The first one, at 54,9kHz, corresponds then to the first visible mode. The other peaks are at 94,4kHz; 129kHz; 141,2kHz; 153,7kHz and 180,22kHz respectively.

V.2.b Vibrometer

The devices are now analyzed with a Vibrometer OFV 3001 from Polytec. It is measuring the velocity of a reflective moving surface thanks to a laser split into two beams and a Doppler interferometry. In this case an AC voltage tuned in frequency is applied to the electrodes of the structure and the velocity of its surface is measured. When the applied voltage is close to a resonance frequency the velocity of the vibrating membrane should increase. The difference between this characterization method and the LCR lies in the fact that with the vibrometer we measure directly the mechanical response of the membrane while with the LCR we measure the electrical response. Theoretically, with the LCR, all the resonant modes are visible, if the materials is enough coupled, while with the optical method only the modes having an amplitude where the laser is focused onto.

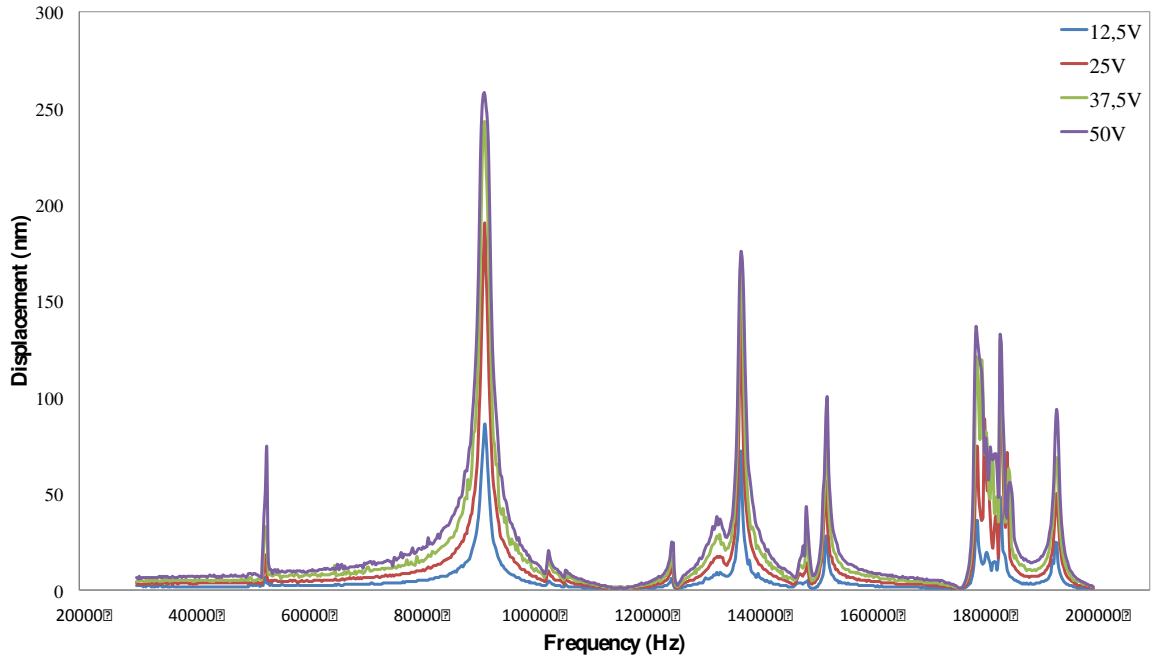

Figure V-18 Displacement under different voltage amplitude of a 1400x700 plate

The same device tested in LCR is now observed under the vibrometer: a 1400x700 plate with 0,5µm of AlN and 0,5µm of Al. Its mechanical response is presented in the Fig. V-18 for different actuation voltage amplitude. The vibrometer is measuring directly the velocity of the surface, so we converted this velocity into displacement, dividing the velocity by the angular frequency ω. Much more peaks are observed than in LCR, but all the peaks observed in LCR are visible in the vibrometer at the same frequencies.

Table V-6 Resonance frequencies of LCR and Vibrometer

LCR f_r (Hz)	54943	94475	-	-	129000	-	141260	-	153670	180220
Vibrometer f_r (Hz)	53015	91959	103417	105125	125125	133165	137437	147990	152512	183417

The Table V-6 sums up all the resonant frequencies observed on both the LCR and vibrometer. One possible explanation that more modes are visible on the vibrometer compared to the LCR-meter might be the electrode geometry does not fit to the mode symmetry, thus cancelling the piezoelectric response, but that is nevertheless excited. In other words, actuating the membrane electrically will make it move so we will detect all the modes (flexural and torsional) where the focus point of the laser is moving. In contrast, the variation of the impedance or capacitance at resonance for weakly coupled modes might not be enough to be detected.

V.2.c Comparison with Finite Elements Simulations

The experimental results obtained in the two previous paragraphs are now compared to finite elements simulations performed on ANSYS. The 2D geometrical model is the same as in Chapter III, we used the SHELL181 layered element, to which we applied the equivalent stress from the experimental stress values.

As in Chapter III, a first static analysis is performed in order to initially deform the structure, and then the analysis is restarted to perform a modal analysis through the “perturb” option, which allows us to use both the non-linear geometry option (nlgeom) and the prestress option (prestres) in the first static analysis. The first resonance frequency obtained in finite elements is situated at 21,086kHz, which corresponds to the first flexural mode shape. The closest resonance frequency from the experimental value is at 52,178kHz and corresponds to the seventh mode as illustrated in Fig. V-19. Increasing the effective stress from -47MPa to -90MPa, the first resonance frequency goes up to 28,842kHz and is a torsional mode, but the

closest resonance frequency from the experimental value is at 55,33kHz and corresponds to exactly the same mode shape.

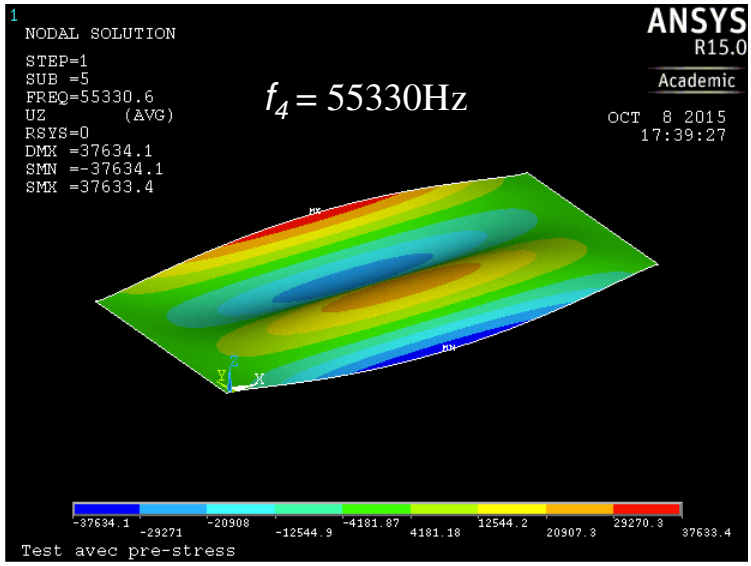

Figure V-19 Shape mode corresponding to the experimental first resonance frequency observed.

Even when the effective stress value is twice higher than the experimental value, the same mode shape is observed around the first experimental frequency value. It seems that the residual stress does not affect this mode in particular. The resonant modes at lower frequencies are not visible experimentally, maybe because of the design of the electrodes that does not allow us to see them.

These finite element simulations give an overview of the possible mode shape of the structure as well as its resonance frequencies. But it is limited to the fact that only uniform stress can be applied to the anchor of the plate. Indeed maybe for the same effective stress, but with a different distribution of the stresses between the layers, the resonance frequencies and/or the shape modes would be totally different. Only a 3D model can perform this kind of analysis.

V.3 Mechanical Excitation

In order to have the pure piezoelectric signal of the structure during the buckling, one way is to cause the buckling by pushing mechanically the membrane. We conceived a setup constituted by a piezoelectric actuator from Noliac, which can be displaced in the three directions and a chuck holding the wafer. To be able to both contact the structures on the front side and actuate them from the back side, the wafer is positioned vertically as shown in the

schematic of Fig. V-20 - 21. On one side of the sample we have the actuation part with the wave generator that drives the amplifier, which is powering the multilayer piezoelectric actuator. An insulating tip is fixed at the end of the piezoelectric stack, thin and long enough to pass through the backside holes to reach the membrane.

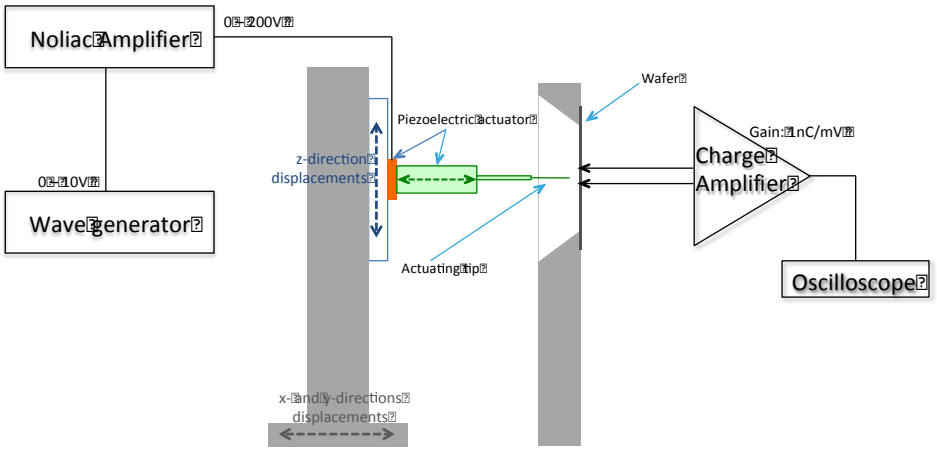

Figure V-20 Schematic of the mechanical actuation setup with the charge amplifier

Two micromanipulators are contacting the Pt electrodes on the front side and the charges are collected in two different ways:

- a charge amplifier (Brüel & Klær type 2634) with a gain of 1nC/mV,
- an instrumentation amplifier (Burr – Brown INA116) with an adjustable gain and a variable load resistance placed in parallel of the two inputs.

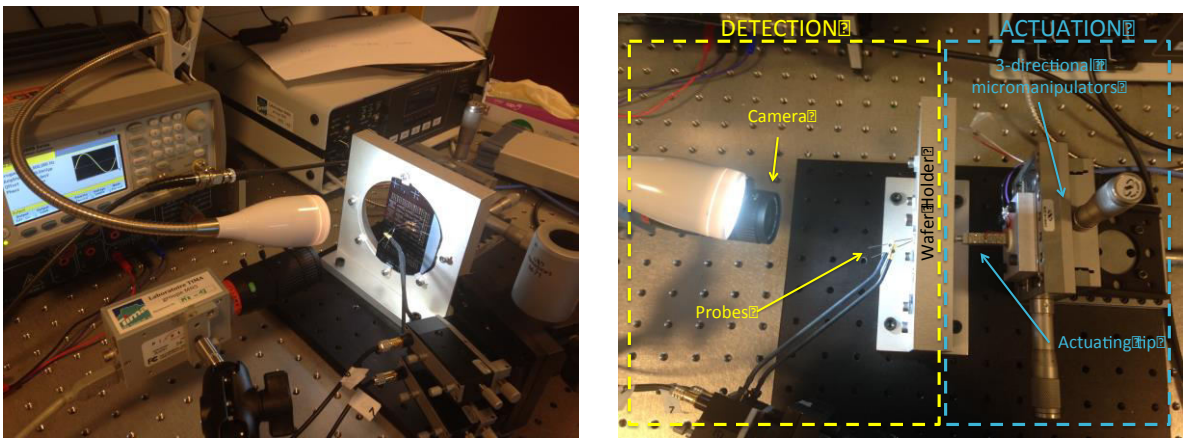

Figure V-21 Images of the mechanical actuation setup

The choice of the instrumentation amplifier is crucial due to the very low electrical signals expected and also the very short and quick signal to be detected during the snapping of the

membrane. The INA116 is well suited to our application, it has an ultra low input bias current of 3fA typically, and the bandwidth for a gain of 1 is 800kHz, and for a gain of 10 it is 500kHz.

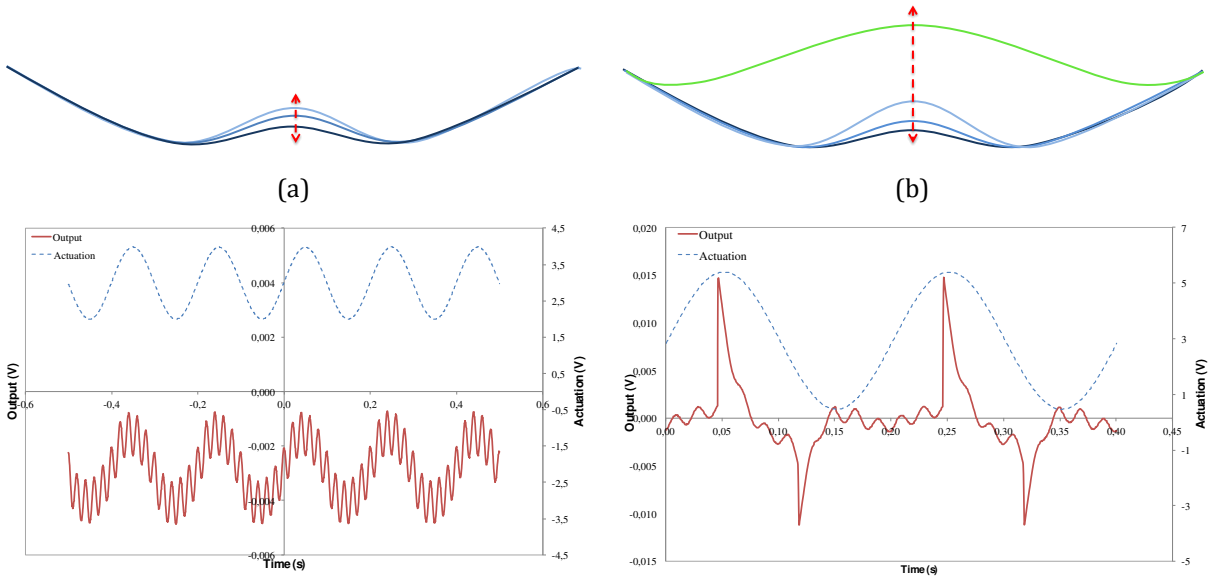

Figure V-22 Schematic of the cross-section displacement and output voltage with a charge amplifier of a 1400x700 structure

A 1400x700 membrane with 0,5µm of AlN and 0,5µm of Al was tested with a charge amplifier as described before with a sinusoidal actuation of the mechanical tip at 5Hz. The sinusoidal signal on the graph of Fig. V-22 c and d represents the driving voltage of the amplifier. The minimum value of the sinus corresponds to the position where the tip is just in contact with the membrane, and the maximum value to the position where the tip is pushing the most the membrane. On the Linear Displacement graph, the driving voltage corresponds to a displacement of the tip of 10µm and for the Buckling graph the displacement is 20µm. The initial deflection of the membrane is of 7µm, so the displacement furnished during the linear displacement is not sufficient to induce the mechanical instability of the structure. While with a higher displacement of the tip, the limit of stability of the structure is reached and the curvature of the membrane change suddenly. At this moment the tip is pushing so much the membrane that the whole plate is buckling. This second position is mechanically stable only due to the contact with the tip in the center, so the membrane is going back in its initial position by buckling back when the tip is going backward.

With the charge amplifier the device is virtually short-circuited to be able to measure the electrical charge flow generated by the piezoelectric layer during the buckling. By replacing the

charge amplifier by an instrumentation amplifier we measure directly the voltage generated by the AlN layer. The output peak is much quicker than with the charge amplifier due to a higher cutoff frequency. But there is one more parameter to tune: the load resistance, in order to maximize the power.

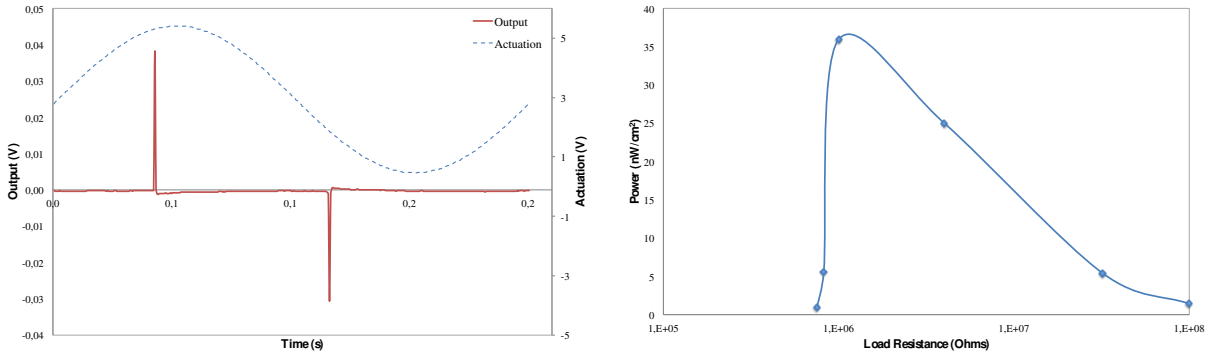

(a) Output Signal during buckling (b) Output Power

Figure V-23 Output signal (a) with a load resistance of 1MΩ and the Output power (b) in function of the load resistance

In order to determine the optimal load resistance, the power furnished by the device has been calculated for several values of resistance (Fig. V-23). The average power during one peak corresponds to the following formula:

$$P_i = \frac{1}{T}\int_T \frac{u^2(t)}{R_{load}}dt \qquad \text{Eq. V-16}$$

Where $u(t)$ is the voltage measured, R_{load} is the load resistance and T is the integration period. The optimum power is obtained for a resistance of 1MΩ. From now on, all the measurements will be done using this optimal load resistance value.

The rectangular structure measuring 1400x700 furnishes a mean value of the average power per peak of 3,3nW/cm² when the tip is actuating the membrane at 5Hz. We can also calculate the energy generated by peak (averaged over 8 to 12 peaks) and then multiply it by twice the frequency of actuation, as there is two peaks per cycle. The energy is calculated using the following formula:

$$E = \int_T \frac{u^2(t)}{R_{load}}dt \qquad \text{Eq. V-17}$$

The product of the energy per peak and the frequency gives then an estimation of the power harvested by the functional device. For the same structure and the same actuating conditions,

the average value of the power harvested by the device is 0,19nW/cm², which is much lower than the instantaneous power per peak calculated before.

Table V-7 Evolution of the Instantaneous power and Power over frequency

Frequency	5Hz	10Hz	20Hz	30Hz
Average Power per peak (nW/cm²)	3,3	16,7	48,1	41,5
Energy per peak (pJ/cm²)	19	28	36	32
Power (nW/cm²)	0,19	0,57	1,45	1,94

The frequency of actuation of the tip is then increased to observe the behavior of the device over frequency. The Table V-7 sums up the values of Instantaneous Power and Power calculated. As noticed at 5Hz, the instantaneous power is always one order of magnitude higher than the power. They are both increasing until 20Hz, but at 30Hz, the instantaneous power is slightly decreasing while the power is still increasing to reach nearly 2nW/cm². One could think that if the structure is able to thermally buckle at a higher frequency the harvested power will continue to increase.

V.4 Thermal Actuation

The devices have been actuated mechanically and the pure piezoelectric signal and power have been calculated. In order to have a real signal that could be harvested by the final devices, it is necessary to include the temperature and to thermally buckle the structures. The first method tested is to heat up the structure by Joule effect. A voltage is applied between two platinum pads that are connecting the central electrode. It is providing a local heating and if the voltage applied is a rectangular signal, we could alternate the heating time and cooling time by applying a signal between 2V and 0V for instance. The second method consists in putting the devices on a hot plate and to contact the electrode until the buckling happens. The heating is more homogeneous throughout the device but we cannot alternate heating and cooling period as quickly as with the Joule heating.

V.4.a Joule Heating

Due to the Pt electrodes configuration, it is possible to heat up locally the membrane by applying an electrical current (or voltage) across two pads that are connected under the device by the central electrode (Fig. V-24). The two thinnest parts are the most resistive parts and are heating the most. A rectangular signal was applied across the electrodes to simulate the heating phase (+2V) and the cooling phase (0V). The membrane was moving and buckling with the temperature change, and the following electrical signal was observed (Fig. V-23).

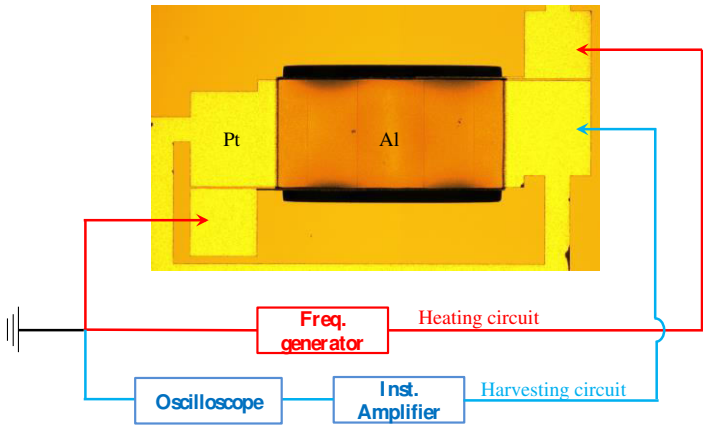

Figure V-24 Schematic of the Joule heating setup

In order to be sure that the signal is due to piezoelectric charges and not to some parasitic capacitance charges, we changed the sign of the applied voltage. This means that during the heating period we applied -2V and during the cooling period 0V as before. As the heating power is proportional to the square of the voltage, it should deliver the same power applying a positive and a negative voltage. The output signals should be the same in both configurations.

The images of Fig. V-25 are showing a 2000µmx200µm device contacted by two micromanipulators which are applying the heating current. The upper one is the structure just before the buckling, and the lower one the same structure after the buckling. The typical output signal obtained for this kind of Joule heating is presented on the graph of Fig. V-23c. The output voltage corresponding to the two types of heating, positive applying +2V and negative applying -2V, is shown. For a same phase, heating or cooling, the peaks are of opposite signs. The sign of the peaks are corresponding to the sign of the slope of the actuation voltage. For instance in the case of a negative heating, the transition between the heating and cooling phases corresponds to a positive slope, which is the sign of the peak. The same observation can be made in the case of a positive heating.

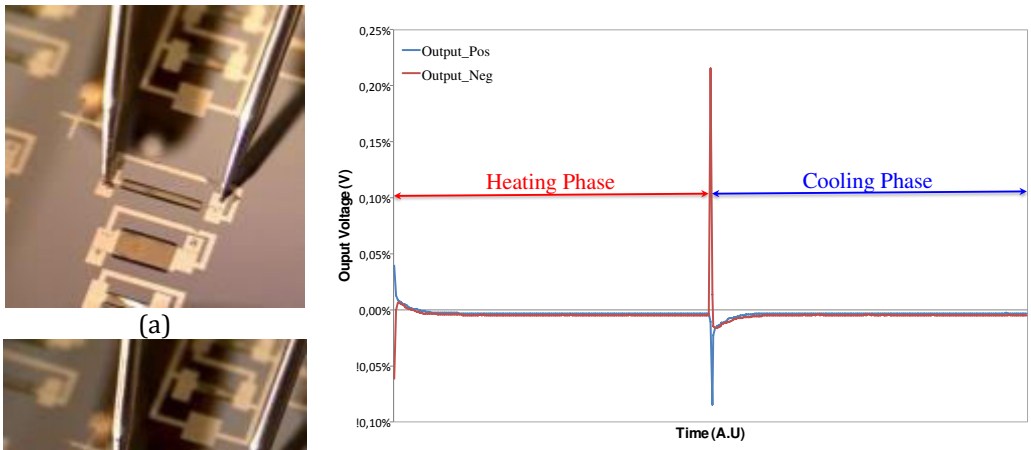

Figure V-25 Image of a 2000x200 plate before (a) and after (b) buckling and the typical output signal (c) obtained with an instrumentation amplifier.

The output signals are by consequence not piezoelectric charges but only parasitic signal. It is due to the fact that we use the central electrode to both heat up and collect the charges generated. Indeed the central electrode is polarized because the two small Pt paths connecting the electrode to the pads are acting as a voltage divider. Even if we apply +/-2V, the polarization on the electrode is +/-1V, which is largely over the expected piezoelectric signal seen during the mechanical actuation. At this moment, this method does not allow us to see correctly the charges generated by the thermal buckling of the structure.

V.4.b Hot Plate Heating

Another method to avoid the heating by Joule effect and the parasitic signals is to directly put the entire wafer on a hot plate. The wafer and the device are homogeneously heated, but the thermal cycles are very slow, one has to wait for the hot plate to cool down. But we have a more precise idea of the temperature of the structure that causes the buckling up and the buckling down. We tested different structures (1400x700 and 1000x250) with both the charge amplifier and the instrumentation amplifier. The structures are contacted in the usual way, between the central electrode and the two electrodes at the anchors. The stresses measured in the different layers are the following:

- AlN seed-layer and Pt: 230MPa (tensile)
- AlN active layer: -410MPa (compressive)
- Al top layer: 150MPa (tensile)

Table V-8 Thermal buckling temperatures and power density

	Electrode Surface (cm^2)	Temperature Snap Up	Energy (pJ/cm^2)	Charges (pC)	Temperature Snap Down	Energy (pJ/cm^2)	Charges (pC)
1400x700	$5{,}12.10^{-3}$	114°C	13	3,3	82°C	30	4,1
1000x250 – a	$0{,}96.10^{-3}$	72°C	5	1,37	46°C	1	1,23
1000x250 – b		89°C	5	1,3	53°C	3	1,28
1000x250 – c		105°C	2	1,26	59°C	2	1,18

The Table V-8 sums up the different buckling temperatures of a structure 1400x700 and three different structures 1000x250 connected in series. Unfortunately the slightest change in the curvature of the devices changes drastically the buckling temperature. The 1000x250 structures, even connected in series are not buckling at the same temperature, so their piezoelectric buckling peaks cannot add to increase the output power.

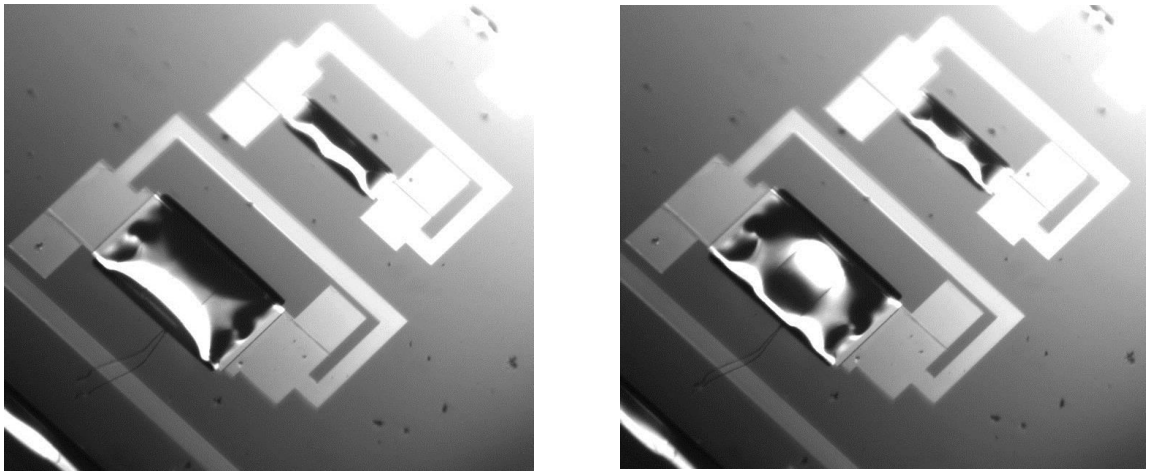

(a) (b)

Figure V-26 Images of a 1400x700 and 1000x250 plates before (a) and after (b) thermal buckling

The thermal hysteresis is very interesting. For the 1400x700 structure, it is of 32°C, and for the three 1000x250 it is respectively 26°C, 36°C and 46°C. Different cycles were performed on these structures and the buckling temperatures are varying of 5°C around the value presented here. But the value of the hysteresis remains exactly the same in all the cycles. This shows that the buckling temperatures can vary due to change in ambient temperature and not

exactly the same thermal conditions as before, but the hysteresis, which is depending only on material properties and geometry, is not varying.

The instantaneous power density during the buckling of the 1400x700 is 0,18µW.mm^{-3}, which is comparable with the values of Defosseux (0,28µW.mm^{-3}) and Marzencki (0,11µW.mm^{-3}) [26] which are using also AlN thin films for vibration energy harvesting. The average power of the devices could be calculated but would not signify anything on the real capacity of the device to furnish power regularly. Indeed to provoke the snap back of the sample, the hot plate is only switched off and its cooling down is very slow. The calculated average power would be very low. In a future work the conception of a complete thermal setup enabling the quick heating up and cooling down of the structure is planned, with a precise control of the temperature of the device.

V.5 Improvements: new geometries

The rectangular structures fabricated and characterized before are functional as thermal harvester, but the thermal hysteresis of buckling, i.e. the difference between the snap up and the snap down temperatures is relatively high. In order to improve the sensitivity of the device, it is necessary to decrease this hysteresis. We have shown that the rectangular structures present a longitudinal curvature but also a transverse curvature to form a kind of "boat" shape. This is due to the non-homogeneous distribution of the stress in the length of the plate. One possible solution to decrease this inhomogeneity is to design and fabricate devices based on the principle of tapered beams. In [156] and [157] showed that for a cantilever beam with a proof mass, the tapered shape is making the stress more homogeneous in the structure, and by consequence increase the output power for the piezoelectric energy harvesters.

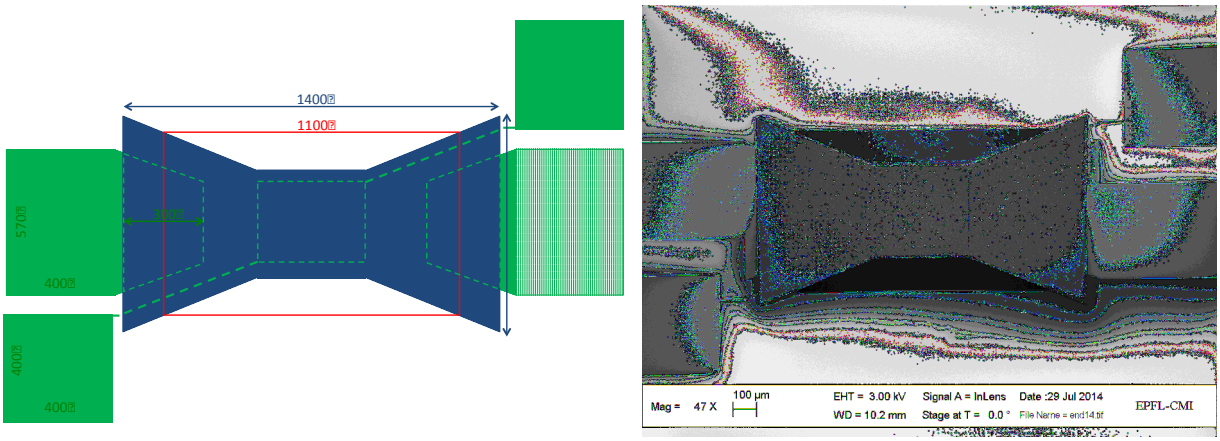

(a) (b)

Figure V-27 Schematic (a) and SEM image (b) of a butterfly structure with an angle of 24°

The butterfly structures were realized with two different lengths: 2000µm and 1400µm, each of them with three different aperture angles: 12°, 24° and 45°, in order to vary the width ratio between the anchor and the end of the triangular part of the plate. In Fig. V-27 is shown a schematic and an SEM image of a butterfly structure 1400µm long with an aperture angle of 24°. After fabrication, the transverse curvature is still present, but the major effect of the butterfly shape is on the mid-point deflection: for the same length, for instance 1400µm, the deflection decreases for the butterfly shape compared to the rectangular one, and the higher is the aperture angle, the smaller becomes the mid-point deflection. Moreover, the buckled shape of the plate is modified. For the rectangular plate, the boundary conditions are clamped so the buckled shape is curved all along, while for the butterfly plate, the deflection is the center is flattened, which reveals that the boundary conditions are not completely clamped anymore, but more hinged. The residual moments are then flattening the curvature in the central part, as shown in [51].

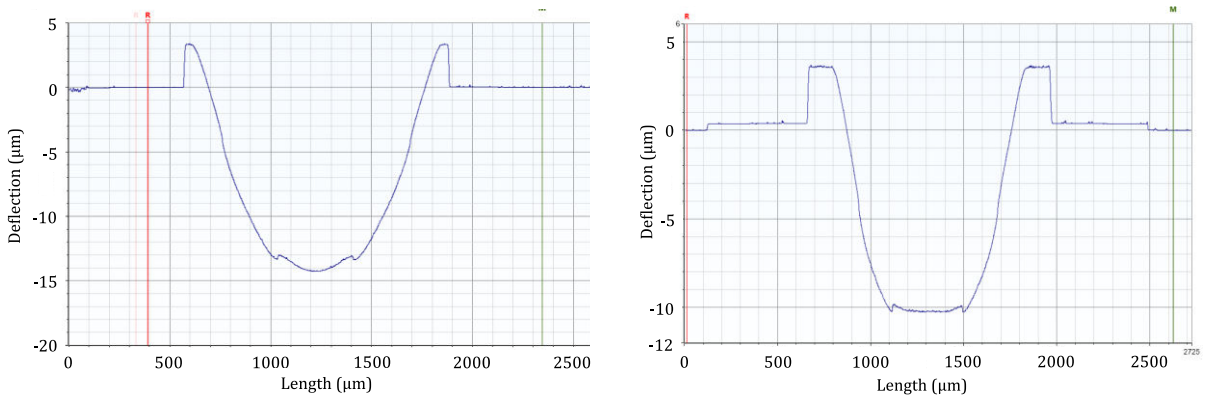

(a) (c)

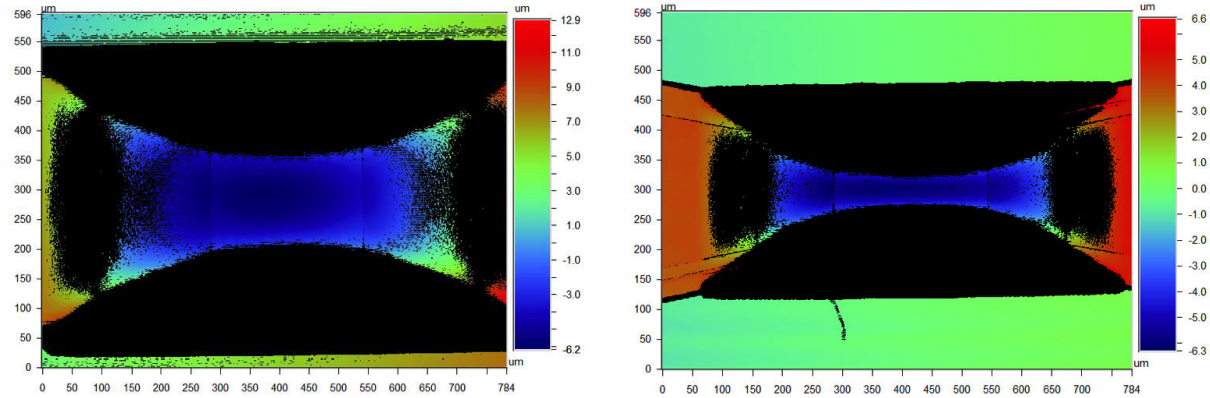

(b) (d)

Figure V-28 Mechanical and optical profilometer images of a 1400x700 plate ((a) and (b) resp.) and of a butterfly 1400 – 12° ((c) and (d) resp.)

The example of Fig. V-28 is taken from a structure with 1µm of AlN and 2µm of Al. The rectangular plate 1400x700 presents an initial mid-point deflection of 14µm, while the butterfly structure, 1400µm long with an angle of 12° presents a deflection of 10µm, which means a diminution of nearly 30%. The optical profilometer shows that the transverse curvature is still present on the butterfly structure. But the flattening of the curvature on 400µm in the center of the plate is clearly visible on both optical and mechanical profilometer images. The mid-point deflection for 24° and 45° aperture angles is respectively 8µm and 7µm.

The structures were analyzed the same way as the rectangular ones. Measurements on the LCR-meter and on the vibrometer are performed to investigate the resonance frequencies. Then the butterfly plates are placed on a hot plate to get the output power of the devices when they are thermally buckling. The buckling temperatures (snap-up and snap-down), especially the hysteresis are measured and compared to the rectangular structures.

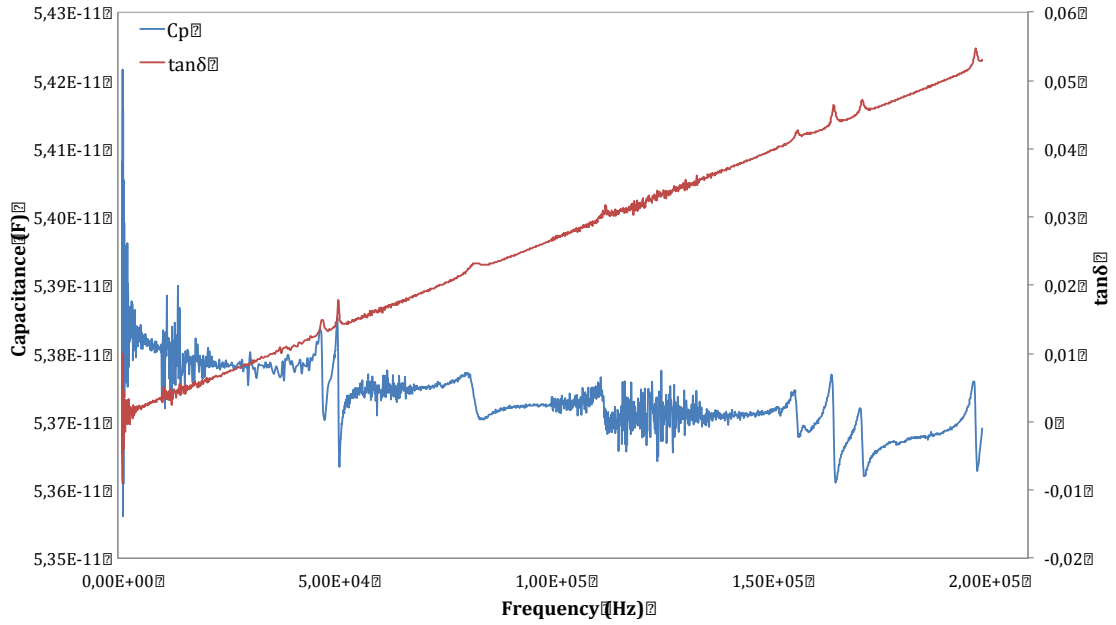

(a)

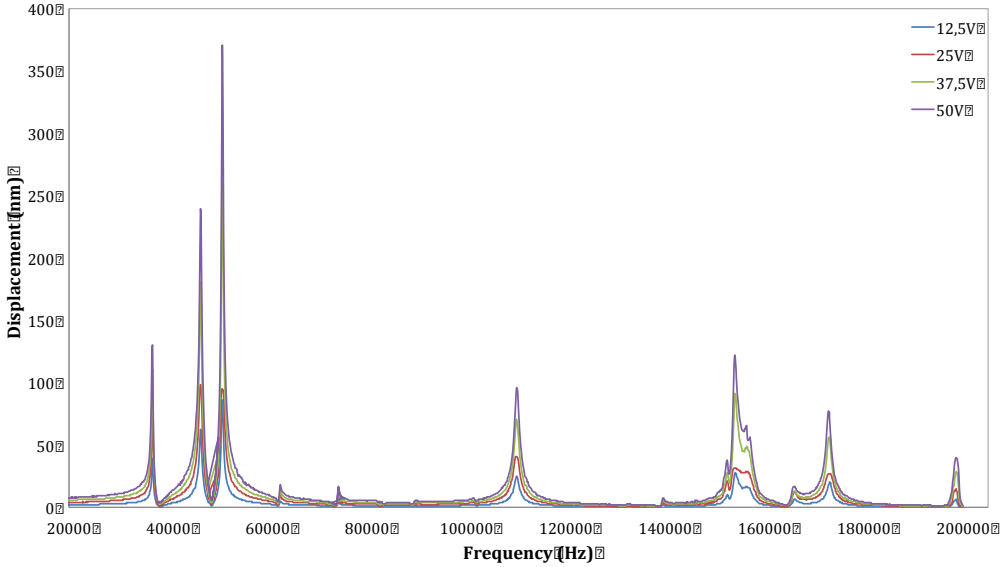

(b)

Figure V-29 LCR-meter (a) and vibrometer (b) analysis of a butterfly 2000 - 45° plate

In Fig. V-29 are presented the measurements on LCR-meter and vibrometer of a butterfly structure, 2000µm long and 45° of aperture angle, with 0,5µm of AlN and 0,5µm of Al. The LCR measurement is showing the evolution of the parallel capacitance C_p and the dielectric losses $tan\delta$ while applying a small AC voltage to the structure on a frequency range. The vibrometer is showing the displacement of the structure while applying high amplitude AC signal on the same frequency range as for the LCR. The resonance frequencies are summarized in Table V-10. We can observe a good correlation between the frequencies measured in LCR-meter and vibrometer, even if, as for the rectangular structure, more resonance frequencies are observed in vibrometry. Larger displacements at lower frequencies are observed for the butterfly structure compared to the rectagulare one. This is due to the less constrained boundary conditions.

Table V-9 Resonance frequencies on LCR and vibrometer for a butterfly 2000 – 45°

LCR f_r (Hz)	46335	50909	-	-	107400	-	156890	165220	171820	198050
Vibrometer f_r (Hz)	46482	50879	62487	74246	110175	152512	154145	166080	173115	198492

The butterfly structures were then tested to investigate their thermal harvesting capabilities. As the rectangular structures, they are put onto a hot plate with a thermocouple to measure the temperature and probes to harvest the electrical charges produced during the buckling.

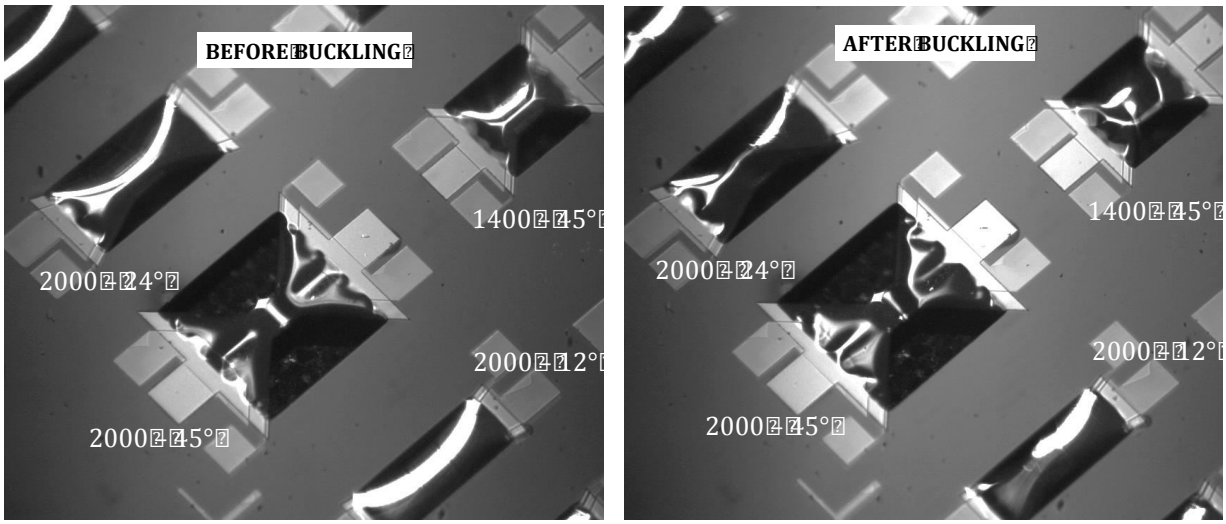

(a) (b)

Figure V-30 Images of butterfly structures before (a) and after (b) thermal buckling

The buckling shapes of different butterfly structures are represented in Fig. V-30. For the structures 2000-12° and 2000-24°, the buckling seems to be of the first order, which means that the maximum displacement occurs at the center of the plate and it is the only maximum of the plate. Whereas for the 2000 – 45° and also 1400 – 45°, the buckling is more complicated and seems to occur mostly on the anchors without changing the curvature of the central part of the plate.

Table V-10 Buckling temperatures and energy generated by butterfly structures

	Electrode Surface (cm^2)	**Temperature Snap Up**	**Energy (pJ/cm^2)**	**Temperature Snap Down**	**Energy (pJ/cm^2)**	**Thermal Hysteresis**
1400x700	$5{,}12.10^{-3}$	114°C	13	82°C	30	32°C
1400 – 12°	$2{,}3.10^{-3}$	87°C	0,15	85°C	2,32	2°C
1400 – 24°	$2{,}5.10^{-3}$	93°C	0,61	86°C	1,98	7°C
1400 – 45°	3.10^{-3}	100°C	3,27	90°C	13,67	10°C

The buckling temperatures of the butterfly structures are very interesting, especially the hysteresis. Indeed we can see that for a rectangular structure with the same length, the hysteresis is of 32°C, while for the corresponding butterfly structure, the hysteresis is of 2°C for the 12° aperture, 7°C for the 24° aperture and 10°C for the 45° aperture. The temperature of buckling is lower than the rectangular structure for all the butterfly plates, but increases with

the increase of the aperture angle. The same observation can be made for the hysteresis: it is always lower than for the rectangular plate but is increasing with the increase of the angle.

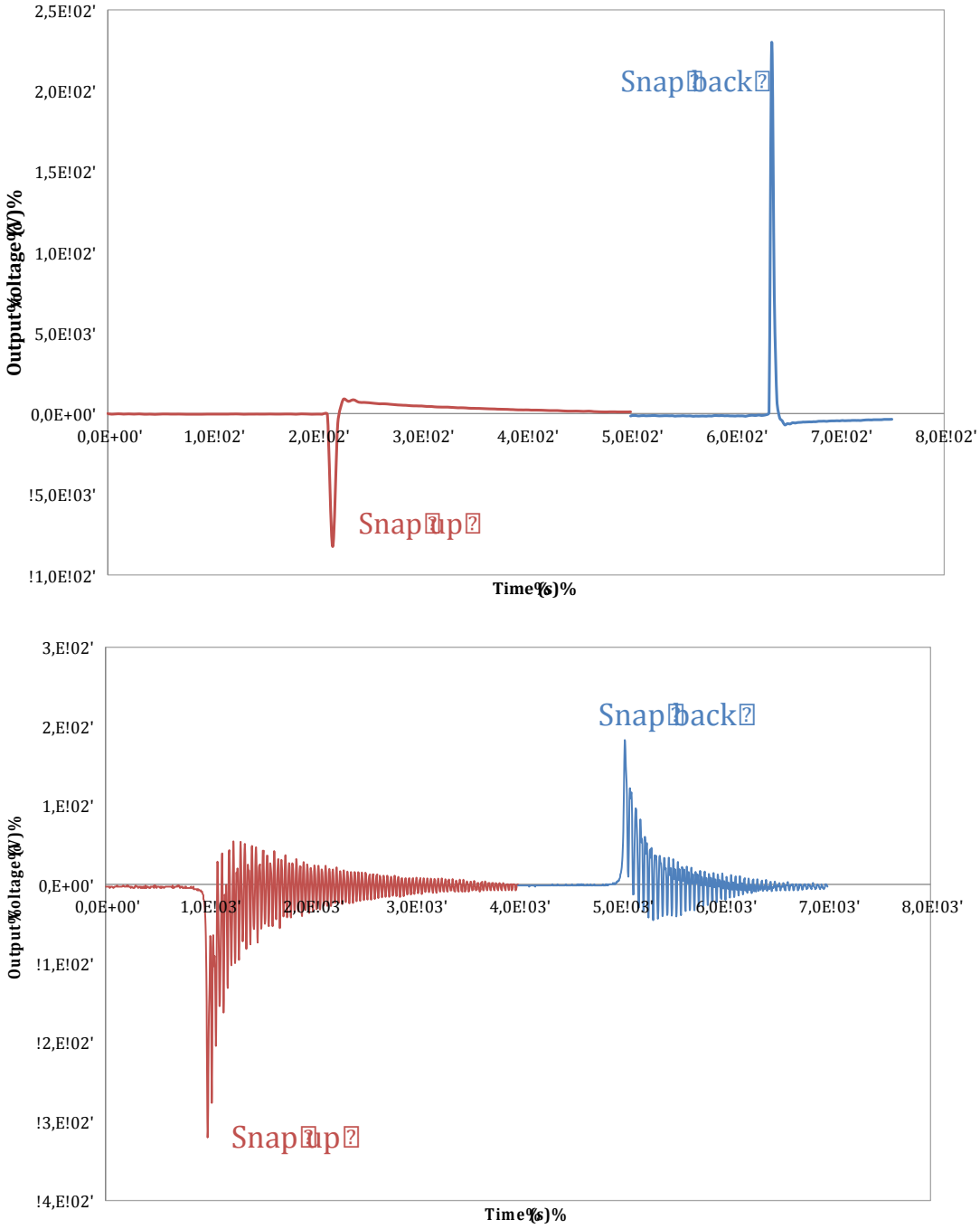

Figure V-31 Output signal of a butterfly 1400 – 45° plate (a) and butterfly 2000 – 12° plate (b)

The output signal of the devices is collected with an instrumentation amplifier with a load resistance of 1MΩ, which is not an optimized value. Moreover, for the butterfly structure 2000 – 12°, during the snap up and snap back, we don't observe a single electrical peak but oscillations as shown in Fig. V-31. When buckling, the structure is vibrating at its natural frequency, which is

22kHz. This is a very promising structure and we can expect an increase of the output power due to the oscillations. For this specific structure we obtained 4,77pJ.cm^{-2} for the snap up and 1,83pJ.cm^{-2} for the snap back, which is comparable to the values obtained before.

The butterfly structures are very promising devices. We have demonstrated that the butterfly shape is softening the boundary conditions of the plate, rendering them not completely clamped. This is reducing the mid-point deflection and flattens the curvature in the central part of the plate. As their initial deflection as well as their mechanical constraints is reduced, their buckling temperature is also lower compared to a rectangular structure with the same length. They have reduced thermal hysteresis, which can make them very sensitive and suitable for industrial applications.

V.6 Conclusion

In this chapter we presented the characterization means used to evaluate the initial deflection of the devices as well as its distribution over en entire wafer. The quality of the piezoelectric film in terms of orientation and piezoelectric coefficients is discussed. The $e_{31,f}$ coefficient is evaluated in two different ways and its value is closed to the best value of the literature. The pyroelectric response of the AlN thin film has been analyzed. Finally the electro-mechanical behavior of the structures is presented. The resonance frequencies observed electrically and optically are coherent, even if some modes are not visible electrically. Then the plate is actuated mechanically to observe its response without involving the temperature, which is giving the pure piezoelectric signal during buckling. We manage to get 1,94nW.cm^{-2} for a plate measuring 1400µm by 700µm at 30Hz. Finally the same structure is actuated thermally and generated up to 30pJ.cm^{-2} in one peak. The temperature difference between the snap up and snap down of the structures is relatively high, from 28°C up to 46°C depending on the geometries. In order to decrease this hysteresis, new geometries were fabricated with a butterfly shape. For an equal length, the hysteresis is decreased down to 10°C or less. These structures, having less rigid anchors, are very promising, especially in terms of aging. Indeed the stresses are reduced at the anchors because they are better distributed along the length and the butterfly devices are expected to be more reliable in time.

Conclusions and Perspectives

The work presented in this PhD manuscript is centered on the thermal energy harvesting at microscale, combining thermo-mechanical transduction by way of the thermal buckling of a bilayer plate and piezoelectric transductions. The aim of the project is to downscale a macro-prototype using CMOS compatible processes.

We have conceived, fabricated and characterized micro energy harvesters based on AlN/Al bilayer plates. The processes are standard micro-machining processes used in MEMS technologies. The fabrication was realized entirely in the Center of Micro-nanotechnology from EPFL, from the writing of the photolithography masks to the final liberation of the structures. Different rectangular geometries were fabricated and characterized. The initial curvature of the device is controlled and tuned only by the deposition parameters. Cantilever test structures have been fabricated to characterize the piezoelectric thin film in order to be able to compare the results to the literature. The AlN film has an $e_{31,f}$ of $1 C.m^{-2}$ is comparable to the best results shown in the literature.

The resonance frequencies of the devices are measured both by optical vibrometer and impedance-meter and are coherent. From the resonance frequencies the parameters necessary to represent the piezoelectric material are extracted. The buckling of the plate is first caused mechanical by an actuating tip in order to harvest pure piezoelectric signal. Then the thermal buckling is observed. The energy produced during one buckling peak has been measured up to $30 pJ.cm^{-2}$ for a snap up temperature at 114°C. The thermal hysteresis between the snap up and snap down of the rectangular devices are relatively high. In order to decrease this hysteresis and also lower the snap up temperature, we conceived new geometries with a butterfly shape. They are very promising, because for an equal length, the snap up temperature has decrease of 30°C and the hysteresis went down to 10°C or even less. These devices can be considered for potential future applications of thermal energy harvesting.

The perspectives of the present work are numerous. First of all, the numerical model with finite elements has to be improved in order to take into account the several thermal cycles to which the deposited layers are submitted and have a better initial shape of the plate.

One of the greatest challenges of this project is to maintain the thermal gradient around the structure for the buckling to occur without increasing too much the size of the system by

adding bulky heat sink. The way of heating the harvester needs improvement. The temperature has to be brought locally to the device. Three different ways are possible.

The first one consists in bringing the heat through the silicon wafer by conduction and cool down the membrane by contact when it is buckled up. But mechanical energy is lost in the impact and the output power might be decreased. The second solutions would be to bring the heat close to the membrane from the backside holes with conducting pillars. For instance silicon pillars are micro-machined and the wafer is glued to the wafer devices with thermal insulation glue. But the air around the hot point might thermalize quickly, so a packaging of the system under vacuum may overcome this issue. The final proposition consists in bringing the heat by a laser. This solution presents several advantages: the temperature can be adjusted easily by tuning the laser power and the heating of the device can be stopped quickly by switching off the laser. But the laser needs optics to focus on the device and the wavelength needs to be carefully chosen in order to minimize the reflected light.

From a global point of view, a new kind of micro thermal energy harvesters have been conceived, fabricated and fully characterized. Optimized structures decreasing the thermal hysteresis are very promising. But improvements need to be made in terms of thermal characterization and optimization of the overall system in order to maintain a good temperature gradient. Some efforts are still needed to integrate in 3D the devices and propose a functional system that could be commercialized.

Résumé

Ce manuscrit présente mes travaux de thèse concernant la récupération d'énergie à partir de sources d'énergie présentes dans l'environnement. La raison qui justifie la récupération d'énergie dans l'espace nous entourant est l'alimentation de capteurs et/ou d'actionneurs afin de les rendre autonome énergétiquement. C'est-à-dire qu'ils peuvent fonctionner normalement, effectuer leurs tâches et envoyer les informations recueillies simplement en tirant profit de la source d'énergie présente autour d'eux. Ces appareils peuvent faire partie d'un réseau plus large de capteurs, pouvant mesurer des données environnementales, envoyer l'information et même agir pour modifier certains paramètres. Les applications possibles pour ce type de réseau sont très séduisantes, en particulier pour les édifices connectés, dits « intelligents », ces capteurs peuvent être placés dans de nombreux endroits de manière à récupérer différentes énergies. Des applications dans le contrôle de la pression extérieure ou de l'hydrométrie par exemple, ou bien encore pour le suivi médical d'êtres humains (pression artérielle, taux de glucose dans le sang…) présentent un grand intérêt de part leur accès difficile et le problème de leur remplacement. Toutes ces actions sont rendues possibles grâce à l'électronique alimentant les capteurs et les actionneurs qui consomme toujours moins de puissance, et de fait l'énergie récupérée dans l'environnement est suffisante pour les alimenter correctement. De plus en plus de batteries sont vont être remplacées par des systèmes de récupération d'énergie dans les prochaines années, car cette énergie est toujours disponible et n'a donc pas besoin d'être changée régulièrement.

Différentes sortes d'énergies sont disponibles dans l'environnement : les radiations, comme l'énergie solaire, la température sous forme de gradient spatial ou temporel, les vibrations mécaniques… Nous avons décidé de focaliser ce travail sur la récupération d'énergie thermique, qui est toujours présente contrairement à la lumière ou aux vibrations mécaniques. Des modes de transductions divers sont à notre disposition pour récupérer l'énergie thermique en fonction de la source d'énergie thermique dont nous disposons. En effet, pour un gradient spatial de température, the mode de transduction le plus utilisé est l'effet Seebeck présent dans les matériaux thermoélectriques. D'un autre côté, si la température change dans le temps, la transduction pyroélectrique est plus adaptée. Ces technologies ont toutes le même effet : elles convertissent une variation de température (spatiale ou temporelle) en charges électriques.

Dans ce travail nous proposons une alternative aux matériaux thermoélectriques, qui sont difficilement compatibles avec des procédés CMOS. Dans un précédent travail de thèse, un macro prototype basé sur le principe d'une plaque bimétallique a été étudié. Une transduction

en étapes convertie dans un premier temps un gradient spatial de température en énergie mécanique à travers le flambage de la plaque. Ensuite dans un deuxième temps ces grands déplacements dus au flambage sont convertis en charges électriques grâce à un élément piézoélectrique. La finalité de ce projet est de réduire l'échelle de ce prototype de manière à augmenter sa fréquence d'oscillation et en même temps sa puissance de sortie. Ce nouveau micro prototype doit être fabriqué uniquement avec des procédés standards de la microélectronqiue de manière à pouvoir être intégré à grande échelle. Le défi de cette étude est donc d'adapter à l'échelle micronique le prototype déjà réalisé à l'échelle macroscopique, de le concevoir et de le fabriquer avec des procédés standards et de le caractériser en termes de puissance de sorties.

Ce manuscrit est organisé en cinq chapitres. Dans le premier chapitre, le domaine des récupérateurs d'énergie est présenté, avec une description des dispositifs récupérant les différentes catégories d'énergies. Leur puissance de sortie est comparée ainsi que les mécanismes impliqués dans les différents types de transductions. Nous nous focalisons principalement sur des dispositifs d'échelle microscopique.

Le deuxième chapitre décrit les mécanismes de la piézoélectricité. Les moyens et les techniques de caractérisations pour évaluer la qualité d'un film mince piézoélectrique ainsi que son rendement sont détaillés. Les procédés classiques de dépôt utilisés pour les films minces piézoélectriques sont décrits. Les applications concrètes des films minces piézoélectriques pour récupérer les différentes énergies sont discutées, en nous focalisant sur les films minces.

Le troisième chapitre décrit le modèle analytique et numérique gouvernant le mécanisme de flambage thermique d'une poutre bicouche. Dans un premier temps, la forme de la structures après fabrication est recherchée ainsi que les températures de cloquage et décloquage. Enfin dans un deuxième temps une analyses numérique permet de modéliser plus précisément la structure durant le flambage thermique.

Le quatrième chapitre décrit en détails les différentes étapes de fabrication utilisées pour réaliser les récupérateurs d'énergie. Le choix des matériaux et les géométries sont discutées, notamment la manière de créer la déflexion initiales des plaques. Malgré les nombreux problèmes rencontrés, qui seront décrits et résolus, des structures fonctionnelles ont été fabriquées.

Le cinquième et dernier chapitre discute de tous les moyens de caractérisations utilisés au cours de ce projet, de la qualité du film mince piézoélectrique avec la mesure des coefficients piézoélectriques à la déflexion initial des plaques. Nous nous focaliserons plus particulièrement sur la caractérisation électromécanique pour rechercher les fréquences de résonance des

différentes géométries fabriquées et la réponse à l'actionnement mécanique. Finalement, la puissance de sortie lors du flambage thermique est mesuré ainsi que les différentes températures de cloquage et décloquage.

Le manuscrit se conclut par une conclusion générale résumant tous les résultats importants obtenus durant cette étude ainsi que les pistes d'amélioration et de continuation de ce projet.

Chapitre I : Contexte de la récupération d'énergie à l'échelle microscopique

Comme expliquer précédemment, la récupération d'énergie c'est l'action de tirer profit de l'énergie présente dans notre environnement proche et qui n'est pas utilisée et de la convertir en énergie utile, par exemple comme énergie mécanique ou électrique. La récupération d'énergie à l'échelle microscopique signifie que cela concerne uniquement les systèmes en dessous du centimètre, contrairement aux dispositifs macroscopiques ayant des dimensions au-delà du centimètre. Ces systèmes sont conçus pour alimenter de petits dispositifs avec une consommation de faible puissance de manière à les rendre autonome d'un point de vue énergétique.

Dans un premier temps, l'état de l'art de la récupération d'énergie à l'échelle microscopique est présenté. Toutes les catégories d'énergie récupérables sont détaillées, de même que les équations de bases les régissant : l'énergie photovoltaïque, les vibrations mécaniques and finalement l'énergie thermique. Les récupérateurs d'énergie thermique sont présentés plus en détails : les récupérateurs thermoélectriques, pyroélectriques, mais aussi utilisant d'autres techniques plus exotiques. Finalement, le contexte du présent travail est énoncé, les résultats obtenus avec le macro prototypes sont examinés et les motivations pour réduire les dimensions du prototype sont discutées.

La récupération d'énergie photovoltaïque est le système le plus connu et le plus répandu à l'échelle macroscopique. Les technologies à l'échelle microscopique se basent sur le même principe et utilisent la même technologie pour avoir un rendement maximal : la cellule photovoltaïque à concentration, c'est-à-dire qu'une lentille est placée au dessus de la cellule photovoltaïque pour focalisé les photons dessus. Cela permet de réduire facilement les dimensions de la cellule tout en maintenant son efficacité. Mais il y a un inconvénient majeur : concentrer les rayons du soleil en un point provoque un échauffement de la cellule ce qui augmente aussi les pertes et diminue son efficacité. Cet inconvénient est très nettement réduit à l'échelle microscopique grâce à l'augmentation de la vitesse des transferts thermiques. Réduire

l'échelle des cellules photovoltaïques présente donc un réel avantage par rapport à un panneau solaire et présente de multiples applications possibles, notamment l'intégration à des téléphones portables ou à des textiles.

L'entreprise Semprius commercialise des cellules photovoltaïques mesurant 600μm de diamètre et ayant un rendement entre 20 et 35%. Sandia Labs ont fabriqué une cellule photovoltaïque avec des techniques standard de la micro-fabrication ayant une épaisseur entre 2 et 30μm et une largeur entre 100 et 1000μm. Ils ont atteint un rendement de 14,9% avec une épaisseur de 14μm. L'avantage de cette dernière est la faible épaisseur qui permet son intégration sur des substrats flexibles.

Les vibrations mécaniques sont très répandues dans notre environnement, notamment en milieu industriel, mais aussi dans les appareils domestiques ou bien encore lors du mouvement du corps humain. Trois modes de transductions peuvent être utilisés pour récupérer les vibrations mécaniques : l'électrostatique, l'électromagnétisme et la piézoélectricité. Les transductions électrostatique et électromagnétique sont détaillées dans ce chapitre, la piézoélectricité quant à elle sera présentée plus en détails dans le chapitre suivant. Tout d'abord, quel que soit le mode de transduction, un générateur résonant inertiel peut être représenté par un système oscillant constitué d'une masse et d'un ressort (modèle William et Yates). Ce modèle permet de calculer le déplacement de la structure en fonction de l'amplitude des vibrations, du facteur de qualité mécanique et de l'amortissement du système.

Les transducteurs électrostatiques reposent sur la variation de capacité du dispositif en fonction des vibrations. La capacité peut être variée de trois manières différents : en variant la surface des électrodes, l'épaisseur du milieu diélectrique ou la constante diélectrique du milieu. Deux conditions de circuit permettent de récupérer les charges générées par le changement de capacité : charge constante ou tension constante, en fonction de l'application souhaitée. Une structure classique MEMS est présentée par Basset *et al.*[15] et permet de récupérer 2,2μW à une fréquence de 150Hz et sous une accélération de 1g.

Pour simplifier le circuit de gestion de puissance (power management) des électrets peuvent être implanté dans une des électrodes. Des électrets sont des charges piégées dans un matériau diélectrique. Les structures incluant des électrets ne sont pas encore à l'échelle microscopique mais cette technique présente un avantage : elle permet de récupérer une grande quantité de puissance électrique avec de petits déplacements. Par exemple Boisseau *et al.*[17] ont réussi de récupérer 50μW avec un déplacement de 10μm de la partie libre d'une poutre encastrée libre sous une accélération de 1g. Différentes autres techniques électrostatiques incluant des électrets sont présentées.

La transduction électromagnétique est très présente à l'échelle macroscopique mais est assez difficilement réalisable à petite échelle. Elle repose sur la conversion des vibrations mécaniques par le mouvement d'un aimant à l'intérieur de spirales conductrices provoquant la création d'un courant induit à l'intérieur de ces spirales. Réaliser un tel dispositif à l'échelle microscopique oblige à relever plusieurs défis, notamment limiter l'interaction du champ magnétique avec les circuits environnants et fabriquer un aimant de petite taille. Beeby et al. ont développé un prototype mésoscopique qui peut produire 46µW à une fréquence de 52Hz sous une accélération de 0,06g. Le plus petit prototype réalisé avec des techniques de la micro-fabrication permet de récupérer 0,36mW à une fréquence de 64Hz sous une accélération de 1g. Une alternative à la récupération d'énergie électromagnétique classique est l'utilisation de matériaux magnétostrictifs, qui ont la propriété de se déformer lorsqu'ils sont soumis à un champ magnétique. Combinés à un système piézoélectrique, la déformation magnétostrictive peut générée des charges électriques.

Une autre source d'énergie de nos jours très présente dans notre environnement mais qui reste assez peu étudiée et très problématique est la récupération des ondes radio fréquence (RF) créées notamment par les télécommunications (GSM, WLAN…). Le capteur doit être obligatoirement situé proche de la source d'ondes car la densité de puissance récupérable diminue grandement avec la distance capteur-source.

La dernière grande énergie récupérable à laquelle nous allons tout particulièrement nous intéressés dans ce travail est l'énergie thermique. La technique la plus répandue pour la récupérer est l'utilisation de matériaux thermoélectriques. Il existe trois phénomène thermoélectriques différents : l'effet Seebeck, l'effet Peltier et l'effet Thomson. L'effet Seebeck est le seul qui permet de générer une circulation de charges électriques lorsque deux matériaux semi-conducteurs, l'un dopé n, l'autre dopé p, sont placés entre un point chaud et un point froid. Le gradient de température qui se crée à l'intérieur du matériau crée une tension électrique à ses bornes. Ces binômes de matériaux semi-conducteurs peuvent être organisés en module avec en dessous le circuit de gestion et au-dessus un radiateur qui permet de maintenir le point froid en évacuant la chaleur. Il est donc nécessaire que le matériau présente d'une part une bonne conductivité électrique de manière à favoriser la circulation des charges électriques, mais d'autre part une mauvaise conductivité thermique de manière à réduire la conduction de la chaleur à travers le matériau et maintenir un gradient thermique. Une figure de mérité appelée ZT permet d'évaluer l'efficacité des matériaux en prenant en compte les paramètres décrits

auparavant. Le défi dans la réduction d'échelle des modules thermoélectriques est justement le maintient du gradient thermique car comme déjà évoqué précédemment à l'échelle microscopique les transferts thermiques sont favorisés et plus rapides. La société Micropelt commercialise un module ayant un volume de 8,7mm^3 permettant de générer 6mW avec un gradient de température de 30°C. Par contre si on prend en compte le dispositif avec son système de radiateur, le volume est de l'ordre du cm^3.

Un autre mode de transduction permettant de récupérer un gradient temporel de température est la pyroélectricité. Certains matériaux, présentant une asymétrie dans leur maille cristalline, ont la particularité de générer des charges électriques lors d'un changement temporel de température. En effet le dipôle initialement présent et du à l'asymétrie de la maille va être modifié lors du chauffage ou du refroidissement du matériau et la contraction ou expansion de la maille qui l'accompagne. Chang *et al.*[37] proposent un système avec une plaque laminée composée d'un matériau pyroélectrique et un matériau non-pyroélectrique. Cette plaque, placée entre un point chaud et un point froid et retenue par des ressorts à mémoire de forme, va se déplacer entre les points de température différente. Sa température va donc cycliquement changer. Le système va donc produire des charges primitives générées par le matériau pyroélectrique dues au changement temporel de température dans la plaque, et des charges secondaires piézoélectriques dues à la différence de coefficient de dilatation thermique des deux matériaux. Le système a été capable de générer 12,35μW avec une différence de température entre le point chaud et le point froid de 10°C.

Les gradients de température peuvent aussi être récupérés par des systèmes ne comportant ni matériau pyroélectrique ni matériau thermoélectrique. Ces systèmes utilisent des matériaux qui changent de propriété avec la température, par exemple des matériaux ferromagnétiques doux. Sous une température seuil appelée température de Curie, ces matériaux sont magnétiques, mais lorsque leur température est au-dessus de cette température, ils perdent leur magnétisation et deviennent paramagnétique. Carlioz *et al.*[38] ont réalisé un interrupteur sensible à la température, où le matériau ferromagnétique est placé en dessous d'une membrane piézoélectrique avec un aimant permanent au centre. Lorsque la température est en-dessous de la température de Curie du matériau ferromagnétique, l'aimant permanent est attiré par ce dernier et la membrane est courbée vers le bas. Lorsque la température passe le seuil de la température de Curie, la membrane piézoélectrique est subitement relâchée et génère des charges. De même lorsque la température repasse en-dessous de la température seuil de Curie, la membrane est brusquement attiré par l'aimant ferromagnétique et génère une nouvelle fois des charges. Ils ont produit 4,2mW pour une différence de température de 10°C.

Le projet HEATec lancé par STMicroelectronics permet de proposer une nouvelle voie pour récupérer de l'énergie thermique à partir d'un gradient temporel ou spatial de température. En utilisant le flambage d'une plaque bimétallique combiné avec soit une couche piézoélectrique placée au dessus de la plaque, soit des électrets placés de part et d'autre du bilame, des macro prototypes ont été réalisés et caractérisés et ont permis de faire la preuve de concept du projet. Par ailleurs ces dispositifs ont été modélisé et ont permis de montrer que si toutes les dimensions de la structure étaient divisées par un facteur k, la fréquence d'oscillation serait augmentée d'un facteur k^2 et la densité de puissance d'un facteur k. Le défi réside dans l'adaptation du circuit de gestion qui doit être capable de travailler avec des tensions divisées par un facteur k par rapport au prototype macroscopique. Dans le cas du dispositif microscopique, nous avons choisi de positionner la couche piézoélectrique directement sur le bilame pour éviter des systèmes de packaging trop complexes.

Chapitre II : Matériaux piézoélectriques à l'échelle microscopique

Après une introduction sur la récupération d'énergie en général, ce chapitre se focalise sur la récupération d'énergie par des dispositifs microscopiques utilisant des films minces piézoélectriques. Dans un premier temps nous allons expliquer ce qu'est la piézoélectricité, les équations de bases seront détaillées de manière à mieux comprendre les différentes familles de matériaux piézoélectriques (pur piézoélectrique, pyroélectrique, ferroélectrique). Une fois que nous sommes familiarisé avec la piézoélectricité, plusieurs récupérateurs d'énergie à case de piézoélectricité seront analysés et leurs performances seront comparées. Dans un dernier temps, les moyens de caractérisation de la qualité des films minces piézoélectrique et des performances des dispositifs seront expliqués, ainsi que la représentation électrique d'un transducteur piézoélectrique et sa réponse électro-mécanique.

La piézoélectricité a été découverte par Jacques et Pierre Curie en 1880. Ils ont démontré que certains matériaux comme le quartz ont la propriété de générer des charges électriques lorsqu'ils sont soumis à une contrainte mécanique. C'est ce que l'on appelle l'effet piézoélectrique direct. L'effet inverse est également prédit thermodynamiquement et démontré expérimentalement une année plus tard en appliquant un champ électrique à un matériau piézoélectrique qui se compresse ou se dilate en fonction de l'amplitude du signal appliqué. Les matériaux piézoélectriques sont énormément utilisés de nos jours dans de multiples applications d'actionnement et de détection.

Pour qu'un matériau soit piézoélectrique une seule condition doit être remplie : son groupe cristallographique ne doit pas présenter de centre de symétrie. Lorsque la maille non symétrique est soumise à une contrainte, les ions vont bouger et modifier le dipôle interne initialement présent. Pour pouvoir écrire les équations de la piézoélectricité un système conventionnel impose la direction de la polarisation suivant l'axe z. Les différentes équations de la piézoélectricité permettant de relier le champ électrique, les contraintes et le déplacement de la densité de charge sont décrites. Les matériaux piézoélectriques englobent différentes familles de matériaux : les matériaux piézoélectriques purs (comme le nitrure d'aluminium AlN ou le zirconate ZnO) ayant une polarisation initiale fixe, les matériaux pyroélectriques (tantalate de lithium $LiTaO_3$) pouvant générer des charges lorsqu'ils sont soumis à un changement temporel de température et enfin les matériaux ferroélectriques (titano-zirconate de plomb PZT) dont le sens de la polarisation peut être modifié grâce à l'application d'un fort champ électrique.

Lorsque après la déposition d'un film mince ferroélectrique la température est retournée à l'ambiante et le champ électrique est nul, les régions du matériau où les dipôles microscopiques présentent la même orientation sont appelées domaines ferroélectriques. Ils se forment pour minimiser l'énergie électrostatique et élastique lors du refroidissement de l'échantillon et la transition de la phase paraélectrique à la phase ferroélectrique. Après l'application d'un fort champ électrique (poling), les dipôles s'alignent le long de la direction du champ et le matériau présente une polarisation macroscopique appelée polarisation rémanente. Ce procédé est applicable uniquement aux matériaux ferroélectriques qui ont la possibilité de changer l'orientation de leurs dipôles microscopiques.

Ensuite les huit équations de la piézoélectricité permettant de décrire les quatre coefficients piézoélectriques sont exprimées. Les matrices de la raideur et du coefficient e_{ij} pour un matériau piézoélectrique sont présentées.

Une grande partie des applications des films piézoélectriques pour la récupération d'énergie sert pour la récupération des vibrations mécaniques. En effet, la piézoélectricité peut convertir directement une contrainte en charges électriques. La configuration la plus répandue est la poutre encastrée libre avec une masse sismique en bout. C'est un dispositif facile à fabriquer avec les techniques classiques de la microélectronique et la fréquence de résonance est ajustable en modifiant le poids de la masse sismique.

Deux possibilités peuvent être envisagées concernant la position du film piézoélectrique : la poutre unimorphe où le film est déposé sur un matériau élastique et la poutre bimorphe où le matériau élastique est pris en sandwich entre deux films piézoélectriques avec des polarisations opposées. La poutre bimorphe agit donc comme deux générateurs

piézoélectriques en série. Ces dispositifs sont optimisés lorsqu'ils travaillent à leur fréquence de résonance, mais leur efficacité diminue rapidement si la vibration que l'on veut récupérer diffère de cette valeur.

Une manière de modifier la fréquence de résonance de la poutre est de modifier ces dimensions Par exemple en augmentant l'épaisseur de la poutre, la fréquence de résonance va augmenter, par contre si on augmente la longueur de la poutre sa fréquence va diminuer. L'inconvénient des poutres encastrées libres à l'échelle microscopique est qu'avec la diminution de toutes les dimensions les fréquences de résonance augmentent souvent au dessus de 1kHz. Or les fréquences utilisées dans les applications pour la récupération d'énergie sont très inférieures, de l'ordre d'une centaine de Hz maximum.

La puissance de sortie et l'énergie récupérée peuvent aussi être augmentées grâce à l'optimisation de la position des électrodes. En effet la géométrie la plus commune est deux électrodes parallèles placées de part et d'autre du film piézoélectrique. De ce fait lorsque la poutre va vibrer elle va solliciter le coefficient e_{31}. Or si les électrodes sont sous forme de peignes inter-digités, le coefficient sollicité sera le e_{33} qui est plus élevé que le e_{31}.

Des dispositifs permettant d'augmenter la bande de fréquence sur laquelle le système peut récupérer de l'énergie sont présentés. Une solution est de mettre différentes poutres avec des fréquences de résonance différentes en série. Une autre est d'introduire de la non-linéarité sous forme de stoppeurs.

Les résonateurs acoustiques à onde de surface (SAW) ou de volume (BAW) ont aussi permis l'expansion du domaine d'application des piézoélectriques, notamment l'AlN. Ces filtres électroniques sont très demandés à cause du développement exponentiel du marché des téléphones portables. En effet ils sont constitués d'un film piézoélectrique sur lequel sont déposés deux réseaux de peignes inter-digités : un actionneur et un récepteur. Ces filtres permettent de sélectionner une fréquence précise d'onde électromagnétique.

De nombreuses techniques sont disponibles pour déposer des matériaux piézoélectriques, en fonction de l'application désirée ou bien du type de matériau (ferroélectrique ou seulement piézoélectrique). En effet, un matériau purement piézoélectrique nécessite d'être texturé lors de la déposition pour qu'il soit fonctionnel, alors qu'un matériau ferroélectrique n'a pas besoin d'être texturé car sa polarisation peut être orientée car un fort champ électrique.

La technique la plus répandue disponible pour beaucoup de matériaux piézoélectriques est la pulvérisation cathodique. Ce procédé de dépôt physique consiste à bombarder une cible

du matériau que l'on veut déposer par des ions formés dans un plasma. Les ions accélérés bombardant la cible arrachent des atomes de la cible qui vont se déposer sur le substrat. Dans le cas de l'AlN, la cible est faite en aluminium pur et en plus des ions argon du plasma de l'azote est injecté pour ensuite réagir avec les atomes d'Al arrachés.

Une autre méthode employée est la déposition chimique en phase vapeur de métalorganique (MOCVD). Cette technique produit un film d'une excellente qualité et est très reproductible, avec une composition très contrôlée. Par contre l'inconvénient majeur est la très haute température nécessaire à la réaction chimique et la très lente déposition.

La dernière technique, largement employée pour les matériaux ferroélectriques comme le PZT, est la déposition par solution chimique, dit « sol-gel ». Des solutions de précurseurs sont déposées sur le substrat et pyrolisées à haute température (environ 350°C). Après le dépôt et la pyrolise de plusieurs couches, le film est recuit à très haute température (environ 600°C), puis l'opération est répétée jusqu'à l'obtention de l'épaisseur voulue.

Les moyens de caractérisation des matériaux piézoélectriques sont nombreux. Parmi les paramètres les plus intéressants à contrôlés : l'orientation du film par diffraction par rayons X, la polarisation par la microscopie à force piézoélectrique (PFM) et les coefficients piézoélectrique $e_{31,f}$ et $d_{33,f}$. Le coefficient $d_{33,f}$ peut être caractérisé grâce à un double interféromètre laser permettant de mesurer le changement d'épaisseur du à l'actionnement. Le coefficient e31,f peut être caractérisé de deux manières différentes, en utilisant l'effet inverse mais aussi l'effet direct piézoélectrique. Ces méthodes seront détaillées dans le chapitre V. Un autre paramètre très important pour évaluer la capacité d'un matériau piézoélectrique à convertir les contraintes en charges électriques est le coefficient de couplage k_{31}. Des figures de mérites peuvent être définies qui permettent ainsi de comparer les performances des différents matériaux.

Finalement, pour pouvoir caractériser le matériau piézoélectrique précisément de manière électrique simplement en mesurant son impédance, le matériau peut être modélisé par un circuit équivalent dit de Van Dyke. Une branche RLC série représentant la partie mécanique résonante est mise en parallèle avec une capacité C_0, la partie statique diélectrique, et une résistance d'accès R_a représentant les résistance de contact.

Chapitre III : Modélisation analytique et numérique

Dans ce chapitre nous allons présenter un modèle analytique du comportement d'une structure bicouche de type poutre. Sa forme flambée après les procédés de fabrication sera

recherchée ainsi qu'une estimation des température de cloquage et décloquage en fonction de la déflection et la déformée trouvées précédemment. Ce modèle est valide uniquement pour une structure de type Bernoulli, c'est-à-dire une poutre élancée dont la largeur est nettement inférieure à sa longueur et peut être considérée comme unitaire. Les structures fabriquées dans ce projet, pour la plupart, ne rentrent pas dans cette catégorie car leur largeur est de dimension comparable à leur longueur. Elles sont donc considérées comme des plaques et le modèle analytique correspondant est bien plus complexe que pour les poutres, il ne va donc pas être traité ici. Par contre il va permettre de manière pédagogique de voir l'influence des contraintes initiales dans les différentes couches sur la déformée et la déflexion initiale de la structure, ainsi que l'évolution des températures de flambage avec ces différents paramètres. Une rapide analyse par éléments finis sur ANSYS est aussi présentée.

Dans un premier temps un modèle analytique est mis en place pour déterminer l'influence des contraintes dans les différentes couches sur la courbure initiale de la structure. Ce modèle est uniquement valable pour des structures de type poutre élancée. Tout d'abord nous allons définir ce qu'est le flambage d'une poutre élancée. Le flambage (buckling en anglais) a lieu lorsque la force axiale compressive du à une contrainte mécanique appliquée sur les bords de la poutre ou à des contraintes thermiques lors du chauffage de la poutre encastrée dépasse une certaine limite, dite la charge d'Euler. A ce moment, les petites déformations dans le plan donnent lieu à de très larges déplacements hors-plan. Une des applications les plus courantes du flambage est l'interrupteur thermique présent dans les fers à repasser ou les bouilloires. Une poutre bicouche initialement courbée vers le bas par exemple est chauffée. La différence de dilatation thermique des deux matériaux va créer des contraintes thermiques qui vont mener au flambage de la poutre et à la rupture du contact électrique avec l'inversion de la courbure.

Dans ce modèle, qui est largement inspiré de la thèse de M. Aron nous allons être capable de prédire la déflexion initiale de la poutre en fonction des différents niveaux de contraintes dans les couches, et ainsi avoir une idée de la déformée de la poutre en fonction par ailleurs de la rigidité de torsion aux ancrages. Les structures étudiées ici sont composées de quatre couches de matériaux différents : une première couche d'AlN de 200nm et une couche de platine Pt de 100nm qui seront égales pour toutes les configurations étudiées, et une couche d'AlN et d'Al actives dont les épaisseurs sont des paramètres à faire varier.

La poutre multicouche peut être considérée comme une poutre monocouche avec des paramètres équivalents. Après avoir calculé la fibre neutre de l'empilement considéré, l'épaisseur, le module d'Young, les contraintes équivalentes et la rigidité de flexion équivalents sont calculés en fonction de la position de la fibre neutre. Ensuite, d'un point de vue mécanique,

nous pouvons considérer que la poutre est soumise à différentes charges : la charge net axiale, le moment résiduel du à la non-homogénéité des contraintes dans les couches, un moment de torsion aux ancrages introduisant la rigidité de torsion et enfin un moment de flexion du à la déformation de la poutre en flexion. En supposant que la poutre ne subit que de petites déflexions, la condition d'équilibre se résume à annuler la somme de tous les moments agissant sur la structure. Après avoir dérivé l'équation deux fois, nous obtenons une équation différentielle nous permettant de calculer la déformée de la poutre. Après avoir appliqué les conditions aux limites et trouver les quatre constantes, la déformée est trouvée dépendante de la déflexion maximale, des paramètres géométriques et de la condition de flambage d'Euler. Grâce à cette équation nous pouvons remonter à la déflexion maximale en fonction des conditions initiales de contraintes. Sur Matlab nous avons étudié quatre configurations d'épaisseurs différents : 0,5µm d'AlN et 0,5µm d'Al ; 0,5µm d'AlN et 1µm d'Al ; 2µm d'AlN et 1µm d'Al ; 1µm d'AlN et 4µm d'Al. La contrainte dans la couche d'épaisseur constante d'AlN/Pt est fixée dans un premier temps à une valeur classique de 50MPa. Dans tous les cas, nous remarquons que la déflexion à faible valeur de contraintes est faible et surtout assez stable. Alors que lorsque les valeurs de contraintes dépassent environ 100MPa, la déflexion maximale devient très sensible au moindre changement dans la valeur de contrainte. Maintenant si la contrainte dans la couche d'AlN/Pt est augmentée à 100MPa, cela a un effet surtout pour la déflexion maximale à faible valeur de contraintes qui augmente légèrement.

Maintenant que nous avons la déflexion initiale de la structure en fonction des contraintes, nous pouvons regarder l'influence des ancrages sur la déformée. En faisant varier la rigidité de torsion aux ancrages, cela influence surtout la déformée au niveau des ancrages et dans une moindre mesure la valeur de la déflexion maximale. En effet une valeur faible (tendant vers 0) de la rigidité de torsion modélise une poutre simplement supportée alors que une valeur élevée (tendant vers l'infini) de rigidité de torsion modélise une poutre encastrée. La rigidité axiale, quant à elle, influence la valeur de la déflexion maximale uniquement, mais dans la limite de quelques pourcents.

Dans un deuxième temps, une fois que la déflexion maximale et la déformée de la poutre sont calculés, nous pouvons nous intéresser aux températures de cloquage et décloquage. Timoshenko a étudié intensivement les bilames pour les applications des thermostats. Nous nous baserons sur son modèle. Néanmoins, il est nécessaire d'émettre plusieurs hypothèses, notamment que la structure est toujours une poutre élancée de Bernoulli, mais aussi que la température est considérée uniforme dans la poutre. A partir de là, nous pouvons calculer la force axiale nécessaire à provoquer un changement de déflexion de la déflexion initiale δ_0 à une

déflexion seuil δ_1 à laquelle aura lieu de flambage. En calculant par ailleurs la force axiale nécessaire pour empêcher le flambage, il arrive, en combinant les deux équations, à calculer la température de cloquage à laquelle la poutre va passer d'un état à un autre. Pour le décloquage il procède exactement de la même manière en faisant attention d'adapter les équations au fait que la courbure ait changé de signe. Nous avons ainsi pu calculer les températures de cloquage et décloquage des structures précédemment étudiées, en prenant comme valeur de déflexion initiale la valeur prédite par le modèle de M. Aron. Certaines configurations ont des températures de fonctionnement proches de l'ambiante, ce qui se révèle très intéressant et permet d'envisager de multiples applications. Par contre, certaines températures, notamment de décloquage, se retrouvent bien en dessous de zéro, ce qui réduit considérablement l'intérêt de ces configurations pour de futures applications concrètes.

Finalement, des simulations par éléments finis ont été menés en utilisant ANSYS v15. Dans une première étape la forme initiale de la structure est préformée, c'est-à-dire qu'un arc de cercle est tracé et extrudé pour former la surface de la structure. En utilisant l'élément SHELL181, qui est un élément coque, nous pouvons définir une surface multicouche. En appliquant une force mécanique en son centre, nous pouvons voir l'évolution de la force nécessaire au flambage en fonction de la déflexion initiale pour les différentes structures qui seront fabriquées ensuite.

Dans une deuxième étape, nous avons voulue nous rapprocher plus des conditions réelles pour la déformation initiale de notre plaque en appliquant des forces de part et d'autre de la plaque pour introduire des contraintes à l'intérieur. A partir de cette déformée nous pouvons réaliser une analyse modale et voir les fréquences de résonance de la structure ainsi que ses différents modes de résonance. Par contre les tentatives de modéliser la structure en 3D se sont révélées infructueuses.

Chapitre IV : Procédés de fabrication

L'objectif de ce projet est de concevoir et fabriquer des plaques bicouches pour la récupération d'énergie thermique avec une transduction piézoélectrique. Dans le chapitre précédent nous avons prédis l'impact des contraintes sur la courbure initiale de la poutre, ainsi que les températures de flambage correspondantes. Maintenant il s'agit de fabriquer une structure fonctionnelle en tenant compte des précédentes observations.

Tout d'abord, il faut justifié le choix de l'AlN comme matériau piézoélectrique. En effet à l'échelle microscopique il existe deux principaux matériaux utilisés pour la récupération

d'énergie : l'AlN et le PZT. Tous les deux présentent une faible dilatation thermique et leur procédé de déposition est parfaitement maîtrisé. Par contre l'AlN a un procédé de fabrication plus rapide que le PZT, les contraintes dans le film sont contrôlables en ajustant les paramètres de dépôt et il n'a pas besoin d'être pré-polarisé comme le PZT pour pouvoir fonctionner car il est purement piézoélectrique. Pour toutes ces raisons l'AlN a été choisi. Ensuite, contrairement au prototype macroscopique, nous avons décidé d'intégrer directement la couche piézoélectrique sur le bilame, et l'Al avait l'avantage d'être métallique, il pouvait donc servir d'électrode supérieure, et surtout son coefficient de dilatation thermique était très différent de celui de l'AlN, il était donc un bon candidat pour le bilame.

Le procédé de fabrication comporte quatre niveaux de masques de photolithographie : un masque pour définir les électrodes de Pt, un masque pour libérer les marque d'alignement après dépôt de l'AlN et de l'Al, un masque pour définir la membrane rectangulaire et un masque pour libérer la membrane par la face arrière. Sur le wafer seront donc présentes des plaques suspendues rectangulaires avec six combinaisons différentes de longueur/largeur et aussi des structures de test de type poutre élancée de quelques mm de longueur pour la caractérisation du film piézoélectrique.

Tout le processus de fabrication a été réalisé au Centre de Micro et Nanotechnologies de l'EPFL (CMi). Cette salle blanche universitaire est composée de deux étages, un étage inférieur de classe 100 avec tous les procédés sensibles de dépôts, de photolithographie et de microscopie, et un étage supérieur de classe 1000 avec des procédés moins sensibles. Les machines sont optimisées pour des wafers de 100mm de diamètre. Tous les utilisateurs de la salle blanche sont formés préalablement sur les machines nécessaires à leur projet et sont ensuite aptes à réaliser eux-mêmes leur procédés, avec le support technique du personnel. Dans un premier temps, les différents masques ont été dessiné sur le logiciel Expert et fabriqué sur une machine d'écriture par laser. Le masque de verre est initialement recouvert d'une couche de chrome Cr et d'une couche de photorésine. La résine est ensuite insolée par un laser qui va reproduire ligne par ligne le design voulu. Après le développement de la résine, le chrome est gravé par voie chimique et la résine est enlevée. Les masques sont prêts.

Les structures vont être réalisées sur des wafers de silicium Si de 100mm orientés (100) et recouverts d'1µm d'oxyde thermique. La première étape de fabrication est la déposition d'une fine couche d'AlN de 200nm et d'une couche de Pt de 100n par pulvérisation cathodique. Les dépositions se font à 300°C et 350°C respectivement. Ensuite le Pt est gravé par gravure plasma en utilisant de la chlorine Cl_2. Cette étape est critique car ce gaz est très réactif et attaque la résine. Une fois que les électrodes sont gravées, on dépose toujours par pulvérisation cathodique

une couche d'AlN entre 500nm et 1µm et une couche d'Al entre 500nm et 2µm. Ces dépôts sont réalisés à 300°C et 330°C. Une très fine couche de titane Ti de 50nm est déposée par pulvérisation cathodique à température ambiante sur l'Al pour le protéger de la solution de développement lors de la photolithographie. Ensuite l'Al est gravé par plasma en utilisant un mélange de BCl_3 et Cl_2. Sans enlever la résine, l'AlN est gravé dans un premier temps entièrement par gravure humide dans l'acide phosphorique chaud jusqu'à atteindre le Pt ou le Si. Il ne reste plus qu'à libérer les membranes par la face arrière. Pour cela, la face avant est protégée grâce à une couche de 2 à 5µm de parylène C. Sa déposition est faite à température ambiante et c'est un film qui ne présente aucune contrainte. De plus on peut facilement l'enlever par plasma oxygène. La gravure face arrière est réalisée par une gravure profonde par ions réactifs (Deep Reactive Ion Etching). La fine couche d'AlN en dessous de la couche de Pt sert de couche d'arrêt à la gravure pour ne pas abîmer les électrodes de Pt.

Certaines étapes présentent un intérêt tout particulier. En effet, c'est en ajustant les contraintes dans la couche inférieure d'AlN que la courbure initiale peut être modifiée. L'AlN, du fait qu'il soit un matériau diélectrique, a besoin d'un procédé spécial de pulvérisation cathodique, appelé pulvérisation magnétron réactive, pulsée à courant direct (reactive, pulsed, direct current magnetron sputtering). Une cible en Al pure à 99,99% est utilisée dans un plasma réactif à base d'azote. Un courant DC est appliqué entre la cathode (la cible) et l'anode (le substrat) pour créer le plasma. Du fait que l'AlN est un matériau diélectrique, les charges ont tendance à s'accumuler sur la surface du substrat. Il est donc nécessaire de pulser le courant direct à 20kHz, c'est-à-dire qu'il est inversé toutes les 5µs pour décharger la surface et ainsi éviter l'apparition d'arcs électriques. Le magnétron est un aimant créant un champ magnétique juste en dessous de la cible pour concentrer le plasma à cet endroit et augmenter le libre parcours moyen des ions. En ajustant la densité de puissance appliquée au substrat, il est ainsi possible d'ajuster l'intensité du bombardement des ions et in fine les contraintes dans le film. Cela a cependant des inconvénients : si la densité de puissance appliquée est trop faible, la qualité piézoélectrique du film sera diminuée. C'est pour cela que les contraintes sont ajustées dans la couche inférieure d'AlN et non pas dans la couche active pour garder de bonnes propriétés piézoélectriques.

Après chaque déposition d'une couche de matériau, les contraintes sont mesurées par un interféromètre laser. Le rayon de courbure du wafer « nu » a été initialement mesuré et il est ensuite mesuré après chaque dépôt. En utilisant la formule de Stoney, la différence de rayon de courbure peut nous donner les contraintes générées dans le film. Une étude a ainsi été réalisé sur l'empilement de 200nm d'AlN et 100nm de Pt en faisant varier la densité de puissance

appliquée au substrat : les contraintes dans le film sont passées de 500MPa tensiles à faible puissance à -1500MPa compressives à forte puissance.

Les étapes de gravures ont été tout particulièrement difficiles à optimiser. En effet, comme évoqué précédemment, lors de la gravure du Pt, le plasma réagit avec la résine en formant une couche de résine durcie sur le dessus. En respectant un procédé standard pour enlever la résine, nous observions toujours un film très mince sur les électrodes, qui ensuite aurait empêché de collecter les charges piézoélectriques par les électrodes inférieures. La solution trouvée a été de limiter le plus possible de temps d'exposition de la résine gravée à l'air libre. Dès que la gravure du Pt est terminée, le wafer est immédiatement sorti de la chambre de gravure et plongé dans la solution de « stripping » chauffée à 70°C.

Une deuxième étape de gravure critique fut la gravure combinée de l'Al et de l'AlN. Dans un premier temps, comme décrit avant, une fine couche de Ti a du être rajoutée pour protéger l'Al de la solution de développement de la résine qui est basique et attaquait l'Al. Ensuite, après la gravure plasma de l'Al, le procédé standard de gravure de l'AlN était la gravure humide dans l'acide phosphorique chaud. Or, le temps de gravure était d'environ 3min pour 1µm d'AlN, et l'acide gravait en même temps l'Al, ce qui provoquait une très grande sous gravure. La solution trouvée a été de graver par plasma l'AlN jusqu'à atteindre les électrodes de Pt en utilisant du Cl_2. Une fois les électrodes atteintes, il fallait stopper la gravure pour ne pas les endommager. Pour finir la gravure et atteindre le Si, le wafer est plongé quelques secondes dans l'acide phosphorique chaud. Ce procédé limite considérablement la sous-gravure et permet d'avoir des structures rectangulaires bien définies.

Chapitre V : Caractérisations

La caractérisation des dispositifs précédemment fabriqués est présentée dans ce chapitre. La déflexion initiale ainsi que la qualité du film piézoélectrique seront examinées. Le coefficient piézoélectrique $e_{31,f}$ est mesuré à la fois en mode actionneur et en mode capteur. L'orientation cristallographique de l'AlN est contrôlée et sa réponse pyroélectrique à de faibles variations de température autour de la température ambiante est caractérisée. La réponse électromécanique de la structure est mesurée pour déterminer ses fréquences de résonance. Les résultats sont comparés aux simulations par éléments finis. Les performances du récupérateur d'énergie lors du flambage actionné mécaniquement et thermiquement sont présentées. Différentes géométries sont testées et leur puissance de sortie est mesurée. Finalement, de nouvelles géométries ayant une forme de papillons sont introduites et caractérisées.

A la fin du processus de fabrication, le paramètre le plus important à caractériser est la courbure initiale des structures. Cette dernière, comme expliqué auparavant, va dépendre de la combinaison des contraintes dans les différentes couches. Nous avons utilisé deux méthodes différentes pour mesurer cette déflexion : une méthode mécanique et une méthode optique. Avec le profilomètre mécanique, une pointe appuie sur la surface de la plaque avec une force donnée et se déplace le long de celle-ci en maintenant cette force constante. Après avoir ajuster correctement la valeur de la force pour qu'elle ne soit ni trop faible ni trop forte (elle risquerait alors de faire flamber la plaque) nous obtenons un profil en 1D de la structure. D'autre part le profilomètre optique se base sur le principe de l'interféromètre de Michelson pour réaliser une image 2D de la courbure de la plaque. On règle l'appareil pour créer des interférences sur la surface de l'échantillon et ensuite l'échantillon est déplacé verticalement, ce qui va décaler les interférences et on peut avoir comme cela l'image en 2D de la surface de l'échantillon. Cette méthode, moins précise que le profilomètre optique, présente cependant un avantage : elle permet de voir que les plaques ont non seulement une courbure longitudinale mais aussi transversale.

Une cartographie d'un wafer entier a été réalisée où la courbure de chaque dispositif a été mesurée en fonction de sa géométrie et de son emplacement sur le wafer. On peut remarquer qu'il existe toujours une certaine dispersion de la courbure quelle que soit la structure, mais pour les structures les plus longues comme les 2000μm x 200μm, la dispersion est très importante et certains dispositifs ont même des courbures de sens opposé. Par ailleurs lorsque ces valeurs sont comparées aux valeurs calculées par le modèle analytique, aucune conclusion ne peut être tirée à cause de la trop grande dispersion des valeurs. Cela peut être expliquer de plusieurs manières, notamment par le fait que les contraintes ne sont pas homogènes partout dans le wafer à cause des procédés de gravures qui ne sont pas homogènes. Ensuite la mesure des contraintes comporte des approximations. La déflexion maximale étant très sensible à la valeur des contraintes dans cette gamme de valeurs, le moindre changement de quelques pourcents sur les contraintes peut introduire une grande différence de déflexion maximale.

Un autre paramètre important pour savoir si notre dispositif final sera fonctionnel est de contrôler la qualité du film piézoélectrique d'AlN. Pour ce faire, on mesure d'abord l'orientation cristalline du film par diffraction aux rayons X en mode θ - 2θ. Cette mesure révèle des pics suivants les plans (002) d'AlN ce qui montre une très bonne orientation du film. Ensuite viennent les pics du (111) Pt, qui est donc orienté lui aussi dans la bonne direction, et le (004) Si qui correspond à l'orientation du substrat.

La qualité du film piézoélectrique passe aussi par la mesure du coefficient $e_{31,f}$, le plus intéressant dans notre cas de récupération d'énergie. Pour ce faire, nous utiliserons deux méthodes de caractérisation différentes, l'une mettant à contribution le film piézoélectrique en mode actionneur et l'autre en mode capteur. La méthode la plus directe pour mesure de coefficient $e_{31,f}$ est la méthode en mode capteur. Dans cette configuration, la structure de test en forme de poutre est encastrée d'un côté et libre de l'autre. Le côté libre de la poutre est déformé par un actionneur piézoélectrique sur lequel est monté une pointe isolante qui déplace la poutre à une fréquence et une amplitude très contrôlée. Les charges ainsi générées dans la poutre sont récupérées par des pointes qui envoient les charges dans un amplificateur de charges. Comme l'aire de l'électrode et l'endroit où la pointe déforme la poutre sont parfaitement connus, il est aisé de remonter aux déformations générées sous l'électrode ainsi qu'aux charges électriques, et donc au coefficient $e_{31,f}$. Nous avons comparé différentes combinaisons d'épaisseurs d'AlN et d'Al ainsi que des poutres orientées différemment sur le wafer et dans tous les cas le coefficient $e_{31,f}$ est aux environs de 0,9 C .m^{-2}. La qualité du film piézoélectrique est reproductible quelque soit l'épaisseur et quelque soit l'orientation de la poutre sur le wafer, le coefficient reste inchangé.

La caractérisation en mode actionneur est assez similaire : la poutre est encastrée sur un support d'un côté et libre de l'autre. Les pointes connectées aux électrodes supérieures et inférieures actionnent le film piézoélectrique avec une tension donnée et le déplacement en bout de poutre libre est mesuré grâce à un interféromètre laser. De la même manière, connaissant le déplacement en bout de poutre en fonction de la tension appliquée, on peut remonter aux contraintes générées sous l'électrode et ainsi trouver la valeur du coefficient $e_{31,f}$. Les mêmes échantillons que précédemment ont été testé et cette fois-ci la valeur du coefficient $e_{31,f}$ est légèrement supérieure, autour de 1 C.m^{-2}. Cette différence est due aux différentes erreurs de mesures dans les deux cas.

Dans notre cas d'usage du dispositif final, l'AlN va être soumis à des variations de température, nous allons donc caractériser sa réponse pyroélectrique pour avoir une idée de sa contribution dans les charges finales récupérées. Pour ce faire l'échantillon est placé sur une cellule Peltier dans une chambre isolée thermiquement. La température de la cellule Peltier est variée de quelques degrés autour de la température ambiante et les charges pyroélectriques générées sont collectées par un amplificateur de charges. Lorsque la rampe de température est positive, le courant pyroélectrique est positif et d'environ 20pA. Lorsque la rampe est négative, le courant pyroélectrique s'inverse tout en gardant la même valeur absolue. A partir de ces valeurs et des dimensions des électrodes nous pouvons estimer la valeur du coefficient pyroélectrique $p_{3,f}$ à environ 3,9µC.m^{-2}.K^{-1}. Ce coefficient reste très faible par rapport à ceux des matériaux ferroélectriques comme le PZT (268µC.m^{-2}.K^{-1}).

La prochaine étape de caractérisation consiste à regarder la réponse électromécanique du film piézoélectrique d'AlN. Lors des premières mesures des dispositifs sur un RLC-mètre, nous avions remarqué une très grande capacité de fuite que l'on suppose être dans le substrat. C'est le rôle de la couche d'oxyde sur la face avant du wafer : pour bloquer la fuite de charges à travers le substrat. Une fois ce problème résolu, les mesures d'impédance des dispositifs ont montré de nombreuses fréquences de résonance, à des valeurs toujours supérieures à 10kHz. Grâce à un programme réalisé sous Matlab, il est possible d'extraire les paramètres électriques équivalent de la structure à la résonance en utilisant la représentation de Van Dyke. Nous obtenons ainsi le facteur de qualité mécanique mais aussi tous les autres paramètres électriques équivalents. Par ailleurs nous observons une bonne corrélation entre la valeur théorique de la capacité et celle extraite par le programme Matlab.

Avec l'analyseur d'impédance, nous avons donc observé les fréquences de résonance du film piézoélectrique de manière électrique. Il est aussi possible de les observer optiquement grâce à un vibromètre laser focalisé sur la structure. Nous procédons de la manière suivante : la membrane est actionnée avec une tension relativement élevée (quelques dizaines de volts) et la vitesse ou le déplacement de la surface est mesurée avec l'interféromètre laser en fonction de la fréquence d'actionnement. Lorsque la fréquence atteint une fréquence de résonance du dispositif, son déplacement sera maximal et un pic sera observé par le vibromètre. En testant exactement la même structure qu'auparavant, nous observons toutes les fréquences de résonance observées au RLC-mètre. Par contre, il y a des fréquences de résonance supplémentaires. Cela peut être expliqué par la géométrie des électrodes qui, électriquement, ne permettent pas de voir tous les modes, par exemple si elles sont situées sur un ventre de vibration.

Maintenant, nous avons caractérisé aussi bien la qualité du matériau que sa performance. On peut donc passer à la caractérisation, plus complexe, du flambage. Dans un premier temps, comme nous ne connaissons pas du tout la réponse qu'aura le dispositif en flambage thermique, nous allons mesurer la réponse d'une structure au flambage purement mécanique. Ainsi, nous évitons toute éventuelle contribution de charges pyroélectriques dans le signal. Pour cela, nous avons conçu un banc de mesure qui permet, grâce à une pointe isolante en verre montée sur un actionneur piézoélectrique, de venir pousser la membrane par la face arrière jusqu'à provoquer le flambage. Des pointes contactent les électrodes en face avant et récupèrent les charges avec un amplificateur de charges ou d'instrumentation. La difficulté a été de trouvé un amplificateur qui permette de mesurer des signaux électriques très rapides et

d'amplitude inférieure au volt. Nous avons préféré travailler avec l'amplificateur d'instrumentation car il avait une bande passante plus élevée et le signal était moins bruité qu'avec l'amplificateur de charges. Dans le cas de l'amplificateur d'instrumentation, nous avons optimisé la résistance de charge pour une structure qui permet d'avoir la puissance de sortie maximale. Les énergies récupérées par pic de cloquage ou décloquage sont de l'ordre de $30 pJ.cm^{-2}$.

Nous savons donc maintenant quel type de signal de sortie nous allons avoir lors du cloquage, nous pouvons donc caractériser la structure dans son application finale, c'est-à-dire le flambage thermique. Pour cela nous posons le wafer entier sur une plaque chauffante dont la température à la surface est mesurée avec un thermocouple et augmentons la température jusqu'à ce que la structure flambe. A ce moment là, la structure change visiblement de courbure, la plaque chauffante est donc éteinte et laissée à refroidir. La température à sa surface est toujours mesurée par le thermocouple et lorsque la structure décloque, nous avons donc la température de décloquage. L'énergie récupérée par pic de cloquage/décloquage pour la même structure que celle testée durant le flambage mécanique est inférieure. Mais surtout l'hystérésis de température, c'est-à-dire la différence entre la température de cloquage et décloquage est relativement élevée, et n'est pas compatible avec une application de détection sensible. Par ailleurs, trois structures de même géométrie situées à côté sur le wafer présentent des températures de cloquage et décloquage très différentes. Nous observons donc bien la non-homogénéité des contraintes sur le wafer mais surtout l'extrême sensibilité des températures de cloquage aux valeurs des contraintes.

Finalement, pour résoudre le problème de la grande valeur d'hystérésis observée précédemment, de nouveaux designs sont introduits pour essayer d'homogénéiser les contraintes à l'intérieur de la plaque et diminuer la raideur aux ancrages. La plaque aura ainsi une forme de papillon plutôt que rectangulaire. Différentes longueurs et angles d'ouverture des papillons seront fabriqués La même procédure est utilisée pour les caractérisés. Tout d'abord, la courbure initiale des structures est mesurée et nous observons l'effet attendu par la géométrie. En comparant une structure de 1400μm de long rectangulaire et en papillon, la déflection maximale est légèrement inférieure chez le papillon et surtout il y a un aplatissement de la courbure au centre, ce qui traduit un assouplissement des ancrages. Ensuite les fréquences de résonance sont mesurées aussi bien au RLC qu'au vibromètre et une bonne corrélation est toujours observée entre les deux, bien que plus de fréquences de résonance soient observées optiquement. Enfin le flambage thermique des structures est caractérisé. Comme la résistance de charge de l'amplificateur d'instrumentation n'a pas été optimisée, les énergies récupérées

sont plus faibles qu'avec la structure rectangulaire. Par contre, lorsqu'avec la structure rectangulaire l'hystérésis de température est de 30°C, avec les papillons elle oscille entre 2°C et 10°C en fonction de l'angle d'ouverture du papillon. C'est un résultat très prometteur qui permet d'envisager une application de détection de température très sensible, avec une fragilité aux ancrages réduite.

En conclusion, ces travaux de thèse ont permis de concevoir, fabriquer et caractériser les premiers prototypes à l'échelle microscopique d'un récupérateur d'énergie thermique basé sur le principe d'une poutre bicouche avec une transduction piézoélectrique. C'est la première preuve de concept à l'échelle microscopique qui ouvre la porte à de nombreuses pistes d'améliorations. En effet le design n'est pas optimum, notamment en ce qui concerne les électrodes ou les épaisseurs des différentes couches. Ensuite la caractérisation thermique des échantillons reste à améliorer pour avoir une mesure précise de la température de la membrane ou bien trouver un moyen de chauffer efficacement la structure pour avoir un chauffage et un refroidissement rapide, comme avec un laser par exemple. Enfin le packaging destiné au dispositif final doit permettre d'apporter la chaleur efficacement au dispositif tout en maintenant un point froid pour que le flambage ait lieu.

Bibliography

[1] "Photovoltaics," *Wikipedia*, 2015. [Online]. Available: https://en.wikipedia.org/wiki/Photovoltaics.

[2] "New world record for solar cell efficienty at 46%," *Fraunhofer Institut for Solar Energy Systems*. [Online]. Available: https://www.ise.fraunhofer.de/en/press-and-media/press-releases/press-releases-2014/new-world-record-for-solar-cell-efficiency-at-46-percent.

[3] "Growth of photovoltaics," *Wikipedia*. [Online]. Available: https://en.wikipedia.org/wiki/Growth_of_photovoltaics#Forecast.

[4] M. Paire, L. Lombez, F. Donsanti, M. Jubault, S. Collin, J.-L. Pelouard, J.-F. Guillemoles, and D. Lincot, "Cu(In, Ga)Se2 microcells: High efficiency and low material consumption," *J. Renew. Sustain. Energy*, vol. 5, no. 1, p. 011202, 2013.

[5] K. Bourzac, "Micro Solar Cells handle more intense Sunlight," *MIT Technology Review*, 2010. [Online]. Available: http://www.technologyreview.com/news/417431/micro-solar-cells-handle-more-intense-sunlight/.

[6] "Sphelar Power - Enable Electronics Integrated Photovoltaic series," *Sphelar Power*. [Online]. Available: http://sphelarpower.com/product/sphelar_eipv.html.

[7] K. Robinson-Avila, "Sandia Labs expands, upgrades solar R&D," *Albuquerque Journal*. [Online]. Available: http://www.abqjournal.com/155484/biz/sandia-labs-expands-upgrades-solar-rampd.html.

[8] J. L. Cruz-Campa, G. N. Nielson, P. J. Resnick, C. Sanchez, P. J. Clews, M. Okandan, T. Friedmann, V. P. Gupta, and others, "Ultrathin flexible crystalline silicon: microsystems-enabled photovoltaics," *Photovolt. IEEE J. Of*, vol. 1, no. 1, pp. 3–8, 2011.

[9] C. B. Williams and R. B. Yates, "Analysis of a micro-electric generator for microsystems," *Sensors*, vol. 52, no. 1–3, pp. 8–11, 1996.

[10] S. Roundy, "On the Effectiveness of Vibration-based Energy Harvesting," *J. Intell. Mater. Syst. Struct.*, vol. 16, no. 10, pp. 809–823, Oct. 2005.

[11] S. Boisseau, G. Despesse, and B. Ahmed, "Electrostatic Conversion for Vibration Energy Harvesting," in *Small-Scale Energy Harvesting*, M. Lallart, Ed. InTech, 2012.

[12] P. Basset, D. Galayko, A. M. Paracha, F. Marty, A. Dudka, and T. Bourouina, "A batch-fabricated and electret-free silicon electrostatic vibration energy harvester," *J. Micromechanics Microengineering*, vol. 19, no. 11, p. 115025, Nov. 2009.

[13] G. Despesse, J. J. Chaillout, T. Jager, F. Cardot, and A. Hoogerwerf, "Innovative structure for mechanical energy scavenging," in *Solid-State Sensors, Actuators and Microsystems Conference, 2007. TRANSDUCERS 2007. International*, 2007, pp. 895–898.

[14] D. Hoffmann, B. Folkmer, and Y. Manoli, "Fabrication and characterization of electrostatic micro-generators," presented at the PowerMEMS, 2008.

[15] P. Basset, D. Galayko, F. Cottone, R. Guillemet, E. Blokhina, F. Marty, and T. Bourouina, "Electrostatic vibration energy harvester with combined effect of electrical nonlinearities and mechanical impact," *J. Micromechanics Microengineering*, vol. 24, no. 3, p. 035001, Mar. 2014.

[16] M. Mizuno and D. G. Chetwynd, "Investigation of a resonant microgenerator," *J. Micromechanics Microengineering*, vol. 13, no. 2, 2003.

[17] S. Boisseau, G. Despesse, T. Ricart, E. Defay, and A. Sylvestre, "Cantilever-based electret energy harvesters," *Smart Mater. Struct.*, vol. 20, no. 10, p. 105013, Oct. 2011.

[18] D. Miki, M. Honzumi, Y. Suzuki, and N. Kasagi, "Large-amplitude MEMS electret generator with nonlinear spring," in *Micro Electro Mechanical Systems (MEMS), 2010 IEEE 23rd International Conference on*, 2010, pp. 176–179.

[19] M. Edamoto, Y. Suzuki, N. Kasagi, K. Kashiwagi, Y. Morizawa, T. Yokoyama, T. Seki, and M. Oba, "Low-resonant-frequency micro electret generator for energy harvesting application," in *Micro Electro Mechanical Systems, 2009. MEMS 2009. IEEE 22nd International Conference on*, 2009, pp. 1059–1062.

[20] Y. Naruse, N. Matsubara, K. Mabuchi, M. Izumi, and K. Honma, "Electrostatic micro power generator from low frequency vibration such as human motion," presented at the PowerMEMS2008, Japan, 2008.

[21] S. Beeby and T. O'Donnell, *Energy Harvesting Technologies*, Springer. Priya Shashank and Inman Daniel J., 2009.

[22] C. R. Saha, T. O'Donnell, H. Loder, S. Beeby, and J. Tudor, "Optimization of an Electromagnetic Energy Harvesting Device," *IEEE Trans. Magn.*, vol. 42, no. 10, pp. 3509–3511, Oct. 2006.

[23] S. P. Beeby, R. N. Torah, M. J. Tudor, P. Glynne-Jones, T. O'Donnell, C. R. Saha, and

S. Roy, “A micro electromagnetic generator for vibration energy harvesting,” *J. Micromechanics Microengineering*, vol. 17, no. 7, pp. 1257–1265, Jul. 2007.

[24] H. Liu, B. W. Soon, N. Wang, C. J. Tay, C. Quan, and C. Lee, “Feasibility study of a 3D vibration-driven electromagnetic MEMS energy harvester with multiple vibration modes,” *J. Micromechanics Microengineering*, vol. 22, no. 12, p. 125020, Dec. 2012.

[25] M. Han, Q. Yuan, X. Sun, and H. Zhang, “Design and Fabrication of Integrated Magnetic MEMS Energy Harvester for Low Frequency Applications,” *J. Microelectromechanical Syst.*, vol. 23, no. 1, pp. 204–212, Feb. 2014.

[26] S.-G. Kim, S. Priya, and I. Kanno, “Piezoelectric MEMS for energy harvesting,” *MRS Bull.*, vol. 37, no. 11, pp. 1039–1050, Nov. 2012.

[27] T. Ueno, H. Miura, and S. Yamada, “Evaluation of a miniature magnetostrictive actuator using Galfenol under tensile stress,” *J. Phys. Appl. Phys.*, vol. 44, no. 6, 2011.

[28] J. A. Hagerty, F. B. Helmbrecht, W. H. McCalpin, R. Zane, and Z. B. Popovic, “Recycling ambient microwave energy with broad-bad rectenna arrays,” *IEEE Transations Microw. Theory Tehcniques*, vol. 52, no. 3, pp. 1014–1024, 2004.

[29] M. Pinuela, P. D. Mitcheson, and S. Lucyszyn, “Ambient RF Energy Harvesting in Urban and Semi-Urban Environments,” *IEEE Trans. Microw. Theory Tech.*, vol. 61, no. 7, pp. 2715–2726, Jul. 2013.

[30] G. J. Snyder and E. . Toberer, “Thermoelectrics,” *Thermoelectrics - Northwestern Materials Science and Engineering*. [Online]. Available: http://thermoelectrics.matsci.northwestern.edu/thermoelectrics/index.html.

[31] T. . Tritt and M. A. Subralanian, “Thermoelectric Materials, Phenomena, an Applications: A Bird’s Eye View,” *MRS Bull.*, vol. 31, 2005.

[32] “Micropelt - Technology,” *Micropelt*. [Online]. Available: http://micropelt.com/technology.php.

[33] A. Moser, M. Erd, M. Kostic, K. Cobry, M. Kroener, and P. Woias, “Thermoelectric Energy Harvesting from Transient Ambient Temperature Gradients,” *J. Electron. Mater.*, vol. 41, no. 6, pp. 1653–1661, Jun. 2012.

[34] E. Hourdakis and A. Nassiopoulou, “A Thermoelectric Generator Using Porous Si Thermal Isolation,” *Sensors*, vol. 13, no. 10, pp. 13596–13608, Oct. 2013.

[35] J. Xie, X. P. Mane, C. W. Green, K. M. Mossi, and K. K. Leang, “Performance of Thin Piezoelectric Materials for Pyroelectric Energy Harvesting,” *J. Intell. Mater. Syst. Struct.*,

vol. 21, no. 3, pp. 243–249, Feb. 2010.

[36] G. Sebald, D. Guyomar, and A. Agbossou, “On thermoelectric and pyroelectric energy harvesting,” *Smart Mater. Struct.*, vol. 18, no. 12, p. 125006, Dec. 2009.

[37] H. H. S. Chang and Z. Huang, “Laminate composites with enhanced pyroelectric effects for energy harvesting,” *Smart Mater. Struct.*, vol. 19, no. 6, p. 065018, Jun. 2010.

[38] L. Carlioz, J. Delamare, and S. Basrour, “Temperature threshold tuning of a thermal harvesting switch,” in *Solid-State Sensors, Actuators and Microsystems Conference, 2009. TRANSDUCERS 2009. International*, 2009, pp. 1385–1388.

[39] M. Ujihara, G. P. Carman, and D. G. Lee, “Thermal energy harvesting device using ferromagnetic materials,” *Appl. Phys. Lett.*, vol. 91, no. 9, p. 093508, 2007.

[40] T.-K. Chung, U. Shukla, C.-Y. Tseng, C.-C. Chen, and C.-M. Wang, “A magnetic/piezoelectric-based thermal energy harvester,” 2013, p. 86880M.

[41] L. Carlioz, “Générateur piézoélectrique à déclenchement thermo-magnétique,” Institut National Polytechnique de Grenoble-INPG, 2009.

[42] S. Whalen, M. Thompson, D. Bahr, C. Richards, and R. Richards, “Design, fabrication and testing of the P3 micro heat engine,” *Sens. Actuators Phys.*, vol. 104, no. 3, pp. 290–298, May 2003.

[43] S. Monfray, O. Puscasu, G. Savelli, U. Soupremanien, E. Ollier, C. Guerin, L. G. Frechette, E. Leveille, G. Mirshekari, C. Maitre, and others, “Innovative thermal energy harvesting for zero power electronics,” in *Silicon Nanoelectronics Workshop (SNW), 2012 IEEE*, 2012, pp. 1–4.

[44] U. Soupremanien, E. Ollier, N. Salamon, S. Monfray, and T. Skotnicki, “Experimental device designed to obtain repeatable condensation peaks in a close system,” presented at the 5th International Conference on Energy and Sustainability, 2014.

[45] O. Puscasu, S. Monfray, G. Savelli, C. Maitre, J. P. Pemeant, P. Coronel, K. Domanski, P. Grabiec, P. Ancey, P. J. Cottinet, and others, “An innovative heat harvesting technology (HEATec) for above-Seebeck performance,” in *Electron Devices Meeting (IEDM), 2012 IEEE International*, 2012, pp. 12–5.

[46] S. Boisseau, G. Despesse, S. Monfray, O. Puscasu, and T. Skotnicki, “Semi-flexible bimetal-based thermal energy harvesters,” *Smart Mater. Struct.*, vol. 22, no. 2, p. 025021, Feb. 2013.

[47] O. Puscasu, “Dispositifs innovants pour la récupération de l’énergie thermique,” INSA de Lyon, 2014.

[48] J. Boughaleb, S. Monfray, G. Vine, P. J. Cottinet, A. Arnaud, S. Boisseau, A. B. Duret, S. Quenard, O. Puscasu, C. Maitre, S. Trochut, F. Hasbani, T. Di Gilio, V. Heinrich, P. Urard, J. C. Grasset, F. Boeuf, D. Guyomar, and T. Skotnicki, “SPICE modelling of a coupled piezoelectric-bimetal heat engine for autonomous Wireless Sensor Nodes (WSN) power supply,” *J. Phys. Conf. Ser.*, vol. 557, p. 012091, Nov. 2014.

[49] G. B. Torri, X. Rottenberg, D. M. Karabacak, M. Vandecasteele, C. Van Hoof, R. Puers, and H. A. C. Tilmans, “Optimized design and placement of piezoelectric transducers for micromechanical structures subject to membrane stress,” in *Thermal, Mechanical and Multi-Physics Simulation and Experiments in Microelectronics and Microsystems (EuroSimE), 2012 13th International Conference on*, 2012, pp. 1–8.

[50] B. Ando, S. Baglio, A. R. Bulsara, V. Marletta, I. Medico, and S. Medico, “A double piezo—snap through buckling device for energy harvesting,” in *Solid-State Sensors, Actuators and Microsystems (TRANSDUCERS & EUROSENSORS XXVII), 2013 Transducers & Eurosensors XXVII: The 17th International Conference on*, 2013, pp. 43–45.

[51] A. Michael and C. Y. Kwok, “Buckling shape of elastically constrained multi-layered micro-bridges,” *Sens. Actuators Phys.*, vol. 135, no. 2, pp. 870–880, Apr. 2007.

[52] A. F. Arrieta, P. Hagedorn, A. Erturk, and D. J. Inman, “A piezoelectric bistable plate for nonlinear broadband energy harvesting,” *Appl. Phys. Lett.*, vol. 97, no. 10, p. 104102, 2010.

[53] “Piezoelectricity,” *Wikipedia*. [Online]. Available: https://en.wikipedia.org/wiki/Piezoelectricity.

[54] “Quartz Clock,” *Wikipedia*. [Online]. Available: https://en.wikipedia.org/wiki/Quartz_clock.

[55] “Piezoelectric generators: Applications,” *American Piezo*. [Online]. Available: https://www.americanpiezo.com/piezo-theory/generators.html.

[56] “Piezon Products,” *Electro Medical Systems*. [Online]. Available: http://new.ems-company.com/en/dental/piezon-method/piezon-products.html.

[57] “Pyroelectric Detectors: Materials, Applications and Working Principle,” *Laser Components Pyro Group*. [Online]. Available: http://www.lasercomponents.com/de-en/news/pyroelectric-detectors-materials-applications-and-working-principle/.

[58] G. Bertotti and I. D. Mayergoyz, Eds., *The science of hysteresis*, 1st ed. Amsterdam ; Boston: Academic, 2006.

[59] M. Pozzi and M. Zhu, "Plucked piezoelectric bimorphs for knee-joint energy harvesting: modelling and experimental validation," *Smart Mater. Struct.*, vol. 20, no. 5, p. 5007, 2011.

[60] N. S. Shenck and J. A. Paradiso, "Energy scavenging with shoe-mounted piezoelectrics," *IEEE Micro*, vol. 21, no. 3, pp. 30–42, 2001.

[61] "Harvesting kinetic energy from every foosteps," *PaveGen Systems*. [Online]. Available: http://pavegen.com/home.

[62] H.-B. Fang, J.-Q. Liu, Z.-Y. Xu, L. Dong, L. Wang, D. Chen, B.-C. Cai, and Y. Liu, "Fabrication and performance of mems-based piezoelectric power generator for vibrations energy harvesting," *Microelectron. J.*, vol. 37, no. 11, pp. 1280–1284, 2006.

[63] E. Lefeuvre, A. Badel, C. Richard, L. Petit, and D. Guyomar, "A comparison between several vibration-powered piezoelectric generators for standalone systems," *Sens. Actuators Phys.*, vol. 126, no. 2, pp. 405–416, Feb. 2006.

[64] M. Marzencki, M. Defosseux, and S. Basrour, "MEMS Vibration Energy Harvesting Devices With Passive Resonance Frequency Adaptation Capability," *J. Microelectromechanical Syst.*, vol. 18, no. 6, pp. 1444–1453, Dec. 2009.

[65] M. Renaud, T. Sterken, A. Schmitz, P. Fiorini, C. Van Hoof, and R. Puers, "Piezoelectric harvesters and MEMS technology: fabrication, modeling and measurements," in *Solid-State Sensors, Actuators and Microsystems Conference, 2007. TRANSDUCERS 2007. International*, 2007, pp. 891–894.

[66] R. Elfrink, M. Renaud, T. M. Kamel, C. de Nooijer, M. Jambunathan, M. Goedbloed, D. Hohlfeld, S. Matova, V. Pop, L. Caballero, and R. van Schaijk, "Vacuum-packaged piezoelectric vibration energy harvesters: damping contributions and autonomy for a wireless sensor system," *J. Micromechanics Microengineering*, vol. 20, no. 10, p. 104001, Oct. 2010.

[67] N. M. White, P. Glynne-Jones, and S. P. Beeby, "A novel thick-film piezoelectric micro-generator," *Smart Mater. Struct.*, vol. 10, no. 4, p. 850, 2001.

[68] S.-J. Jeong, J.-S. Kim, and H.-K. Lee, "Two-layered piezoelectric bender device for micro-power generator," *Sens. Actuators Phys.*, vol. 148, no. 1, pp. 158–167, 2008.

[69] T. J. Kaźmierski and S. Beeby, Eds., *Energy Harvesting Systems*. New York, NY:

Springer New York, 2011.

[70] M. Defosseux, "Conception et caractérisation de microgénérateurs piézoélectriques pour microsystèmes autonomes," Université de Grenoble, 2011.

[71] N. Chidambaram, A. Mazzalai, and P. Muralt, "Comparison of lead zirconate titanate (PZT) thin films for MEMS energy harvester with interdigitated and parallel plate electrodes," in *Applications of Ferroelectrics held jointly with 2012 European Conference on the Applications of Polar Dielectrics and 2012 International Symp Piezoresponse Force Microscopy and Nanoscale Phenomena in Polar Materials (ISAF/ECAPD/PFM), 2012 Intl Symp*, 2012, pp. 1–4.

[72] K. Nam, Y. Park, B. Ha, D. Shim, and I. Song, "Piezoelectric properties of aluminum nitride for thin film bulk acoustic wave resonator," *J. Korean Phys. Soc.*, vol. 47, pp. S309–S312, Sep. 2005.

[73] M. W. Hooker, "Properties of PZT-Based piezoelectric Ceramics between-150 and 250 C." NASA/CR-1998-208708, 1998.

[74] B. Ahmed Seddik, G. Despesse, and E. Defay, "Wideband mechanical energy harvester based on piezoelectric longitudinal mode," in *New Circuits and Systems Conference (NEWCAS), 2012 IEEE 10th International*, 2012, pp. 453–456.

[75] H. Xue, Y. Hu, and Q. M. Wang, "Broadband piezoelectric energy harvesting devices using multiple bimorphs with different operating frequencies," *IEEE Trans. Ultrason. Ferroelectr. Freq. Control*, vol. 55, no. 9, pp. 2104–2108, 2008.

[76] H. Yu, J. Zhou, L. Deng, and Z. Wen, "A Vibration-Based MEMS Piezoelectric Energy Harvester and Power Conditioning Circuit," *Sensors*, vol. 14, no. 2, pp. 3323–3341, Feb. 2014.

[77] R. Ramlan, M. J. Brennan, B. R. Mace, and I. Kovacic, "Potential benefits of a non-linear stiffness in an energy harvesting device," *Nonlinear Dyn.*, vol. 59, no. 4, pp. 545–558, Mar. 2010.

[78] B. Andò, S. Baglio, C. Trigona, N. Dumas, L. Latorre, and P. Nouet, "Nonlinear mechanism in MEMS devices for energy harvesting applications," *J. Micromechanics Microengineering*, vol. 20, no. 12, p. 125020, Dec. 2010.

[79] A. F. Arrieta, T. Delpero, A. E. Bergamini, and P. Ermanni, "Broadband vibration energy harvesting based on cantilevered piezoelectric bi-stable composites," *Appl. Phys. Lett.*, vol. 102, no. 17, p. 173904, 2013.

[80] Z. Wang, S. Matova, R. Elfrink, M. Jambunathan, C. de Nooijer, R. van Schaijk, and R. J. M. Vullers, "A piezoelectric vibration harvester based on clamped-guided beams," in *Micro Electro Mechanical Systems (MEMS), 2012 IEEE 25th International Conference on*, 2012, pp. 1201–1204.

[81] N. Heidrich, F. Knöbber, V. Polyakov, V. Cimalla, W. Pletschen, R. E. Sah, L. Kirste, S. Leopold, S. Hampl, O. Ambacher, and V. Lebedev, "Corrugated piezoelectric membranes for energy harvesting from aperiodic vibrations," *Sens. Actuators Phys.*, vol. 195, pp. 32–37, Jun. 2013.

[82] M. Ferrari, V. Ferrari, M. Guizzetti, B. Andò, S. Baglio, and C. Trigona, "Improved energy harvesting from wideband vibrations by nonlinear piezoelectric converters," *Sens. Actuators Phys.*, vol. 162, no. 2, pp. 425–431, 2010.

[83] H. Liu, C. Lee, T. Kobayashi, C. J. Tay, and C. Quan, "Investigation of a MEMS piezoelectric energy harvester system with a frequency-widened-bandwidth mechanism introduced by mechanical stoppers," *Smart Mater. Struct.*, vol. 21, no. 3, p. 035005, Mar. 2012.

[84] I.-T. Tang, H.-J. Chen, W. . Hwang, Y. . Wang, M.-P. Houng, and Y.-H. Wang, "Applications of piezoelectric ZnO film deposited on diamond-like carbon coated onto Si substrate under fabricated diamond SAW filter," *J. Cryst. Growth*, vol. 262, no. 1–4, pp. 461–466, Feb. 2004.

[85] M. Clement, L. Vergara, J. Sangrador, E. Iborra, and A. Sanz-Hervás, "SAW characteristics of AlN films sputtered on silicon substrates," *Ultrasonics*, vol. 42, no. 1–9, pp. 403–407, Apr. 2004.

[86] M. Gorisse, A. Reinhardt, C. Billard, M. Borel, E. Defay, T. Bertaud, T. Lacrevaz, and C. Bermond, "Lateral Field Excitation of membrane-based Aluminum Nitride resonators," 2011, pp. 1–5.

[87] M.-A. Dubois and P. Muralt, "Properties of aluminum nitride thin films for piezoelectric transducers and microwave filter applications," *Appl. Phys. Lett.*, vol. 74, no. 20, pp. 3032–3034, 1999.

[88] R. Elfrink, V. Pop, D. Hohlfeld, T. M. Kamel, S. Matova, C. De Nooijer, M. Jambunathan, M. Goedbloed, L. Caballero, M. Renaud, and others, "First autonomous wireless sensor node powered by a vacuum-packaged piezoelectric MEMS energy harvester," in *Electron Devices Meeting (IEDM), 2009 IEEE International*, 2009, pp. 1–4.

[89] M. Renaud, K. Karakaya, T. Sterken, P. Fiorini, C. Van Hook, and R. Puers, "Fabrication, modelling and characterization of MEMS piezoelectric vibration harvesters," *Sens. Actuators Phys.*, vol. 145, pp. 380–386, 2007.

[90] P. Muralt, M. Marzencki, B. Belgacem, F. Calame, and S. Basrour, "Vibration Energy Harvesting with PZT Micro Device," *Procedia Chem.*, vol. 1, no. 1, pp. 1191–1194, Sep. 2009.

[91] Y. Jeon, R. Sood, L. Steyn, and S.-G. Kim, "Energy harvesting MEMS devices based on d33 mode piezoelectric Pb (Zr, Ti) O3 thin film cantilever," in *CIRP Seminar on Micro and Nano Technology*, 2003.

[92] R. Bruchhaus, D. Pitzer, R. Primig, M. Schreiter, and W. Wersing, "Sputtering of PZT thin films for surface micromachine IR-detector arrays," *Integr. Ferroelectr.*, vol. 25, pp. 1–11, 1999.

[93] K. Tsuchiya, T. Kitagawa, and E. Nakamachi, "Development of RF magnetron sputtering method to fabricate PZT thin film actuator," *Precis. Eng.*, vol. 27, no. 3, pp. 258–264, 2003.

[94] F. A. Pizzarello and J. E. Coker, "Structural and piezoelectric propoerties of epitaxial AlN on Al2O3," *J. Electron. Mater.*, vol. 4, no. 1, pp. 25–36, 1975.

[95] Y. M. Kim, W. J. Lee, and H. G. Kim, "Deposition of PZT films by MOCVD at low temperature and their change in properties with annealing temperature and Zr/Ti ratio," *Thin Solid Films*, vol. 279, no. 1–2, pp. 140–144, 1996.

[96] E. Hong, J. C. Shin, J. Choi, C. S. Hwang, and H. J. Kim, "Perparation and characterization of PZT thin films by MOCVD using a solid delivery system," *J. Mater. Res.*, vol. 15, no. 6, pp. 1284–1290, 2000.

[97] F. Calame and P. Muralt, "Growth and properties of gradient free sol-gel lead zirconate titanate thin films," *Appl. Phys. Lett.*, vol. 90, no. 6, p. 062907, 2007.

[98] G. Piazza, V. Felmetsger, P. Muralt, R. H. Olsson III, and R. Ruby, "Piezoelectric aluminum nitride thin films for microelectromechanical systems," *MRS Bull.*, vol. 37, no. 11, pp. 1051–1061, Nov. 2012.

[99] P. Muralt, T. Maeder, L. Sagalowicz, S. Hiboux, S. Scalese, D. Naumovic, R. G. Agostino, N. Xanthopoulos, H. J. Mathieru, L. Patthey, and E. L. Bullock, "Texture control of PbTiO3 and Pb(Zr,Ti)O3 thin films with TiO2 seeding," *J. Appl. Phys.*, vol. 83, no. 7, pp. 3835–3841, 1998.

[100] N. Ledermann, P. Muralt, J. Baborowski, S. Gentil, K. Mukati, M. Cantoni, A. Seifert, and N. Setter, "{100}-textured, piezoelectric Pb(Zrx,Tix)O3 thin films for MEMS: integration, deposition and properties," *Sens. Actuators Phys.*, vol. 105, pp. 162–170, 2003.

[101] A. Artieda, "AIN Thin Film Structures for High-Q Resonators," ÉCOLE POLYTECHNIQUE FÉDÉRALE DE LAUSANNE, 2010.

[102] N. Chidambaram, A. Mazzalai, and P. Muralt, "Measurement of effective piezoelectric coefficients of PZT thin films for energy harvesting application with interdigitated electrodes," *IEEE Trans. Ultrason. Ferroelectr. Freq. Control*, vol. 59, no. 8, pp. 1624–1631, Aug. 2012.

[103] M. Foeth, "Determination of the Thermal Broadening of Ferroelectric Domain Walls using Quantitative Transmission Electron Microscopy," Ecole Polytechnique Fédérale de Lausanne, 1999.

[104] Y. Arimoto and H. Ishiwara, "Current Status of Ferroelectric Random-Access Memory," *MRS Bull.*, vol. 29, no. 11, pp. 823–828, Nov. 2004.

[105] T. Jungk, A. Hoffmann, and E. Soergel, *Ferroelectric Crystals for Photonic Applications: Including Nanoscale Fabrication and Characterziation Techniques*, Springer Series in Materials Science. P. Ferraro et al., 2014.

[106] S. V. Kalinin, S. Jesse, B. J. Rodriguez, J. Shin, A. P. Baddorf, H. N. Lee, A. Borisevich, and S. J. Pennycook, "Spatial resolution, information limit, and contrast transfer in piezoresponse force microscopy," *Nanotechnology*, vol. 17, no. 14, pp. 3400–3411, Jul. 2006.

[107] S. Trolier-McKinstry and P. Muralt, "Thin film piezoelectrics for MEMS," *J. Electroceramics*, vol. 12, no. 1–2, pp. 7–17, 2004.

[108] P. Gerber, A. Roelofs, C. Kugeler, U. Bottger, R. Waser, and K. Prume, "Effects of the top-electrode size on the piezoelectric properties (d33 and S) of lead zirconate titanate thin films," *J. Appl. Phys.*, vol. 96, no. 5, 2004.

[109] E. Defaÿ, C. Zinck, C. Malhaire, N. Baboux, and D. Barbier, "Modified free vibrating beam method for characterization of effective e[sub 31] coefficient and leakage resistance of piezoelectric thin films," *Rev. Sci. Instrum.*, vol. 77, no. 10, p. 103903, 2006.

[110] A. Mazzalai, D. Balma, N. Chidambaram, L. Jin, and P. Muralt, "Simultaneous piezoelectric and ferroelectric characterization of thin films for MEMS actuators," in

Applications of Ferroelectric and Workshop on the Piezoresponse Force Microscopy (ISAF/PFM), 2013 IEEE International Symposium on the, 2013, pp. 363–366.

[111] K. Wasa, T. Matsushima, H. Adachi, I. Kanno, and H. Kotera, "Thin-Film Piezoelectric Materials For a Better Energy Harvesting MEMS," *J. Microelectromechanical Syst.*, vol. 21, no. 2, pp. 451–457, Apr. 2012.

[112] S. Priya, "Criterion for material selection in design of bulk piezoelectric energy harvesters," *Ultrason. Ferroelectr. Freq. Control IEEE Trans. On*, vol. 57, no. 12, pp. 2610–2612, 2010.

[113] D. Ambika, V. Kumar, H. Imai, and I. Kanno, "Sol-gel deposition and piezoelectric properties of {110}-oriented Pb(Zr[sub 0.52]Ti[sub 0.48])O[sub 3] thin films," *Appl. Phys. Lett.*, vol. 96, no. 3, p. 031909, 2010.

[114] D. Isarakorn, "Epitaxial Piezoelectric MEMS on Silicon," EPFL, 2011.

[115] K. Wasa, I. Kanno, H. Kotera, N. Yamauchi, and T. Matsushima, "Thin films of PZT-based ternary perovskite compounds for MEMS," 2008, pp. 213–216.

[116] D. Isarakorn, D. Briand, P. Janphuang, A. Sambri, S. Gariglio, J.-M. Triscone, F. Guy, J. W. Reiner, C. H. Ahn, and N. F. de Rooij, "The realization and performance of vibration energy harvesting MEMS devices based on an epitaxial piezoelectric thin film," *Smart Mater. Struct.*, vol. 20, no. 2, p. 025015, Feb. 2011.

[117] M. Brissaud, *Matériaux Piézoélectriques - Caractérisation, modélisation et vibration*. PPUR.

[118] D. Guyomar, A. Badel, E. Lefeuvre, and C. Richard, "Toward energy havresting using active materials and conversion improvement by nonlinear processing," *Ultrason. Ferroelectr. Freq. Control IEEE Trans. On*, vol. 52, no. 4, pp. 584–595, 2005.

[119] E. Lefeuvre, A. Badel, C. Richard, and D. Guyomar, "Piezoelectric energy harvesting device optimization by synchronous electric charge extraction," *J. Intell. Mater. Syst. Struct.*, vol. 16, no. 10, pp. 865–876, 2005.

[120] M. Deterre, E. Lefeuvre, and E. Dufour-Gergam, "An active piezoelectric energy extraction method for pressure energy harvesting," *Smart Mater. Struct.*, vol. 21, no. 8, p. 085004, Aug. 2012.

[121] A. Badel and E. Lefeuvre, "Wideband Piezoelectric Energy Harvester Tuned Through its Electronic Interface Circuit," *J. Phys. Conf. Ser.*, vol. 557, p. 012115, Nov. 2014.

[122] F. E. Vanslager, “THE LATERAL BUCKLING OF A STRAIGHT OR CURVED BEAM SUBJECTED TO PURE BENDING,” DTIC Document, 1968.

[123] C. Hsu and W. Hsu, “Instability in micromachined curved thermal bimorph structures,” *J. Micromechanics Microengineering*, vol. 13, no. 6, p. 955, 2003.

[124] S. Park and D. Hah, “Pre-shaped buckled-beam actuators: Theory and experiments,” *Sens. Actuators Phys.*, vol. 148, no. 1, pp. 186–192, Nov. 2008.

[125] P. Cazottes, A. Fernandes, J. Pouget, and M. Hafez, “Bistable Buckled Beam: Modeling of Actuating Force and Experimental Validations,” *J. Mech. Des.*, vol. 131, no. 10, p. 101001, 2009.

[126] F. Chapuis, F. Bastien, J.-F. Manceau, F. Casset, and P. L. Charvet, “FEM modelling of Piezo-actuated Microswitches,” in *Thermal, Mechanical and Multiphysics Simulation and Experiments in Micro-Electronics and Micro-Systems, 2006. EuroSime 2006. 7th International Conference on*, 2006, pp. 1–6.

[127] A. Michael, “MEMS Micro-Bridge Actuator For Potential Application In Optical Switching,” The University of New South Wales Sydney, Australia, 2007.

[128] M. Taher and A. Saif, “On a tunable bistable MEMS - Theory and experiment,” *J. Microelectromechanical Syst.*, vol. 9, no. 2, pp. 157 – 170, 2000.

[129] C. T. Leondes, Ed., *MEMS/NEMS Handbook - Techniques and Applications*, Springer., vol. 1: Design methods, 5 vols. 2005.

[130] “Technical data Element Periodic Table,” *Periodictable*. [Online]. Available: http://periodictable.com/Elements/013/data.html.

[131] S. Timoshenko and J. N. Goodier, *Theory of Elasticity*. McGraw-Hill Book Company, Inc., 1951.

[132] S. Timoshenko and others, “Analysis of bi-metal thermostats,” *J Opt Soc Am*, vol. 11, no. 3, pp. 233–255, 1925.

[133] A. Arnaud, J. Boughaleb, S. Monfray, F. Boeuf, O. Cugat, and T. Skotnicki, “Thermo-mechanical efficiency of the bimetallic strip heat engine at the macro-scale and micro-scale,” *J. Micromechanics Microengineering*, vol. 25, p. 104003.

[134] C. B. Yeager and S. Trolier-McKinstry, “Epitaxial Pb(Zrx,Ti1−x)O3 (0.30 ≤ x ≤ 0.63) films on (100)MgO substrates for energy harvesting applications,” *J. Appl. Phys.*, vol. 112, no. 7, p. 074107, 2012.

[135] R. Matloub, M. Hadad, A. Mazzalai, N. Chidambaram, G. Moulard, C. S. Sandu, T. .

Metzger, and P. Muralt, “Piezoelectric Al1−xScxN thin films: A semiconductor compatible solution for mechanical energy harvesting and sensors,” *Appl. Phys. Lett.*, vol. 102, no. 15, p. 152903, 2013.

[136] T. M. Kamel, R. Elfrink, M. Renaud, D. Hohlfeld, M. Goedbloed, C. de Nooijer, M. Jambunathan, and R. van Schaijk, “Modeling and characterization of MEMS-based piezoelectric harvesting devices,” *J. Micromechanics Microengineering*, vol. 20, no. 10, p. 105023, Oct. 2010.

[137] M.-A. Dubois and P. Muralt, “Measurement of the effective transverse piezoelectric coefficient e 31, f of AlN and Pb (Zr x, Ti 1- x) O 3 thin films,” *Sens. Actuators Phys.*, vol. 77, no. 2, pp. 106–112, 1999.

[138] V. V. Felmetsger, P. N. Laptev, and S. M. Tanner, “Innovative technique for tailoring intrinsic stress in reactively sputtered piezoelectric aluminum nitride films,” *J. Vac. Sci. Technol. Vac. Surf. Films*, vol. 27, no. 3, p. 417, 2009.

[139] M.-A. Dubois and P. Muralt, “Stress and piezoelectric properties of aluminum nitride thin films deposited onto metal electrodes by pulsed direct current reactive sputtering,” *J. Appl. Phys.*, vol. 89, no. 11, p. 6389, 2001.

[140] L. B. Freund, J. A. Floro, and E. Chason, “Extensions of the Stoney formula for substrate curvature to configurations with thin substrates or large deformations,” *Appl. Phys. Lett.*, vol. 74, no. 14, p. 1987, 1999.

[141] M. A. Hopcroft, W. D. Nix, and T. W. Kenny, “What is the Young’s Modulus of Silicon?,” *J. Microelectromechanical Syst.*, vol. 19, no. 2, pp. 229–238, Apr. 2010.

[142] T. I. Toho, “Toho_FLX2320Sv4.pdf.” [Online]. Available: www.tohotechnology.com.

[143] F. Martin, P. Muralt, M.-A. Dubois, and A. Pezous, “Thickness dependence of the properties of highly c-axis textured AlN thin films,” *J. Vac. Sci. Technol. Vac. Surf. Films*, vol. 22, no. 2, p. 361, 2004.

[144] E. Trioux, S. Monfray, T. Skotnicki, P. Muralt, and S. Basrour, “Fabrication of bilayer plate for a micro thermal energy harvester,” in *SENSORS, 2014 IEEE*, 2014, pp. 2171–2174.

[145] T. C. Hodge, S. A. Bidstrup-Allen, and P. A. Kohl, “Stresses in Thin Film Metallization,” *IEEE Trans. Compon. Packag. Manuf. Technol. - Part A*, vol. 20, no. 2, p. 241, 1997.

[146] M.-A. Dubois, "Aluminium Nitride and Lead Zirconate-Titanate thin films for ultrasonic applications: Integration, Properties and Devices," Ecole Polytechnique Fédérale de Lausanne, 1999.

[147] E. Milyutin, S. Harada, D. Martin, J. F. Carlin, N. Grandjean, V. Savu, O. Vaszquez-Mena, J. Brugger, and P. Muralt, "Sputtering of (001)AlN thin films: Control of polarity by a seed layer," *J. Vac. Sci. Technol. B Microelectron. Nanometer Struct.*, vol. 28, no. 6, p. L61, 2010.

[148] D. Bouvet, "Dektak Manual," *CMi - EPFL*. [Online]. Available: https://cmi.epfl.ch/metrology/dektak.php.

[149] C. Hibert, "Veeco Manual," *CMi - EPFL*. [Online]. Available: https://cmi.epfl.ch/metrology/Wyko_NT1100.php.

[150] X. Feng, Y. Huang, H. Jiang, D. Ngo, and A. J. Rosakis, "The effect of thin film/substrate radii on the Stoney formula for thin film/substrate subjected to nonuniform axisymmetric misfit strain and temperature," *J. Mech. Mater. Struct.*, vol. 1, no. 6, pp. 1041–1053, 2006.

[151] M. Akiyama, T. Kamohara, K. Kano, A. Teshigahara, Y. Takeuchi, and N. Kawahara, "Enhancement of Piezoelectric Response in Scandium Aluminum Nitride Alloy Thin Films Prepared by Dual Reactive Cosputtering," *Adv. Mater.*, vol. 21, no. 5, pp. 593–596, Feb. 2009.

[152] R. van Schaijk, R. Elfrink, J. Oudenhoven, V. Pop, Z. Wang, and M. Renaud, "A MEMS vibration energy harvester for automotive applications," 2013, p. 876305.

[153] E. Trioux, S. Monfray, T. Skotnicki, S. Basrour, and P. Muralt, "Characterization of piezoelectric material for micro thermal harvesters," *J. Phys. Conf. Ser.*, vol. 557, p. 012087, Nov. 2014.

[154] N. Chidambaram, D. Balma, R. Nigon, A. Mazzalai, R. Matloub, C. S. Sandu, and P. Muralt, "Converse mode piezoelectric coefficient for lead zirconate titanate thin film with interdigitated electrode," *J. Micromechanics Microengineering*, vol. 25, no. 4, p. 045016, Apr. 2015.

[155] M. Hadis and O. Umit, *Zinc Oxide: Fundamentals, Materials and Devices Technology*. John Wiley & Sons, 2008.

[156] S. P. Matova, M. Renaud, M. Jambunathan, M. Goedbloed, and R. Van Schaijk, "Effect of length/width ratio of tapered beams on the performance of piezoelectric

energy harvesters," *Smart Mater. Struct.*, vol. 22, no. 7, p. 075015, Jul. 2013.

[157] D. Benasciutti, L. Moro, S. Zelenika, and E. Brusa, "Vibration energy scavenging via piezoelectric bimorphs of optimized shapes," *Microsyst. Technol.*, vol. 16, no. 5, pp. 657–668, May 2010.